



UNIVERSITÄT  
BAYREUTH

---

# Coherent ionization dynamics induced by intense X-ray free-electron laser pulses

---

Von der Universität Bayreuth  
zur Erlangung des Grades eines  
Doktors der Naturwissenschaften (Dr. rer. nat.)  
genehmigte Abhandlung

von

André Brand

geboren am 3. April 1987 in Neustadt a.d. Waldnaab

1. Gutachter: Prof. Dr. Vollrath Martin Axt
2. Gutachter: Prof. Dr. Stephan Kümmel

Tag der Einreichung: 4. September 2015

Tag des Kolloquiums: 18. Januar 2016



## Abstract

### Coherent ionization dynamics induced by intense X-ray free-electron laser pulses

In this dissertation, theoretical models of atoms, clusters, and solids irradiated by ultrashort and intense pulses from an (X-ray) free-electron laser are investigated with the objective to find appropriate conditions where coherent dynamics manifests itself in physical observables. The ionization dynamics induced by an X-ray or extreme ultraviolet laser pulse is typically dominated by inner-shell one-photon absorption and subsequent relaxation processes, ultimately leading to sequential multiphoton ionization. If atoms are exposed to laser pulses with a photon energy well separated from absorption edges, a rate-equation description is generally sufficient for describing the temporal evolution of charge states. As this thesis is geared towards *coherent* ionization dynamics, scenarios have been selected for further analysis where the energy of incident photons is either in the vicinity of or below the most relevant absorption edge.

Resonant two-photon absorption is discussed within a generic model comprising a two-level system plus an energetically separated continuum of states. The two discrete states are in resonance with the electric field of a laser pulse; the ground state energy (relative to the lowest continuum state) is less than twice the photon energy, allowing for an ionization process based on the absorption of two photons. Under these circumstances, the results of two distinct approaches are compared. In the Markovian theory, on the one hand, the coupling to the continuum is reduced to the rate-equation level while possible Rabi cycling between the two discrete states is fully taken into account. The rate-equation approach, on the other hand, further simplifies the situation by treating the two-level system analogous to the Einstein rate equations. It is demonstrated that the ionization probability grows quadratically with increasing number of incident photons for weak pulses, which goes over into a linear scaling behavior for more intense pulses. This finding is supported by both approaches despite the fact that the underlying mechanisms are fundamentally different in the Markovian and the rate-equation theory. The observed phenomenon is attributed to either Rabi cycling or equal populations induced by an equilibrium of absorption and stimulated emission. Even though the ionization yield does not allow drawing a conclusion which of the two theories is more adequate over a broad intensity range, they turn out to be still distinguishable with regard to the crossover between these two intensity regimes of quadratic and linear scaling. If, for instance, the Markovian theory is applicable, the onset of the transition is hence governed by the Rabi frequency instead of the photon number. Finally, it is shown that the Rabi frequency as a key variable in this scenario is subject to a renormalization due to the coupling to the continuum.

Furthermore, an atomic crystal is simulated in one space dimension (1d) based on a Kronig-Penney model while disregarding the electron-electron interaction. Correspondingly, emphasis is placed on the short-time dynamics during sub- and few-femtosecond pulses, where the Auger processes are assumed to be virtually frozen. The direct one-photon absorption is allowed in all cases, but the photon energy is always chosen to have similar values as the *K*-edge, thus generating only slow photoelectrons. As long as the analyses are confined to the short times before the onset of relaxation processes, the rate equations for independent atoms would yield no dependence of the ionization probability on the pulse duration if the total photon number is kept constant. In contrast, time-dependent Schrödinger equation calculations demonstrate a

strong dependence on the duration of transform-limited pulses. This observation is the combined result of different causes. Transform-limited subfemtosecond pulses are spectrally very broad, causing a large portion of the spectrum to overlap with the band gaps. Therefore, the ionization probability tends to decrease for short pulses or, conversely, longer pulse durations enhance the radiation damage to the crystal. This trend breaks for few-femtosecond pulses as soon as the energy selection rule becomes sufficiently strong so that fewer states are available for efficiently driven transitions. Hence, the radiation damage decreases with increasing pulse durations on the longer time scale. Provided that the relaxation of off-diagonal elements of the one-body reduced density matrix is not too fast, the ionization probability turns out to be close to zero for a certain pulse duration of a few femtoseconds. This is interesting because returning the sample back to its initial state by the very same pulse responsible for the excitation might open up entirely new experimental possibilities at free-electron lasers. Complicating a potential experimental realization, a heavy dependence on the pulse characteristics of this feature is seen. For stronger pulses, Rabi-like dynamics is observed, reflected in both the occupation numbers and the electron density, which exhibits characteristics of a standing wave before being partially reabsorbed. In this context, the tuning of the photon energy for systematically coming as close as possible to an ideal scenario for prominent Rabi-like dynamics is investigated.

To address the discrepancies between the dynamics of the isolated atom and the model crystal with respect to the anticipated ionization probability, one investigates short ordered chains of atoms as an intermediate level between a single atom and an infinite crystal. For this purpose, all approximations from the model crystal are retained including the reduction to one space dimension so that the considered chains contain a crystal similar to the model system studied before in the limiting case of a large number of atoms. This approach deliberately disregards electrostatic trapping in order to identify another trapping mechanism based on a coherent time evolution, analogous to the findings obtained from the crystal model. Likewise, it is seen that the forming of standing waves inhibits the electron flux away from the atom chain and may lower the ionization probability via Pauli blocking, resulting in a localization effect and a reduced ionization. Focusing on the charge density in the vicinity of the middle atom, one surprisingly discovers that the infinite-crystal limit is reached for comparatively low number of atoms. Relatedly, a significant modification of the evolution of the charge density is seen for a chain comprising only three atoms, thereby clearly showing another trapping effect which does not originate from electrostatic interactions. Further simulations with reduced models indicate that these observations do neither require the buildup of a band structure –accompanied by a modified density of states– nor efficient potential scattering of photoelectrons. It is concluded that the coherent trapping phenomenon can be traced back to quantum interferences. Moreover, two generalizations of the model address further questions. Firstly, it is demonstrated that introducing disorder to the chain only marginally affects the results. Secondly, a time-dependent Hartree-Fock approach, which takes electrostatic trapping into account, turns out to even weaken the localization effect in comparable scenarios. In particular, no enhancement of the trapping is seen by considering both mechanisms simultaneously.

In summary, a pronounced impact of coherent dynamics is seen in all considered systems due to the choice of photon energies close to an absorption edge or a resonant transition. This condition is often met in the region of vacuum and extreme ultraviolet or in the soft X-ray region, and may also be fulfilled in the X-ray regime the presence of heavy atoms such as iron  ${}_{26}\text{Fe}$  or highly charged ions.

## Kurzfassung

### Kohärente Ionisationsdynamik hervorgerufen von den intensiven Pulsen eines Röntgenlicht-Freie-Elektronen-Lasers

In dieser Dissertation werden theoretische Modelle von mit ultrakurzen und intensiven Pulsen eines (Röntgenlicht-)Freie-Elektronen-Lasers wechselwirkenden Atomen, Clustern und Festkörpern untersucht, wobei das Ziel darin besteht geeignete Bedingungen zu finden unter denen sich kohärente Dynamik in physikalischen Größen manifestiert. Die Ionisationsdynamik, die von einem Röntgen- oder XUV-Laserpuls hervorgerufen wird, wird typischerweise von Ein-Photon-Absorption aus inneren Schalen und deren nachfolgenden Relaxationsprozessen beherrscht, was letztlich zu sequentieller Multiphotonionisation führt. Wenn Atome Laserpulsen ausgesetzt werden, deren zugehörige Photonenenergie weit von den Absorptionskanten entfernt ist, dann ist eine Beschreibung der zeitlichen Entwicklung von Ladungszuständen im Rahmen von Ratengleichungen im Allgemeinen ausreichend. Da diese Arbeit aber auf *kohärente* Ionisationsdynamik ausgerichtet ist, wurde eine Auswahl von Parameterbereichen vorgenommen, für welche die Energie der einfallenden Photonen entweder in der Nähe oder unterhalb der wichtigsten Absorptionskante liegt.

Zunächst wird resonante Zwei-Photon-Ionisation innerhalb eines generischen Modells bestehend aus einem Zwei-Niveau-System und einem energetisch abgegrenzten Kontinuum an Zuständen behandelt. Die zwei diskreten Zustände sind in Resonanz mit einem den Laserpuls repräsentierenden elektrischen Feld und die Grundzustandsenergie (relativ zum energetisch niedrigsten Kontinuumszustand) ist kleiner als die zweifache Photonenenergie, so dass ein Ionisationsprozess auf der Grundlage einer Absorption zweier Photonen mit der Energieerhaltung verträglich ist. Unter diesen Umständen werden die Ergebnisse zweier verschiedener Herangehensweisen gegenübergestellt. Die Markovsche Theorie auf der einen Seite reduziert die Kopplung an Kontinuumszustände auf die Stufe von Ratengleichungen, während gleichzeitig Rabi-Oszillationen zwischen den beiden diskreten Zuständen vollständig wiedergegeben werden können. Die Ratengleichungen auf der anderen Seite vereinfachen die Situation weiter, indem das Zwei-Niveau-System analog zu den Einsteinschen Ratengleichungen behandelt wird. Es wird dargelegt, dass die Ionisationswahrscheinlichkeit für schwache Pulse einem quadratischen Anstieg mit der Zahl der einfallenden Photonen unterworfen ist und für intensive Pulse in eine lineare Skalierung übergeht. Dieser Befund ist zwar in beiden Modellen gültig, die dahinterstehenden Mechanismen in der Markovschen Theorie und in den Ratengleichungen sind jedoch grundsätzlich verschieden. Das beobachtete Phänomen kann entweder auf Rabi-Oszillationen oder auf eine Gleichbesetzung bedingt durch ein Gleichgewicht zwischen Absorption und stimulierter Emission zurückgeführt werden. Obwohl die Ionisationswahrscheinlichkeit in einem breiten Intensitätsbereich keine Rückschlüsse darauf erlaubt, welche der beiden Theorien angemessen ist, erweisen sie sich dennoch als unterscheidbar in Bezug auf den Übergang zwischen der quadratischen und der linearen Skalierung. Unter der Voraussetzung der Zulässigkeit der Markovschen Theorie ist das Einsetzen jenes Übergangs nämlich durch die Rabi-Frequenz anstelle der Photonenzahl bestimmt. Zuletzt wird gezeigt, dass die Schlüsselgröße Rabi-Frequenz in diesem Szenario aufgrund der Kopplung an das Kontinuum einer Renormalisierung unterliegt.

Anschließend wird ein Atomkristall in einer Raumdimension auf Basis eines Kronig-Penney-Modells ohne Berücksichtigung einer Elektron-Elektron-Wechselwirkung simuliert. Dementsprechend wird der Schwerpunkt auf die Kurzzeitdynamik während der Laserpulse mit Dauern von unterhalb einer Femtosekunde bis zu wenigen Femtosekunden gelegt, wobei Augerzerfall als praktisch erstarrt angenommen wird. Direkte Ein-Photon-Absorption wird zwar in allen Fällen zugelassen, aber für die Photonenenergie werden stets Werte in der Nähe der  $K$ -Kante gewählt, so dass nur langsame Photoelektronen erzeugt werden. Solange die Untersuchungen auf die kurzen Zeiten vor dem Eintreten der Relaxationsprozesse eingeschränkt werden, ergäbe eine Anwendung von Rattengleichungen für unabhängige Atome bei fester Gesamtzahl von Photonen keine Abhängigkeit der Ionisationswahrscheinlichkeit von der Pulsdauer. Rechnungen basierend auf der zeitabhängigen Schrödingergleichung weisen im Gegensatz dazu bei Fourier-limitierten Pulsen eine starke Pulslängenabhängigkeit auf. Diese Beobachtung ergibt sich aus dem Zusammenspiel verschiedener Ursachen. Fourier-limitierte Sub-Femtosekunden sind spektral sehr breit und bewirken, dass ein großer Anteil des Spektrums mit den Bandlücken überlappt. Folglich zeigt die Ionisationswahrscheinlichkeit eine abnehmende Tendenz für kurze Pulse, beziehungsweise der Strahlenschaden am Kristall nimmt mit längerer Pulsdauer zu. Dieser Trend bricht für Pulsdauern von wenigen Femtosekunden ab, sobald die Energieauswahlregel hinreichend scharf wird, so dass weniger Zustände für effizient getriebene Übergänge zur Verfügung stehen. Infolgedessen weist der Strahlenschaden auf der längeren Zeitskala eine abnehmende Tendenz mit steigender Pulsdauer auf. Falls die Relaxation von Nichtdiagonalelementen der reduzierten Ein-Teilchen-Dichtematrix nicht zu schnell vonstatten geht, erhält man für eine bestimmte Pulsdauer von wenigen Femtosekunden eine beinahe verschwindende Ionisationswahrscheinlichkeit. Dies ist insofern interessant, als eine Rückführung einer Probe zu ihrem Anfangszustand durch genau denselben Puls, der auch für die Anregung verantwortlich ist, völlig neue experimentelle Möglichkeiten für Freie-Elektronen-Laser eröffnen könnte. Allerdings lässt sich eine starke Abhängigkeit dieses Merkmals von den Pulseigenschaften feststellen, wodurch eine mögliche experimentelle Umsetzung erschwert wird. Für stärkere Pulse beobachtet man Rabi-ähnliche Dynamik. Dies spiegelt sich sowohl in den Besetzungszahlen als auch in der Elektronendichte, welche vor einer teilweisen Reabsorption Charakteristika von stehenden Wellen zeigt, wider. In diesem Kontext wird eine systematische Abstimmung der Photonenenergie zur Herstellung möglichst idealer Bedingungen für eine hervorstechende Rabi-ähnliche Dynamik untersucht.

Aufgrund der gravierenden Unterschiede der Dynamik in puncto erwarteter Ionisationswahrscheinlichkeit zwischen einem einzelnen Atom und dem Modellkristall werden schließlich kurze geordnete Ketten von Atomen als Mittelweg zwischen dem einzelnen Atom und dem unendlichen Kristall untersucht. Zu diesem Zweck werden alle Näherungen des Modellkristalls beibehalten, inklusive der Einschränkung auf eine Raumdimension. Demzufolge enthalten die in Betracht gezogenen Ketten einen Kristall, der starke Ähnlichkeiten zum vorher beleuchteten Modellsystem hat, als Grenzfall für eine sehr große Anzahl von Atomen. Diese Herangehensweise lässt elektrostatischen Einfang bewusst außer Acht, um einen davon verschiedenen Einfangmechanismus identifizieren zu können, der analog zu den aus dem Kristallmodell gewonnenen Erkenntnissen auf kohärenter Zeitentwicklung basiert. Es offenbart sich ebenso, dass das Ausformen von stehenden Wellen den sich von der Atomkette wegbewegenden Elektronenfluss hemmt und dass die Ionisationswahrscheinlichkeit durch das Pauli-Verbot gemindert wird. Dies hat einen Lokalisationseffekt und eine reduzierte Ionisation zur Folge. Erstaunlicherweise wird

der Grenzfall eines unendlichen Kristalls hinsichtlich der Ladungsdichte in der Umgebung des mittleren Atoms bereits für eine verhältnismäßig kleine Anzahl von Atomen erreicht. In diesem Zusammenhang ergeben sich bereits für eine Kette bestehend aus nur drei Atomen signifikante Änderungen in der Zeitentwicklung der Ladungsdichte. Dabei wird offensichtlich ein weiteres Einfangphänomen demonstriert, das nicht von elektrostatischer Wechselwirkung herrührt. Weitere Simulationen mit vereinfachten Modellen geben Aufschluss darüber, dass diese Beobachtungen weder des Aufbaus einer Bandstruktur –einhergehend mit einer abgewandelten Zustandsdichte– noch effizienter Potentialstreuung von Photoelektronen bedürfen. Es wird geschlussfolgert, dass das kohärente Einfangphänomen auf quantenmechanische Interferenzen zurückzuführen ist. Darüber hinaus werden zur Beantwortung weitergehender Fragen zwei Verallgemeinerungen des Modells herangezogen. Zum einen wird gezeigt, dass sich Unordnung in der Kette nur geringfügig auf die Ergebnisse auswirkt. Zum anderen stellt sich heraus, dass eine zeitabhängige Hartree-Fock-Methode, die den elektrostatischen Einfang berücksichtigt, den Lokalisationseffekt in vergleichbaren Situationen sogar abschwächt. Insbesondere wird der Einfang nicht dadurch begünstigt, dass beide Mechanismen gleichzeitig in Betracht gezogen werden.

Insgesamt zeichnet sich ein markanter Einfluss kohärenter Dynamik in allen betrachteten Systemen ab, was vor allem auf die Photonenenergien in der Nähe einer Absorptionskante oder eines resonanten Übergangs zurückzuführen ist. Diese Voraussetzung lässt sich im Spektralbereich von Vakuum- oder Extrem- Ultravioletter Strahlung oder weicher Röntgenstrahlung leicht erfüllen, kann beim Vorhandensein schwerer Atome wie etwa Eisen  ${}_{26}\text{Fe}$  oder stark geladener Ionen aber auch für Röntgenstrahlung vorliegen.



# Contents

<b>Abbreviations</b>	<b>IX</b>
<b>I. Introduction and current state of research</b>	<b>1</b>
I.1. X-ray free-electron lasers (XFELs)	2
I.2. Overview on science with XFELs	4
I.2.1. Ionization of atoms by XFELs	4
I.2.2. Ionization of clusters and molecules by XFELs	6
I.2.3. Ionization of solids by XFELs	9
I.2.4. Applications of XFELs	10
I.3. Serial femtosecond crystallography	10
I.3.1. General concept of SFX	12
I.3.2. The phase problem in crystallography	13
I.3.3. Recent developments in SFX	15
I.4. Theoretical methods	16
<b>II. Basic assumptions of the applied models</b>	<b>19</b>
II.1. Electron-photon interaction	20
II.2. Electron-electron interaction	21
II.3. Discussion	23
<b>III. Resonant two-photon ionization</b>	<b>27</b>
III.1. Generic model	27
III.2. Equations of motion	29
III.2.1. Resonant approximation	30
III.2.2. Markovian theory	31
III.2.3. Rate-equation approach (REA)	31
III.2.4. Interpretation of the parameters	32
III.3. Results	34
III.3.1. Ionization yield	34
III.3.2. Renormalization of Rabi frequencies	39
<b>IV. Coherent ionization dynamics in crystals</b>	<b>41</b>
IV.1. Theory	41
IV.2. Equations of motion	44
IV.2.1. Schrödinger equation for non-interacting electrons	44
IV.2.2. Resonant approximation	45
IV.2.3. Markovian theory	47
IV.2.4. Atomic and spectrally averaged rates	48

IV.3. Results . . . . .	49
IV.3.1. Ionization dynamics at moderate doses . . . . .	49
IV.3.2. Rabi cycling . . . . .	53
IV.3.3. Spatiotemporal behavior of the electron density . . . . .	54
<b>V. Coherent ionization dynamics in clusters</b>	<b>57</b>
V.1. Theory . . . . .	58
V.1.1. Collective-atoms model (CAM) . . . . .	58
V.1.2. Independent-atoms model (IAM) . . . . .	60
V.1.3. Reflectionless potential . . . . .	61
V.1.4. Time-dependent Hartree-Fock (TDHF) model . . . . .	61
V.2. Results . . . . .	62
V.2.1. Time-dependent charge density in the crystal limit . . . . .	63
V.2.2. Evolution of the charge density in short ordered chains (SOCs) . . . . .	65
V.2.3. Ionization yield of SOCs . . . . .	68
V.2.4. The impact of reflections . . . . .	70
V.2.5. The impact of disorder . . . . .	72
V.2.6. The impact of electrostatic trapping . . . . .	73
<b>VI. Numerical methods</b>	<b>75</b>
VI.1. Boundary conditions . . . . .	76
VI.2. Discrete variable representation (DVR) . . . . .	78
VI.3. Lobatto DVR . . . . .	81
VI.4. Finite-element DVR (FEDVR) . . . . .	85
VI.5. Numerical time propagation . . . . .	88
VI.6. Time-dependent Hartree-Fock . . . . .	92
<b>VII. Conclusions and outlook</b>	<b>95</b>
<b>A. Atomic units</b>	<b>97</b>
<b>B. Technical details of the FEDVR</b>	<b>99</b>
<b>C. Test cases</b>	<b>105</b>
<b>Bibliography</b>	<b>107</b>
<b>Publications</b>	<b>133</b>
<b>Acknowledgments</b>	<b>135</b>
<b>Eidesstattliche Versicherung</b>	<b>137</b>

# Abbreviations

XATOM	X-ray and atomic physics [computational toolkit]
1RDM	one-body reduced density matrix
1d	one [space] dimension, 1-dimensional
2LS	two-level system
3d	three [space] dimensions, 3-dimensional
AL	Anderson localization
ATI	above-threshold ionization
BMBF	Bundesministerium für Bildung und Forschung
BZ	Brillouin zone
CAM	collective-atoms model
CAMP	CFEL-ASG Multi-Purpose [instrument at LCLS]
CAP	complex absorbing potential
CDI	coherent diffractive imaging [of non-periodic objects]
CN	Crank-Nicolson [method]
CSPAD	Cornell-SLAC Pixel Array Detector
CXI	Coherent X-ray Imaging, refers to the CXI instrument at LCLS
DVR	discrete variable representation
EM	electron microscopy
ESRF	European Synchrotron Radiation Facility
European XFEL	European X-Ray Free-Electron Laser
FDM	finite difference method
FEDVR	finite-element discrete variable representation
FEL	free-electron laser
FEM	finite element method
FERMI	An FEL user facility in Trieste, Italy
FiPy	A finite volume PDE solver using Python
FLASH	Freie-Elektronen-Laser in Hamburg
FWHM	full width at half maximum
GAMESS	General Atomic Molecular and Electronic Structure System [suite of programs]
GDR	giant (dipole) resonance
GL	Gauss-Lobatto [quadrature]
GMRES	generalized minimal residual [method]
GPL	GNU General Public License
HDF5	Hierarchical Data Format 5
HF	Hartree-Fock [method]
HFS	Hartree-Fock-Slater [model]

HGHG	high-gain harmonic generation
HHG	high-harmonic generation
I/O	input/output
IAM	independent-atoms model
IBS	inverse bremsstrahlung
ICD	interatomic or intermolecular Coulombic decay
IMEX	implicit-explicit [method]
IPD	ionization potential depression
IVP	(pure) initial value problem
KP	Kronig-Penney [potential]
LCLS	Linac Coherent Light Source
MAD	multiwavelength anomalous diffraction
MCTDHF	multiconfigurational time-dependent Hartree-Fock [method]
MD	molecular dynamics
MPI	Message Passing Interface
NEGF	nonequilibrium Green's function
NMR	nuclear magnetic resonance
NTI	near-threshold ionization
NWChem	NorthWest computational Chemistry [software package]
ODE	ordinary differential equation
OPA	one-photon absorption
PDB	Protein Data Bank
PDE	partial differential equation
PETRA III	Positron-Elektron-Tandem-Ring-Anlage III
PETSc	Portable, Extensible Toolkit for Scientific Computation
pnCCD	p-n junction charge-coupled device
REA	rate-equation approach
REXMI	resonance-enabled X-ray multiple ionization
RIXS	resonant inelastic X-ray scattering (also referred to as resonant X-ray Raman scattering)
RK	Runge-Kutta [method]
RK3BS	Runge-Kutta-Bogacki-Shampine [method]
RK5DP	Runge-Kutta-Dormand-Prince [method]
RK5F	Runge-Kutta-Fehlberg [method]
RWA	rotating wave approximation
SACLA	SPring-8 Angstrom Compact free electron LAser
SAD	single-wavelength anomalous diffraction
SAR	spectrally averaged rates
SASE	self-amplified spontaneous emission
SC	soft-core [potential]
SFX	serial femtosecond [X-ray] crystallography
SI	International System of Units
SLEPc	Scalable Library for Eigenvalue Problem Computations

SO	split-operator [technique]
SOC	short ordered chain
SSP	strong stability-preserving [time discretization method]
SUSY	supersymmetry
SwissFEL	Swiss Free-Electron Laser
TbCatB	Trypanosoma brucei Cathepsin B
TDCIS	time-dependent configuration-interaction singles
TDDFT	time-dependent density-functional theory
TDHF	time-dependent Hartree-Fock [method]
TDRDM	time-dependent reduced density-matrix [theory]
TDSE	time-dependent Schrödinger equation
TOF	time-of-flight [spectroscopy]
TPA	two-photon absorption
TVD	total variation diminishing [property]
VUV	vacuum ultraviolet, refers to the region of the electromagnetic spectrum which corresponds to photon energies from 10 eV to 50 eV [1]
VUV-FEL	Vacuum-Ultra-Violet Free-Electron Laser
WS	Wigner-Seitz [cell]
X-ray	refers to the region of the electromagnetic spectrum which corresponds to photon energies from 250 eV to 100 keV [2]
XFEL	X-ray free-electron laser
XFELo	X-ray free-electron laser oscillator
XPCS	X-ray photon correlation spectroscopy
XUV	extreme ultraviolet (the acronym EUV is also common in the literature), refers to the region of the electromagnetic spectrum which corresponds to photon energies from 30 eV to 250 eV [1]

By and large, the acronyms introduced above are used consistently in the literature. If the full names are rarely used and do not provide additional insights, as it is, inter alia, the case with the names of synchrotron and free-electron laser facilities, only the abbreviations will be printed in the main text.



# I

# Introduction and current state of research

This dissertation is concerned with the interaction of extremely intense, ultrashort X-ray pulses provided by an X-ray free-electron laser (XFEL) with various forms of matter, ranging from individual atoms to an extended solid. To give a precise idea of the meaning of the terms *extremely intense* and *ultrashort* in the context of XFELs, consider, for instance, the following recently conducted experiment: Yoneda et al. (2014) [3] reported intensities up to  $10^{20}$  W/cm<sup>2</sup> within a pulse duration of less than 7 fs at a photon energy of 7.1 keV. Owing to their unique capabilities, XFELs have been demonstrated to create solid-density plasmas (see Sec. I.2) and to provide the possibility for new experimental techniques such as the so-called serial femtosecond crystallography (SFX), which allows to outrun the limitations of conventional crystallography on ultrafast time scales (see Sec. I.3). In essence, one expects from this method nothing less than to revolutionize the field of structural biology. The basic concept of SFX, often described as *diffraction before destruction*, may seem simple at first glance, but in fact it assumes a detailed understanding of the ionization dynamics. Thus, a variety of experiments have been devoted to this matter, leading to the observation of strongly ionized atoms such as fully-stripped neon Ne<sup>10+</sup> and highly charged xenon Xe<sup>36+</sup> (see Sec. I.2). The present work is conceived as a contribution to the research on ionization dynamics with a particular focus on a coherent time evolution and its implications on XFEL experiments. Although many experiments which indicated no signatures of coherent dynamics have been performed at XFEL facilities so far (such as the measurement of the charge-state distribution of isolated atoms irradiated with XFEL pulses, see Sec. I.2), coherent dynamics proves to be crucial in other cases (see Sec. I.4). In this context, it is emphasized that the aim is not to work out small corrections to certain experiments but to identify and qualitatively understand scenarios in similar XFEL based experiments where a coherent quantum mechanical approach is crucial for the theoretical description of the experiment. This approach is interesting for several reasons. Firstly, it may support deepening the understanding of the limitations of an incoherent time evolution via a rate-equation approach. Secondly, one can address the question whether coherent dynamics may be beneficial for experimental techniques such as SFX even though initial estimates of its feasibility relied on rate equations. Thirdly, it is future-oriented insofar as XFEL beam conditions will improve (see Sec. I.1), thereby potentially revealing quantum phenomena.

This thesis is structured as follows. Chapter I is dedicated to an in-depth overview on the current status of the science with XFELs with a special focus on SFX to acknowledge its rapid progress in the course of the recent years. Moreover, current developments of XFEL facilities are briefly discussed and the experimental limitations are emphasized. Chapter II is a summary of the assumptions and simplifications that are employed in the model systems throughout the thesis. Chapters III, IV, and V are intended to highlight coherent phenomena in ultrafast ionization dynamics induced by an XFEL pulse under appropriate conditions in various physical systems: Chapter III addresses the ionization dynamics of individual atoms, Chapter IV discusses an infinitely extended crystal, and Chapter V investigates small groups of atoms. Next, Chapter VI

deals with the numerical procedures that were implemented in order to obtain the results of Chapters III, IV, and V while mentioning the anticipated obstacles to a potential extension of the theory from a numerical perspective. Eventually, a summary is given in Chapter VII.

The present thesis is, along with the work by Kaiser (2014) [4], part of a BMBF project with emphasis placed on the impact of XFEL pulses on atomic scattering factors and the scattering pattern [5]. For more information on the topic closer to the project specification, it is referred to the findings of, e.g., Son et al. (2011) [6], who extensively dealt with this problem in the early stages of the project, thus leading to a shifted focus of the present work.

Important note: Atomic units are used throughout in all equations; see App. A for details.

## I.1. X-ray free-electron lasers (XFELs)

Presently, XFEL facilities are still rare in comparison to synchrotron radiation sources based on storage rings [7], so it is virtually inevitable in the scientific XFEL community to be aware of the following four prominent XFEL facilities. Two of them, namely FLASH (Germany, formerly VUV-FEL, first user operation in 2005) [8, 9] and FERMI (Italy, first user operation in 2011) [10, 11], operate in the soft X-ray regime. The other two, LCLS [12–14] (USA, first user operation in 2009) and SACLA [15–17] (Japan, first user operation in 2012), provide harder X-rays with photon energies up to 20 keV [18]. The number of XFELs will grow in the near future due to upcoming facilities such as European XFEL [19, 20] (Germany, first user operation scheduled for 2016) and the SwissFEL [21, 22] (Switzerland, first use operation scheduled for 2017). For an up-to-date overview on current and planned XFELs including the parameter ranges, consult, e.g., Refs. [7, 23]. The principle and functionality of XFELs will not be addressed due to the availability of extensive literature [24–35], but instead some background and recent developments will be presented in order to illustrate the difficulties and limitations of current XFEL experiments. Furthermore, the differences between XFELs and conventional lasers or third generation synchrotron radiation sources will be accentuated<sup>1</sup>.

Unlike the rapid recent development of XFEL suggests, FELs in general have a long history that goes back over forty years. Madey (1971) [36] constructed an FEL operating at infrared wavelengths in a cavity, whereas the aforementioned XFEL facilities and ongoing projects are designed as single-pass amplifiers [32] other than early proposals suggested [37]. Contemporary XFELs do not obey this design principle because of the lack of high reflectivity normal-incidence mirrors<sup>2</sup> in the X-ray regime [30, 40]. For the sake of completeness, it is pointed out that X-ray mirrors are not the only challenge; a detailed discussion of technical problems that FELs are subject to for X-ray but not for infrared wavelengths can be found in Ref. [27, p. 53 et seq.]. On a side note, recent progress with high-reflectivity normal-incidence X-ray mirrors based on Bragg diffraction in synthetic diamond crystals could potentially pave the way for so-called X-ray free-electron laser oscillators (XFELOs) [41–43].

<sup>1</sup>It is assumed that the reader is familiar with the general layout of XFELs, conventional lasers, and storage-ring-based X-ray radiation sources.

<sup>2</sup>Note that grazing-incidence mirrors in the X-ray regime are feasible and extensively utilized in, e.g., Kirkpatrick-Baez geometry for focusing the XFEL beam (see Ref. [38] for details). These mirrors are based on external total reflection, which is a distinguished feature of the X-ray regime [39].

Compared to a conventional quantum (X-ray) laser, the theory of XFELs is based on classical electrodynamics and is –without the requirement for discrete states– thus useful in a wide range of the electromagnetic spectrum. In principle, a continuous wavelength tunability is possible. FELs designed in accordance with the principle of self-amplified spontaneous emission (SASE) [44] start from shot noise in the electron beam and, accordingly, generate radiation with stochastic features (cf. [45] and references therein). As an alternative to SASE, an external laser can be used to initiate the emission of coherent radiation, which reduces the adaptability and the accessible wavelength range but in return improves temporal coherence and stability [11, 46, 47]. Seeding is typically achieved by high-harmonic generation (HHG) as demonstrated by Ackermann et al. (2013) [46] at FLASH with the 21st harmonic of a Ti:sapphire laser pulse or high-gain harmonic generation (HG), which constitutes the basis for FERMI [11]. Additionally, a technique called *self-seeding* has been shown to improve temporal coherence at LCLS [48].

Rohringer et al. (2012) [49] demonstrated the feasibility of a conventional X-ray laser provided that a sufficiently fast and intense pump laser is available in order to achieve population inversion despite dominating nonradiative decay channels such as Auger decay. Indeed, a SASE XFEL was employed as pump laser in order to create a population inversion of the  $K\alpha$  transition of singly ionized neon [49, 50]. This scheme is capable of improving pulse properties such as temporal coherence by taking advantage of the fact that Doppler and collisional broadening are negligible for low-density gases and short time scales. However, the pulse intensity suffers at an energy conversion efficiency of 0.4%. Other concepts for X-ray lasers are based on plasma physics, achieving population inversion via electron collisions and recombination [40]. Ritson (1987) [51] reported another ambitious attempt to realize an X-ray laser as a part of the *US Strategic Defense Initiative*, namely a nuclear-explosion pumped X-ray laser. This scheme –aside from being still science fiction 30 years later– has the serious disadvantage that the device itself is destroyed after its first use by the initial nuclear explosion.

Compared to third generation synchrotron radiation sources such as PETRA III or ESRF, the *spectral brightness*<sup>3</sup>, i.e., the number of photons per second, mm<sup>2</sup>, mrad<sup>2</sup>, and 0.1% bandwidth (definition from Ref. [30]), is roughly 8 orders of magnitude larger at XFELs, reflecting the simultaneous increase in total power, the decrease in beam divergence, and the narrower spectrum [30, p. 165 et seqq.]. It should also be noted that for technical reasons, linear accelerators are indispensable for XFELs because even modern storage rings cannot provide the necessary electron beam quality [30].

Despite the variety of distinguished features of XFELs, such as the unprecedented peak spectral brightness, there are still a lot of nontrivial technical limitations which have been overcome only recently and are to some extent subject of ongoing research. For example, the characterization of XFEL pulses is a challenging task [53]. An early experiment by Young et al. (2010) [54] suggested that the so-called *nominal pulse duration*, a widespread term for the electron bunch length in the accelerator [55], overestimates the actual X-ray pulse duration. The pulse-length measurements by Düsterer et al. (2011) [56] confirmed this finding via a cross-correlation technique developed for pulse durations over 40 fs. The interpretation is also consistent with streaking spectroscopy, which was shown to enable full temporal characterization of pulses with durations below 10 fs in single-shot measurements, so it allows to investigate

<sup>3</sup>The terms (*spectral*) *brightness* and *brilliance* are often used interchangeably (e.g., by Schmüser et al. (2014) [30]). Unfortunately, the nomenclature is not consistent throughout the literature; see Refs. [27, 52] for details.

non-reproducible temporal profiles of [SASE](#) pulses [57–59]. Furthermore, synchronization is an important issue in pump-probe experiments due to the intrinsic timing jitter of [SASE XFELs](#) [60–66]. Other examples of current technical development involve polarization control [67], focusing [38], coherence properties [68], and detector design [69].

## I.2. Overview on science with XFELs

The present section is primarily devoted to the fundamental phenomena of ionization dynamics of atoms, molecules, clusters, and solids irradiated by [XFEL](#) pulses as this topic alone led to a variety of recent publications in high-ranking journals. The most important results reported in the literature for the different types of samples are outlined separately, divided into subsections according to the size of the samples, i.e., atoms, molecules and clusters, and solids, reflecting the overall structure of the present thesis. Finally, in the last part of this section, some applications for [XFELs](#) are presented which to a greater or lesser extent require a thorough understanding of ionization pathways.

### I.2.1. Ionization of atoms by XFELs

The electronic response of noble-gas atoms from  ${}^6\text{Ne}$  to  ${}_{54}\text{Xe}$  at photon energies from 800 eV up to 5.5 keV was extensively studied in Refs. [54, 55, 70–73] using by and large the same basic experimental setup<sup>4</sup>: a supersonic gas jet of noble-gas atoms is intersected with a focused [XFEL](#) beam in an ultrahigh-vacuum reaction chamber in order to best possibly reproduce the same conditions at each shot by automatically replenishing the sample according to the repetition rate of the laser system (up to 120 Hz at [LCLS](#)). After irradiation of the gas target, the charge states of ions are measured by means of a [time-of-flight \(TOF\)](#) analyzer. This technique can also be used to record photoelectron and Auger spectra [79] or ion kinetic-energy distributions [80]. Additionally, [Rudek et al. \(2012\)](#) [55] simultaneously recorded fluorescence spectra for xenon using [pnCCD](#) detectors.

The resulting charge-state distributions are predominantly interpreted within a [rate-equation approach \(REA\)](#) based on the [Hartree-Fock-Slater \(HFS\)](#) approximation (see also Secs. [I.4](#) and [II.2](#)) as a theoretical model, referring to the continuously extended [X-ray and atomic physics \(XATOM\)](#) computational toolkit. Remarkably, each of these experiments provided evidence for multiphoton ionization at a photon energy of up to 5.5 keV [72]. Note that only a few years earlier [Wabnitz et al. \(2005\)](#) [74] were the first to demonstrate multiphoton ionization at a photon energy above 10 eV [81], and this experiment, in turn, was performed at a considerably lower photon energy of 12.7 eV at [FLASH](#).

It should be borne in mind that multiphoton ionization is fundamentally different in the [X-ray](#) and in the long-wavelength regime: the absorption of only one [X-ray](#) photon usually permits a transition to a (more highly) charged state, whereas at long wavelengths typically many photons are needed to trigger an ionization event. Accordingly, sequential [one-photon absorption \(OPA\)](#) of inner-shell electrons plays a key role in the ionization dynamics of noble-gas

<sup>4</sup>Similar experiments with noble-gas atoms have also been performed earlier at [FLASH](#) at lower photon energies between 12.7 and 93 eV in Refs. [74–78].

atoms at the aforementioned photon energies of 0.8 to 5.5 keV. Each absorption process leaves behind an ion that occupies a core-hole state, initiating –potentially even a cascade of– relaxation processes such as the Auger (Coster-Kronig) decay and fluorescence. In the case of low atomic numbers  $Z < 20$ , radiationless Auger decay dominates over fluorescence [82], so, instead of emitting a photon, another electron is ejected and possibly another core-hole state is created. Simultaneously, shakeoff processes may enhance the occurrence of higher charge states as well [70, 72]. In general, autoionization is vital for understanding the charge-state distribution: for instance, in Ref. [72] each 5.5 keV OPA causes in xenon on average 5 ionization events due to subsequent processes, ultimately producing up to  $\text{Xe}^{26+}$ . As a result, the associated time scales of these mechanisms are crucial for an estimate of charge states based on a theoretical model. For example, the photoabsorption cross section decreases considerably in the presence of inner-shell vacancies, which eventually leads to *intensity-induced X-ray transparency* (also referred to as *frustrated absorption*) for short pulse lengths [54]. This phenomenon is similar to *saturable absorption*, defined as the decrease of photon absorption with increasing intensity. Although this effect is well-known at longer wavelengths, the experimental evidence in the XUV and X-ray regime is significantly more challenging to obtain because of the rapid relaxation processes associated with the excited states created by high-energy photons. In fact, saturable absorption in core-electron transitions was observed only shortly before at FLASH by Nagler et al. (2009) [83]. If, however, inner-shell vacancies are refilled within the pulse duration by sufficiently fast relaxation processes, sequential OPA of inner-shell electron continues and leads to highly charged ions.

On the one hand, the processes described so far allow a basic understanding of the dynamics of atoms irradiated by XFEL pulses, for instance, the charge-state distributions for neon and xenon observed in Refs. [54, 55] at 2.0 keV photon energy, which include fully-stripped neon  $\text{Ne}^{10+}$  and xenon charge states up to  $\text{Xe}^{32+}$ . On the other hand, there are many situations requiring a more elaborated theory where the situation differs only with respect to the photon energy. Three examples shall be discussed in the following.

Firstly, the experimental value of the *two-photon absorption (TPA)* cross section for highly charged neon ions  $\text{Ne}^{8+}$  at a photon energy of 1.11 keV reported by Doumy et al. (2011) [70] deviates from the theoretical value based on HFS by two orders of magnitude. It was concluded that the  $1s^2 - 1s4p$  resonance is likely to be responsible for the large discrepancy between experiment and theory. However, the comparison is complicated by the fact that the TPA cross section strongly depends on the spectral density of the pulse [84] and thus cannot be assessed theoretically for an insufficiently characterized XFEL pulse.

Secondly, Rudek et al. (2012) [55] experimentally observed xenon charge states up to  $\text{Xe}^{36+}$  at a photon energy of 1.5 keV, whereas the theory outlined so far predicts an entirely different charge-state distribution with the highest charge state being  $\text{Xe}^{27+}$ . This outcome is intriguing insofar as the prediction of  $\text{Xe}^{32+}$  at a photon energy of 2.0 keV and  $\text{Xe}^{26+}$  at 5.5 keV [72] was in good agreement with the experiment. The contradiction between experiment and theory is resolved by taking another mechanism into account, namely, *resonance-enabled X-ray multiple ionization (REXMI)*. As certain photon energies are distinguished, it is natural to suppose that resonances play an important role. Indeed, for charge states from  $\text{Xe}^{19+}$  to  $\text{Xe}^{35+}$ , OPA is energetically forbidden at 1.5 keV photon energy, and resonant excitations into Rydberg orbitals are favored instead. Accordingly, core-hole states are generated, and subsequently the ion is

subject to Auger decay, thereby ejecting an electron. The configurations that include excited states with initially unoccupied orbitals were omitted in calculations because the number of states would drastically increase<sup>5</sup>. Similar results in Refs. [71, 73] were also attributed to REXMI.

Thirdly and lastly, In the XUV regime, many experiments [75, 77, 86, 87] at FLASH were performed in order to investigate the intensely discussed collective behavior of xenon which potentially manifests itself in the form of the *giant (dipole) resonance (GDR)*<sup>6</sup> and the *giant enhancement* in the HHG spectrum [91, 92] at photon energies around 100 eV. Sorokin et al. (2007) [75] observed Xe<sup>21+</sup> –corresponding to an absorption of at least 57 XUV photons– as the maximum charge state in TOF spectra at a photon energy of 93 eV, an irradiance up to 10<sup>16</sup>W/cm<sup>2</sup>, and an estimated pulse duration of roughly 10 fs. The occurrence of high charge states is under similar conditions significantly lower for lighter noble-gas atoms due to the strong enhancement of the photoionization cross section of xenon by the *giant resonance* [77]. For both the xenon GDR [93, 94] and the giant enhancement in the HHG spectrum [92], extensive theoretical analyses can be found in the literature that go beyond the scope of a short summary.

### 1.2.2. Ionization of clusters and molecules by XFELs

The aim of this subsection is to highlight the differences in XFEL experiments when clusters and molecules are irradiated instead of virtually isolated atoms, particularly with regard to the charge-state distributions obtained from TOF spectra. Note in advance that the description of molecules and clusters which consist of only one atomic species is easier to comprehend because the OPA cross section strongly depends on the atomic number  $Z$ . In more detail, the OPA cross section  $\sigma_{ens}$  for a hydrogen-like atom is analytically calculated as  $\sigma_{ens} \propto Z^5 \cdot n^{-3} \cdot \omega^{-7/2}$  if the  $n$ -shell is (singly) occupied and the photon energy is considerably larger than the ground-state energy [95, p. 416]. This relation correctly reflects the fact that inner-shell electrons are ejected preferably and that heavy atoms are strong absorbers although, phenomenologically, the dependence on the atomic number  $Z$  is rather approximately proportional to  $Z^{2.7}$  [96]. Consequently, the absorption of heteronuclear molecules such as biomolecules is spatially inhomogeneous and thus leads to local distortions under irradiation [97].

Therefore, it is instructive to start with the simple case of a small homonuclear molecule. Hoener et al. (2010) [98] measured the charge-state distribution of irradiated N<sub>2</sub> molecules at a photon energy of 1.1 keV at LCLS. Even though the absorption process involves primarily inner-shell electrons, a REA based on independent atoms analogous to Ref. [54] predicts qualitatively wrong results. The most conspicuous deviation from the theory of independent atoms is that the relative abundances of charge states, which were also obtained from TOF spectra, are higher for N<sup>+</sup> than for N<sup>2+</sup>. A contrary behavior is anticipated from the idea of independent atoms because an inner-shell ionization is typically followed by Auger decay, i.e., the absorption of one photon most likely leads to the ejection of two electrons, thus producing rather N<sup>2+</sup> than N<sup>+</sup>.

<sup>5</sup>This numerical problem was later solved by Ho et al. (2014) [85] (see also Sec. I.4).

<sup>6</sup>The term *giant (dipole) resonance* is commonly associated with collective excitations of atomic nuclei via irradiation with gamma rays, dominating the absorption for photon energies between 10 and 30 MeV [88, 89]. Here, however, (*atomic*) *giant resonance* refers to a collective electronic resonance in xenon, which has a major impact on absorption at photon energies around 100 eV [90, p. 1537]. Note that both the nuclear and the atomic giant resonance have been observed long before the first XFEL was operational (cf. review articles [88, 90]).

However, an adequate theory for the charge-state distribution of the nitrogen molecule developed as an extension of the REA for independent atoms requires to include the dissociation channels. For instance, after photoionization and Auger decay of only one nitrogen atom, i.e.,  $N^{2+}$ -N, the excited molecule may dissociate into two singly ionized atoms,  $N^+$  and  $N^+$ . The physics prior to the fragmentation of the molecule is, by contrast, captured by the rate equations of independent atoms. This interpretation is supported by the observation of *frustrated absorption* for  $N_2$  analogous to Ref. [54] for neon atoms.

The theoretical description of macromolecules and clusters has to be significantly modified compared to independent atoms and the diatomic molecule  $N_2$  because further processes such as *collisional ionization* (also referred to as *secondary ionization* or *impact ionization* [80, 99]), *electron trapping* and (*three-body*) *recombination* gain in importance for a group of  $N \gg 1$  atoms. This can be understood as follows. Imagine for simplicity a group of identical atoms undergoing simultaneous ionization. Analogous to the atomic case, the ionic potential grows with increasing charge state, and thus slower photoelectrons are generated at later times during the pulse. The crucial difference is now that the ejected electrons require a higher amount of kinetic energy to escape the attractive potential of positively charged ions, which approximately rises by a factor of  $N$  compared to the isolated atom as the total charge increases by a factor of  $N$ . As a result, a portion of the emitted electrons will eventually be trapped inside the sample by the Coulomb attraction of positively charged ions. Additionally, Auger electrons and slow electrons stemming from collisional ionization contribute to the trapped-electron population while recombination events reduce the final charge state. Under sufficiently intense irradiation, the combination of these processes creates a nanoplasma, which due to quickly thermalized trapped electrons consists of a net-neutral core localized within a shell of positively charged ions. Later, the nanoplasma expands on the time scale of atomic motion and evaporates within nanoseconds [80, 100].

More specifically, Thomas et al. (2012) [101] conducted an experiment at LCLS at 850 eV photon energy with a xenon-cluster target of roughly 11 000 atoms and identified two key processes which are negligible for independent atoms, namely collisional ionization and three-body recombination. The latter reduces the highest observed charge state in a theoretical model drastically from  $Xe^{26+}$  to  $Xe^{5+}$ . In reality, higher charge states still appear, possibly caused by the phenomenon of a reduced recombination probability for the shell ions around the nanoplasma core. By measuring the kinetic-energy distribution of the ions, evidence for a hydrodynamic expansion of the xenon plasma was found, similar to the observation made by Krikunova et al. (2012) [102] at a lower photon energy of 90 eV at FLASH.

In contrast, Murphy et al. (2014) [80] inferred a Coulombic expansion of fullerene  $C_{60}$  samples from the scaling of the mean ion kinetic energy. The experiment was conducted at LCLS for pulse durations between 4 and 90 fs at a comparatively low photon energy of 485 eV in order to enhance the OPA cross section<sup>7</sup>. Consequently, fully-stripped carbon atoms  $C^{6+}$  were detected based on an efficient photoabsorption of 180 photons per molecule, corresponding to an absorbed energy of 87 keV or a dose of 11.65 GGy. As seen before, collisional ionization and recombination have a significant impact on charge-state distributions. These processes are not directly reliant on the XFEL pulse, i.e., trapped electrons may evaporate or recombine long after

<sup>7</sup>Recall that the *K*-edge of atomic carbon  ${}_6C$  is at  $E_{1s} \approx 284.2$  eV [103, Table 1-1].

the pulse. In fact, the simulations in Ref. [80, Fig. 7b] suggest that recombination persists on a picosecond time scale. Further, molecular Auger effect was taken into account in order to improve the agreement between theoretical and experimental charge-state distributions. Compared to collisional ionization and recombination, however, the contribution from the molecular Auger effect is less pronounced.

Another important question in the context of *serial femtosecond crystallography* (SFX) raised by Murphy et al. (2014) [80] is whether a mechanism analogous to frustrated absorption for neon and molecular nitrogen causes a suppression of photoabsorption also in  $C_{60}$  for sufficiently short pulses even though the number of ionization events due to collisions increases for shorter pulses [80, Fig. 5b]. In the case of atomic neon and molecular nitrogen, frustrated absorption was decisively influenced by atomic Auger decay lifetime in absence of collisional ionization. Here, without a quantitative analysis it cannot even be ruled out that *KLL* Auger decay is entirely suppressed based on an potentially efficient removal of *L*-shell electrons by collisional ionization. However, it turned out that the averaged experimental final charge state is still reduced for decreasing pulse length for  $C_{60}$ , but the driving force behind this behavior is the enhancement of electron trapping in conjunction with recombination.

Interestingly, Murphy et al. (2014) [80] also estimated the impact of chemical bonds and concluded that the disregard of chemical bonds in the theoretical description with respect to the predicted kinetic energies and charge state distribution is applicable for short pulse durations and high intensities. This finding is in accordance with assumptions in early simulations where molecular binding forces were neglected in dynamic calculations compared to the forces between ions [104].

In addition to the studies of homonuclear molecules and clusters, different polyatomic molecules were investigated in Refs. [105–108]. For example, Erk et al. (2013) [108] studied methylselenol under irradiation with intense XFEL pulses at 2 keV photon energy and 5 fs pulse duration at LCLS. A methylselenol molecule  $CH_3SeH$  consists, apart from the light constituents hydrogen and carbon, of one heavy atom, namely selenium  ${}_{34}Se$ . With the photon energy being well below the *K*-edge of neutral selenium of 12.66 keV, *K*-shell OPA is forbidden. In contrast, *L*-shell OPA is feasible; the binding energies of *L*-shell electrons range from 1.43 keV to 1.65 keV [103, Table 1-1]. As mentioned in the beginning of this subsection, heavy atoms are usually stronger absorbers: in quantitative terms, the *L*-shell photoionization for selenium is in this case almost two orders of magnitude more probable than photoabsorption of other atoms. Therefore, the initial absorption is strongly localized at the selenium atom. The *L*-shell vacancy of selenium is most likely refilled by *LMM* Auger decay, similar to the case of isolated atoms. The subsequent relaxation processes which are responsible for the decay of the *M*-shell holes may involve valence electrons of neighboring atoms (*MVV* Auger decay on a time scale of roughly 10 fs). This leads, even without taking collisional ionization into account, to an ultrafast charge rearrangement within the molecule. Furthermore, Erk et al. (2013) [108] found evidence for significant distortions  $> 1 \text{ \AA}$  of the molecule in the vicinity of the heavy atom during the ionization process in spite of the short pulse duration of 5 fs.

Whether processes other than that mentioned above are relevant, critically depends on the wavelength and time scale. Wabnitz et al. (2002) [109] observed a maximum charge state  $Xe^{8+}$  for clusters comprising 1 500 xenon atoms at a photon energy of 12.7 eV despite the fact that only singly ionized xenon was reached for isolated atoms. This substantial difference was attributed

to **inverse bremsstrahlung (IBS)** [109–111]. However, **IBS** plays a minor role for higher photon energies  $\omega$  due to the scaling  $\propto \omega^{-8/3}$  [112, 113]. Likewise, cluster **interatomic or intermolecular Coulombic decay (ICD)** [114–118] can be of importance depending on the time scale. For instance, Schnorr et al. (2013) [118] estimated the **ICD** lifetime of an excited neon dimer  $\text{Ne}_2^+$  ( $2s^{-1}$ ) to be of the order of 100 fs.

### 1.2.3. Ionization of solids by XFELs

In principle, it can be expected that the fundamental phenomena occurring in solids under irradiation with **XFEL** pulses are already known from the studies of large clusters. The situation might be even simpler from a theoretical point of view because boundary effects, such as escaped electrons and the distinction of the positively charged shell around the generated nanoplasma, play a minor role. From an experimental perspective, however, one has to deal with the fact that the charge-state distribution is no longer directly accessible via **TOF** spectra. Indeed, it was seen in the previous subsection that for a sample as small as molecular nitrogen  $\text{N}_2$  the abundance of different charge states sheds light on the dissociation channels rather than on the ionization dynamics during the pulse. For this reason, similar to the aforementioned study on xenon by Rudek et al. (2012) [55], experiments with solid targets are interpreted by means of **X-ray** emission spectroscopy instead. In Refs. [119–121], for instance, an aluminum<sup>8</sup> foil  $_{13}\text{Al}$  was irradiated with **X-ray** pulses of 80 fs duration at photon energies between 1.5 and 1.83 keV at **LCLS** while simultaneously recording the fluorescence spectra, specifically around the  $K\alpha$  line. The  $K\alpha$  line provides information about the electronic configuration of the emitting atom owing to the fact that the values of  $K$ - and  $L$ -shell energies are not equally affected by an increase of the charge state. In general, the  $K\alpha$  line is shifted towards larger frequencies for more highly charged ions. By this means, Vinko et al. (2012) [119] found experimental evidence for the pivotal role of collisional ionization in the solid target. Similar to the study of Murphy et al. (2014) [80] devoted to the fullerene, collisional processes compete with –and may even surpass– Auger decay.

Interestingly, the aluminum foil is heated isochorically due to the comparatively slow atomic nuclei during the pulse duration. To be specific, Vinko et al. (2012) [119] estimated an expansion time of 20 ps for a 1  $\mu\text{m}$  aluminum target. By contrast, the electrons thermalize quickly, and, as a result, a *solid-state density plasma* is formed benefiting from an enhancement of collisional ionization because of the high concentrations of both free electrons and ions.

The theoretical description of the environment-dependent process known as **ionization potential depression (IPD)** based on classical models by, e.g., Stewart and Pyatt (1966) [122] of solid samples was refined for solid-density plasmas [123, 124]. **IPD** has a substantial influence on ionization dynamics of solids by modifying the free-electron temperature and the density distribution, which is in turn imprinted on the collisional rates [121].

One can conclude from the present and the previous subsection that the environment of individual atoms is crucial for a correct description of the ionization dynamics under irradiation with **XFEL** pulses. On the one hand, three-body recombination and trapping effects reduce the radiation damage and, on the other hand, collisional processes enhance the ionization.

<sup>8</sup>Note that the binding energy of  $K$ -shell electrons in neutral  $_{13}\text{Al}$  is 1.56 keV.  $L$ -shell binding energies range from 72.55 eV to 117.8 eV [103, Table 1-1].

#### I.2.4. Applications of XFELs

Naturally, there is a variety of existing and potential applications that profit from XFELs besides basic research on ionization mechanisms, which has been focused on so far. The most prominent technique based on XFELs is undoubtedly *serial femtosecond crystallography* (SFX) to which a separate section, Sec. I.3, in the present chapter is devoted, accordingly. To give a broader view and to avoid the impression of XFELs being single-purpose machines, additional examples of other techniques shall be referred to without going into detail.

The ultraintense X-ray pulses enable nonlinear phenomena that are widespread in the literature for longer wavelengths to be extended to the X-ray regime. For instance, Glover et al. (2012) [125] achieved *X-ray and optical wave mixing*, Shwartz et al. (2014) [126] observed *X-ray Second Harmonic Generation* in diamond at a photon energy of 7.3 keV, and Tamasaku et al. (2014) [127] found experimental evidence for *two-photon absorption* (TPA) at a photon energy of 5.6 keV in germanium.

Furthermore, Raman spectroscopy, which is a standard technique in molecular physics and most commonly employed at optical wavelengths [128], benefits from XFELs as well. Recall that there are several variations of the basic idea behind Raman spectroscopy such as *resonant Raman spectroscopy*, also called *resonant inelastic X-ray scattering* (RIXS) in the X-ray regime. In fact, RIXS is established as a reliable tool, whose feasibility has been shown long before the construction of early XFELs [129], but still the issues of radiation damage and low fluorescence rates compared to Auger decay rates have to be addressed<sup>9</sup>. Based on the high intensities provided by XFELs, it has been shown that one can take advantage of stimulated emission in order to enhance fluorescence yields while simultaneously reducing sample damage inflicted by Auger decay [129–131].

*X-ray photon correlation spectroscopy* (XPCS) [132] in its present state is suitable for the investigation of comparatively slow dynamics down to microseconds at nanometer resolution [133]. For instance, Leitner et al. (2009) [134] reported measurements of dynamics on a time scale of 10 s at atomic resolution at the synchrotron radiation source ESRF. Also XPCS is anticipated to profit from the development of XFELs [133, 135, 136]; in particular, XFELs might be the stepping stone to achieve a temporal resolution on the femtosecond time scale in XPCS.

Finally, it is worth mentioning a few examples of the numerous pump-probe experiments performed at FLASH and SACLA devoted to the investigation of the dissociation of small molecules [137, 138], the temporal evolution of ultrafast phase transitions [139], and spin dynamics [140].

### I.3. Serial femtosecond crystallography

X-ray crystallography [142, 143] as a method for structure determination of macromolecules plays alongside *electron microscopy* (EM) [144] and *nuclear magnetic resonance* (NMR) a major role in the subject area *structural biology* [145] as reflected by the *Protein Data Bank* (PDB)

<sup>9</sup>On a side note, this issue is similar to SFX dealing with low elastic scattering cross sections and, likewise, with radiation damage.

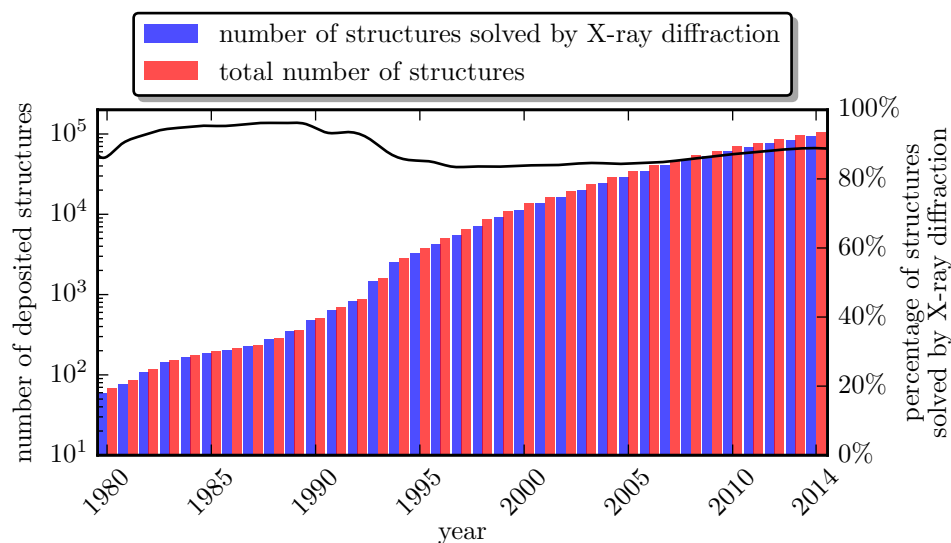


**Figure I.1.:** Amount of structures of macromolecules deposited in the [Protein Data Bank \(PDB\)](#) over the period from 1980 to 2014 with a special focus on the amount structures derived from [X-ray](#) diffraction experiments. The relative importance of the latter is depicted as a black line for clarity, referring to the right y axis. Data obtained from the [PDB](#) web page [141].

[146], which is a well-established<sup>10</sup> archive for structural data of proteins, nucleic acids and their complexes. By the end of 2014, exactly 105 407 structures were available in the [PDB](#), and 93 695 of them have been solved based on [X-ray](#) diffraction experiments. Fig. I.1 shows the development of the [PDB](#) over more than 30 years. The bars indicate the near-exponential growth of deposited structures, demonstrating not only the capacities of the aforementioned methods but also the interest in understanding the function and structure of biological macromolecules for applications such as drug discovery [147, 148]. Also highlighted in Fig. I.1 is the continuous predominance of data based on [X-ray](#) crystallography over time even though crystallography faces the issue of *radiation damage* [96]: photoabsorption cross sections are typically much larger than elastic scattering cross section in the [X-ray](#) regime, so a potentially uncontrolled alteration of the sample during the measurement via absorption is more probable than the mechanism which gives rise to the measured signal [149]. At this point, it is important to note that the radiation damage, quantified by the absorbed dose<sup>11</sup>, is largely independent of the crystal size. The scattering probability of incident photons, quite the contrary, increases with the crystal size while the measured signal may at the same time benefit from coherence. Therefore, a *minimum crystal size* of typically tens of  $\mu\text{m}$  in each direction is required for solving the structure of a macromolecule by [X-ray](#) diffraction [96]. As a result, crystallography is not applicable for approximately 40% of all proteins because they do not form suitable crystals [54]. Examining the situation in more detail, one can estimate a *tolerable dose* limit characterized by the property that the radiation damage to the average protein crystal inflicted by the measurement itself does

<sup>10</sup>As a measure for the popularity of the [PDB](#): the number of citations in the *Web of Science* database of [Berman et al. \(2000\)](#) [146] is 14 054 (status as of 2 September 2015).

<sup>11</sup>The (absorbed) dose is defined as the energy deposited in the crystal divided by its mass and is measured in *gray*,  $1 \text{ Gy} = 1 \text{ J/kg}$ .

not prevent a reconstruction of the structure. At room temperature, the tolerable dose is of the order of 1 MGy, which can be extended up to approximately 30 MGy for crystals cooled to liquid nitrogen temperature [150, 151].

For a protein of average composition  $H_{50}C_{30}N_9O_{10}S_1$ , a simple back-of-the-envelope calculation analogous to Chapman et al. (2014) [149] gives clearer insight into the underlying mechanisms. It is important to note that an exposure of 30 MGy corresponds to 2.27 eV per atom for this average protein. This implies that at the high photon energies of, e.g., 8 keV on average only  $2.27 \text{ eV}/8 \text{ keV} \approx 0.03\%$  of the atoms in the protein crystal absorb a single photon. Assuming an ideally efficient energy redistribution by Auger decay and collisional ionization, it is immediately plausible that only few photoionization events are capable of inflicting severe damage to the whole sample during slow exposure since 2.27 eV per atom are of the order of the energy of chemical bonds. This estimate is consistent with simulations of a urea crystals where one 6 keV photoelectron causes a cascade of secondary electrons and thereby induces 285 ionization events after approximately 100 fs. Hence, due to secondary ionization, an exposure of 400 MGy, which corresponds to  $\approx 0.4\%$  of the atoms in the average-protein crystal absorbing one 8 keV photon, is in general sufficient to trigger one ionization event per atom [149].

### I.3.1. General concept of SFX

The basic idea behind *serial femtosecond crystallography* (SFX) is to overcome radiation damage induced limitations in crystallography by recording the diffraction pattern on a time scale shorter than the dominant ionization mechanisms [152]. In simple words, one uses pulses that deliver just as many photons as needed for collecting the data, ignoring the fact that the resulting dose would utterly destroy the sample after a sufficiently long time. Ultrashort pulse durations are then supposed to solve the issue of radiation damage as they limit the time window of elastic scattering to the initial stage of damage processes. This principle is often summarized as *diffraction before destruction* [149, 153, 154] and holds promise for providing conclusive scattering patterns at doses exceeding 1 GGy, which surpasses the conventional dose limits by orders of magnitude [149]. Accordingly, SFX is applicable for nanocrystals that are too small for structure determination with conventional crystallography [149, 152, 154, 155] and might eventually enable the structure of single molecules to be solved. The prerequisites for SFX can be fulfilled by the distinguished properties of XFELs, most importantly delivering ultrahigh intensities in pulse durations as short as femtoseconds.

A correct interpretation of the diffraction pattern obtained by SFX requires thorough understanding of ionization processes discussed in Sec. I.2. For example, exposing the sample to the same amount of photons on a shorter time scale implies an increase in intensity and thus an enhancement of nonlinear processes such as *two-photon absorption* (TPA) [127]. Fortunately, the probability for these transitions is generally negligible compared to *one-photon absorption* (OPA) for light atoms in the X-ray regime. Moreover, phenomena such as *frustrated absorption* [6, 54, 98, 152] and electron trapping plus recombination [80] result in a reduction of the radiation damage for femtosecond pulses. In fact, hollow atoms are beneficial for imaging experiments insofar as the scattering cross section typically decreases significantly less than the absorption cross section upon the presence of inner-shell vacancies [6, 149, 156]. Collisional ionization can be suppressed with subfemtosecond pulse durations [6, Sec. III E] or by using isolated molecules

instead of crystals [149]. Damage reduction via single-particle imaging assumes, however, that the photoelectron mean free path is larger than the size of the individual molecule, which is not guaranteed in general. Further, single-particle imaging has also certain disadvantages compared to SFX. For instance, one has to consider incoherent scattering [157] and one cannot exploit the phenomenon of *self-terminating Bragg diffraction* [158]. The latter rests upon the idea that the collection of the diffraction pattern is not necessarily terminated by a short X-ray pulse but by the onset uncorrelated motion of atoms destroying the crystalline order and thus the Bragg diffraction.

Principally, the direct retrieval of structures from single-shot diffraction patterns in single-particle imaging of comparatively large samples, such as *bacteriophage T4* at 20 to 40 nm, is feasible [159]. For imaging of biomolecules, however, a high number of diffraction patterns is indispensable in order to improve the signal-to-noise ratio. In fact, this is the origin of the term *serial* in *serial femtosecond crystallography* (SFX). Correspondingly, the sample has to be replaced after the collection of each diffraction pattern because severe radiation damage sets in after the pulse. The continuous supply of pristine samples is realized by a liquid jet intersected with the XFEL beam. As a result, snapshots contain diffraction patterns of the sample in random orientations or—in case the pulse does not hit a sample—no diffraction pattern at all. For instance, Redecke et al. (2013) [151] recorded 4 million snapshots that consisted of 293 195 diffraction patterns, which is obviously a challenge with respect to data processing. Software devoted to this problem has already been developed and is openly available under the GNU General Public License (GPL) [160, 161]. Dealing with the randomly oriented samples is still an important issue, which is addressed in different ways. First, sophisticated solutions for orientation determination have been published in Refs. [154, 162, 163]. Second, diffraction based on aligned single molecules is discussed in the literature [164–167] in order to facilitate the data analysis for structure determination [154].

### 1.3.2. The phase problem in crystallography

The so-called *phase problem* [168] plays a pivotal role in both conventional crystallography and SFX. It can be briefly summarized as follows: by recording the diffraction pattern, one acquires only the magnitude of the elastic scattering factor. Therefore, after having the experimental data collected, the solution of the structure is equivalent to the knowledge of the phases. Correspondingly, structure determination is often also referred to as *phasing*. The key questions are now whether the phases are relevant for structure determination in the first place, and, if so, how to obtain them.

The phase problem can be nicely illustrated by making use of the fact that the Fourier transform not only constitutes the relationship between the elastic scattering factor and the electron density [39] but is also a common image processing technique [169]. Fig. I.2 demonstrates, analogous to Taylor (2003) [168], the issues of a naive attempt at structure determination of a randomly chosen object about which no prior knowledge is assumed. Assume that Fig. I.2a is the measured coherent diffraction pattern, i.e., the intensity pattern produced by the Fourier transform of the structure shown in Fig. I.2b. For an intuitive understanding of the significance of phase information, Figs. I.2c and d answer the question of what can go wrong if incorrect phase information is used in an attempt to derive the structure. It turns out in Fig. I.2c that using the

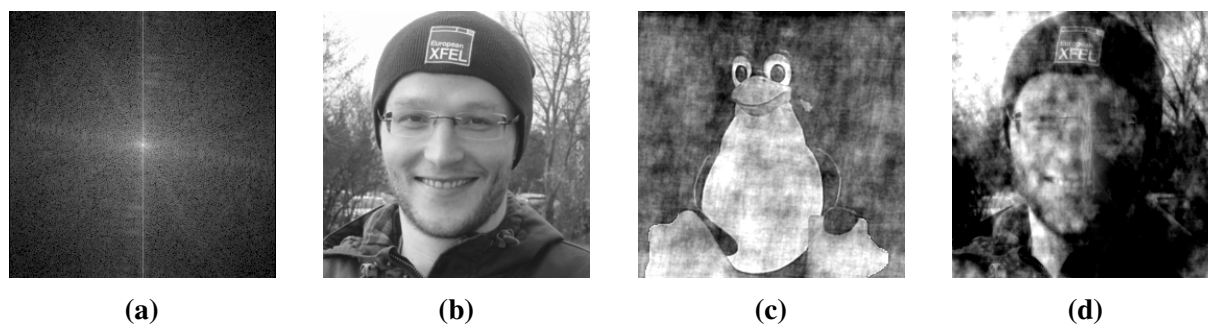


**Figure I.2.:** Illustration of the phase problem by means of the Fourier transform as a standard image processing tool [169] analogous to Taylor (2003) [168] with  $256 \times 256$  pixel images. (a) represents the coherent diffraction pattern of (b) [on a logarithmic scale] or, seen from the opposite perspective, (b) is the structure derived from (a) using the correct phase information. The importance of phase information is demonstrated in (c) and (d): (c) is the result of the attempt to derive the structure (b) from its diffraction pattern using the phase information produced from an entirely different structure, in this case Tux (mascot of the Linux kernel, by Larry Ewing, lewing@isc.tamu.edu, and The GIMP). Inversely, (d) is obtained by using the phase information of the original image (b) and the amplitudes of Tux.

amplitudes produced by the original structure Fig. I.2b in combination with the phases generated from a penguin gives a grasp of the penguin but looks nothing like the original structure. As seen in Fig. I.2d, it works vice versa as well. This visual example demonstrates that phase information is crucial for structure determination, i.e., only amplitudes and phases together reveal nature's beauty in Fig. I.2b.

A lot of techniques have been developed in conventional crystallography to address the phase problem: *single-wavelength anomalous diffraction (SAD)*, *multiwavelength anomalous diffraction (MAD)*, *molecular replacement*, *isomorphous replacement* [143, 168], and *oversampling* [170–172]. The latter method was originally designed for noncrystalline samples and is thus, strictly speaking, developed for another extension of conventional crystallography which is commonly referred to as *coherent diffractive imaging (CDI)* [142]. Miao et al. (2003) [170] demonstrated that oversampling enables solutions of nonperiodic  $\mu\text{m}$ -sized structures at 7 nm resolution at a synchrotron radiation source. The basic idea behind oversampling can be applied to *SFX* by measuring the diffraction amplitudes between Bragg peaks [173–175].

It is not self-evident that these phasing methods, particularly *SAD* and *MAD*, can be easily transferred to *SFX*. Both *SAD* and *MAD* are used at wavelengths near absorption peaks [168] because dispersive effects are most dominant due to the Kramers-Kronig relation between real and imaginary part of the dispersion corrections associated with the atomic scattering factor [39, 143, 176]. To this end, comparatively heavy atoms have to be targeted in accordance with the desired resolution. For example, the *K*-edge of  $_{26}\text{Fe}$  is roughly 7.1 keV [103, Table 1-1], which corresponds to a wavelength of  $\lambda \approx 1.75 \text{ \AA}$  and, in turn, to a diffraction-limited resolution length of approximately  $3.37 \text{ \AA}$  if the angular acceptance of the detector is  $15^\circ$  [177]. Consequently, the sample is subject to strong ionization enhanced by both heavy atoms and the vicinity to absorption edges (cf. Sec. I.2.2). These complications were previously addressed in theoretical studies, and, in this context, novel phasing methods have been proposed which turn the ionization processes into an advantage for phasing [176, 178–180].

### 1.3.3. Recent developments in SFX

In the following, selected milestones and some of the recent accomplishments in SFX or related CDI experiments are summarized while briefly mentioning the respective phasing method. An early proof-of-principle experiment of *diffraction before destruction* at a comparatively large wavelength of  $\lambda = 32$  nm, corresponding to a photon energy of  $\approx 39$  eV, was conducted at FLASH by Chapman et al. (2006) [177]. The concept of *diffraction before destruction* was experimentally demonstrated for a known non-periodic  $\mu\text{m}$ -sized sample with 25 fs long, near transform-limited pulses. In this work, no radiation damage was observed in the reconstructed images, which were obtained from single-shot coherent diffraction patterns and phasing through oversampling. A second measurement of the same sample revealed that it was completely destroyed by the first FEL pulse. Hence, all characteristics of *diffraction before destruction* were present. This technique was used, e.g., for analyzing a single mimivirus with a diameter of  $0.75 \mu\text{m}$  [181].

With the research on SFX gaining impetus from the success of CDI experiments [172, 174], first publications demonstrating the feasibility of SFX with protein nanocrystals at an XFEL with subnanometer resolution appeared in 2011 [150, 182–184]. These early findings were based on diffraction patterns recorded with pnCCD detector modules at the CFEL-ASG Multi-Purpose (CAMP) instrument at LCLS at photon energies around 2 keV. For instance, Chapman et al. (2011) [182] found evidence that at 1.8 keV the conventional dose limit of 30 MGy for nanocrystals of photosystem I, a structure previously solved by means of conventional crystallography [185], can be circumvented by using XFEL pulses. Indeed, pulse durations of 70 fs enabled to overcome the limitations of radiation damage at doses up to 700 MGy at the observed resolution of  $8.5 \text{ \AA}$ .

After the commissioning of the LCLS Coherent X-ray Imaging (CXI) instrument, photon energies in the range from 5 to 11 keV and Cornell-SLAC Pixel Array Detectors (CSPADs) specifically designed for imaging at LCLS [186] became available. Boutet et al. (2012) [187] demonstrated SFX for microcrystals of a well-known protein at comparatively low average dose rates of 33 MGy with 40 fs pulse duration at room temperature surpassing the conventional dose limit of 1 MGy (see page 11). No significant signs of radiation damage were observed at the obtained resolution of  $1.9 \text{ \AA}$ . The phasing of the structure was accomplished via molecular replacement.

The first previously unknown high-resolution structure of a protein [188] was obtained by Redecke et al. (2013) [151] at the LCLS CXI instrument. In this work, a  $2.1 \text{ \AA}$  resolution structure of natively inhibited *Trypanosoma brucei* Cathepsin B (TbCatB) was determined based on 178 875 diffraction patterns of microcrystals of TbCatB collected at room temperature with 9.4 keV pulses, a duration of 40 fs, and doses up to 31 MGy. This result was considered as a first breakthrough of SFX even though the phase retrieval by molecular replacement gave cause for criticism [188]. The reason was that Redecke et al. (2013) [151] took advantage of prior knowledge of TbCatB, namely the coordinates of the mature enzyme sequence of TbCatB [183] as a search model, implying that SFX was not yet proven to be an autonomous technique. Similarly, further accomplishments in structure determination at XFELs such as Refs. [189–194] at photon energies between 8 and 10 keV relied on phasing via molecular replacement. Furthermore, the predicted dose limits (see above) are often not exhausted in

order to avoid damage to the detector [149]. For instance, Kern et al. (2012) [189] reported an average dose of 200 MGy. The fact that the radiation dose required for the solution of TbCatB by Redecke et al. (2013) [151] is of the order of the conventional dose limit of cryogenically cooled samples suggests a potential reproducibility of the experiment at a synchrotron. Indeed, Gati et al. (2014) [195] collected consistent data at the third-generation synchrotron radiation source PETRA III using the same microcrystals as Redecke et al. (2013) [151], a photon energy of 10 keV, and similar dose. In this case, however, the sample receives the dose on a time scale of seconds, i.e., orders of magnitude slower than in SFX. This indicates the superiority of XFELs for imaging experiments where time resolution is crucial [196–207].

Ultimately, direct, or *de novo*, structure determination for finite crystals in SFX experiments was achieved by Barends et al. (2014) [208] at the LCLS CXI instrument by means of single-wavelength anomalous diffraction (SAD) phasing.

## I.4. Theoretical methods

The rate-equation approach (REA) [39] for the simulation of inner-shell multiphoton ionization in the X-ray regime has a variety of advantages. First and foremost, the conceptual simplicity provides an intuitive understanding of the relevant mechanisms behind the ionization dynamics of atoms. Moreover, the numerical effort is comparatively low and the theory is nevertheless capable of capturing the quantitative results obtained from the majority of experiments mentioned in Sec. I.2. For larger samples, the REA for atoms can be combined with a screening model [209], a molecular dynamics (MD) [80, 97, 100, 152, 210] or a transport approach [100, 211]. These extensions allow, e.g., a description of the formation of nanoplasmas [80]. As mentioned in Sec. I.2.1, the predominant part of the cited references refer to the same implementation of the REA, the so-called xATOM toolkit. This approach relies on rates based on the HFS method for transitions between all possible  $q$ -hole electronic configurations of an atom where  $q$  ranges from zero to the atomic number  $Z$  if fully-stripped atoms are considered. For instance, in the case of neon, there are one zero-hole configuration,  $1s^22s^22p^6$ , three one-hole configurations,  $1s^12s^22p^6$ ,  $1s^22s^12p^6$ , and  $1s^22s^22p^5$ , etc.

At optical wavelengths, different approximations are employed depending on the so-called Keldysh parameter  $\gamma_K = \sqrt{\frac{1}{2}\epsilon_B/U_p}$ , which results from the ratio between the ionization potential  $\epsilon_B$  and the ponderomotive energy  $U_p$  [212, 213]. In this situation, the latter can be expressed in terms of the irradiance  $I$  and the photon energy  $\omega$  according to  $U_p = 2\pi\alpha I/\omega^2$ . Naively applying this concept to XFEL experiments yields numerical values of  $U_p$  that vary by orders of magnitude since FELs are greatly tunable. Extracting  $U_p$  according to the aforementioned formula for prominent experiments such as Refs. [54, 55] at LCLS reveals that  $U_p$  is significantly lower than 1 eV even for the comparatively low photon energy of 800 eV. Hence, the Keldysh parameter  $\gamma_K \ll 1$  suggests a perturbative approach [75, 211]. However, even though the REA indeed had a great success in describing the experimental data in, e.g., Ref. [54], this is not a valid justification because this analysis is not applicable in the XUV and X-ray regime [77].

It should be noted that even the REA is computationally very demanding for heavy atoms. The number of configurations that are needed in a simulation that includes the fully-stripped atom are shown in Fig. I.3. Following the procedure described in Ref. [54], one easily calculates the

number of configurations as a simple exercise in combinatorics. An exponential fit is shown to guide the eye and highlight the overall trend. This figure reproduces, e.g., the 27 configurations of carbon  ${}_6\text{C}$  from Ref. [6], the 63 configurations of  ${}_{10}\text{Ne}$  from Refs. [49, 54], and the 27 783 configurations of  ${}_{26}\text{Fe}$  from Ref. [176]. The experiment by Rudek et al. (2012) [55] with  ${}_{54}\text{Xe}$  at photon energies of 1.5 and 2.0 keV involved no  $K$ - or  $L$ -shell absorption, so the number of configurations, 13 774 524, can be divided by 63 (equal to the number of configurations of  ${}_{10}\text{Ne}$ ), which yields 1 120 581 configurations in total. These configurations are then coupled by processes such as photoionization and Auger decay, which are represented by a sparse matrix in dynamical calculations. However, it has been pointed out by Son and Santra (2012) [214] that a Monte Carlo implementation of the REA is capable of avoiding the requirement for keeping track of all configurations simultaneously in the algorithm. Furthermore, recent progress by Ho et al. (2014) [85] allows to take the REXMI mechanism into account within the framework of the theory behind XATOM.

Of course, not all phenomena can be explained based on only the REA. One example is the intensity pattern obtained by coherent diffractive imaging (CDI). The latter is, strictly speaking, given by two-particle correlations, which cannot be deduced from the occupation numbers of configurations without approximation. In the case of nanocrystals considered in SFX the two-particle correlations effects are negligible due to Bragg scattering [215, 216]. Furthermore, a more elaborated treatment is required when coherences play a role [217–222]. For instance, Demekhin and Cederbaum (2012) [222] theoretically investigated the impact of dynamic interference on the photoelectron spectra for atomic hydrogen under pulsed XUV irradiation at a photon energy 40 eV above the  $K$ -edge of 13.6 eV. This analysis cannot be performed within the typical REA because the latter reduces the computational costs by modeling only the residual ion, i.e., these spectra are usually not calculated in the first place. Similarly, Chapters IV and V of the present dissertation address situations where the interference of photoelectrons becomes important as it even affects the ionization dynamics of populations.

Although Murphy et al. (2014) [80] state with regard to the ionization dynamics of the fullerene  $\text{C}_{60}$  discussed in Sec. I.2.2 that a quantum simulation might be required for a better agreement with the experiment, they also stress that such a calculation is not generally feasible with respect to computational costs and that the quantum mechanical approach (as seen in Chapters III, IV, and V) is sensitive to pulse parameters which have not yet been fully characterized for XFELs. For future development and in appropriate special cases one may consider a variety of more sophisticated theoretical approaches [223]: the time-dependent Hartree-Fock (TDHF) theory [224, 225] and related [226–228], the multiconfigurational time-dependent Hartree-Fock (MCTDHF) theory [223, 229, 230], the nonequilibrium Green's function (NEGF) approach [231–235], the time-dependent configuration-interaction singles (TDCIS) method [84, 87, 92,

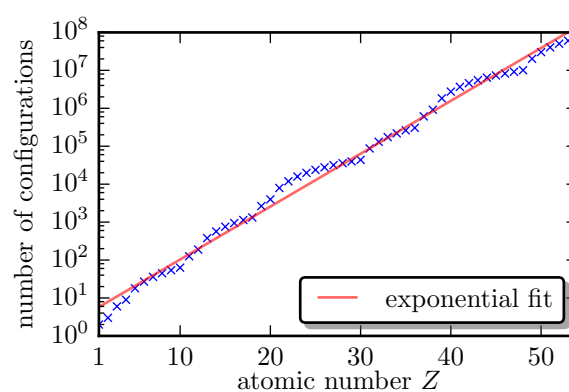


**Figure I.3.:** Number of configurations considered within the XATOM toolkit for different atomic species if fully-stripped atoms are predominantly produced by sequential  $K$ -shell absorption and subsequent processes.

220, 236], the **time-dependent density-functional theory (TDDFT)** [231, 237–240], and the **time-dependent reduced density-matrix (TDRDM)** [4, 223, 241–243].

The present thesis focuses on **TDHF** and related approximations (see Sec. II.2). In the context of the previous work within the scope of the aforementioned **BMBF** project [5], a potential extension of the theory to **TDRDM** will be discussed occasionally but not in depth. The theoretical background for this technique adapted to the present situation is provided in, e.g., Ref. [4, page 65 et seqq.]. Note that the dependence on the system size of the **TDRDM** theory is relatively weak, contrary to the radical increase of the numerical effort with the number of electrons in the framework rate equations. Nevertheless, **TDRDM** is computationally considerably more challenging than the **REA** for typical **XFEL** based experiments. The reasons are discussed below.

The decisive advantage of both **TDHF** and **TDRDM** over the **REA** is, above all, their capability of describing a coherent time evolution. For this reason, the present dissertation, as its title suggests, is primarily concerned with coherent phenomena that are for the most part identified via comparison with the **REA**.

# II

## Basic assumptions of the applied models

The present chapter provides an overview of the approximations and simplifications in the models employed in Chapters III to V and, associated therewith, the limitations that have to be borne in mind for a correct interpretation of the results obtained in this framework. Naturally, rigorous simplifications are mandatory for taking into account the coherent ionization dynamics for a generic solid (Chapter IV) or for an arbitrary number of atoms (Chapter V). The most far-reaching approximation in the present thesis is the reduction to **one space dimension (1d)**, which nevertheless has been proven useful to capture qualitative features of ionization dynamics in many cases [229, 234, 237, 238, 241, 244–257]. On a side note, there is also an extensive 1d theory for FEL radiation [24, 30].

Carrying over the **time-dependent Schrödinger equation (TDSE)** to 1d implies an ambiguity with respect to the Coulomb operator because the straightforward replacement  $1/r \rightarrow 1/|x|$  leads to an infinite binding energy. Thus, different strategies for truncating the Coulomb potential arose [244, 245]. Besides the softened Coulomb operator [258, 259] (also referred to as **soft-core (SC)** potential), which is probably most common in the literature, other model potentials such as the Mathieu or the **Kronig-Penney (KP)** potential are sometimes employed [260, 261]. The choice of the model potential is in fact crucial for the present purposes. It turns out that the SC potential, and similarly any other differentiable potential with a local minimum, displays characteristics of the harmonic oscillator for high binding energies. Even on a qualitative level, the results obtained within such a model are largely artificial [262], which led to the utilization of the KP model in Chapter IV.

The restriction to 1d has further implications. These shall be discussed in the following along with the introduction of further simplifications divided into two categories: approximations related to electron-photon and electron-electron interaction. Lastly, Sec. II.3 is devoted to a discussion of limiting cases where the assumptions outlined in this chapter are most suitable.

Generally, the time scale plays a key role for all applied models. The simulations are limited to the dynamics during the interaction with the XFEL pulse, i.e., processes that occur on the femtosecond time scale and below<sup>1</sup>. Therefore, no effort is made to capture the Coulomb explosion initiated by ionic repulsion after electrons escape from the sample because, typically, the time scale of atomic displacement is tens of femtoseconds [80]. Accordingly, pulse durations of the order of only a few femtoseconds are considered throughout Chapters IV and V in order to maintain consistency with experiments in neglecting the atomic motion.

---

<sup>1</sup>Note that even subfemtosecond pulses are within reach [3].

## II.1. Electron-photon interaction

The interaction of the electromagnetic field with matter is assumed to be captured by a semiclassical<sup>2</sup> description, i.e., the Schrödinger equation coupled to a classical electromagnetic field. This premise is only partially justified by the intensities and coherence properties of seeded XFEL pulses [264, p. 511 et seq.]. Indeed, the situation is more complicated in the X-ray regime since relevant processes such as, first, inelastic Compton scattering and, second, fluorescence are axiomatically disregarded [2]. The first deficiency could prove problematic because the scattered intensity is known to be dominated by Compton scattering for strong incident pulses [263, p. 390 et seq.]. However, this issue can be bypassed by focusing on other physical quantities such as sample damage, which is only slightly affected by Compton scattering compared to photoabsorption [95, p. 416]. The absence of inelastic scattering in the semiclassical model is therefore only a minor drawback. This is far from being the case for the neglect of fluorescence processes, which are vital for the simulation of heavy atoms according to the dependence of X-ray fluorescence rates of approximately  $\propto Z^4$  on the atomic number  $Z$ . For instance, the  $K$ -hole lifetime in krypton  ${}_{36}\text{Kr}$  is as short as  $\tau_{1s} \approx 0.24$  fs at a  $K$ -edge of  $E_{1s} \approx 14.3$  keV and is dominated by fluorescence [39, 265].

A realistic semiclassical modeling of SASE pulses includes an ensemble of temporal envelopes consisting of several intensity spikes that form a flat-top pulse on average [50]. Although this approach is inherently parallel and thus efficiently implementable with respect to computational runtime, it is not applied here because it might conceal signatures of coherent dynamics, whose identification is the main target of the present dissertation. Therefore, the focus is placed on seeded pulses with ideal temporal profiles and coherence properties. On a side note, recent theoretical progress by McNeil et al. (2013) [266] suggests that a so-called high-brightness SASE FEL might be capable of generating (near) transform-limited pulses even without seeding.

Photoionization is the most important process based on electron-photon interaction (see [95, p. 416]) in the range of the electromagnetic spectrum accessible with contemporary XFELs. Even though photoionization can be principally well described within the semiclassical approach, the 1d model is incapable of reflecting the rich structure of the photoabsorption cross sections as functions of the wavelength due to phenomena such as Fano resonances, Cooper minima, and GDR [267]. Even simpler properties –for example, the observation that via one-photon absorption (OPA) predominantly inner-shell electrons are ejected if energetically feasible– are not guaranteed for arbitrary 1d model potentials [262]. Consider, for instance, a 1d rectangular potential, whose periodic continuation leads to the KP model used in Chapter IV. In this case, the eigenvalue spectrum exhibits no accumulation point at zero energy, but all bound eigenstates [268, p. 48 et seqq.] decrease exponentially outside the support of the potential similar to the 3d hydrogen atom. The latter is important as it influences the transition rates [39, 95, 269]. By contrast, the relative magnitudes of partial cross section in the 1d models considered here are not consistent with the 3d hydrogen atom. This deviation is of qualitative nature because ionization pathways may be altered. Hence, 1d models are best suited for situations where only one ionization channel is investigated.

<sup>2</sup>This term is used ambiguously in the literature. Here, the definition of *semiclassical* is consistent with standard textbooks of quantum optics such as Refs. [263, 264].

Furthermore, the wavevector  $\vec{k}$  and the magnetic field  $\vec{B}$  of the electromagnetic wave are omitted in the **1d** calculation because  $\vec{k}$  and  $\vec{B}$  are perpendicular to the electric field  $\vec{E}$ . Strictly speaking, the electromagnetic wave considered here should be rather denoted *oscillating electric field*. It is nevertheless assumed that there is an associated intensity given by  $I = \frac{1}{8\pi\alpha} E_0^2$ . Consequently, the spatial dependence of the pulse is disregarded as well because the envelope of **XFEL** pulses is typically orders of magnitude larger than the length scale dictated by the wavevector (see Sec. **II.3**). The implication is that one may introduce the dipole approximation without loss of generality or, in other words, nondipole effects are neglected. The applicability of this approximation in the **X-ray** regime is questionable due to the short wavelengths [2, 270–272]. For example, two-photon **above-threshold ionization (ATI)** [273] is known to be essentially a nondipole effect in the **X-ray** regime [272].

Finally, the broad angular distribution of photoelectrons stemming from **OPA** [2, p. 119 et seqq.] is reduced to two directions. In real systems, the situation is completely different: the distribution depends strongly on the initial orbital of the ejected electron and is largely independent of the field strength but is rather affected by high photon energies of the incident pulse [2, 27]. On a side note, the first effect is well-known and useful for experimental purposes. For instance, collecting the signal from  $2s$  photoelectrons can be avoided by detecting only electrons perpendicular to the polarization axis of the **XFEL** pulse [219].

## II.2. Electron-electron interaction

The models presented in the ensuing chapters rely on the assumption that the electron-electron interaction can be treated to a good approximation on a **Hartree-Fock (HF)** level [274–276]. Indeed, the major part of the models, where adequate, completely neglects all many-particle effects except for the Pauli exclusion principle. This strategy is accompanied by severe limitations although many of the references cited in Chapter **I** rely on an even simpler theory, namely the **Hartree-Fock-Slater (HFS)** approximation<sup>3</sup> [277, 278]. However, **HFS** is only the starting point for the calculation of orbitals and rates; additionally, one has to determine the transition rates of processes that go beyond a straightforward time-dependent **HFS** approach. One important example of such a process is Auger decay. In this work, the dynamical equations are the **time-dependent Hartree-Fock (TDHF)** equations [224, 225, 279–281] without further amendments.

Let  $\varrho$  be the **one-body reduced density matrix (1RDM)**, let  $V_{\text{core}}$  be a one-body potential, and let  $V_{\text{ee}}$  be a two-body potential. For simplicity, it is assumed that  $V_{\text{ee}}(x_1, x_2)$  depends only on the distance  $|x_1 - x_2|$  between  $x_1$  and  $x_2$ , so there is no distinction made between the notations  $V_{\text{ee}}(x_1, x_2)$  and  $V_{\text{ee}}(x_1 - x_2)$ . Moreover, the analysis is restricted to systems without spin polarization to avoid explicitly dealing with the spin variable, i.e., each orbital is postulated to be doubly occupied. Then, including a time-dependent spatially homogeneous electric field  $E(t)$ , the **TDHF** equations in **1d** coordinate space are given by [89, p. 485 et seqq.]:

<sup>3</sup>In order to emphasize the widespread use of this approximation consider the following list of references [6, 55, 70, 84, 92, 117, 123, 156, 157, 209, 214, 217, 265], which is only a subset where **HFS** was employed.

**Time-dependent Hartree-Fock (TDHF) equation**

$$\begin{aligned}
& i \frac{\partial}{\partial t} \varrho(x_1, x_2) + \frac{1}{2} \left( \frac{\partial^2}{\partial x_1^2} - \frac{\partial^2}{\partial x_2^2} \right) \varrho(x_1, x_2) \\
& - (V_{\text{core}}(x_1) - V_{\text{core}}(x_2)) \varrho(x_1, x_2) + E(t) (x_1 - x_2) \varrho(x_1, x_2) \\
& = \int dx [V_{\text{ee}}(x_1 - x) - V_{\text{ee}}(x_2 - x)] [\varrho(x_1, x_2) \varrho(x, x) - \frac{1}{2} \varrho(x_1, x) \varrho(x, x_2)].
\end{aligned} \tag{II.1}$$

A direct simulation of Eq. (II.1) evidently requires a larger computational effort than the solution of an exact two-particle problem. In exchange, Eq. (II.1) can in principle be used for any number of particles without a substantial increase of the numerical costs. Note that the TDHF equations based on the 1RDM can be simplified on the basis of the conservation of the product character,  $\varrho = \varrho^2$  [89, p. 489]. Therefore, Eq. (II.1) is consistent with the orbital formulation of TDHF [225]:

**Time-dependent Hartree-Fock (TDHF) equation (orbital formulation)**

$$\begin{aligned}
i \frac{\partial}{\partial t} \varphi_i(x) &= \left( -\frac{1}{2} \frac{\partial^2}{\partial x^2} + V_{\text{core}}(x) - xE(t) \right) \varphi_i(x) + \\
&+ \int dy V_{\text{ee}}(x - y) [\varrho(y, y) \varphi_i(x) - \frac{1}{2} \varrho(x, y) \varphi_i(y)],
\end{aligned} \tag{II.2}$$

where  $\varphi_i$  for  $i = 1, \dots, N$  are the  $N$  doubly occupied orthonormal orbitals of the Slater determinant that generates a 1RDM  $\varrho$  according to

$$\varrho(x_1, x_2) = 2 \sum_{i=0}^N \varphi_i^*(x_2) \varphi_i(x_1). \tag{II.3}$$

In this case, the number of electrons,  $2N$ , explicitly appears in the dynamical equations.

There are several shortcomings of the TDHF method regarding ionization experiments. Even in the optical regime, TDHF is long known to be incapable of describing the famous knee structure in the intensity dependence of double-ionization yield of helium [251, 282, 283]. This effect is attributed to correlations, similar to the GDR phenomenon around 100 eV discussed in Sec. I.2.1. Additionally, the TDHF description of ionization dynamics contains further *basic flaws*<sup>4</sup> [250, 256, 284]. There are even cases where qualitative discrepancies between the TDHF and the full solution occur, whereas a model neglecting the electron-electron interaction completely predicts the correct tendencies [256]. For this reason, the major part of this dissertation is based on the special case  $V_{\text{ee}} \equiv 0$ . The only exception can be found in Sec. V.2.6 where the significance of electrostatic trapping is estimated.

For a correct interpretation of the results obtained via TDHF, it is indispensable to be aware of the general limitations of this approach. Correspondingly, the phenomena that shaped the dynamics of the experiments reported in Chapter I and are affected by the TDHF approximation shall be briefly analyzed in the following.

<sup>4</sup>exact quote from Ref.[284, p. 139]

Auger decay, which is essential in most **XFEL** based experiments, is beyond the **TDHF** approach [39]. Particularly for light atoms, inner-shell vacancies are subject to fast Auger processes: in the case of neon  ${}_{10}\text{Ne}$  ( $K$ -edge  $E_{1s} \approx 870$  eV) the  $K$ -hole lifetime  $\tau_{1s} \approx 2.4$  fs is dominated by Auger decay [49, 285]; the prevalent decay mechanism of inner-shell vacancies for heavy atoms is fluorescence (see Sec. II.1).

Moreover, **TDHF** is inconsistent with the wide-spread contrary assumption that trapped electrons quickly reach thermal equilibrium [104, 123, 216]. In reality, the truth lies, of course, in between these two extreme cases of absent and instantaneous thermalization. Obviously, electron-electron collision of trapped electrons is essential for the simulation of macromolecules, clusters, and solids irradiated by **XFEL** pulses, but it is also discussed that electrons may not equilibrate within the short pulse durations [215]. One can estimate that the thermalization proceeds on the time scale of a few femtoseconds, benefiting from high density and low photon energy of ejected electrons [123].

**IPD** in solids is only partly included. On the one hand, the impact of the charged environment is captured on the **Hartree-Fock (HF)** level [123]. On the other hand, **IPD** depends on the free-electron density distribution [121], which is, in turn, not correctly modeled due to the aforementioned omission of interaction processes.

Lastly, as established in Sec. I.2, charge state distributions are strongly affected by collisional ionization, which is also implicitly disregarded in the **TDHF** approach. Still, it is intuitively clear that the role of collisional ionization depends on the kinetic energies of ejected electrons and their mean free path. Therefore, depending on the photon energy and the sample, it might be possible to outrun this ionization process with subfemtosecond pulses (cf. the following section). The absence of collisions implies further that **IBS** does not contribute to the ionization within this model [110]. This is not an issue here because the importance of **IBS** decreases with higher photon energies.

## II.3. Discussion

All in all, the assumptions introduced above are accompanied by severe limitations regarding the applicability to real **XFEL** based experiments. One can argue that the model is overly restrictive to describe the irradiation of a real sample with **X-rays**: the simulation of heavy atoms within this model is fundamentally incompatible with the neglect of fast fluorescence processes, and light atoms cannot be satisfactorily treated without taking Auger decay into account<sup>5</sup>.

Therefore, the focus lies on situations where the pulse duration is short compared to the inner-shell decay lifetimes, which is reasonable for subfemtosecond pulses [26, 32] and light atoms. Longer pulses may be adequate as well depending on the specific Auger lifetime of typically a few femtoseconds. The implication is that the cases of interest are similar to the situation of *frustrated absorption* [54, 98], i.e., the decay channel is virtually frozen on the ultrashort time scale. This phenomenon enables the restriction on the initial dominating photoionization channel.

<sup>5</sup>On a side note, the equation of motion based on the **IRD** in Eq. (II.1) can in principle be phenomenologically extended to incorporate Auger decay [221].

As mentioned in Sec. II.2, subfemtosecond pulses are required to avoid collisional ionization at a photon energy of 12 keV. This time scale  $t_c$  is characterized by  $t_c = \lambda_c/v_{el}$  for a photoelectron with an average velocity of  $v_{el}$  and an electron mean free path  $\lambda_c$  [6, Sec. III E]. If high photon energies  $\omega$  and light atoms are considered,  $\lambda_c$  can be estimated by the Bethe formula and the electron velocity is approximately given by  $v_{el} \propto \sqrt{\omega}$  [286], and thus  $t_c$  grows with increasing photon energy, i.e., high photon energies inhibit collisional ionization by photoelectrons. For **near-threshold ionization (NTI)**, however,  $v_{el} \propto \sqrt{\omega}$  is not valid because the binding energy is not negligible compared to  $\omega$  and also the Bethe formula does not apply [286]. Nevertheless,  $\lambda_c$  varies between a few  $\text{\AA}$  and 100  $\text{\AA}$  for practical conditions [286], and thus the photon energy and the pulse duration can be chosen appropriately, aiming at a  $t_c$  longer than the pulse duration. Note that the case of slow photoelectrons implies a possible onset of **resonance-enabled X-ray multiple ionization (REXMI)** or **two-photon absorption (TPA)** in the corresponding experiment.

Upgrading the level of the theory to **TDRDM** might enable to capture transitions such as Auger decay, shakeoff and potentially the relevant collisional processes [4]. However, the **TDRDM** treatment of ionization dynamics initiated by **XUV** pulses is computationally not feasible in **3d**, and a **1d** implementation is likely to exhibit many artificial properties discussed above. Intuitively, one might expect that the **1d** approximation will break down entirely if electron-electron collisions –even if consistently modeled within the **1d** model– have a considerable influence on the quantities of interest.

Next, the level of theory discussed above is analyzed from a numerical perspective. Interestingly, the models without electron-electron interaction are similar to the **1d** system for a study of **above-threshold ionization (ATI)** that was numerically solved by **Javanainen et al. (1988)** [246] via the **Crank-Nicolson (CN)** method. Although the findings in this reference are roughly as old as the author of the present thesis, the numerical task is not trivial on modern computers. The computational costs of the simulations performed in the course of this dissertation depend substantially on the time and length scales. Consider, e.g., the simplest situation in Chapter V, i.e., a single atom irradiated by a coherent **XUV** or **X-ray** pulse without taking the electron-electron interaction into account. The length scales are largely given by the kinetic energy of the ejected electrons: the *computational* system size, for which a lower bound –typically much larger than the atom– exists in order to correctly model ejected electrons without artificial reflections at the boundaries of the grid (see Sec. VI.1), and the discretization, which needs to be appropriate for the description of the spatial variation of the wave function of free electrons. Likewise, there are usually two well-separated time scales, namely the duration and the frequency of the **XFEL** pulse.

For a quantitative analysis of the length and time scales in a **TDHF** description (even if  $V_{ee}$  vanishes identically) of a typical **SFX** experiment, a wavelength of  $\lambda = 1 \text{ \AA}$  is assumed as a starting point<sup>6</sup>. Then, the photon energy  $E_{ph}$  is given as  $E_{ph} = \frac{2\pi}{a\lambda} \approx 456 \text{ a.u.} \approx 12.4 \text{ keV}$ . Provided that the sample contains light atoms such as carbon, the kinetic energy of photoelectrons is of the order of the photon energy  $E_{el} \approx E_{ph}$ . In the nonrelativistic approximation, this corresponds to a de Broglie wavelength of  $\lambda_{el} = 2\pi/\sqrt{2E} \approx 0.21 \text{ a.u.} < \lambda_{ph}$ , which determines the discretization far away from the atom. Moreover, there are two distinct inherent time scales,

<sup>6</sup>The wavelength  $\lambda = 1 \text{ \AA}$  is currently available only at **SACLA**. The minimum wavelength at **LCLS** is 1.2  $\text{\AA}$  [12], whereas **SACLA** provides wavelengths down to 0.634  $\text{\AA}$  [15]. The wavelength range will be extended further at **European XFEL** [23].

namely the pulse duration around  $1 \text{ fs} \approx 41 \text{ a.u.}$  and the period of the classical light field  $T_{\text{ph}} = \alpha \lambda_{\text{ph}} \approx 1.38 \cdot 10^{-2} \text{ a.u.}$

Note that of all the mentioned length and time scales only the pulse duration is explicitly present in the rate-equation approach described in Sec. I.4. The implication is that the photon energy crucially affects the performance of the simulations based on TDHF but is irrelevant from the numerical perspective within the framework of rate equations. Therefore, when extending the TDHF approach to the X-ray regime, one has to keep in mind that the computational costs increase with increasing photon energy. Naturally, this problem is even more serious for a theory beyond TDHF such as TDRDM: in previous work by Kaiser (2014) [4], converged results within the TDRDM approach, despite comparatively low photon energies below 100 eV, were obtained only in special cases.

In summary, the complexity of the scenario requires several assumptions that entail a lot of constraints on XFEL based experiments which can be adequately described within this approach. The premises of the models partially exceed the contemporary experimental capabilities. To assess the discrepancies originating from the 1d theory, a more advanced theoretical description is required.



# III

## Resonant two-photon ionization

This chapter is devoted to coherent phenomena that might become apparent in the ionization dynamics of isolated atoms irradiated by XFEL pulses. In particular, the nonlinear process **two-photon absorption (TPA)** close to an intermediate resonance will be addressed. This phenomenon has been experimentally studied in the **VUV** and the **X-ray** regime: the **TPA** cross section was measured for helium  ${}^2\text{He}$  at photon energies between 20 and 23 eV around the  $1s^2 - 1s\ 2p$  and  $1s^2 - 1s\ 3p$  resonances [287], and similar investigations were performed for the case of helium-like neon  ${}_{10}\text{Ne}^{8+}$  in the vicinity of the  $1s^2 - 1s\ 4p$  resonance at 1.11 keV photon energy [70, 84]. Non-resonant **TPA** has also been observed in solid germanium  ${}_{32}\text{Ge}$  at 5.6 keV photon energy.

It should be noted that this mechanism can become important in cases where the photon energy is above the  $K$ -edge of the neutral atom and, accordingly, **one-photon absorption (OPA)** dominates initially. However, as the ionization under irradiation with the XFEL pulse progresses via **OPA**, ions with significantly enhanced binding energies are created. Hence, the  $K$ -edge of a (highly) charged configurations potentially surpasses the photon energy and thus inhibits further **OPA**. For example, the positions of the  $K$ -edge are at  $E_{1s} \approx 870$  eV for  ${}_{10}\text{Ne}$  [103, Table 1-1] and at 1195 eV for  ${}_{10}\text{Ne}^{8+}$  [84]. Note that depending on the specific situation, this scenario can alternatively be dominated by **REXMI**.

This chapter includes a general approach for resonant **TPA** in Sec. III.1, which consistently treats the aforementioned cases of **TPA** in the **XUV** [287] and soft **X-ray** regime [70, 84]. This strategy enables one, firstly, to reduce the physical system to its essentials and, secondly, to investigate phenomena that do not depend on a specific sample. Contrary to the simulations which are the basis for the results in Chapters IV and V, this model is not based on a reduction to **1d**. The content of this chapter is based on Ref. [288], to which the author of the present thesis contributed. Compared to the original publication, the theory is simplified without loss of generality and the focus is slightly shifted towards the coherent saturation phenomenon while pointing out the differences to comparable results obtained by means of a **rate-equation approach (REA)**.

### III.1. Generic model

The aim of this section is to develop a model that captures the substantial physics behind resonant **TPA**. Accordingly, the corresponding Hilbert space  $\mathcal{H}$  is required to contain at least two discrete bound states, namely the ground state  $|G\rangle$  (eigenenergy  $\omega_G < 0$ ) and an excited state  $|X\rangle$  (eigenenergy  $\omega_X < 0$ ). Further,  $\mathcal{H}$  comprises a continuum of states  $|\omega\nu\rangle$  representing the singly ionized atom (eigenenergy  $\omega > 0$ , degeneracy  $\nu$ ). The usual orthogonality relations are assumed. In the case of helium in Ref. [287],  $|G\rangle$  corresponds to the ground-state configuration  $1s^2$  and  $|X\rangle$  to one of the excited charge-neutral configurations  $1s\ 2p$  or  $1s\ 3p$ , depending on the

intermediate resonance that is driven by the respective photon energy. The continuum of states  $|\omega\nu\rangle$  describes a state “1s plus a photoelectron with a kinetic energy  $\omega$ ”. Then, the Hamiltonian  $H_0$  of the system without light-matter interaction reads

$$H_0 = \omega_G |G\rangle\langle G| + \omega_X |X\rangle\langle X| + \int_0^\infty d\omega \sum_\nu \omega |\omega\nu\rangle\langle \omega\nu|. \quad (\text{III.1})$$

Next, the eigenstates of  $H_0$  are coupled by a time-dependent laser pulse described within the semiclassical approximation (cf. page 20) in the form of a linearly polarized, spatially independent electric field  $\vec{E}(t) = E(t) \vec{e}_L$  where  $|\vec{e}_L| = 1$ . For the sake of brevity, the following parameters are introduced:

$$\begin{aligned} \mu_{\omega\nu} &:= \vec{e}_L \cdot \langle \omega\nu | \vec{r} | X \rangle, \\ \mu_0 &:= \vec{e}_L \cdot \langle X | \vec{r} | G \rangle. \end{aligned} \quad (\text{III.2})$$

The dipole coupling Hamiltonian  $H_L(t)$  is then assumed to be of the form

$$H_L(t) = E(t) [\mu_0^* |G\rangle\langle X| + \mu_0 |X\rangle\langle G| + \int_0^\infty d\omega \sum_\nu (\mu_{\omega\nu}^* |X\rangle\langle \omega\nu| + \mu_{\omega\nu} |\omega\nu\rangle\langle X|)]. \quad (\text{III.3})$$

Ultimately, the model system defined by

$$H(t) = H_0 + H_L(t) \quad (\text{III.4})$$

will hereafter be referred to as *generic model*.

Although the generic model is, in contrast to the major part of this dissertation, not limited to 1d, a lot of simplifying assumptions are implied in Eq. (III.4). The following elements of real systems are disregarded: (i) all discrete excited states except for  $|X\rangle$ , (ii) direct ionization from  $|G\rangle$  to  $|\omega\nu\rangle$ , (iii) transitions between distinct continuum states  $|\omega\nu\rangle$ , (iv) decay mechanisms from  $|X\rangle$  to  $|G\rangle$  via fluorescence or from  $|X\rangle$  to a continuum state  $|\omega\nu\rangle$  via Auger decay, and (v) the statistical properties introduced by SASE pulses.

The basic scenario described by the model is sketched in Fig. III.1. Provided that  $E(t)$  has a main frequency component at  $\omega_L$  where  $\omega_L$  is tuned to the vicinity of the resonant transition,  $\omega_L \approx \omega_X - \omega_G$ , the omission of further bound states can be expected to be legitimate. At this point, one assumes at least near-resonant TPA, i.e., a potentially nonzero but small detuning  $\delta\omega = \omega_X - \omega_G - \omega_L$ . For a discussion of the implications of a detuning  $\delta\omega \neq 0$ , the reader is referred to Ref. [4, p. 35 et seqq.]; the analysis below in Sec. III.3 concentrates on resonant TPA. Assuming  $\omega_L + \omega_X > 0$ , one guarantees the presence of the following ionization pathways

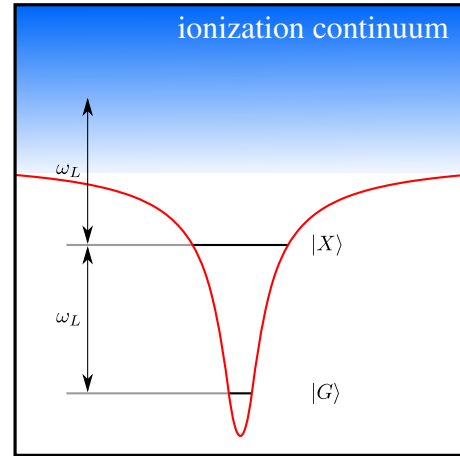


**Figure III.1.:** Schematic representation of the generic model

for a system initially in the state  $|G\rangle$  (see Fig. III.1): two sequential OPAs, the (near-)resonant excitation from  $|G\rangle$  to  $|X\rangle$  followed by a promotion to a continuum state  $|\omega\nu\rangle$ , and the direct TPA from second-order perturbation theory. Energy conservation suggests that this process requires the absorption of two photons. Hence, all the key ingredients of resonant TPA are contained in the model.

The validity of approximation (iv), i.e., the neglect of decay mechanisms, depends strongly on the system of interest. Situations favorable for these simplifications are the cases of light atoms where fluorescence lifetimes are comparatively long and Auger decay is suppressed. For instance, the excited states in the aforementioned cases,  $1s\ 2p$  in  ${}_2\text{He}$  and  $1s\ 4p$  in  ${}_{10}\text{Ne}^{8+}$ , are obviously not subject to Auger decay. The situation can be completely different in other cases. If  $|G\rangle$  and  $|X\rangle$  are given by the configurations  $1s^2\ 2s^2\ 3p^6$  (neon ground state) and  $1s^{-1}\ 3p$  [217] of neutral neon atoms or by the configurations  $2p^{-1}$  and  $1s^{-1}$  of singly-charged neon atoms [219, 221], Auger decay is important and a calculation based on the density matrix is required.

Here, however, there is no controversy at all: if the initial state is pure, it remains pure during the time evolution defined by the generic model. Accordingly, an ansatz for the time-dependent solution with respect to the initial condition

$$\lim_{t \rightarrow -\infty} |\psi(t)\rangle = |G\rangle \quad (\text{III.5})$$

can be written as a pure state

$$|\psi(t)\rangle = \alpha_G(t) e^{-i\omega_G t} |G\rangle + \alpha_X(t) e^{-i\omega_X t} |X\rangle + \int_0^\infty d\omega \sum_\nu \alpha_{\omega\nu}(t) e^{-i\omega t} |\omega\nu\rangle. \quad (\text{III.6})$$

Note that  $p_G := |\alpha_G(t)|^2$  and  $p_X := |\alpha_X(t)|^2$  are the occupation probabilities of the states  $|G\rangle$  and  $|X\rangle$ , respectively. The initial condition Eq. (III.5) in terms of the coefficients  $\alpha_G$ ,  $\alpha_X$ , and  $\alpha_{\omega\nu}$  now reads

$$\lim_{t \rightarrow -\infty} \alpha_G(t) = 1, \quad \lim_{t \rightarrow -\infty} \alpha_X(t) = \lim_{t \rightarrow -\infty} \alpha_{\omega\nu}(t) = 0. \quad (\text{III.7})$$

The coupling to the continuum does not cause decoherence as in Ref. [220] because the continuum states  $|\omega\nu\rangle$  consist of both the ion and a photoelectron. Although  $\alpha_{\omega\nu}$  is not explicitly calculated in the following (cf. Eq. (III.8)), there is no trace over the photoelectron involved.

Finally, it should be mentioned that the generic model is, of course, not newly invented. Similar models have been used in the past without connections to FELs [289–292] and have also contributed to the understanding of FEL based experiments in the context of resonant Auger decay [217, 218] or resonant TPA [293].

## III.2. Equations of motion

Although the generic model is easily solvable from a numerical perspective, different levels of simplifications are introduced in the following. This strategy enables one to obtain analytical solutions and to identify the features that emerge only in the sufficiently thorough treatments.

This section is devoted to the derivation and the additional assumptions of the three levels of theory considered here: the *resonant approximation*, the *Markovian theory*, and the *rate-equation approach* (REA). Note that the generic model and these approximations can be arranged hierarchically because each method can be obtained as a reduction of the previously mentioned method, i.e., the resonant approximation reduces the complexity of the generic model, the Markovian theory is a simplified version of the resonant approximation, and, lastly, the REA provides the most primitive perspective considered here. The results based on these models will be presented later in Sec. III.3.

### III.2.1. Resonant approximation

Let the electric field be of the form  $E(t) = \Re(E_0(t)e^{i\omega_L t})$ , where  $\omega_L = \omega_X - \omega_G$  and  $E_0(t)$  changes slowly on the time scale of  $1/\omega_L$ . For instance,  $E_0(t)$  may represent the temporal envelope of the laser pulse and/or may contain a detuning.

An equation of motion for  $\alpha_G$  and  $\alpha_X$  can now be easily derived from the ansatz in Eq. (III.6). Starting with the *time-dependent Schrödinger equation* (TDSE) corresponding to the Hamiltonian from Eq. (III.4), one straightforwardly employs the *rotating wave approximation* (RWA) to further reduce the complexity of the generic model<sup>1</sup>. Then, in seeking for the solution with respect to the initial condition in Eq. (III.5), one eliminates the variables  $\alpha_{\omega\nu}$  at the expense of a memory integral and directly obtains the following equations of motion, which are hereafter referred to as the *resonant approximation*:

#### Resonant approximation

$$\begin{aligned}\dot{\alpha}_G(t) &= -\frac{1}{2}iE_0^*(t)\mu_0^*\alpha_X(t), \\ \dot{\alpha}_X(t) &= -\frac{1}{2}iE_0(t)\mu_0\alpha_G(t) - \frac{1}{4}E_0^*(t)\int_{-\infty}^t d\tau \gamma(t-\tau)\alpha_X(\tau)E_0(\tau),\end{aligned}\quad (\text{III.8})$$

$$\text{where } \gamma(\tau) := \int_0^\infty d\omega \sum_\nu |\mu_{\omega\nu}|^2 e^{-i(\omega-\omega_L-\omega_X)\tau}.\quad (\text{III.9})$$

The material-dependent parameters  $\mu_0 \in \mathbb{C}$  and the function  $\gamma: \mathbb{R} \rightarrow \mathbb{C}$  can be adjusted to the specific atomic species and states. For instance, the parameters can be obtained within a **1d** model (see Sec. III.3). Note that Eq. (III.8) is computationally trivial; it can be reduced to a linear system of *ordinary differential equations* (ODEs) with three complex variables,  $\alpha_G$ ,  $\alpha_X$ , and an auxiliary variable. Alternatively, for the special case of near-resonant TPA with detuning  $\delta\omega$  and a constant electric field amplitude  $E_0(t) \propto e^{i\delta\omega t}\theta(t)$ , Eq. (III.8) can be analytically solved in Laplace space [288].

<sup>1</sup>Non-RWA contributions in bound-free transitions are not discussed here because they have been subject to extensive studies in the past [294, 295].

### III.2.2. Markovian theory

In order to investigate the influence of the memory integral in Eq. (III.8), a *Markovian approximation* can be applied. This idea is based on the assumption that  $\gamma(\tau)$ , defined in Eq. (III.9), decreases rapidly compared to the time scale of the variations of  $\alpha_X(\tau)$  and the temporal envelope of the electric field  $E_0(\tau)$ . This enables the resonant approximation, Eq. (III.8), to be simplified by neglecting the contribution of the memory according to

$$\int_{-\infty}^t d\tau \gamma(t-\tau) \alpha_X(\tau) E_0(\tau) \approx \int_{-\infty}^t d\tau \gamma(t-\tau) \alpha_X(t) E_0(t) \approx \gamma_0 \alpha_X(t) E_0(t)$$

$$\text{with } \gamma_0 = \int_0^{\infty} d\tau \gamma(\tau). \quad (\text{III.10})$$

The physical implications of this approximation are elucidated below in Sec. III.2.4. For now, one benefits from even simpler equations of motion, which are written as

#### Markovian theory

$$\frac{d}{dt} \begin{pmatrix} \alpha_G(t) \\ \alpha_X(t) \end{pmatrix} = \begin{pmatrix} 0 & -\frac{1}{2}iE_0^*(t)\mu_0^* \\ -\frac{1}{2}iE_0(t)\mu_0 & -\frac{1}{4}\gamma_0|E_0(t)|^2 \end{pmatrix} \begin{pmatrix} \alpha_G(t) \\ \alpha_X(t) \end{pmatrix}. \quad (\text{III.11})$$

Strictly speaking, Eq. (III.11) assumes the validity of both the resonant and the Markovian approximation, but, for the sake of brevity, it is referred to only as *Markovian theory*. The equations of motion Eq. (III.11) contain just two material-dependent parameters  $\mu_0, \gamma_0 \in \mathbb{C}$  and thus enable a comprehensive parameter study to be performed without focusing on a specific atom and/or transition. The implications of the Markovian approximation are most easily demonstrated in the special case  $\mu_0 = 0$  and the initial condition  $\lim_{t \rightarrow -\infty} |\psi(t)\rangle = |X\rangle$ . Eq. (III.11) yields then without further assumptions

$$\frac{d}{dt} |\alpha_X(t)|^2 = -\frac{1}{2}\Re(\gamma_0) |E_0(t)|^2 |\alpha_X(t)|^2. \quad (\text{III.12})$$

Hence, Eq. (III.11) can be reduced to Fermi's golden rule for a single discrete level coupled to a continuum, which is a standard textbook model [264, page 19 et seqq.].

### III.2.3. Rate-equation approach (REA)

It follows from Eq. (III.12) that the coupling to the continuum is virtually treated on the rate-equation level. Although a density matrix approach would be beneficial for an exact theoretical comparison to rate equations, it is omitted here for the reason of being analogous to what can be found in pertinent literature. One proceeds analogous to the calculation of the Einstein coefficients [296, p. 52 et seqq.]. Let  $I$  be the intensity and

$$J_{\text{ph}} = \frac{I}{\omega_L} = \frac{1}{8\pi\alpha} \frac{|E_0|^2}{\omega_L} \quad (\text{III.13})$$

be the photon flux. The **rate-equation approach (REA)** is then defined as

### Rate-equation approach (REA)

$$\frac{d}{dt} \begin{pmatrix} p_G \\ p_X \end{pmatrix} = J_{\text{ph}}(t) \begin{pmatrix} -\sigma_{GX} & \sigma_{GX} \\ \sigma_{GX} & -\sigma_{GX} - \sigma_X \end{pmatrix} \begin{pmatrix} p_G \\ p_X \end{pmatrix}. \quad (\text{III.14})$$

The cross section  $\sigma_{GX}$  depends on the spectral properties of the pulse due to the sharp energy levels of the discrete states and thus, in the case of transform-limited pulses,  $\sigma_{GX}$  depends also on the pulse duration. The cross section  $\sigma_X$  follows directly from the Markovian theory and does not depend on pulse characteristics except for the photon energy  $\omega_L$ . Recall that a further assumption was made in Sec. III.2.2 to ensure this property. Eventually, the cross sections for Gaussian pulses read

$$\begin{aligned} \sigma_{GX} &= 4\pi\alpha\omega_L\sqrt{2\pi\tau}|\mu_0|^2, \\ \sigma_X &= 4\pi\alpha\omega_L\Re(\gamma_0). \end{aligned} \quad (\text{III.15})$$

To check against inconsistencies in the derivation, the cross sections in Eq. (III.15) in conjecture with the **REA** were tested to predict the same final populations as the Markovian theory in the limit of weak pulses with the photon flux being described by Gaussian temporal envelopes of different standard deviations  $\tau$  (see Fig. III.2a on page 35).

As mentioned above, the Markovian theory and the **REA** produce the same results –more precisely speaking, the same occupation probabilities– in the special case  $\mu_0 = 0$ . Note also that the **REA** depends only on two real-valued parameters,  $\sigma_{GX}$  and  $\sigma_X$ , with a ratio  $\sigma_{GX}/\sigma_X$  being proportional to the pulse duration. Accordingly, the latter is not only a material-dependent property, and it is thus reasonable to examine scenarios where the cross sections are varied independently of one another.

### III.2.4. Interpretation of the parameters

Comparing the Markovian theory, Eq. (III.11), and the **REA**, Eq. (III.14), one notices a considerable reduction of the number of parameters in the rate limit. In particular, it can be inferred from Eq. (III.15) that the phase of  $\mu_0$  and the imaginary part of  $\gamma_0$  are presumably of minor importance for the dynamics of occupation probabilities. This speculation will be discussed before the presentation of the results in order to provide an intuitive view on the relevant parameters.

It is easily proven that in the resonant case of the Markovian theory, Eq. (III.11),  $E_0(t)$  and  $\mu_0$  can be chosen to be real valued without loss of generality or, to be more precise, the occupation probabilities do not depend on the phase of the product  $\mu_0 E_0(t)$  due to the **RWA**. Therefore, it is sufficient to choose the parameter  $\sigma_{GX}$  to specify the relevant part of  $\mu_0$  for a fixed pulse duration within the Markovian theory.

Furthermore, it is self-evident that the imaginary part of  $\gamma_0$  does influence the occupation probabilities in the framework of the Markovian theory. Indeed,  $\Im(\gamma_0) \neq 0$  introduces a time-dependent detuning. Subsequently adding an imaginary part to  $\gamma_0$  in Eq. (III.11) is equivalent to

the substitution

$$\begin{aligned}\alpha_X(t) &\rightarrow \alpha_X(t) \exp\left(2\pi i \alpha \omega_L \Im(\gamma_0) \int_0^t J_{\text{ph}}(t') dt'\right), \\ E_0(t) &\rightarrow E_0(t) \exp\left(2\pi i \alpha \omega_L \Im(\gamma_0) \int_0^t J_{\text{ph}}(t') dt'\right).\end{aligned}\quad (\text{III.16})$$

This means that  $\gamma_0$  introduces a constant detuning for a flat-top pulse. Note that the detuning must not be large, i.e., the parameter must be consistent with the resonant approximation and the **RWA**. Correspondingly, results for  $\gamma_0 \notin \mathbb{R}$  have to be interpreted with caution. Since the impact of detuning was already extensively studied by [Kaiser \(2014\) \[4\]](#),  $\gamma_0$  is assumed to be real valued here. Seen from the opposite perspective, a detuning  $\delta\omega$  can be introduced to effectively render  $\gamma_0$  real.

Most importantly, the physical meaning of  $\gamma_0$  shall be addressed. It is instructive to examine the premise of the Markovian theory from another perspective: let  $g(\omega)$  be an auxiliary quantity defined by

$$g(\omega) := \sum_{\nu} |\mu_{\omega\nu}|^2, \quad (\text{III.17})$$

which is related to the absorption spectrum of atoms prepared in the state  $|X\rangle$  (see below). If the ionization dynamics, the pulse envelope, and  $\alpha_X(\tau)$  evolve on the femtosecond time scale, one can estimate from Eq. (III.9) that  $g(\omega)$  must decrease slowly on the energy scale of 1 eV to ensure the applicability of the Markovian theory. The question as to whether this premise is valid cannot be clarified within the generic model because it crucially depends on the specific system and  $\omega_L$ .

For now, it follows from the definition of  $\gamma_0$  (see Eq. (III.10)), Eq. (III.9), and Eq. (III.17):

$$\gamma_0 = \int_0^{\infty} d\tau \gamma(\tau) = \pi \int_0^{\infty} d\omega g(\omega) \delta(\omega - \omega_L - \omega_X) - i\mathcal{P} \int_0^{\infty} d\omega \frac{g(\omega)}{\omega - \omega_L - \omega_X}, \quad (\text{III.18})$$

provided that  $g(\omega)$  is a “well-behaved” function of  $\omega$ . Apparently,  $\gamma_0^*$  as a function of  $\omega_L$  satisfies the Kramers-Kronig relation [39, 297]. More technically,  $\gamma_0^*$  can be (apart from an additive constant) interpreted as the dynamic polarizability  $\alpha_P^X$  in the state  $|X\rangle$  disregarding the coupling to states other than the continuum and assuming the validity of the **RWA** [39, 95], i.e.,  $\alpha_P^X = i\gamma_0^*$ . However, this model contains only the dispersion corrections and not the contribution of Thomson scattering in forward direction. The absent term is real and identical to the number of electrons located at the atom [39]. Nevertheless, the imaginary part of  $\alpha_P^X$  can be inferred from  $\gamma_0$  as it fulfills the optical theorem: recall that the knowledge of the dynamic polarizability yields the atomic scattering factor in forward direction  $f(\omega_L, \vec{e}_L)$  according to  $f(\omega_L, \vec{e}_L) = -\omega_L^2 \alpha_P^X$ . Then, the optical theorem is written in the form

$$\Im(f(\omega_L, \vec{e}_L)) = -\omega_L^2 \Re(\gamma_0) = -\frac{\omega_L}{4\pi\alpha} \sigma_X.$$

This is consistent with the definition of the cross section  $\sigma_X$  in Eq. (III.15) and with Eq. (III.12). Similarly, the Markovian theory ensures that  $\sigma_X$  is positive due to  $\Re(\gamma_0) = g(\omega_X + \omega_L) \geq 0$ .

In summary,  $\Re(\gamma_0)$  and  $\Im(\gamma_0)$  are associated with the absorption and the anomalous scattering cross section, respectively. Without a specific model or experimental data, the relative importance of the real and the imaginary part cannot be decided. In general, however, absorption processes are more probable than scattering in the **X-ray** regime [152], so one may anticipate that the relation  $\Re(\gamma_0) > |\Im(\gamma_0)|$ , which will become important at a later stage, holds in most cases.

### III.3. Results

In the following, results will be shown that demonstrate the influence of the key parameters  $\sigma_X$  and  $\sigma_{GX}$  within the Markovian approximation and the **REA**. In particular, the ionization probability  $P_I(t)$ , which is defined as

$$P_I(t) := 1 - p_G(t) - p_X(t), \quad (\text{III.19})$$

after the pulse, i.e., for  $t \rightarrow \infty$ , and the renormalization of Rabi frequencies are discussed.

#### III.3.1. Ionization yield

The resonant **TPA** probability will be investigated in the frameworks of the Markovian theory, Eq. (III.11), and the **REA**, Eq. (III.14). No distinction is made between the terms **TPA** probability and the (overall) ionization yield since **OPA** is forbidden in all considered models and other multiphoton processes are usually not distinguished in experiments. In order to facilitate comparisons with experiments, the study does not concentrate on time-dependent phenomena but on the more conveniently accessible ionization yield after the pulse. It is assumed in all calculations that the initial condition is given by Eq. (III.5), i.e., the initial state for  $t \rightarrow -\infty$  is the ground state  $|G\rangle$ .

Let  $J_{\text{ph}}(t)$  be the photon flux with a Gaussian temporal profile

$$J_{\text{ph}}(t) = \frac{N_{\text{ph}}}{\sqrt{2\pi}\tau} \exp\left(-\frac{t^2}{2\tau^2}\right), \quad (\text{III.20})$$

where  $\tau$  is the standard deviation and  $N_{\text{ph}}$  is the total photon number. Then, the integrated flux  $N_{\text{ph}}(t)$  can be expressed in terms of the error function  $\text{erf}(t)$ :

$$N_{\text{ph}}(t) := \int_{-\infty}^t J_{\text{ph}}(t') dt' = \frac{1}{2}N_{\text{ph}} \left(1 + \text{erf}\left(\frac{t}{\sqrt{2}\tau}\right)\right) \quad (\text{III.21})$$

Note that  $\lim_{t \rightarrow \infty} N_{\text{ph}}(t) = N_{\text{ph}}$ . The time-dependent solution of the **REA**, Eq. (III.14), can be easily obtained analytically:

$$\begin{aligned} p_G(t) &= \left[ \cosh(\kappa N_{\text{ph}}(t)) + \frac{\sigma_X}{2\kappa} \sinh(\kappa N_{\text{ph}}(t)) \right] \exp(-\eta N_{\text{ph}}(t)), \\ p_X(t) &= \frac{\sigma_{GX}}{\kappa} \sinh(\kappa N_{\text{ph}}(t)) \exp(-\eta N_{\text{ph}}(t)), \end{aligned} \quad (\text{III.22})$$

$$\text{where } \kappa = \frac{1}{2} \sqrt{\sigma_X^2 + 4\sigma_{GX}^2}, \quad \eta = \frac{1}{2} (\sigma_X + 2\sigma_{GX}). \quad (\text{III.23})$$

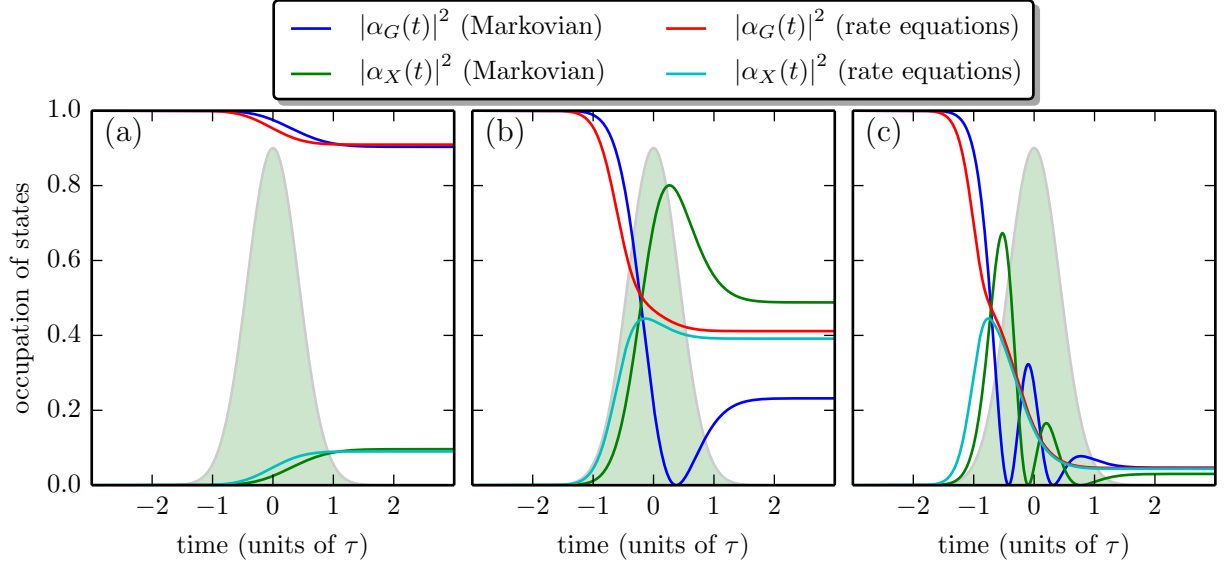


**Figure III.2.:** Time-dependent occupation probabilities of the discrete states  $|G\rangle$  and  $|X\rangle$  for  $\Im(\gamma_0) = 0$  and constant ratio  $\sigma_{GX}/\sigma_X = 10$  in all cases. The individual figures (a), (b), and (c) correspond to different pulse energies (or cross sections)  $\sigma_{GX}N_{\text{ph}} = 0.1$ ,  $\sigma_{GX}N_{\text{ph}} = 5$ , and  $\sigma_{GX}N_{\text{ph}} = 50$ . The temporal pulse envelope of the intensity is sketched in the background in arbitrary units.

The parameters  $\kappa$  and  $\eta$  fulfill the inequality condition  $\eta \geq \kappa \geq 0$ , where equality holds only in the trivial case where at least one cross section  $\sigma_X$  or  $\sigma_{GX}$  vanishes. It is easy to see that the form of the time-dependent solution in Eq. (III.22) is valid for arbitrary pulse shapes.

To provide the necessary background for the parameter study, it is essential to draw the attention to the degrees of freedom. A straightforward analysis reveals that after rescaling the time variable to  $t/\tau$  the REA depends only on two parameters, the *scaled cross sections*  $\sigma_{GX}N_{\text{ph}}$  and  $\sigma_X N_{\text{ph}}$ . Similarly, the Markovian theory has the same two independent parameters but also  $\sigma_A N_{\text{ph}}$  with  $\sigma_A := 2\pi i\alpha\omega_L \Im(\gamma_0)$  as in Eq. (III.16). Likewise, the dependence on  $\tau$  can be circumvented by the same rescaling while keeping the rates, Eq. (III.15), fixed. To prove these assertions [not shown], one assumes  $\mu_0 \in \mathbb{R}$  without loss of generality (cf. Sec. III.2.4). The subsequent analysis focuses on the case  $\sigma_A = 0$ , so both models are fully characterized by  $\sigma_{GX}N_{\text{ph}}$  and  $\sigma_X N_{\text{ph}}$ .

For an intuitive understanding of the differences between the Markovian theory and the REA, selected time traces of the analytic rate-equation solution, Eq. (III.22), and numerical results for the Markovian theory are shown in Fig. III.2. In all cases, the transitions between the discrete states are considerably more likely than promoting an electron to the continuum from the excited state by fixing the ratio  $\sigma_{GX}/\sigma_X = 10$ . Fig. III.2a depicts the temporal monotonic behavior of the occupation probabilities in both models for small doses. The transition between the discrete states is clearly seen, whereas the ionization plays a minor role. The final value of  $p_G$  is estimated by  $\sigma_{GX}N_{\text{ph}} = 0.1$ . As stated before in Sec. III.2.3, the REA reproduces the final occupation numbers for weak pulses. Similar to the well-known two-level system, the time-dependent populations of the discrete levels exhibit a tendency towards a balance of stimulated emission and absorption, i.e., identical occupation probabilities, for higher doses as seen in Figs. III.2b

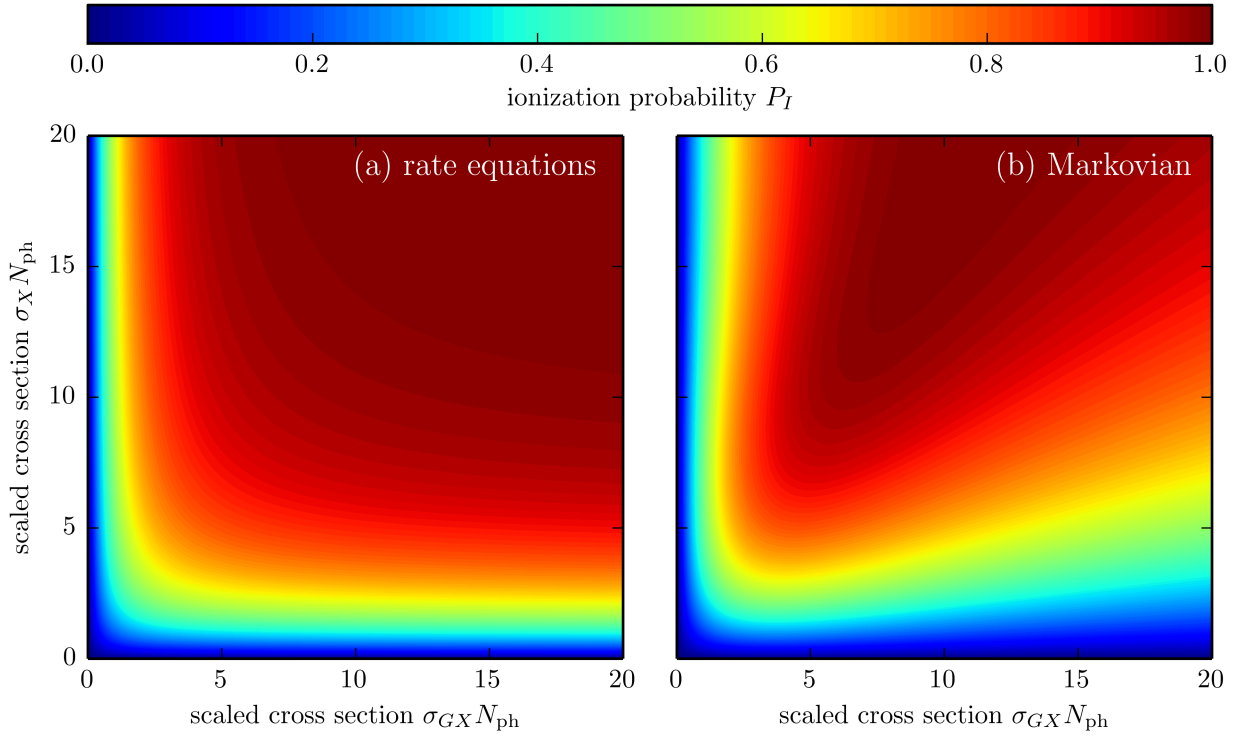


**Figure III.3.:** Ionization probability  $P_I$  after the pulse for different doses and ratios  $\sigma_{GX}/\sigma_X$  as obtained from the REA (a) and the Markovian theory with  $\sigma_A=0$  (b).

and c. The Markovian theory, by contrast, stands out due to the Rabi cycling (further discussed below in Sec. III.3.2). The final populations predicted by the two models deviate strongly for the intermediate dose in Fig. III.2b, which is mitigated again for the highest dose in Fig. III.2c. This feature is universal and will play a key role later in the interpretation of the ionization yield.

Now that the qualitative temporal behavior was demonstrated in both models, the final ionization probability  $P_I$ , Eq. (III.19), will be analyzed for a broad parameter range. Within the REA, it follows immediately from the analytic solution Eq. (III.22):

$$P_I := \lim_{t \rightarrow \infty} P_I(t) = 1 - \left[ \cosh(\kappa N_{\text{ph}}) + \frac{\eta}{\kappa} \sinh(\kappa N_{\text{ph}}) \right] \exp(-\eta N_{\text{ph}}). \quad (\text{III.24})$$

This result, as already mentioned, holds for an arbitrary pulse shape. Therefore, the theory on this level is rather insensitive to fluctuations of SASE pulses and does not suffer from insufficiently characterized pulses as much as the Markovian theory. In the limit of small doses one obtains

$$P_I = \frac{1}{2} \sigma_{GX} \sigma_X N_{\text{ph}}^2 + \mathcal{O}(N_{\text{ph}}^3), \quad (\text{III.25})$$

where the factor  $\frac{1}{2}$  appears compared to the scenario of independent processes with transition probabilities  $\sigma_{GX} N_{\text{ph}}$  and  $\sigma_X N_{\text{ph}}$ . It is easy to show that this is attributed to the simultaneity of the processes rather than stimulated emission.

A false-color representation of Eq. (III.24), i.e., the ionization yield as predicted by the REA, is shown in Fig. III.3a. Along each straight line through the origin, one can trace the monotonic

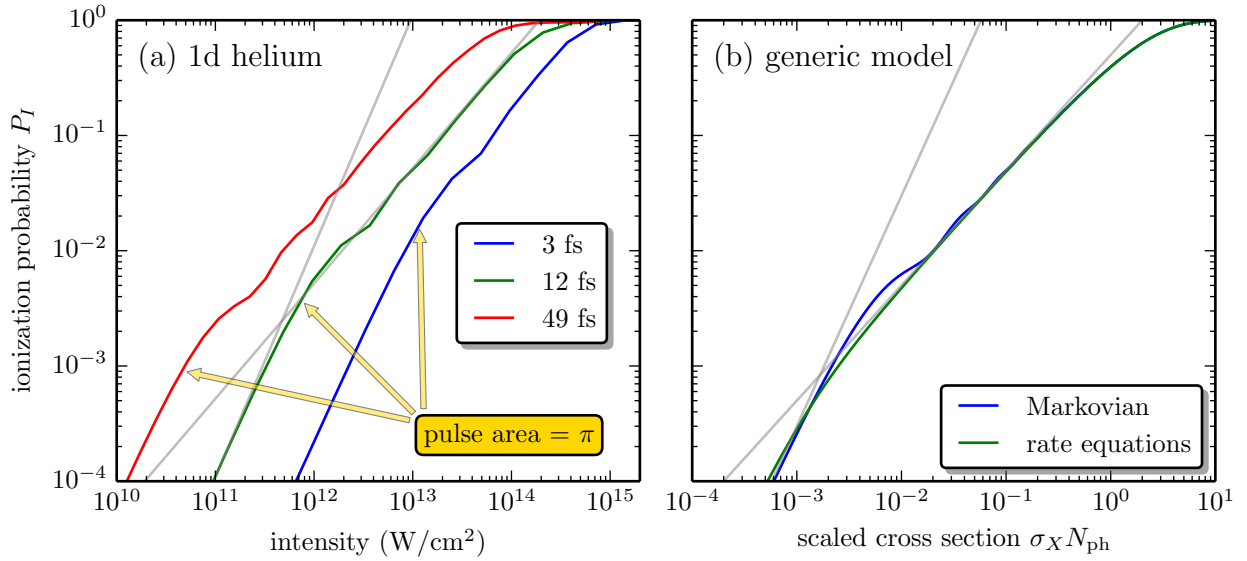


**Figure III.4.:** Log-log plot illustrating the intensity scaling of the ionization yield via resonant TPA obtained (a) from a 1d model for helium (data from Ref. [288]) and (b) from the Markovian theory where  $\sigma_{GX}/\sigma_X = 1000$ . Note that both abscissae can be replaced by the total photon number  $N_{\text{ph}}$  or the pulse energy in arbitrary units because both the intensity for a fixed pulse duration and the scaled cross section are proportional to  $N_{\text{ph}}$  and the pulse energy. The gray lines highlight the power laws  $P_I \propto N_{\text{ph}}$  and  $P_I \propto N_{\text{ph}}^2$ .

dependency of the ionization yield on the absorbed dose for a constant ratio  $\sigma_{GX}/\sigma_X$ . Recall that this ratio can be altered by changing the pulse duration  $\tau$  (cf. Eq. (III.15)). Increasing only one of the two parameters  $\sigma_{GX}N_{\text{ph}}$  and  $\sigma_XN_{\text{ph}}$  generally entails an enhancement of the ionization yield. Obviously, both transitions have to be sufficiently probable in order to promote the ionization yield to 1. For example, the depletion of the bound states is very efficient if both scaled cross sections are around 10. For small doses, the ion yield is constant along rectangular hyperbolae in Fig. III.3a as follows from Eq. (III.25). However, one can easily discern that this approximation breaks down already for comparatively small pulse energies.

In contrast, the analogous results from the Markovian theory for  $\sigma_A = 0$  depicted in Fig. III.3b exhibit a qualitatively different dependency on  $\sigma_{GX}N_{\text{ph}}$ , which can be attributed to the onset of Rabi oscillations around  $\sigma_{GX}N_{\text{ph}} \approx 5$  (see Fig. III.2b). As a result, the population of the ground state grows with increasing pulse energy at the expense of the population of the excited state. Subsequently, a deexcited atom cannot be subject to direct ionization in the present model but requires another excitation preceding the ejection of an electron. It is further interesting to see that the results quantitatively coincide with the REA only for very small doses.

Next, a link between Fig. III.3 and experimentally accessible data in typical XFEL based studies will be established. Consider Fig. III.4a where the ionization probability as a function of the incident intensity for a simulated 1d helium atom in an analogous scenario<sup>2</sup> is shown; similar curves can be obtained from experiments [71, 287]. The pulse duration determines the ratio  $\sigma_{GX}/\sigma_X$  and then the corresponding curve can be extracted from Fig. III.3 along the associated

<sup>2</sup>consult Ref. [288] for details

straight line through the origin. All curves in Fig. III.4 grow quadratically with  $N_{\text{ph}}$  for small pulse energies. Then, a near-linear scaling can be observed for higher pulse energies before  $P_I$  eventually saturates. The scaling behavior is indicated by the gray lines in both Fig. III.4a [for 12 fs pulse duration] and Fig. III.4b. According to perturbation theory the exponent is expected to be approximately 2 because the continuum states are reached through the absorption of two photons. This simplified picture is consistent with experimental observations for non-resonant TPA but not with the exponents around 1 in the resonant case [287]. Here, one discerns both exponents for resonant TPA by varying the intensities over many orders of magnitude: the  $P_I \propto N_{\text{ph}}^2$  dependence is clearly seen for low intensities and also a crossover to a near-linear scaling can be identified.

This phenomenon experienced by the 1d helium is also captured by the minimalistic models considered here, Eq. (III.11) and Eq. (III.14). The simplicity of the models is advantageous for the interpretation of the results. For now, the analysis concentrates on the physics behind Fig. III.4b. Similar to the tendency observed in Fig. III.2, the ionization probabilities for the Markovian approximation and the REA coincide for large photon numbers  $N_{\text{ph}}$  even though the rate equations were obtained in the limit of weak pulses. Thus, for small pulse energies the situation is obvious: the Markovian theory and the REA yield the same scaling behavior for  $P_I$ , where the analytic solution in the framework of rate equations was already obtained in Eq. (III.25).

The linear scaling for higher pulse energies can be derived fairly easily as well. First, in both models it follows straightforwardly from the respective equations of motion Eq. (III.11) and Eq. (III.14) without approximation:

$$\frac{d}{dt}P_I = \sigma_X J_{\text{ph}} p_X. \quad (\text{III.26})$$

An approximation in the shape of a closed ODE for  $P_I$  is obtained within the REA as follows. If stimulated emission and absorption compensate rapidly, i.e.,  $\sigma_{GX} \gg \sigma_X$ , then the populations for both discrete states will have approximately the same values during the ionization process,  $p_X \approx p_G$ . Thus, one can write  $p_X \approx \frac{1}{2}(1 - P_I)$  and finds

$$\frac{d}{dt}P_I = \sigma_X J_{\text{ph}} p_X \approx \frac{1}{2}\sigma_X J_{\text{ph}} (1 - P_I). \quad (\text{III.27})$$

The same equation can be obtained within the Markovian theory as long as large pulse areas are concerned, i.e., the time scale of the Rabi oscillations is assumed to be short compared to the time scale of the ionization process. In this case, the resonantly driven atomic states are subject to fast oscillations as in Fig. III.2c. Consequently, the same estimate  $p_X \approx \frac{1}{2}(1 - P_I)$  holds on time average. Again the same ODE for the ionization yield  $P_I$ , Eq. (III.27), follows despite the fact that the underlying mechanisms are completely different. Finally, one derives the linear scaling of  $P_I$  in the aforementioned limiting cases by solving Eq. (III.27) for an arbitrary pulse profile

$$\begin{aligned} P_I(t) &= 1 - \exp\left(-\frac{1}{2}\sigma_X N_{\text{ph}}(t)\right) \\ \Rightarrow P_I &= 1 - \exp\left(-\frac{1}{2}\sigma_X N_{\text{ph}}\right) = \frac{1}{2}\sigma_X N_{\text{ph}} + \mathcal{O}(N_{\text{ph}}^2) \end{aligned}$$

The conclusion to draw from this result is twofold. Firstly, the REA and the Markovian theory provide two different mechanisms that lead to a linear scaling of the ionization yield  $P_I$  so that

they cannot be distinguished by measuring  $P_I$  in a broad intensity regime. Hence, although the REA fails to take into account the Rabi cycling mechanism, the underlying theory can be extended to higher pulse energies provided that only  $P_I$  is detected. Secondly, seen from the opposite perspective, this result infers that a correct prediction of the ionization yield by rate equations does not imply a correct representation of all relevant processes.

However, if a sufficiently broad energy range is accessible where the crossover between the linear and the quadratic scaling can be observed, it may be possible to distinguish between the two mechanisms, Rabi cycling and the striving for equal populations: on the one hand, the onset of Rabi cycling is characterized by the pulse area, which is proportional to the electric field, and, on the other hand, the saturation between the discrete states within the incoherent REA depends on the integrated photon flux, which is proportional to the intensity. In the case of the fully coherent simulation for a 1d helium shown before in Fig. III.4a, it can be anticipated that the variation in the scaling behavior is attributed to Rabi cycling. The intensities corresponding to the pulses where the Rabi oscillation completes exactly half a cycle, i.e., the pulse area equals  $\pi$ , are indicated. Evidently, the onset of the crossing is well estimated by this consideration.

Finally, it is interesting to note that the ionization yield can be calculated analytically within the Markovian theory for flat-top pulses investigated below in Sec. III.3.2. The occupation probabilities  $p_G$  and  $p_X$  for finite pulses can be easily extracted from Eq. (III.31) in the ensuing section because  $p_G$  and  $p_X$  are constant in each time interval where the electric field vanishes identically. The consequence is that  $p_G$  and  $p_X$  after a flat-top pulse of duration  $T$  are equal to  $|\alpha_G(T)|^2$  and  $|\alpha_X(T)|^2$  from Eq. (III.31). The corresponding ionization probability for a constant electric field amplitude behaves similarly and coincides with the results obtained by the REA for high pulse energies (not shown in Fig. III.4b). As an alternative to the analysis above, one can recover the same scaling behavior for flat-top pulses directly from the analytic solution.

### III.3.2. Renormalization of Rabi frequencies

The Rabi frequency, which was demonstrated to characterize the crossover between the linear and quadratic scaling behavior in the previous subsection, can in fact not be calculated using the formula obtained for the two-level system. The aim of this analysis is to complement the discussion in Refs. [4, 288] because it was already intensely discussed in the original publication [288] and by Kaiser (2014) [4] that the coupling to the continuum leads to a shift of the Rabi frequency. In the course of this, a more straightforward derivation of the analytic result in Ref. [288] is outlined. This subsection addressing the topic of renormalization of Rabi frequencies is, however, kept brief because this phenomenon is supposed to be very challenging to measure at contemporary XFEL facilities. It should be mentioned that the equation of motion considered for this purpose is solely the Markovian theory, Eq. (III.11) because Rabi cycling is not included in the REA (see Fig. III.2 on page 35).

For the simplicity of the analysis, a flat-top pulse  $E_0(t) = \theta(t) E_0$  is assumed so that the Rabi frequency does not depend on time. The initial condition  $|\psi(0)\rangle = |G\rangle$  translates into

$$\alpha_G(0) = 1, \quad \alpha_X(0) = \alpha_{\omega\nu}(0) = 0. \quad (\text{III.28})$$

In this case, Eq. (III.11) reduces to a system of first-order linear ODEs with constant coeffi-

cients:

$$\frac{d}{dt} \begin{pmatrix} \alpha_G(t) \\ \alpha_X(t) \end{pmatrix} = \begin{pmatrix} 0 & -i\Omega_0^* \\ -i\Omega_0 & -2\Gamma \end{pmatrix} \begin{pmatrix} \alpha_G(t) \\ \alpha_X(t) \end{pmatrix}, \quad (\text{III.29})$$

$$\text{where } \Gamma := \frac{1}{8} |E_0|^2 \gamma_0, \quad \Omega_0 := \frac{1}{2} E_0 \mu_0. \quad (\text{III.30})$$

Hence, Eq. (III.29) is trivially solvable by means of standard analytical techniques. The eigenvalues of the coefficient matrix are  $-\Gamma \pm i\Omega$ , where  $\Omega = \sqrt{|\Omega_0|^2 - \Gamma^2} \in \mathbb{C}$ . Then, the solution with respect to the initial condition in Eq. (III.28) can be written in the form

$$\begin{aligned} \alpha_G(t) &= \left[ \cos(\Omega t) + \frac{\Gamma}{\Omega} \sin(\Omega t) \right] e^{-\Gamma t} \\ \alpha_X(t) &= -i \frac{\Omega_0}{\Omega} \sin(\Omega t) e^{-\Gamma t} \end{aligned} \quad (\text{III.31})$$

Note that  $|\Omega_0|$  is the Rabi frequency of the pure two-level system. This limiting case can be obtained by setting  $\Gamma = 0$  or  $\gamma_0 = 0$ . Evidently, the coupling to the continuum leads to a renormalization of the Rabi frequency according to

$$\frac{\Omega}{|\Omega_0|} = \sqrt{1 - \frac{\Gamma^2}{|\Omega_0|^2}} = \sqrt{1 - \frac{\pi\alpha}{2} \frac{\gamma_0^2}{|\mu_0|} I}. \quad (\text{III.32})$$

One can infer from Eq. (III.32) that the general tendency of the reported renormalization mechanism is an initial decrease of the Rabi frequency. This assertion is easily proven by noting that the derivative of  $\Re(\Omega/|\Omega_0|)$  is negative at  $I = 0$  if and only if

$$\Re(\gamma_0^2) = (\Re(\gamma_0))^2 - (\Im(\gamma_0))^2 > 0.$$

Since the latter statement is often true (see page 34), the intensity dependence of the renormalization for the resonant case in Ref. [288] is as expected. However, for the near-resonant case with nonzero detuning, the intensity dependence may deviate from this conclusion because –as discussed above– the introduction of a detuning is equivalent to changing the imaginary part of  $\gamma_0$ . Accordingly,  $\Re(\gamma_0^2)$  may be negative, which, in turn, leads to an increase of the Rabi frequency for small intensities. In fact, this behavior was observed in simulations of 1d helium by Kaiser (2014) [4]. Note that it is not clear whether this interpretation is applicable in general since in the case of a larger detuning  $\delta\omega \neq 0$ , further bound states are indispensable for the theoretical description and the resonant approximation breaks down.

# IV

## Coherent ionization dynamics in crystals

Incoherent ionization dynamics as implicitly postulated in rate descriptions is known to reflect the essential physics behind experiments based on sequential multiphoton inner-shell ionization of atoms under XFEL irradiation (see Sec. I.2.1). Indeed, as concluded in the previous chapter, successful modeling with rate equations is even sufficient for resonant **two-photon absorption (TPA)** in broad intensity regimes where it was anticipated to break down. Applying the rate-equation approach to larger samples such as clusters or macromolecules can be largely reduced to the response of single atoms [6, 298]. This idea is suggested by the well-established experimental and theoretical evidence that **X-ray** photoabsorption primarily involves inner-shell electrons, which are hardly affected by their environment through effects such as chemical bonding. However, secondary processes come into play after the inner-shell excitation and involve the surroundings of the individual atoms; among them are collisional ionization, electrostatic trapping, and recombination. Effective strategies to consistently account –not only from a mathematical perspective but also with respect to physical intuition– for these processes with the atomic rate-equation approach have been developed for molecules [80] and solids [211].

As the previous chapter revealed that the rate description may have deficiencies that are likely not to be unveiled by commonly measured quantities such as the charge-state distribution, the present chapter is devoted to finding favorable conditions for the observation of coherent ionization dynamics in crystals. For this purpose, the lattice periodic potential is accounted for explicitly. The computation of such a system is feasible as long as the absence of electron-electron interaction is assumed, which implies that many well-known phenomena of extended systems are axiomatically disregarded (as described in Chapter II). This approach is not only interesting as a model study, designed in order to identify potentially overlooked processes, but may also be more applicable in the future for fully coherent pulses that are capable of, e.g., outrunning collisional ionization with subfemtosecond pulses [6]. Thus, this idealistic perspective is anticipated to be boosted by the ongoing development and technological advances of XFELs.

In general, the focus lies on photon energies slightly above an inner-shell edge in order to avoid the cases where the rate description is normally well suited, namely far above the ionization threshold. This scenario, hereafter referred to as **near-threshold ionization (NTI)**, is beneficial for the validity of the model since photoelectrons with sufficiently low kinetic energy (and frozen Auger channels) suppress collisional ionization. The major part of the content of this chapter has been published by the author and coworkers in Ref. [299].

### IV.1. Theory

To begin with, a simplistic model of a crystal is introduced as the basis for all numerical simulations that led to the results shown in the present chapter. The model treats both the

inner-shell and free electrons uniformly as Bloch waves. It is shown here, inter alia, that this approach automatically results in different characteristics of wave functions associated with deeply bound and free electrons.

The general assumptions adopted in this chapter were extensively discussed in Chapter II. In particular, the model is based on the dynamical equation for the 1RDM given by the TDHF equations, Eq. (II.1) but even further reduced in computational complexity: the electron-electron interaction is omitted by setting  $V_{ee} \equiv 0$  in Eq. (II.1) (cf. page 22). The electron-core interaction described by  $V_{\text{core}}$  in Eq. (II.1) is approximated by a Kronig-Penney (KP) potential  $V_{\text{KP}}$  for the reasons outlined on page 19:

$$V_{\text{KP}}(x) = \begin{cases} -V_0, & \text{if } x \in \bigcup_{n \in \mathbb{Z}} [-a + nd, a + nd], \\ 0, & \text{otherwise.} \end{cases} \quad (\text{IV.1})$$

The physical meaning of the three parameters  $a$ ,  $V_0$ , and  $d$  is the following: the width and the depth of the potential of an individual atom are given by  $a$  and  $V_0$ , respectively;  $d$  is the core-core distance. For notational simplicity, one defines  $g$  as the reciprocal lattice vector of minimal length, which results directly from  $d$  according to  $g := \frac{2\pi}{d}$ . To enable a numerical analysis, the following parameters are chosen throughout this chapter:

$$d = 5 \text{ a.u.}, \quad a = 1 \text{ a.u.}, \quad \text{and} \quad V_0 = 6 \text{ a.u.} \quad (\text{IV.2})$$

These parameters are appropriate for modeling inner-shell orbitals due to both the large  $V_0 = 6 \text{ a.u.} \approx 163 \text{ eV}$  and the fact that  $a$  is small compared to the core-core distance  $d$ , thereby ensuring that the ground-state orbitals are tightly bound and strongly localized at the cores. Under these conditions, the electronic band structure  $\epsilon_{nk}$  shown in Fig. IV.1a is formed, where  $n$  denotes the band index and  $k$  the Bloch wave vector in the first Brillouin zone (BZ),  $k \in [-\frac{1}{2}g, \frac{1}{2}g]$ . The Bloch states with single-particle eigenenergies  $\epsilon_{nk}$  and spin  $\sigma$  are correspondingly characterized by  $n, k$  and are thus written as  $|\psi_{nk\sigma}\rangle$ . As all considered interactions are spin independent, the spin index  $\sigma$  does not play an important role and is not explicitly written in most cases.

Electrons occupying states with a positive energy  $\epsilon_{nk} > 0$  are interpreted as free electrons because they principally possess sufficient energy to leave the crystal even though the electrons cannot actually exit the infinite crystal. Accordingly, bands  $n$  with  $\epsilon_{nk} > 0$  for all  $k$  will be referred to as *free bands*. To highlight the

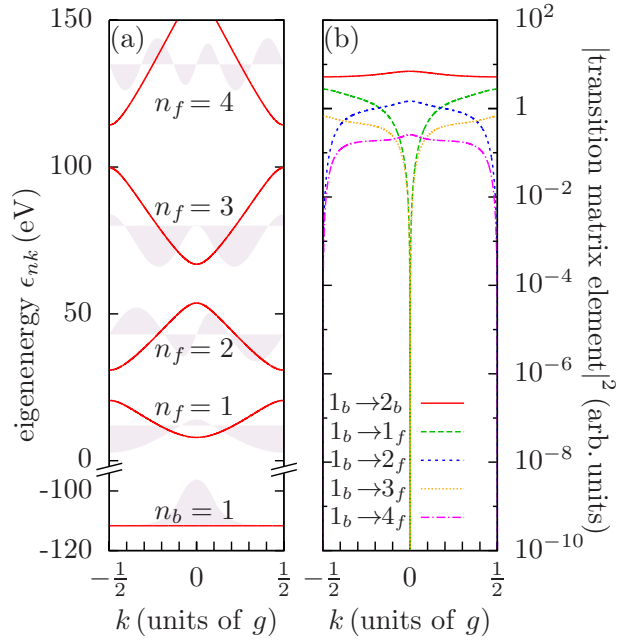


**Figure IV.1.:** (a) Band structure of the Kronig-Penney (KP) model. The real-space representation of the eigenstates  $|\psi_{nk=0}\rangle$  of each band is sketched in the background. (b)  $k$  dependence of transition matrix elements illustrated by  $|\langle\psi_{nk}|\hat{p}|\psi_{mk}\rangle|^2$ .

difference between bound and free bands, two distinct indices  $n_b, n_f \in \mathbb{N}$  are used to label the  $n_b$ -th ( $n_f$ -th) bound (free) band. In the present case, i.e., for a **KP** potential with the parameters chosen in Eq. (IV.2), there are only two bound bands. The first bound band  $n_b = 1$  is seen in Fig. IV.1a at  $-112$  eV. It distinguishes itself from other bands by a small width  $\ll 0.01$  eV and associated electron densities which are strongly localized at the cores as indicated by the real-space representation of the eigenstates at  $k=0$  seen in the background of Fig. IV.1a. This finding is in conformity with the physical intuition that deeply bound electrons exhibit identical eigenenergies because they are not influenced by their environment. The second bound band  $n_b = 2$  has eigenenergies between  $-4.5$  and  $-0.9$  eV and is not shown in Fig. IV.1a. There is a relatively large gap between the  $n_b = 2$  and  $n_f = 1$  bands of roughly 9 eV. Consistent with the interpretation of free bands, the wave functions for positive eigenenergies are subject to a wider spread of the electron density (cf. the depicted cases  $n_f = 1, \dots, 4$  in Fig. IV.1a). There are, however, two aspects that should be mentioned regarding this understanding of free bands. Firstly, in real systems, the finite work function, which increases for a more highly charged sample and ultimately leads to a trapping of electrons as reported in Sec. I.2.2, must be taken into account. Secondly, depending on the choice of parameters in Eq. (IV.2), there may exist a band that has both negative and positive eigenenergies. Hence, it cannot be classified as carried out above.

The gaps between free bands are not artificial by-products of the model. For quasi-free electrons, there is a standard textbook analysis<sup>1</sup> that predicts band gaps proportional to  $|V_{\pm g}|$ . However, for **3d** systems it is immediately plausible that the density of states does not generally vanish in the regions of the **1d** band gaps. To prove this assertion, one can simply consider a **3d** potential that separates into a sum of **KP** potentials. Nevertheless, *van Hove singularities* will still appear due to the critical points of the eigenenergies as a function of the Bloch wave vector  $k$ .

Next, the time-dependent Hamiltonian for describing the dynamics of the system under irradiation with a laser pulse is defined based on the knowledge about the band structure  $\epsilon_{nk}$  and the corresponding Bloch basis. Although the system size is large –or even infinite within this model–, the laser pulse is still assumed to be spatially independent because this premise is inevitable for **1d** models (cf. Sec. II.1). Accordingly, the structure of the associated time-dependent Hamiltonian  $H(t)$  as shown below is significantly simplified. Let  $c_{nk\sigma}^\dagger$  and  $c_{nk\sigma}$  be the creation and annihilation operators of an electron in the Bloch state  $|\psi_{nk\sigma}\rangle$ . Then, one can prove that the minimal-coupling Hamiltonian [39] can be written as

$$H(t) = \sum_{n,m,k,\sigma} (\epsilon_{nk}\delta_{nm} + \alpha A(t) \langle \psi_{nk\sigma} | \hat{p} | \psi_{jk\sigma} \rangle + \frac{1}{2}\alpha^2 A^2(t) \delta_{nm}) c_{nk\sigma}^\dagger c_{mk\sigma}. \quad (\text{IV.3})$$

Since the term  $\propto A^2$  is merely a multiple of unity, it has no physical ramifications. Thus, the term is dropped without loss of generality. Note that –by virtue of the simple form of the vector potential– the Hamiltonian  $H$  is diagonal in  $k$ , which follows directly by exploiting the identity  $\langle \psi_{nk\sigma} | \hat{p} | \psi_{jk'\sigma} \rangle = 0$  for  $k \neq k'$ .

For the interpretation of the results in Sec. IV.3, it turns out that a knowledge of the qualitative  $k$  dependence exhibited by the transition matrix elements  $\langle \psi_{nk} | \hat{p} | \psi_{mk} \rangle$  is extremely useful; their

<sup>1</sup>See, for example, Ref. [261, p. 100 et seqq.]. The estimate therein, however, does not apply to the present situation because  $|V_0|$  is not small compared to the band gaps.

absolute square for transitions between selected bands  $n$  and  $m$  is shown in Fig. IV.1b. It is striking that in the case of the bound-bound transitions  $1_b \rightarrow 2_b$ , only a comparatively weak  $k$  dependence of the matrix elements is seen. Further, the magnitude of the transition matrix elements is large compared to bound-free transitions. The  $k$  dependence of bound-free transitions is easily understood by noting that the parity selection rule holds exactly for  $k=0$ . Hence, the transitions  $1_b \rightarrow 1_f$  and  $1_b \rightarrow 3_f$  are strongly suppressed at  $k=0$  and feature a broad distribution of transition matrix elements varying by orders of magnitude.

## IV.2. Equations of motion

In analogy to Sec. III.2 of the previous chapter, several equations of motion are presented arranged in a hierarchical order, starting with the most sophisticated treatment. Since the most elaborated theory employed here, Sec. IV.2.1, is rather modest with respect to computational costs, there is again no need for further simplifications in order to reduce the numerical effort. However, the different levels of theory are useful for an intuitive interpretation of the results.

In order to avoid confusion, it is explicitly stated that although the resonant approximation and Markovian theory in this chapter are conceptually similar to the eponymous approaches in Chapter III, they differ in many aspects. As a consequence, it is indispensable to specify these methods in the present context.

### IV.2.1. Schrödinger equation for non-interacting electrons

The equations of motion for the spin-independent 1RDM  $\varrho_{nm}(k, k') := \langle c_{nk\sigma}^\dagger c_{mk'\sigma} \rangle$  can be derived from the Heisenberg equations for the creation and annihilation operators:

$$i \frac{d}{dt} \varrho_{nm}(k, k') = (\epsilon_{mk'} - \epsilon_{nk}) \varrho_{nm}(k, k') + \sum_j (W_{mj}(k) \varrho_{nj}(k, k') - W_{nj}^*(k) \varrho_{jm}(k, k')), \quad (\text{IV.4})$$

where the matrix elements are given by  $W_{nj}(k) := \alpha A(t) \langle \psi_{nk\sigma} | \hat{p} | \psi_{jk\sigma} \rangle$ . Due to the simple form of the Hamiltonian  $H$ , the equations of motion automatically decouple for every pair  $k, k'$ . As the analyses in this chapter concentrate on occupation probabilities of bands, it is sufficient to restrict Eq. (IV.4) to the  $k$ -diagonal part of the 1RDM  $\varrho_{nm}(k) := \varrho_{nm}(k, k)$ . Alternatively, one can argue that the  $k$ -off-diagonal parts remain zero for all times according to Eq. (IV.4) if the initial state is diagonal. In both cases, one obtains the following closed set of equations of motion for  $\varrho_{nm}(k)$ :

#### Time-dependent Schrödinger equation (TDSE)

$$i \frac{d}{dt} \varrho_{nm}(k) = (\epsilon_{mk} - \epsilon_{nk}) \varrho_{nm}(k) + \sum_j (W_{mj}(k) \varrho_{nj}(k) - W_{nj}^*(k) \varrho_{jm}(k)). \quad (\text{IV.5})$$

Being a direct consequence of the time-dependent Schrödinger equation (TDSE) with respect to the Hamiltonian in Eq. (IV.3), these equations of motion are referred to as TDSE or Schrödinger theory below.

The physical quantities of interest are the average occupation probabilities of all bands. For this purpose, Eq. (IV.5) has to be solved for an appropriate discretization of the  $k$  domain, the first BZ. To be more precise, the periodic boundary conditions suggest that the  $k$  domain should be divided into a uniform grid [261]. For each Bloch wave vector  $k$ , there is a corresponding equation of the form Eq. (IV.5) that is decoupled from the values of the 1RDM at a distinct  $k' \neq k$ . The average occupation probabilities of a band  $n$  are then obtained as the  $k$  average over  $\varrho_{nn}(k)$ . For the sake of brevity, the parametric dependence on  $k$  is omitted in spite of actually being present in Eq. (IV.5) and equations below.

### IV.2.2. Resonant approximation

The derivation of the rate description in the present and the ensuing subsection follows the procedure from Rossi and Kuhn (2002) [300]. This simplified perspective, where ultimately only the diagonal elements of the 1RDM  $\varrho_{nn}(k)$  appear in the dynamical equations, is known to be applicable if both non-resonant contributions and the memory effects can be safely disregarded. To distinguish the implications of these two distinct approximations, an approach will be introduced which solely requires the assumption of the dominance of resonant terms in the equations of motions. This intermediate level of theory between the TDSE and the rate-equation approach is straightforwardly achieved by using an intermediate result of the aforementioned derivation.

For this purpose, the strategy consists in the first instance of a reformulation of Eq. (IV.5) emphasizing on the occupation probabilities:

$$\frac{d}{dt}\varrho_{nn} = \sum_{j \neq n} g_{jn}(t), \quad (\text{IV.6})$$

$$\text{with } g_{jn}(t) := 2\Im(W_{nj}\varrho_{nj}). \quad (\text{IV.7})$$

In this step, the generation rate  $g_{jn}(t)$  for the occupation of state  $n$  stemming from state  $j$  was introduced. Eqs. IV.6 and IV.7 obviously do not constitute a closed set of equations because the generation rate depends on the off-diagonal elements of  $\varrho_{nm}$ . To resolve this issue, the off-diagonal elements are replaced in Eq. (IV.7) by the formal solution of the TDSE with respect to the initial condition  $\lim_{t \rightarrow -\infty} \varrho_{nm}(t) = 0$ . Step by step, one writes

$$\varrho_{nm}(t) = -ie^{i\omega_{nm}t} \int_{-\infty}^t dt' e^{-i\omega_{nm}t'} \sum_j \left( W_{mj}(t')\varrho_{nj}(t') - W_{nj}^*(t')\varrho_{jm}(t') \right), \quad n \neq m, \quad (\text{IV.8})$$

with the transition frequency  $\omega_{nm} := \epsilon_n - \epsilon_m$ . For a compact notation, one defines the auxiliary quantities  $\tilde{W}_{nj}(t) := e^{i\omega_{nj}t}W_{nj}(t)$  and  $\tilde{\varrho}_{nj}(t) := e^{-i\omega_{nj}t}\varrho_{nj}(t)$ . Then, one obtains the generation rate

$$g_{jn}(t) = 2\Re \left[ \tilde{W}_{nj}(t) \int_{-\infty}^t dt' \sum_l \left( \tilde{W}_{jl}(t')\tilde{\varrho}_{nl}(t') - \tilde{W}_{nl}^*(t')\tilde{\varrho}_{lj}(t') \right) \right]. \quad (\text{IV.9})$$

So far, no further approximation compared to the TDSE has been made. Now, it will be shown that under appropriate conditions the main contribution to the integral in Eq. (IV.9) stems from diagonal elements. This procedure allows to neglect the off-diagonal terms and thus yields a theory that is closer to the rate description. To be able to continue with the derivation, the form of the laser pulse, which is characterized by a time-dependent vector potential  $A(t)$ , is further constrained by assuming that

$$A(t) = A_0(t) \cos(\omega_0 t), \quad (\text{IV.10})$$

where  $\omega_0$  is interpreted as the photon energy and  $A_0$  is the slowly varying amplitude (compared to the fast time scale of  $1/\omega_0$ ). The premise of the approximative treatment is that oscillations on the fast time scale  $1/\omega_0$  and  $1/\omega_{nm}$  for  $n \neq m$  average out in the integral in Eq. (IV.9). Note that the time dependence of  $\varrho_{nm}$  is, based on Eq. (IV.8), roughly given by  $\varrho_{nm}(t) \propto e^{i\omega_{nm}t}$ , i.e.,  $\tilde{\varrho}_{nm}(t)$  has a component on the slow time scale for all  $n, m$ . In contrast,  $\tilde{W}_{nm}(t)$  contributes if and only if  $|\omega_{nm}| \approx \omega_0$ . It is assumed that for each  $k$  there is only one pair of indices  $n, m$  such that this condition is fulfilled. Now, two cases are distinguished.

(i) Let  $n, j$  be the pair of indices such that  $|\omega_{nj}| \approx \omega_0$ . Then, the sum in Eq. (IV.9) is reduced to  $l = n$  in the first term and  $l = j$  in the second term. This procedure yields

$$g_{jn}(t) \approx g_{jn}^{\text{res}}(t) := 2\Re\left(\tilde{W}_{nj}(t) \int_{-\infty}^t dt' \tilde{W}_{jn}(t') (\varrho_{jj}(t') - \varrho_{nn}(t'))\right). \quad (\text{IV.11})$$

(ii) Let  $n, j$  be a pair of indices such that  $|\omega_{nj}| \approx \omega_0$  is not fulfilled. This implies that the factor in front of the integral causes the generation rate itself to vary on the fast time scale and thus even the slowly varying contributions to the integral do not affect the occupation numbers on the time scale of the ionization process. Correspondingly, one can assume that Eq. (IV.11) holds approximately in this case as well. It should be mentioned that this choice is the reason that the fast time scale is still present in the generation rate of the preliminary approach in this subsection.

An alternative derivation of the generation rate Eq. (IV.11) relies on treating the laser pulse as a perturbation. However, the rather complicated consideration presented here based on different time scales has the advantage that it is not limited to weak pulses, so it is able to explain the results close to those obtained with the TDSE for relatively large intensities (see Sec. IV.3). Of course, this is only valid to a certain extent because increasing the intensity leads to faster ionization dynamics and thus a more rapid time scale of occupation probabilities. Therefore, the separation of time scales breaks down for sufficiently high intensities.

Lastly, a **rotating wave approximation (RWA)** is introduced by replacing

$$\begin{aligned} \tilde{W}_{nj}(t) &\rightarrow \alpha A_0(t) e^{i\delta\omega_{nj}t} \langle \psi_{nk\sigma} | \hat{p} | \psi_{jk\sigma} \rangle, \\ \text{where } \delta\omega_{nj} &:= \begin{cases} \omega_{nj} - \omega_0 & \text{for } \omega_{nj} > 0, \\ \omega_{nj} + \omega_0 & \text{for } \omega_{nj} < 0. \end{cases} \end{aligned} \quad (\text{IV.12})$$

The *resonant approximation* is now defined as the equation of motion in Eq. (IV.6) with the approximative generation rate in Eq. (IV.11) including the RWA. It can be equivalently formulated as

**Resonant approximation**

$$\begin{aligned}
i \frac{d}{dt} \varrho_{nn} &= \sum_j \left( \tilde{W}_{mj} \varrho_{nj} - \tilde{W}_{nj}^* \varrho_{jm} \right), \\
i \frac{d}{dt} \varrho_{nm} &= \tilde{W}_{mn} (\varrho_{nn} - \varrho_{mm}), \quad \text{for } n \neq m.
\end{aligned} \tag{IV.13}$$

Evidently, oscillations on the fast time scale are still present in the resonant approximation; despite the assumption that the fast time scale does not contribute to the occupation probabilities, not all of the corresponding terms have been dropped.

**IV.2.3. Markovian theory**

The final step for achieving the rate-equation limit within the procedure by [Rossi and Kuhn \(2002\)](#) [300] is to approximate the integral in the resonant generation rate, Eq. (IV.11), by assuming short-lived memory effects and applying a Markovian approximation (cf. Sec. III.2.2). Provided that the amplitude of the vector potential is described by a Gaussian function, i.e.,

$$A_0(t) = \bar{A}_0 \exp\left(-\frac{t^2}{2\tau_0^2}\right), \tag{IV.14}$$

one obtains the following *Markovian generation rate*:

**Markovian generation rate**

$$g_{jn}^{\text{Markov}}(t) = (\varrho_{jj}(t) - \varrho_{nn}(t)) 2\pi |W_{nj}^{(0)}(t)|^2 S(\delta\omega_{nj}). \tag{IV.15}$$

Here,  $W_{nj}^{(0)}(t)$  is defined as  $W_{nj}^{(0)}(t) := \alpha A_0(t) \langle \psi_{nk\sigma} | \hat{p} | \psi_{jk\sigma} \rangle$  and contains no frequency component in the range of  $\omega_0$  and  $\omega_{nm}$  for  $n \neq m$ . Further, spectral properties of the transform-limited pulse enter the Markovian generation rate through  $S(\omega) := \frac{\tau_0}{\sqrt{2\pi}} \exp(-\tau_0\omega^2)$ . Note that Fermi's golden rule can be recovered from Eq. (IV.15) in the limit  $\tau_0 \rightarrow \infty$  as  $S(\omega) \rightarrow \delta(\omega)$ . The equations of motion defined by the Markovian generation rate in conjunction with Eq. (IV.6) will be referred to as *Markovian theory* in the following. Originally, the Markovian generation rate was termed *semiclassical generation rate* by [Rossi and Kuhn \(2002\)](#) [300] but renamed here in order to avoid confusion with the more common definition of *semiclassical* on page 20.

It should be mentioned that relaxation processes occur in real systems characterized by an energy and a phase relaxation time,  $\tau_E$  and  $\tau_{\text{ph}}$ . There is a relationship between  $\tau_E$  and  $\tau_{\text{ph}}$  that follows directly from the Cauchy-Schwarz inequality [220], namely  $\tau_{\text{ph}} \leq 2\tau_E$ . This means that the decay time of off-diagonal elements  $\tau_{\text{ph}}$  of the **1RDM** is bounded by the decay time of diagonal elements  $\tau_E$  so that the property of the **1RDM** of being positive semidefinite is not violated. Contrariwise, there is no lower bound on  $\tau_{\text{ph}}$ , i.e., the case  $\tau_{\text{ph}} \ll \tau_E$  is conceivable and is known in various physical systems to result from elastic collisions [296]. In the cases considered here, the energy relaxation time  $\tau_E$  is typically fast due to Auger decay or fluorescence (cf. Chapters I and II). To the author's knowledge, there have been no conclusive

results measuring the phase relaxation times  $\tau_{\text{ph}}$  at XFEL based experiments so far; by contrast, the energy relaxation times  $\tau_{\text{E}}$  are widely known [103, 301]. For instance, the  $L$ -hole lifetime in aluminum  $_{13}\text{Al}$  around 19 fs [131], i.e., for hole states corresponding to electron binding energies around 100 eV. There are two things to learn from that. Firstly, the models discussed so far break down if  $\tau_{\text{E}}$  is on the order of the pulse duration  $\tau$  or lower (cf. Chapter II). Secondly, if off-diagonal elements decay rapidly, i.e.,  $\tau_{\text{ph}} \ll \tau_{\text{E}}$ , the Markovian theory may even provide a more accurate description than the TDSE, Eq. (IV.5). Hence, the Markovian theory can be not only regarded as an approximate to the TDSE but can also be interpreted as the limit  $\tau_{\text{ph}} \ll \tau_0 \ll \tau_{\text{E}}$  since the coherences exhibit a fast decay so that memory effects in Eq. (IV.8) are naturally avoided.

#### IV.2.4. Atomic and spectrally averaged rates

In order to identify phenomena that can be traced back to the environment effects contained in the TDSE description, it is instructive to compare the rates obtained for the case of a crystal with the analog in the atomic case. Let  $H_{\text{field}}^{(1)}$  be the term in the minimal-coupling Hamiltonian that is responsible for OPA in perturbation theory [39]:

$$H_{\text{field}}^{(1)} = \alpha \hat{p} A_0(t). \quad (\text{IV.16})$$

Then, time-dependent perturbation theory estimates the transition rate  $\Gamma_{\text{atomic}}$  between a bound state  $|\psi_i\rangle$  and a continuum state  $|\psi_f\rangle$  of an individual atom:

$$\Gamma_{\text{atomic}} := 2\pi |\langle \psi_i | H_{\text{field}}^{(1)} | \psi_f \rangle|^2 D_{\text{atomic}}(\omega_{\text{ex}}), \quad (\text{IV.17})$$

where  $\omega_{\text{ex}}$  is the excess energy  $\omega_{\text{ex}} = \omega_0 + \omega_i > 0$  (or rather the eigenenergy  $\omega_f$  of the final state  $|\psi_f\rangle$ ) and  $\omega_i < 0$  is the eigenenergy of the initial state  $|\psi_i\rangle$ .  $D_{\text{atomic}}(\omega_{\text{ex}})$  is the density of states of the atomic system at the excess energy  $\omega_{\text{ex}} = \omega_f$ .

Contrary to the Markovian theory, Pauli blocking in continuum states is disregarded here. Additionally, the final populations do not depend on pulse parameters other than the total photon number as long as no further processes such as Auger decay with inherent time scales are accounted for. In order to capture spectral effects, one may extend Eq. (IV.17) by replacing the rate with its weighted average with respect to a weight function given by the spectral density – similar to the Markovian generation rate or to Ref. [84] in the case of the TPA cross section. However, this strategy is incapable of describing the pronounced dependency of the ionization yield on the pulse duration that will be shown later in Sec. IV.3. This deficiency can be traced back to the weak variation of the transition rate  $\Gamma_{\text{atomic}}$  as a function of the excess energy  $\omega_{\text{ex}}$  on the scale of  $1/\tau$ . By contrast, the density of states in the present crystal model  $D_{\text{crystal}}(\omega_{\text{ex}})$  is subject to strong variations in the relevant energy range due to van Hove singularities. Hence, it is tempting to replace the atomic orbitals in Eq. (IV.17) and the density of states with those quantities that were obtained in the crystal model, i.e., one writes

### Spectrally averaged rates (SAR)

$$\frac{d}{dt}P_n = -\Gamma_{\text{SAR}}P_n, \quad (\text{IV.18})$$

$$\Gamma_{\text{SAR}} := S(\omega - \omega_{\text{ex}}) * \left( 2\pi |\langle \psi_{nk\sigma} | H_{\text{field}}^{(1)} | \psi_{jk\sigma} \rangle|^2 D_{\text{crystal}}(\omega) \right). \quad (\text{IV.19})$$

where  $P_n$  is the average population of the bound band  $n$ ,  $S(\omega)$  is defined as in Eq. (IV.15), and the symbol  $*$  denotes the convolution operation. These equations of motions will be hereafter referred to as **spectrally averaged rates (SAR)**, and the analogous dynamical equations in conjunction with Eq. (IV.17) are called *atomic rates*. As an alternative to the phenomenological consideration above, the **SAR** approach can be rigorously derived from Eq. (IV.15) if the populations  $\varrho_{nn}$  can be approximated by a constant for each band and Pauli blocking is neglected. Note that the **SAR** approach exhibits no parametric dependence on  $k$  unlike all other equations of motion introduced in the previous sections.

## IV.3. Results

Due to the constraints of the model reported in Chapter II, only one ionization channel is considered. For this purpose, one proceeds as follows. The initial conditions in all simulations are  $\lim_{t \rightarrow -\infty} \varrho_{nm}(t) = \delta_{n1} \delta_{m1}$  and other bound bands (in this case only one) are excluded in the calculation. The excluded states can be physically interpreted as occupied states that are not affected by the laser pulse. The photon energy  $\omega_0$  is chosen such that **OPA** is feasible in all cases. All simulations were performed with the laser field modeled by Gaussian temporal profiles described by Eq. (IV.14) where  $\tau := 2\sqrt{\ln 2} \tau_0$  is the **FWHM** of the intensity.

This section is structured as follows. In the first part, Sec. IV.3.1, moderate intensities are considered and the influence of the spectral density on the ionization yield is discussed. The second part, Sec. IV.3.2, is devoted to phenomena arising for higher intensities, still focusing on the ionization yield. In the last section, other physical quantities such as the time-dependent electron density are shown for a qualitative understanding of the ongoing processes.

### IV.3.1. Ionization dynamics at moderate doses

The following analysis focuses on the pulse-length dependence of the ionization yield in the model crystal under irradiation with a transform-limited laser pulse. For this purpose, the dynamics of occupation numbers is simulated for different durations  $\tau$  but a fixed number of photons per pulse  $N_{\text{ph}}$  and a fixed photon energy  $\omega_0$ . The term *moderate doses* in the title of this subsection refers to the comparatively low photon number  $N_{\text{ph}}$ , which was chosen such that the depletion of the lowest orbital is less than 30% according to the atomic rates. The atomic rates are suitable to characterize the strength of the laser pulse based on solely the photon number because the ionization yield after the pulse depends only on  $N_{\text{ph}}$  and no other pulse properties (cf. Sec. IV.2.4). After rescaling the time axis in units of  $\tau$ , the time-dependent occupation numbers of bound states are independent of  $\tau$ , yielding a universal curve for all  $\tau$ . This curve is

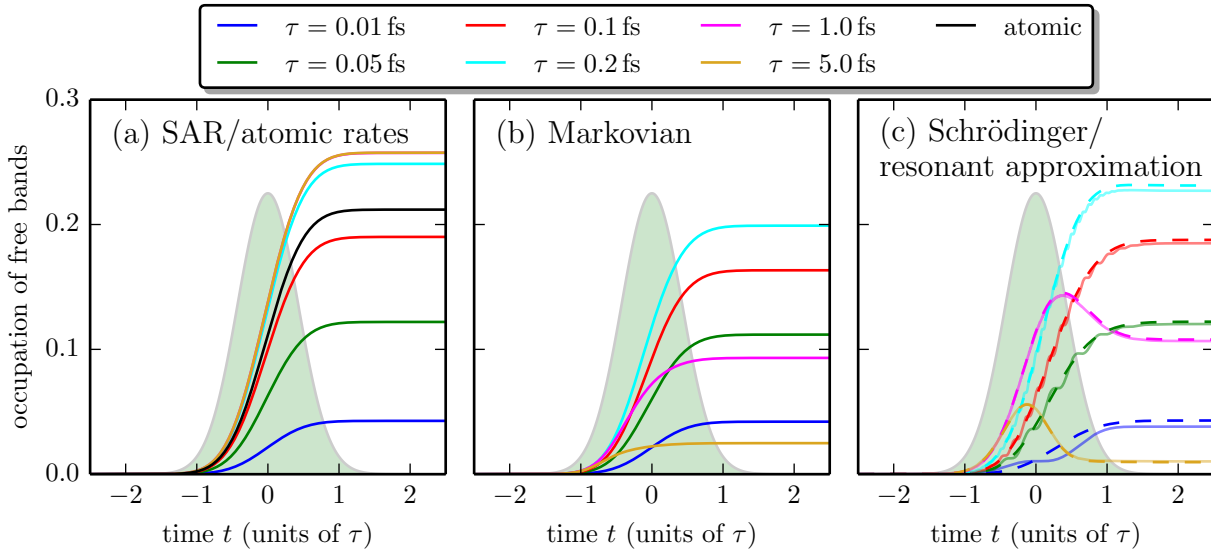


**Figure IV.2.:** Ionization yields at a photon energy  $\hbar\omega_0 = 125$  eV for a fixed total number of photons  $N_{\text{ph}}$ . The time-dependent occupation of free bands is shown for different pulse durations  $\tau$  and for the different levels of theory as described in Sec. IV.2. The pulse durations vary from 0.01 fs to 5 fs and the time axis is scaled accordingly. For this reason, the temporal envelope of the laser intensity (in arbitrary units) sketched in the background overlaps for all pulses. (a) SAR and atomic rates. Since the curves calculated for the atomic rates overlap for all pulse durations, only one of them is shown. Also the time traces for  $\tau = 1.0$  fs and  $\tau = 5.0$  fs overlap (barely distinguishable). (b) Markovian theory. (c) Schrödinger theory (TDSE) and resonant approximation as continuous and dashed lines, respectively.

shown in black in Fig. IV.2a at a photon energy of  $\omega_0 = 125$  eV, tuned to the resonance of the transition  $1_b \rightarrow 1_f$  at  $k = \frac{1}{4}g$ . The monotonic time-dependence of this time trace is –just like the SAR results in Fig. IV.2a– trivially described by Eq. (IV.18) and thus not further examined. Close attention is paid to the pronounced pulse-length dependence in all other levels of theory depicted in Fig. IV.2. In the following, the individual features of the different equations of motions described in Sec. IV.2 are discussed step by step, starting with the simplest approach.

Apparently, the time-dependent ionization yield based on SAR in Fig. IV.2a exhibits a monotonic dependence on the pulse duration. The ionization yield rises strongly between  $\tau = 0.01$  fs and 0.2 fs and approaches a universal curve for  $\tau > 1$  fs, which does not coincide with the curve obtained from atomic rates. This can be easily understood by estimating the spectral width and comparing it with the density of states that is implied by the band structure in Fig. IV.1a. For pulses with a transform-limited Gaussian temporal/spectral profile, the product of the spectral FWHM bandwidth  $\hbar\delta\omega$  and the FWHM pulse duration  $\tau$  is given by<sup>2</sup>

$$\hbar\delta\omega \cdot \tau \approx 1.82 \text{ eV} \cdot \text{fs}. \quad (\text{IV.20})$$

Accordingly, the pulse durations from  $\tau = 0.01$  fs to 5 fs correspond to spectral bandwidths from 182 eV to 0.36 eV FWHM. Hence, for  $\tau = 0.01$  fs the weighted average in Eq. (IV.19) is spread across a large part of the absorption spectrum, including band gaps and occupied bound states.

<sup>2</sup>As an exception to the statement on page 2, atomic units are avoided in this case.

This implies that a large part of the spectrum does not contribute to the ionization rate, which, in turn, leads to a rather weak absorption for short pulses. The time traces converge once the pulse duration is sufficiently long so that the absorption spectrum does not vary significantly<sup>3</sup> on the energy scale given by the associated spectral bandwidth. The converged time trace obviously deviates from the result obtained with atomic rates because they are distinct in both cases due to the modification of the density of states. Note that the observed monotonicity in the pulse-length dependence is not mandatory in general for arbitrary absorption spectra.

The situation in Fig. IV.2b based on the Markovian theory is similar. All time traces are monotonic and the results are close to the SAR estimates for spectrally broad pulses. However, one discerns a significant drop in the ionization yield for spectrally narrow excitations with  $\tau = 1$  and 5 fs. This effect occurs when the spectral bandwidth is around 1 eV or below so that the energy selection rule gives rise to an inhomogeneous distribution of populations as a function of the Bloch wave vector  $k$  in one band. With the requirements for the validity of the SAR approach not being met anymore, the deviations from the SAR results are self-evident. Furthermore, the decrease of the ionization yield can be understood as the outcome of the two selection rules in  $k$  and in energy where the constraints enforced by the energy selection rule become stricter the longer the pulse duration. The combination of both constraints reduces the number of allowed transitions and hence the overall ionization. In this case, Pauli blocking effects, which are neglected in the SAR approach, might increase in importance.

The time-dependent occupation probabilities as calculated by means of the coherent dynamical equations are shown in Fig. IV.2c. The most prominent difference compared to the observations in Figs. IV.2a and b is the qualitatively different behavior of time traces. The non-RWA contributions exhibited by the Schrödinger theory but not on the resonant approximation are most clearly seen for  $\tau = 0.01$  fs, where the spectral bandwidth of 182 eV is of the same order as the photon energy 125 eV. The origin of this feature is immediately clear as it is dealt with few-cycle pulses for low  $\tau$  considering that the photon frequency is  $f \approx 30 \frac{1}{\text{fs}}$ . Based on the fact that the time scales of pulse duration and field frequency obviously do not separate anymore, one might expect the resonant approximation to break down. This treatment can, however, also be justified by a perturbation argument (cf. Sec. IV.2.2) so that the quantitative overall description still turns out to be valid to a good approximation. Next, the non-monotonic behavior of the time traces in the coherent theories for large  $\tau$ , i.e., spectrally narrow pulses, can be understood based on the knowledge about the optical excitation in a two-level system (2LS). If the spectral bandwidth is sufficiently small, one might reduce the system to two bands selected by the resonance and the initial condition. Taking the parametric  $k$  dependence into account, the system can be reinterpreted as a 2LS ensemble with a distribution of the detuning and coupling strength parameters given by the model system. The optical excitation of individual two-level atoms is well-known from standard textbooks [263, 296]: non-monotonic populations, or rather Rabi oscillations, stem from off-diagonal elements of the density matrix, which are omitted in the theories that led to the results in Figs. IV.2a and b (see also the ensuing section, Sec. IV.3.2). If the spectral bandwidth of a pulse is large, these oscillations are effectively averaged out, but if the bandwidth is sufficiently small, they become visible as seen for  $\tau = 1$  and 5 fs in Fig. IV.2c.

<sup>3</sup>This limiting case cannot be reached at van Hove singularities.

For a more concise comparison of the different dynamical equations over a continuous range of pulse lengths, attention is now paid to the final values of the time-dependent populations of free bands considered so far in Fig. IV.2. Accordingly, the ionization yield as a function of  $\tau$ , depicted in Fig. IV.3, will be discussed in the following. The qualitative dependencies have already been investigated and explained before in Fig. IV.2, so the main focus lies on features that are more clearly seen in Fig. IV.3. Though all levels of theory exhibit mostly a fundamentally different  $\tau$  dependence among each other, all curves apart from the atomic limit coincide for the very short pulse durations  $\tau \leq 0.05$  fs. This observation is also true for the time-dependent curves in Fig. IV.2. The SAR results stand out because they approach a constant value for  $\tau > 0.5$  fs as discovered above. To better understand the nature of the deviation from the next-best alternative introduced in Sec. IV.2, i.e., the Markovian theory, an additional intermediate approach is shown, namely the Markovian theory without Pauli blocking. By comparing this approach to the original Markovian theory, one discerns that Pauli blocking significantly reduces the ionization yield but does not result in qualitative changes. Hence, Pauli blocking is not the dominant influencing factor for the non-monotonic behavior because the phenomenon appears even if the blocking is switched off. Therefore, the drop in ionization yield for long pulses in the Markovian theory compared to the SAR approach can be attributed to the interplay between the energy and  $k$  selection rule, which, in turn, effectively implies a reduced number of efficiently driven transitions.

Another prominent feature apparent in Fig. IV.3 is the minimum within the coherent equations of motion in the ionization yield around  $\tau \approx 3.5$  fs with practically no sample damage. If this phenomenon was observed in a real system, one would, in principle, be able to perform SFX (see Sec. I.3) without replacing the crystal after each shot. The strategy would be to tune the pulse duration so that the holes created during irradiation are refilled at the end of each pulse and thus no decay mechanisms are initiated afterwards. However, the pulse profile must be tuned to the respective sample, which is very challenging in experiments. Further, the coherent dynamics is vital to observe this feature in the case of our model crystal: if the phase relaxation is fast  $\tau_{\text{ph}} \ll \tau$ , the Markovian theory is more applicable than the coherent equations of motions and no minimum appears.

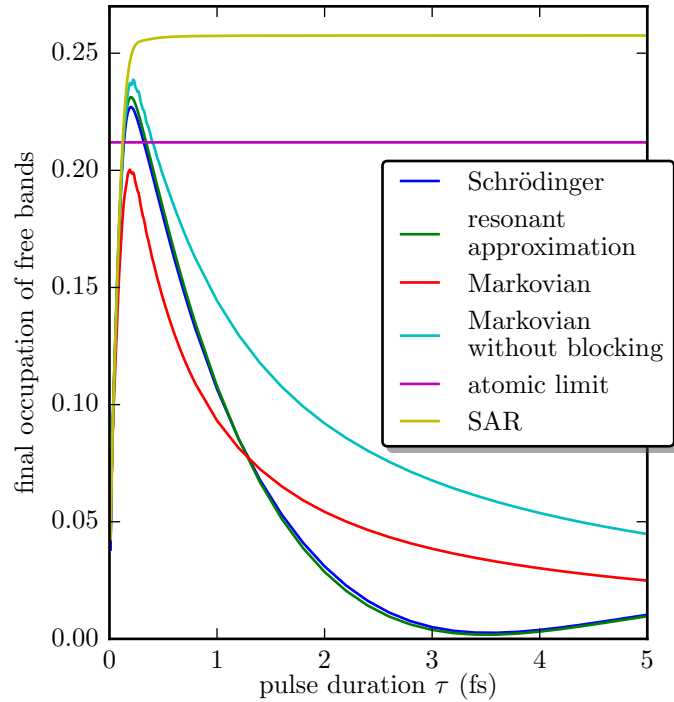


**Figure IV.3.:** Final values of the ion yield over a continuous range of pulse lengths  $\tau$  while keeping the photon number  $N_{\text{ph}}$  fixed. The parameters are identical to those in the previous figure, Fig. IV.2, where the corresponding time traces are depicted for selected values of  $\tau$ .

### IV.3.2. Rabi cycling

Initial indications of Rabi cycling were observed in the previous section for spectrally narrow pulses with pulse lengths of  $\tau = 1$  and  $5$  fs. Now, it is investigated whether Rabi oscillations can be observed more clearly for higher intensities and, if so, how this feature depends on the photon energy. For this purpose, the time traces analogous to Fig. IV.2 are analyzed for a fixed pulse duration  $\tau = 1$  fs, i.e., for a spectral bandwidth of  $1.82$  eV (FWHM), and a hundred times higher intensity than in the corresponding simulation in the previous section. Note that the spectral bandwidth is small compared to the energy range of the free bands  $n_f = 1, 2$  (cf. Fig. IV.1). Therefore, as established on page 51, the occupation probabilities of bands within the TDSE, the resonant approximation, and the Markovian theory can be interpreted as an average over a 2LS ensemble, where the value of  $k$  determines the coupling strength and the detuning of each 2LS.

The time traces for selected photon energies  $\hbar\omega_0 = 120, 125, 153,$  and  $165$  eV are shown in Fig. IV.4, where Fig. IV.4b represents the same scenario as in Fig. IV.2 but with a significantly increased photon flux  $N_{\text{ph}} \rightarrow 100 \cdot N_{\text{ph}}$ . It is striking that the curves obtained in the Markovian theory are monotonic and deviate substantially from the qualitative behavior demonstrated for coherent dynamics by the TDSE and the resonant approximation. As already the Markovian theory fails to reproduce Rabi cycling, lower levels of theory are neither considered in the present discussion nor shown in the respective figures. Additionally, first significant deviations between the resonant approximation and the TDSE appear in the simulations, which is in conformity with expectations at high intensities (cf. Sec. IV.2.2). The non-RWA contributions cause an apparent broadening of time traces due to fast oscillations, especially in Fig. IV.4a. Before going into detail, one obvious observation should be pointed out in advance: although one is effectively dealing with a 2LS ensemble, the time traces are qualitatively entirely different from the dynamics experienced by an individual 2LS.

An intuitive understanding of the Rabi-like dynamics, demonstrated by the individual curves in Fig. IV.4, is provided by means of the band structure and the  $k$  dependence of transition matrix elements shown before in Figs. IV.1a and b, respectively. The photon energy in Fig. IV.4a is tuned to the resonance energy of the transition  $1_n \rightarrow 1_f$  at  $k = 0$ . In this case, a van Hove singularity enhances the resonance condition in a region where the magnitude of the transition matrix elements varies by many orders of magnitude. Accordingly, the occupation probability of a band is based on the contributions from a broad distribution of coupling strengths and thus also a broad distribution of Rabi frequencies. The overall ionization yield exhibits barely visible Rabi-like dynamics because the different oscillations average out. By contrast, the situation for the observation of Rabi-like dynamics is much more preferable in Fig. IV.4b at a photon energy that corresponds to the transition  $1_n \rightarrow 1_f$  at  $k = \frac{1}{4}g$ . Here, the magnitude of the transition matrix elements is smooth in the vicinity of the resonance and the time trace exhibits significantly more apparent Rabi-like oscillations. By comparing the TDSE with the resonant approximation, one recognizes that off-resonant contributions, which are treated differently in both approaches, may also conceal Rabi cycling. The same considerations apply to Fig. IV.4c and also –consistent with the present interpretation– the observations are similar. Most pronounced Rabi cycling is seen in Fig. IV.4d at a photon energy tuned to the transition  $1_n \rightarrow 1_f$  at  $k = 0$ . The energy selection rule is enhanced by the density of states analogous to the case in Fig. IV.4a so that a large part of the 2LS ensemble is in resonance and the resonant approximation captures the

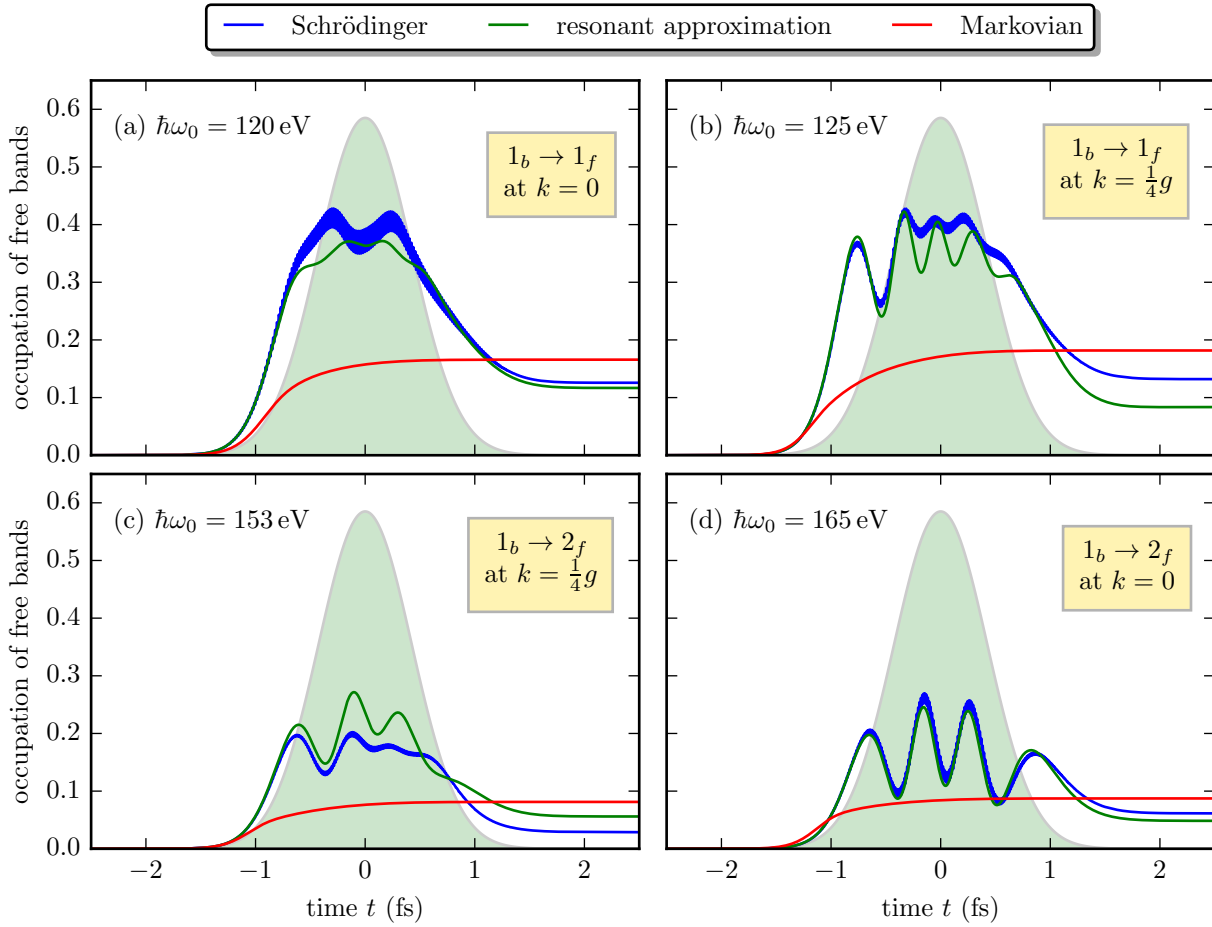


**Figure IV.4:** Ionization dynamics analogous to Fig. IV.2 for  $\tau = 1$  fs but a 100 times higher intensity and varying photon energies in (a) to (d). The photon energy in (b) is the same as in the previous figures, Figs. IV.2 and IV.3. In all cases, the photon energy corresponds to a resonant transition to a  $n_f = 1, 2$  band at a different value of  $k$  shown as insets, respectively.

dynamics of the TDSE to a good approximation. Simultaneously, the 2LSs are weighted by the resonance condition, and therefore the main contribution stems from fairly similar values for the Rabi frequency and the detuning.

In summary, Rabi-like behavior may be unveiled in NTI for ultrashort transform-limited pulses in the XUV regime. Spectrally broader pulses would imply an additional averaging, which is counterproductive for this purpose. To the best of the author's knowledge, this has not been measured so far and will prove both experimentally and theoretically (as far as a more realistic model is concerned) very challenging.

### IV.3.3. Spatiotemporal behavior of the electron density

The observation of Rabi cycling in the previous subsection assumed the full knowledge of the time-dependent ionization yield, which is experimentally challenging in XFEL based studies.

This section is devoted to the influence of the most ideal analyzed Rabi scenario within the model system, namely the one seen in Fig. IV.4d, on the elastic scattering factor. The latter can be, contrary to Compton scattering, assessed in the semiclassical approach through the current density. For this purpose, the spatiotemporal dynamics of the electron and the current density is discussed beforehand in order to support a correct interpretation of the form factor. It should be mentioned that the possibility of an experimental realization of this scheme is highly questionable for fundamental reasons as addressed at the end of this section.

The time-dependent electron density under irradiation with the laser pulse centered around  $t = 0$  is depicted in Fig. IV.5a. For early times  $t < 2$  fs, the density differs only slightly from the initial situation, which is characterized by a strongly localized charge density near the atomic core at  $x = 0$ . With an increasing electric field at later times between  $t = -2$  fs and  $t = -1$  fs, a continuous flow away from the core can be discerned on the logarithmic scale [typically barely noticeable on a linear scale]. Around the maximum of the laser intensity, between  $t = -1$  fs and  $t = 1$  fs, the fluxes emerging from the atom at  $x = \pm d$  form a coherent superposition and show characteristics of a standing wave. This leads to a buildup of a significant part of the density corresponding to free electrons spatially separated from the core region and centered around  $x = \pm d/4$ . Therefore, the free electrons are essentially trapped in the vicinity of the cores and are available for recombination through Rabi cycling. This is also discernible via the oscillatory time dependence synchronous to the corresponding occupation probabilities in Fig. IV.4d. For times  $t > 1.5$  fs the occupation probabilities are virtually constant, and the separated density peaks as well as the oscillation that can be attributed to coherences remain visible. This peculiarity is the result of the absence of both energy and phase relaxation.

The corresponding current density is shown in Fig. IV.5b. It was checked that the main contribution to the current density stems from the term  $\propto \rho A$ , where  $\rho$  is the electron density and  $A$  is the vector potential. This is plausible when comparing Figs. IV.5a and b. Hence, dispersion corrections [39] can be expected to be negligible and elastic scattering is determined by  $\rho$  or rather the form factor calculated as the Fourier transform of  $\rho$ .

As a direct consequence of the periodic broadening of the electron density and the Fourier

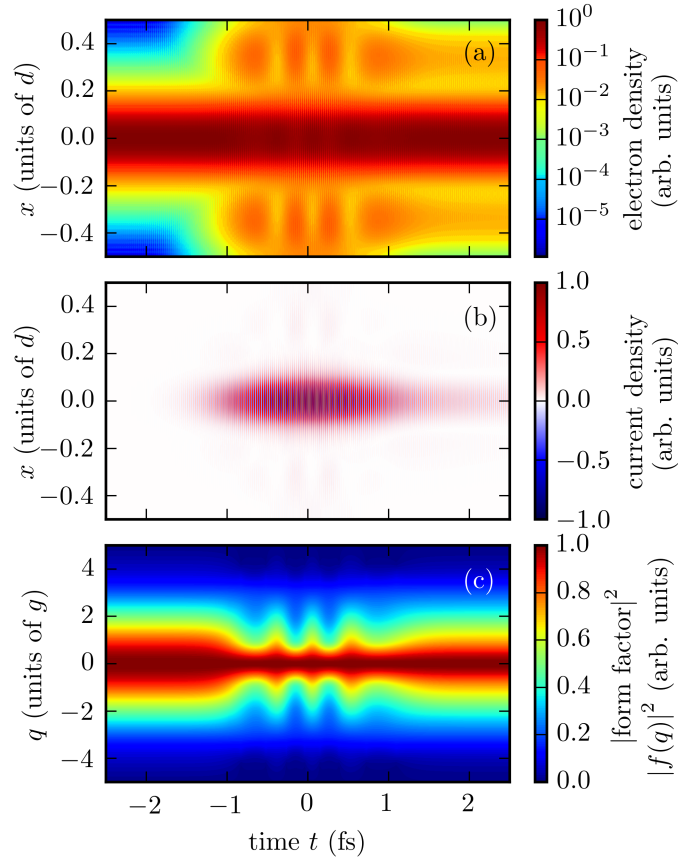


**Figure IV.5.:** (a) Time-dependent electron density in a Wigner-Seitz cell, (b) the corresponding current density, and (c) the atomic form-factor  $f(q)$  calculated within the Schrödinger theory for the parameters chosen in Fig. IV.4d.

relationship, the square of the absolute value of the scattering factor, shown in Fig. IV.5c as a function of the momentum transfer  $q$ , is narrowed repeatedly. Apparently, the Rabi-like dynamics leads to a significant oscillation in time around  $q = 2g$ . By contrast, the presence of inner-shell vacancies is hardly recognizable for small  $|q|$ . This is consistent with the theoretical analysis in Ref. [6] because significant deviations between the form factor for pristine and hollow atoms are only expected for high resolutions, i.e., for large  $q$ , of the order of  $1 \text{ \AA}$ .

However, this consideration faces a fundamental problem because the form factor is only measured for  $|q|$  smaller than the maximum momentum transfer in elastic scattering  $q_{\max}$ . At the low photon energy considered here, the momentum transfer has an upper bound of  $q_{\max} = 2\alpha\omega_0 \approx 0.09 \text{ a.u.}$ , whereas  $g \approx 1.26 \text{ a.u.}$  The consequence is that the atomic form factor in Fig. IV.5c can be obtained from elastic scattering experiments only for  $q \ll g$ .

It is tempting to think that this issue can be avoided by simply adapting the photon energy. However, one does not achieve meaningful results by analyzing the same model system for the analogous case but heavier atoms in order to increase the photon energy of NTI eventually up to  $\hbar\omega_0 \approx 12 \text{ keV}$ , which is the order of magnitude of the photon energy required for typical SFX experiments (see Sec. I.3). This strategy does not work because another fundamental problem arises: heavy atoms with inner-shell vacancies are subject to short fluorescence lifetimes (cf. Sec. II.1), causing the adopted assumptions to break down immediately.

# V

## Coherent ionization dynamics in clusters

Coherent dynamics was demonstrated in the previous chapter to shape the time-dependent behavior of [near-threshold ionization \(NTI\)](#) within a simplistic crystal model under ideal circumstances. It led, *inter alia*, to standing waves of free electrons that recombined via Rabi cycling (cf. Sec. [IV.3.3](#)). In atomic samples, by contrast, it was anticipated from the start that this phenomenon does not occur. Indeed, atoms are supposed to be well captured by the incoherent time evolution as described by the rate approach. The present chapter focuses on elucidating the questions that arise naturally in the light of these two extremes, atom and crystal: how does the system size affect the theoretical observations and what is the role of the ideal ordering of atoms in the crystal?

To clarify these questions, the [NTI](#) of  $N$  equally spaced, identical atoms is analyzed in the following. Obviously, the numerics is required to be sufficiently flexible that the number of atoms  $N$  can be varied over a broad interval, here  $N = 1, \dots, 21$ . For the most part, equidistant spacing between the atoms is assumed in order to simplify the parameter study, *i.e.*, once all atomic parameters are fixed, the Hamiltonian is solely characterized by the number of atoms. It is not immediately clear what this model of a short ordered chain represents physically: one may interpret it as a finite-sized crystal due to the strict order of atoms or as a homonuclear cluster owing to the low number of atoms. In fact,  $N = 21$  is even clearly surpassed by the samples in the cluster studies mentioned in Sec. [I.2.2](#) or by the macromolecules such as [TbCatB](#). Anticipating Sec. [V.2.5](#), the latter interpretation is supported by the finding that the ordering is not vital for the qualitative tendencies of the results. For this reason and for the sake of brevity, the title of this section refers to clusters even though the term [short ordered chain \(SOC\)](#) is, strictly speaking, closest to the model system of interest and will be adopted below.

The main goal of the present chapter is to identify a coherent trapping mechanism that leads to a localization of photoelectrons in the vicinity of the cores from which they were ejected, analogous to the insights into the dynamics of the crystal in Sec. [IV.3.3](#). The simplistic assumptions from the previous chapter, which include the neglect of electron-electron interaction, are kept to ensure comparability and to reduce the computational effort to enable a flexible simulation of  $N = 1, \dots, 21$  atoms. As a consequence, the choice of  $V_{ee} \equiv 0$  in the [TDHF](#) equations, Eq. [\(II.2\)](#), automatically entails the absence of electrostatic trapping, which is vital for the description of the ionization of clusters (see Sec. [I.2.2](#)). This might appear to be a conceptual flaw at first sight; however, this strategy has, in fact, the tremendous advantage of being capable of demonstrating an additional trapping mechanism distinct from electrostatic trapping. In this sense, the present chapter is primarily conceived as a model study, but of course, the analysis is not purely academic as it is most adequate under the same circumstances as the crystal model in Chapter [IV](#).

This chapter is based on Ref. [\[302\]](#).

## V.1. Theory

This section covers all models that are employed in this chapter and can be regarded as an overview of the different theoretical approaches that were implemented to describe the system and/or identify the relevant mechanisms in the context of other more sophisticated strategies. Since the physical implications are discussed later, the reader may skip the remainder of this section after learning about the basic model in Sec. V.1.1 and continue with the main discussion, Sec. V.2 Results. Then, one may consult the respective subsection of the present section once the eponymous theoretical approach is mentioned.

All dynamical equations are special cases of the TDHF equation, Eq. (II.2), where aside from Sec. V.1.4 the electron-electron interaction is completely disregarded, i.e.,  $V_{ee}$  is assumed to vanish identically. Due to the simplistic theory based on the assumptions in Chapter II, it is computationally feasible to simulate a rather general physical system comprising  $N$  distinct atoms at arbitrary positions. Accordingly, one may as well choose a more general situation of arbitrary atomic positions and potentials without additional computational costs, thus mimicking a 1d molecule. However, to achieve a comparable situation to the crystal model only homonuclear clusters with equally spaced atoms (hereafter referred to as **short ordered chains (SOCs)**) are considered for the most part even though this constraint of equidistant spacing turns out to be not crucial for observing the trapping mechanism mentioned at the beginning of the present chapter. To be specific, the identical atomic potentials are assumed to be centered around the atomic positions

$$R_j = (j - \frac{1}{2}(N + 1))d, \quad \text{where } j = 1, \dots, N. \quad (\text{V.1})$$

The SOC spacing  $d$  is the distance between adjacent atoms. This uniform structure resembles the crystal model as in Chapter IV in the limit of a large number of atoms,  $N \gg 1$ .

In order to fully characterize a system that is subject to the dynamics described by the TDHF equations in Eq. (II.2) the potentials  $V_{\text{core}}$  and  $V_{ee}$  and the number of atoms  $N$  have to be provided for each model. This strategy will be pursued in the following while making sure that  $N$  can be treated as a free parameter in order to enable the modeling of a flexible system size.

### V.1.1. Collective-atoms model (CAM)

First, the potential of a single core centered around  $x=0$  is defined, which is later straightforwardly extended to a system of  $N$  equidistant atoms. The **soft-core (SC)** Coulomb potential  $V_{\text{sc}}(x)$  is used as a non-singular approximate to the (bare) 1d Coulomb potential  $-Z/|x|$  [258, p. 101 et seqq.]. It is explicitly written as

$$V_{\text{sc}}(x) = -\frac{Z}{\sqrt{a^2 + x^2}}, \quad (\text{V.2})$$

with adjustable parameters  $a, Z$ . Since  $V_{\text{sc}}(x)$  approaches the bare Coulomb potential in the limit  $x \gg a$ , the parameter  $Z$  is generally chosen to be compatible with the electric charge of the respective atom. The parameter  $a$  can be set to a value that results in the desired ground-state energy of the 3d atom which is intended to be approximated. It is assumed that  $a$  is smaller than

the **SOC** spacing  $d$  so that the spread of the electron density of the lowest orbital is smaller than the distance to the neighboring atom.

Due to the disregard of the electron-electron interaction, it is immediately clear that an ejected photoelectron is subject to a binding force of a fully-stripped atom with charge  $Z$  regardless of the actual charge state of the atom. This becomes more prominent when  $N > 1$  atoms are considered. Then, all electrons would experience a temporally constant trapping due to an electrostatic force of a system with charge  $N \cdot Z$ . In real systems, this charge is initially screened and is usually lower than  $N \cdot Z$  even during very strong pulses because of trapped and remaining bound electrons. This phenomenon is referred to as *electrostatic trapping* and is obviously a dynamical effect contrary to what the name suggests. Electrostatic trapping can be artificially eliminated in a model with  $V_{ee} \equiv 0$  and by using a short-range potential instead of the **SC** potential, Eq. (V.2). For this purpose, the following screening model is introduced. Analogous to the crystal model, Chapter IV, only the two electrons occupying the innermost shell (with a binding energy below the photon energy) are explicitly taken into account. Further electrons of the atom, e.g., valence electrons, are reduced to a homogeneous background density. The **SOC** spacing  $d$  is chosen to determine the length of the region  $[-\frac{1}{2}d, \frac{1}{2}d]$  where the homogeneous background density is located. This choice implies that the background is equally spread over the whole **SOC**, analogous to a jellium-like model. The atomic potential  $V_{\text{atomic}}(x)$  is then written as

$$V_{\text{atomic}}(x) = V_{\text{sc}}(x) + V_{\text{hom}}(x), \quad (\text{V.3})$$

$$\text{where } V_{\text{hom}}(x) = \frac{1}{d} \int_{-\frac{1}{2}d}^{\frac{1}{2}d} \frac{Z}{\sqrt{a^2 + (x-y)^2}} dy = \frac{Z}{d} \ln \left[ \frac{\sqrt{a^2 + (x - \frac{d}{2})^2} - (x - \frac{d}{2})}{\sqrt{a^2 + (x + \frac{d}{2})^2} - (x + \frac{d}{2})} \right]. \quad (\text{V.4})$$

In the limit case  $x \gg d$ , one finds  $V_{\text{hom}} \approx \frac{Z}{|x|}$ . This means that  $V_{\text{atomic}}$  is completely screened for large distances. Alternatively, one might replace  $Z \rightarrow Z - 1$  if the long-range contribution of the potential is only intended to be weakened and not entirely avoided. There is a decisive difference insofar that the long-range potential would add up for multiple atoms, which has to be borne in mind when comparing the dynamics of **SOCs** with different numbers of atoms  $N$ .

Now that the atomic potential is fully characterized, the potential  $V_{\text{core}}$  of the whole **SOC** with an arbitrary number of atoms  $N$  reads

$$V_{\text{core}}(x) = \sum_{j=1}^N V_{\text{atomic}}(x - R_j), \quad (\text{V.5})$$

where  $R_j$  are the atomic positions from Eq. (V.1). The model defined by this potential, the **TDHF** equations, Eq. (II.2), and  $V_{ee} \equiv 0$  is hereafter referred to as the **collective-atoms model (CAM)**. The electric field is specified later on page 63. Due to the elimination of electron-electron interaction, the **TDHF** equations are substantially simplified from a numerical perspective. Provided that the initial state can be expressed as a single Slater determinant, all orbitals can be propagated independently resulting in an inherently parallel algorithm. Therefore, the computation time in parallel execution does in principle not depend on the number of atoms  $N$ . Note that there is a genuine many-particle effect included in this model, namely Pauli blocking, which is implicitly accounted for by using a Slater determinant. For an intuitive picture of this

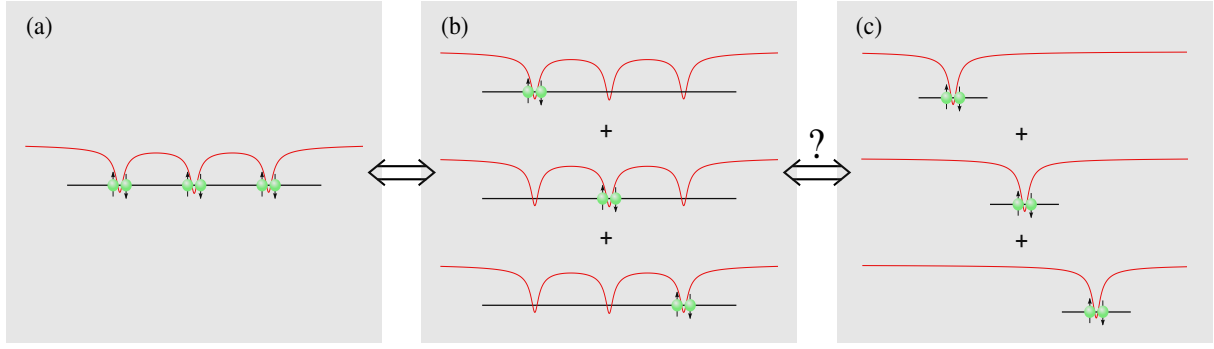


**Figure V.1.:** Schematic representation of the relation between the **CAM** in (a) and (b) and the **IAM** in (c) for a **SOC** that consists of  $N=3$  atoms. The red curves reflect the respective potential based on the shape of the **soft-core (SC)** potential, Eq. (V.2), whereas the homogeneous background density is not shown. The electrons in the innermost shells are illustrated as green spheres with arrows according to the spin degree of freedom.

effect, note that the orthonormality of the orbitals which constitute the initial state (in the form of a Slater determinant) is conserved throughout the simulation period. In this sense, the orbitals repel each other, even if  $V_{ee} \equiv 0$ , because the overlap between distinct orbitals must always lead to a vanishing scalar product.

To avoid confusion, it should be mentioned that the term *collective* in **CAM** does *not* stem from *collective effects* in the context of the **giant (dipole) resonance (GDR)** in xenon (see Sec. I.2.1). The nomenclature will become clear in the following subsection, Sec. V.1.2, where a model of completely independent atoms is introduced. The description *collective* is used to highlight this crucial difference.

### V.1.2. Independent-atoms model (IAM)

In order to assess the influence of neighboring atoms in the **SOC**, an additional dynamical equation is introduced, namely the **independent-atoms model (IAM)**. The **IAM** is the straightforward procedure to obtain the spatiotemporal charge density for a system of  $N > 1$  atoms where all atoms are completely independent. More precisely, let  $\varrho_{\text{CAM}}^{(N)}(x, t)$  be the time-dependent charge density calculated within the **CAM** model for  $N$  atoms. The corresponding **IAM** charge density  $\varrho_{\text{IAM}}^{(N)}(x, t)$  is then defined as

$$\varrho_{\text{IAM}}^{(N)}(x, t) = \sum_{j=1}^N \varrho_{\text{CAM}}^{(1)}(x - R_j, t). \quad (\text{V.6})$$

As no other physical quantity is extracted from this model, the **IAM** is fully characterized. Obviously, for  $N=1$  atom, the **IAM** charge density is identical to the associated **CAM** result. In the general case  $N > 1$ , however, the two models are not equivalent. Their relation is outlined by means of Fig. V.1 for  $N=3$  atoms. Fig. V.1a is closest to the formulation of the **CAM**: according to Eq. (V.5), the potential is given as the sum of individual atomic potentials, and  $2 \cdot N = 6$

electrons occupy single-particle eigenstates with almost identical eigenenergies. As noted above, this situation is mathematically equivalent to what is sketched in Fig. V.1b: the individual orbitals can be propagated independently, and for a Slater determinant comprising orthonormal orbitals the charge density is calculated as the sum of “single-particle” charge densities that are obtained for the individual orbitals [indicated by the plus signs]. Though the corresponding case in the IAM model depicted in Fig. V.1c seems very similar at first sight, it is essential to note that the neighboring atoms are disregarded. The latter is now equivalent to three CAM simulations for  $N = 1$  (which can be reduced to one by virtue of the translational symmetry) and subsequently summing up the charge densities as specified in Eq. (V.6).

### V.1.3. Reflectionless potential

It is natural to suspect that distinct observations within the CAM and IAM can be attributed to potential scattering of photoelectrons and are thus characterized by reflection and transmission. To obtain an intermediate level of theory where one of these two components is absent, one can replace the atomic potential Eq. (V.3) with a reflectionless potential

$$V_{\text{reflectionless}}(x) = -\frac{n(n+1)}{2a^2 \cosh^2\left(\frac{x}{a}\right)}, \quad (\text{V.7})$$

where  $a \in \mathbb{R}$  and  $n \in \mathbb{N}$  are adjustable parameters. The exact energy of the lowest orbital is analytically known and can be expressed as  $\epsilon_0 = -\frac{1}{2} \left(\frac{n}{a}\right)^2$ . By means of supersymmetric quantum mechanics, one can show that all potentials of the form of Eq. (V.7) are related to the zero potential in terms of being supersymmetry (SUSY) partners and thus exhibit no reflection at any energy [303, 304]. There is no additional screening introduced to the modified atomic potential because the reflectionless potentials in Eq. (V.7) are inherently short ranged so that electrostatic trapping is inherently suppressed.

Hereafter, the modified CAM approach where the atomic potential from Eq. (V.3) is substituted by a reflectionless potential Eq. (V.7) is called *reflectionless CAM*. The *reflectionless IAM* is defined analogously. For the interpretation of the results based on reflectionless models, it is assumed that the sum of well-separated reflectionless potentials is likewise reflectionless.

### V.1.4. Time-dependent Hartree-Fock (TDHF) model

So far, all models discarded the electron-electron interaction in the TDHF equations, Eq. (II.2), in order to artificially switch off the trapping mechanism based on electrostatics by introducing a full and temporally constant screening via the background density. Now, the time-dependent screening due to the dynamics of the electrons initially residing in the innermost shell is taken into consideration. The TDHF approach is a rather simple extension of the CAM; it accounts for dynamic screening via the Hartree term. Accordingly, TDHF is the method of choice to assess the influence of electrostatic trapping on the results obtained from the CAM theory. It was noted before in Sec. II.2 on page 22 that the TDHF is subject to fundamental issues in ionization dynamics. Unfortunately, TDHF simulations have to be restricted to the case of low intensities in the case of NTI to allow for drawing reliable conclusions [256]. This is a severe constraint because the electrostatic trapping is obviously weak for a low degree of ionization. In other

words, one is obliged to investigate the phenomenon in the case where it is anticipated to only mildly affect the dynamics.

The TDHF theory corresponding to the CAM is now specified to ensure the best possible comparability with the CAM. Again, only the two inner-shell electrons per atom are explicitly taken into account. These electrons are subject to the electron-electron interaction described by the potential

$$V_{ee}(x) = \frac{1}{\sqrt{a^2 + x^2}}. \quad (\text{V.8})$$

Accordingly, the homogeneous background density is now assumed to consist only of  $Z - 2$  electrons per atom, i.e., one performs the replacement  $Z \rightarrow Z - 2$  in the atomic potential, Eq. (V.4). Then, one constructs  $V_{\text{core}}(x)$  as a sum analogous to Eq. (V.5) of the CAM (see Eq. (V.5)).

This procedure evidently affects the orbital binding energies of the ground state. Hence, when constructing the TDHF extension of a CAM with given parameters  $a$ ,  $Z$ , one may readjust  $a$  in order to optimize the resemblance between these models from a physical perspective. For NTI, the dynamics is presumably sensitive to the kinetic energy of ejected photoelectrons, so it is reasonable to modify  $a$  to obtain the same  $K$ -edge in both approaches. This guarantees that the energetic properties are close. However, the transition matrix elements usually change as well, which can be mitigated, in turn, by adapting the laser intensity using the case  $N = 1$  as a reference. The exact parameters are discussed later in Sec. V.2.6.

## V.2. Results

Since the present chapter is primarily conceived as a model study, the simulations are performed for a seemingly arbitrary system of lithium atoms that does not match any of the experiments alluded to above in Chapter I. The reasons for building the analysis on a 1d lithium model are, firstly, that the approximations of Chapter II are most adequate for light atoms due to long fluorescence lifetimes. Secondly, prior investigations on the ionization dynamics of 1d lithium have been published by Ruiz et al. (2005) [253]. Adopting the strategy of the previous chapters, the discussion contains only qualitative conclusions by comparing theory with theory owing to the simplicity of the model system.

The numerical values for the stationary parameters of the CAM (identical to those of the IAM) are listed at this point, whereas the other models, which come into play only later in the continuing discussion, are specified below. Ruiz et al. (2005) [253] simulated a single 1d lithium atom based on the TDSE while taking the full electron-electron interaction into account. To match the ground-state energy of  $-199.44$  eV, the parameters of the SC potential were chosen to be  $Z = 3$  and  $a = 0.262$  Å; the latter parameter,  $a$ , was also used for the SC potential characterizing the electron-electron interaction. Being clearly more simplistic in the case of a single atom, the present model leads to a different ground-state energy. One can compensate for the energy shift by adjusting the parameter  $a$  to  $a = 0.3078$  a.u. =  $0.163$  Å. The SOC spacing  $d$  is set equal to the lattice parameter in a body-centered cubic lithium crystal,  $d = 6.63$  a.u. =  $3.51$  Å [305].

All simulations are performed for an electric field of the form

$$E(t) = E_{\max} \exp\left(-\frac{t^2}{2\tau^2}\right) \sin(\omega(t - t_0)), \quad (\text{V.9})$$

where the **FWHM** of the electric field,  $2\sqrt{2\ln 2}\tau$ , is chosen to be 5 fs. In other words, the pulse length (referring to the intensity profile) is  $5 \text{ fs}/\sqrt{2} \approx 3.54 \text{ fs}$  (**FWHM**). Similarly, the frequency  $\omega = 4 \text{ a.u.}$ , which is above the *K*-edge of 3.67 a.u., is identical in all calculations. This means that the photoelectrons stemming from **OPA** have an approximate kinetic energy of  $E_{\text{kin}} = 0.33 \text{ a.u.} = 9.1 \text{ eV}$  and thus –assuming the dispersion relation of a free electron– a group velocity of  $v_g = \sqrt{2E_{\text{kin}}} = 0.81 \text{ a.u.} = 18 \frac{\text{\AA}}{\text{fs}}$ . Characterizing the photon flux with a total photon number  $N_{\text{ph}}$ , the maximum field amplitude is varied over the range  $E_{\max} \in [0, 10 \text{ a.u.}]$ . Note that due to the relation  $N_{\text{ph}} \propto E_{\max}^2$ , a factor of 10 in  $E_{\max}$  corresponds to a factor of 100 in  $N_{\text{ph}}$ . The peak intensity is estimated as  $I_{\text{peak}} = \frac{E_{\max}^2}{8\pi\alpha} \approx 545 \text{ a.u.} \approx 3.5 \cdot 10^{18} \frac{\text{W}}{\text{cm}^2}$ .

Even though the assessment of tunneling dynamics via Keldysh parameter is inconclusive in the present case (see page 16), the corresponding values are provided as a rough estimate. Since the maximum ponderomotive energy  $U_p = (\frac{1}{2}E_{\max}/\omega)^2 \approx 1.5625 \text{ a.u.}$  is of the same order of magnitude as the binding energy  $\epsilon_B$ , the Keldysh  $\gamma_K$  parameter may momentarily reach values down to the order of one according to

$$\gamma_K = \sqrt{\frac{\epsilon_B}{2U_p}} = \frac{\sqrt{2\epsilon_B}\omega}{E} \approx \frac{10.83}{E}. \quad (\text{V.10})$$

Nevertheless, tunneling dynamics, which would be important for  $\gamma_K < 1$  at optical wavelengths, is excluded from the discussion.

The figures below visualize almost exclusively the behavior of the electron density during or after the laser pulse and no other physical quantity except for the ground-state population. It is emphasized that the homogeneous background density is not included in all these cases.

### V.2.1. Time-dependent charge density in the crystal limit

The main motivation for considering a **short ordered chain (SOC)** was the creation of a comparable situation to the crystal model from Chapter IV in the limit of a large amount of atoms  $N$ . A rough assessment of the number  $N$  required for achieving a crystal-like evolution of the charge density around the atom in the center of the **SOC** can be made based on the group velocity  $v_g \approx 5 \frac{d}{\text{fs}}$ . During 10 fs (twice the **FWHM** of the electric field) the quasi-free photoelectrons in a crystal pass approximately 50 atoms. Accordingly, one might expect  $N = 101$  to be a reasonable choice for an interpretation as a crystal-like situation. This estimate is in contrast to the simulations shown in Figs. V.2 and V.3, which suggest that the crystal limit is already achieved for significantly smaller  $N$ .

Displayed in Fig. V.2 is the time-dependent charge density in the spatial interval  $x \in [-\frac{1}{2}d, \frac{1}{2}d]$  and a temporal interval centered around the pulse maximum at  $t = 0$  for the cases of  $N = 1$  and 21 atoms. Note that the spatial interval is not chosen at random as it corresponds to the **Wigner-Seitz (WS)** cell in the crystal limit. For finite and odd  $N \geq 3$ , it would be more precise to speak of the Voronoi cell associated with the atom in the center of the **SOC** (in the

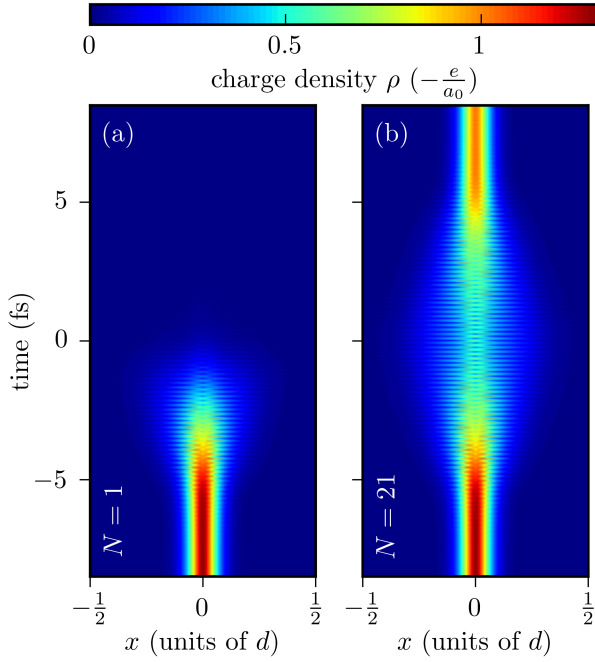


**Figure V.2.:** Time-dependent charge density in the vicinity of the middle atom for  $N=1$  (a) and 21 (b) atoms both simulated within the CAM at the same field amplitude of  $E_{\max} = 5$  a.u.

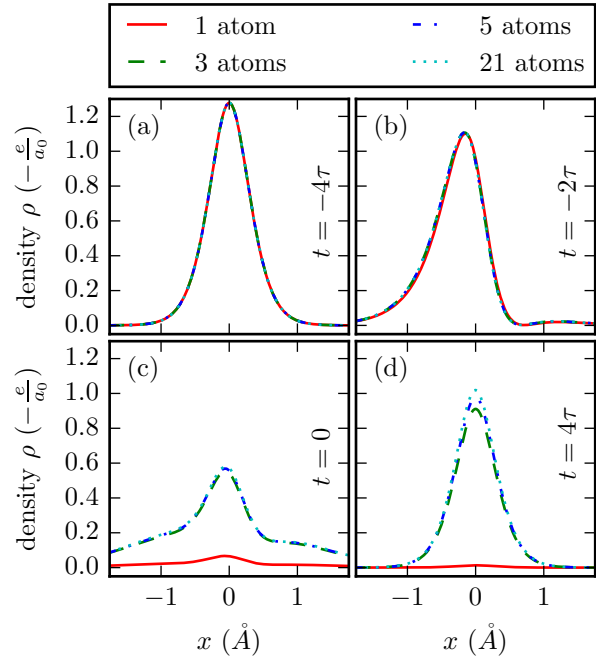


**Figure V.3.:** Slices of the time-dependent charge density in the adjacent figure at different times  $t = -4\tau$  (a),  $t = -2\tau$  (b),  $t = 0$  (c), and  $t = 4\tau$  (d). Additionally, the analogous cases for  $N=3$  and 5 atoms are shown.

Voronoi diagram to the atomic locations  $\{R_j | j = 1, \dots, N\}$ , but for simplicity it is not adhered to this more specific nomenclature here. In fact, the interval  $x \in [-\frac{1}{2}d, \frac{1}{2}d]$  and the term WS cell are used interchangeably here. It is striking in Fig. V.2 that the time-dependent charge density of the individual atom and the atom embedded in a SOC of  $N=21$  atoms are radically different at times around and after the pulse maximum at  $t=0$ . Similarities can be discovered only for early times during the pulse,  $t < -2$  fs. Apparently, the single atom in Fig. V.2a is subject to an efficient ionization process. Bound electrons are promoted to the continuum states and subsequently wave packets are formed that leave the vicinity of the atom at a speed of roughly the group velocity. Even before the pulse maximum is reached at  $t=0$ , the transition is saturated in the sense that no further electrons are available for ionization<sup>1</sup>. In comparison to the observations for the single atom, the ionization dynamics in a SOC is seen to be strongly suppressed in Fig. V.2a. At the pulse maximum  $t=0$ , the electron charge is spread over the WS cell but is largely confined to the vicinity of the atom. After the pulse, a large portion of the electron charge is again localized near the atom, implying a substantially less efficient ionization.

Evidently, the charge density is highly sensitive to the number of atoms  $N$  in the SOC for small  $N$ . This leads to the question of how many atoms are required to eventually reach the crystal limit. This issue is addressed now, whereas the physical reasons for the pronounced dependency on  $N$  are investigated below in the ensuing sections. Fig. V.3 depicts the charge

<sup>1</sup>Recall that other channels are assumed to be frozen on the short time scale of the pulse duration.

density in the WS cell for selected times,  $t = -4\tau, -2\tau, 0,$  and  $4\tau$ . For early times on the rising edge of the pulse envelope in Figs. V.3a and b,  $N$  only slightly affects the charge density, which is evident for Fig. V.3a as the SOCs are essentially still in the respective ground state. Apparently, all ground states exhibit the same charge density in the considered interval, which is an indispensable foundation for a direct comparison of the dynamics. The time evolution changes the situation markedly for later times in Figs. V.3c and d as observed above. There is also one novel insight that can be gained from this figure by noting that the cases  $N = 3$  and 5 behave very similar to  $N = 21$  and not the single atom. This indicates that the crystal limit with respect to the charge density around the middle atom of the SOC is basically reached for very small  $N$ . Since the results for  $N = 5$  and  $N = 21$  coincide, one anticipates no significant changes for  $N$  of the order of 100. This discrepancy with the initial assessment suggests that the photoelectrons do not propagate with the group velocity of free electrons. Alternatively, one may also presume that the charge density is not sensitive to photoelectrons stemming from atoms more than  $2d$  away. Of course, these two explanations are not mutually exclusive. Note that the second conjecture is supported by the remark in Sec. IV.3.3 that a logarithmic scale is required to discern the flow of photoelectrons away from the respective atomic site.

## V.2.2. Evolution of the charge density in short ordered chains (SOCs)

For a detailed understanding of the influence of neighboring atoms on the ionization dynamics, the charge density is now considered as a function of time  $t$  and the spatial coordinate  $x$  with a domain that contains the whole SOC for all times in a nontrivial case  $N > 1$ . Emphasis is put on a SOC comprising  $N = 5$  atoms, which was already analyzed in the vicinity of the middle atom (see Fig. V.3) and found to be close to the crystal limit while still being a relatively small and thus simple system. The corresponding spatiotemporal behavior of the charge density over the whole SOC is illustrated in Fig. V.4a. Further, the analogous case within the IAM is depicted in the adjoining figure, Fig. V.4b, in order to rule out the possibility that the local charge increases with  $N$  only due to photoelectrons which were ejected from other atoms and pass through the surrounding area of the middle atom. It turns out that the photoelectrons hardly affect the charge density near the atomic sites by comparing with the corresponding calculation for the single atom [not shown]. This finding is consistent with the symmetry in Fig. V.4b regarding the similarity of the time evolution undergone by the charge density in the vicinity of inner and boundary atoms, which are actually, depending on the position, subject to a delay of passing photoelectrons from other atomic sites. Accordingly, the IAM simulation in Fig. V.4b can be associated with the  $N = 1$  case in Figs. V.2 and V.3 to a good approximation. It should be pointed out that due to the logarithmic scale, a charge density with a magnitude of  $10^{-2} \frac{e}{a_0}$  and less, though barely noticeable in Figs. V.2 and V.3, remains visible even after the pulse.

When comparing Figs. V.4a and b, one discerns that boundary atoms in the CAM behave similarly to the IAM, whereas the inner atoms reveal a resemblance among each other but differ significantly from the boundary atoms. In particular, the charge density that resides in the vicinity of the respective atom is clearly enhanced. This phenomenon is naturally interpreted as an impact of neighboring atoms, which inhibit the charge flow away from the inner atoms. Intuitively, the time evolution of the charge density of boundary atoms is closer to the case of independent atoms because only one adjacent atom directly affects the photoelectron dynamics. The electrons

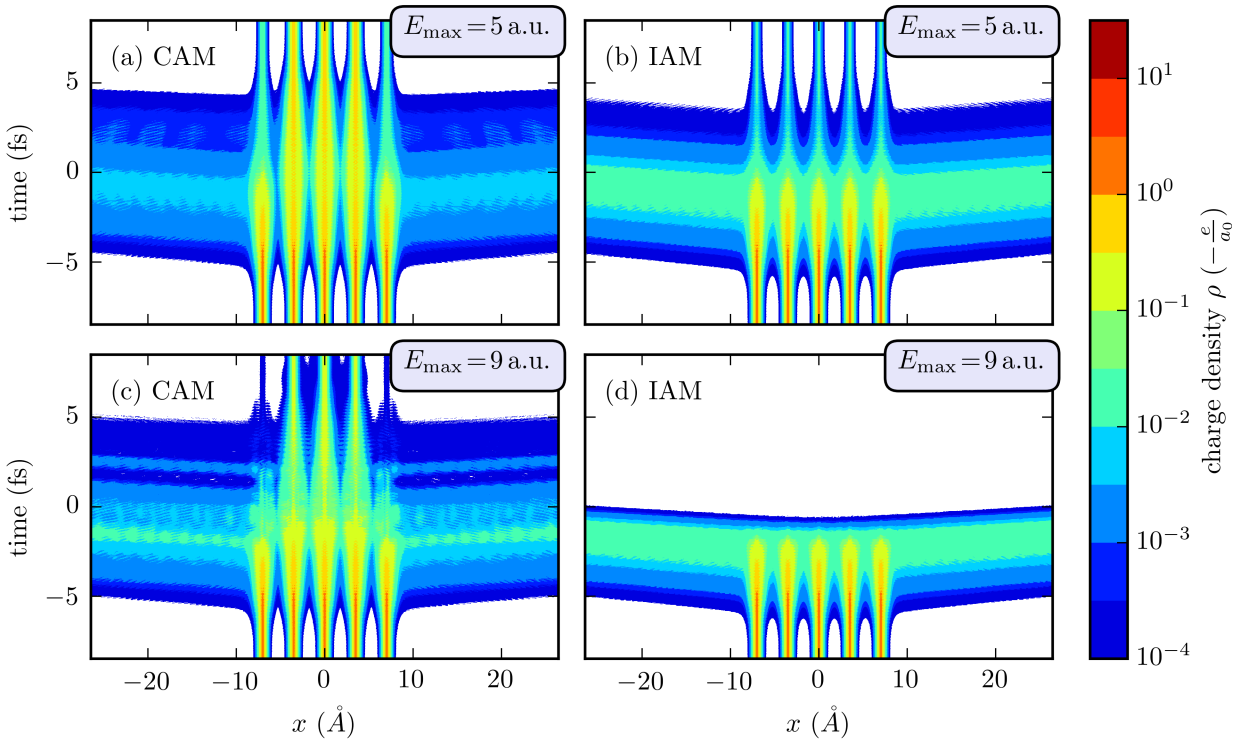


**Figure V.4.:** Logarithmic contour plot of the time-dependent charge density  $\rho(x, t)$  for a SOC with  $N=5$  atoms under irradiation with a laser pulse described by the electric field from Eq. (V.9). The plots in the first row [(a) and (b)] are calculated for  $E_{\max} = 5$  a.u. and in the second row [(c) and (d)] for  $E_{\max} = 9$  a.u. Similarly, the first column [(a) and (c)] is based on the CAM and the second column [(b) and (d)] on the IAM. The white area corresponds to coordinates  $(x, t)$  where the magnitude of the electron density is below  $10^{-4} \frac{e}{a_0}$ .

ejected from inner atoms are essentially trapped by the coherent dynamics despite the fact that the commonly known phenomenon of electrostatic trapping was deliberately disregarded.

To answer the question whether this behavior crucially depends on the laser intensity, the analogous case for a larger field amplitude of  $E_{\max} = 9$  a.u. is shown in Figs. V.4c and d. The increase in intensity leads to numerical values of the IAM charge density below  $10^{-4} \frac{e}{a_0}$  around the atomic positions once the pulse has reached its maximum at  $t = 0$ ; hence, the remaining charge is considerably smaller than for the low intensity case in Fig. V.4b. By contrast, the CAM results, Fig. V.4c, demonstrate again a trapping of electrons near inner atoms, albeit far less pronounced than for low intensity, Fig. V.4a. These two examples,  $E_{\max} = 5$  a.u. and 9 a.u., are now embedded in an extensive model study that is concerned with a broader intensity range. In order to characterize the response of a SOC comprising an arbitrary number of atoms  $N$  to a laser pulse of the form in Eq. (V.9) with respect to the localization phenomenon near inner atoms, one defines the following quantity that simplifies the illustration by eliminating the dependency

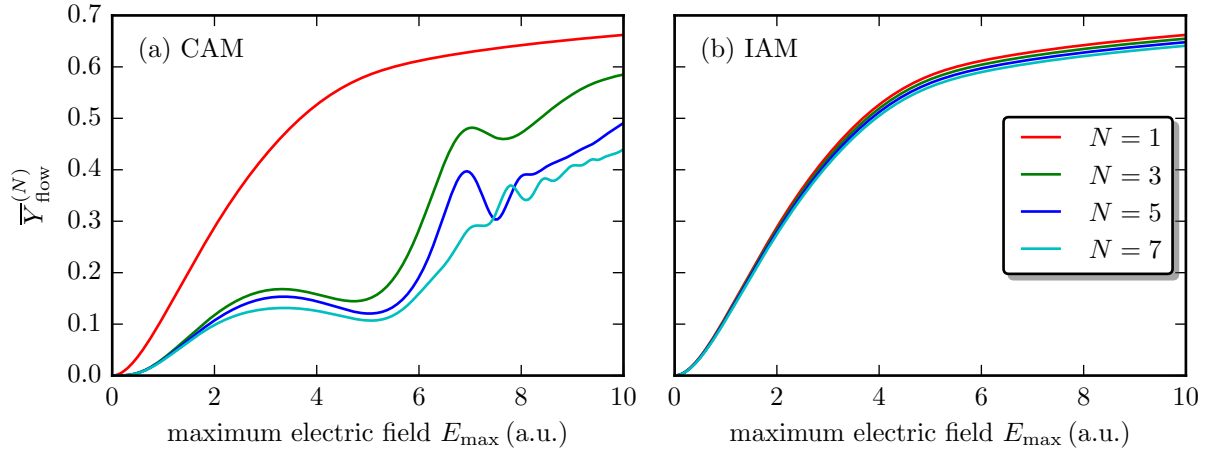


**Figure V.5:** Fraction of electrons flow away from the interval  $[-\frac{1}{2}d, \frac{1}{2}d]$  of a SOC comprising  $N$  atoms, as measured by the time average of  $Y_{\text{flow}}^{(N)}(t)$ , simulated within the CAM (a) and the IAM (b).

on the spatial coordinate  $x$ :

$$Y_{\text{flow}}^{(N)}(t) := 1 - \frac{1}{q_{\text{at}}} \int_{-\frac{1}{2}d}^{\frac{1}{2}d} \rho(x, t) dx, \quad (\text{V.11})$$

where  $q_{\text{at}} = -2$  is the charge per atom minus the homogeneous background density, i.e., the charge corresponding to the explicitly simulated electrons in the innermost shells;  $\rho(x, t)$  is the associated charge density as shown in Fig. V.4. The integration interval is equal to the WS cell in the crystal limit.  $Y_{\text{flow}}^{(N)}$  is a measure for the amount of the charge density that is localized around the middle atom, where  $Y_{\text{flow}}^{(N)} = 0$  means that the interval  $[-\frac{1}{2}d, \frac{1}{2}d]$  contains the same total charge as in the initial state and  $Y_{\text{flow}}^{(N)} = 1$  implies that the whole charge density has left the vicinity of the atom. Accordingly,  $Y_{\text{flow}}^{(N)} = 1$  is referred to as *delocalization yield* below. Next, one evaluates the time average of  $Y_{\text{flow}}^{(N)}(t)$  over the pulse duration, here  $[-4\tau, 4\tau]$ , to obtain the quantity  $\bar{Y}_{\text{flow}}^{(N)}$ , which characterizes how efficiently the middle atom is stripped off its inner-shell electrons by a given pulse.

This strategy allows the illustration of the localization/trapping mechanism for a continuous intensity range and for SOCs of different lengths in Fig. V.5. Here, only SOCs with an odd number of atoms are shown for the trivial reason that the *middle* atom is unambiguously identified. Starting with the simple case of the IAM in Fig. V.5b, one can directly infer a monotonic decrease of the localization as a function of the intensity for independent atoms in accordance with the rate-equation approach for single atoms. The dependence on the number of atoms  $N$  is trivially described by a slight monotonic decrease due to other photoelectrons passing through, which only mildly affects  $\bar{Y}_{\text{flow}}^{(N)}$  for  $N = 1, 3, 5$ , and  $7$  as indicated above. One can conclude that the definition of the delocalization yield  $Y_{\text{flow}}^{(N)}$  is well suitable for highlighting deviations from the model of independent atoms.

The intensity and  $N$  dependence of the delocalization yield depicted in Fig. V.5a strongly contrasts with the IAM. As observed above in Sec. V.2.1, the localization is strongly enhanced for  $N > 1$ , which leads to a large discrepancy between the curves for  $N = 1$  and  $N \in \{3, 5, 7\}$  atoms. For  $E_{\max} = 5$  a.u. one can recognize the already studied case from Figs. V.2 and V.3, where the difference between  $N = 1$  and  $N > 1$  is very pronounced and  $N \in \{3, 5, 7\}$  exhibit similar values among themselves. The non-monotonic behavior of the delocalization yield can be interpreted as evidence of a coherent saturation process. Carefully examining the cases  $N = 5$  and  $N = 7$ , one further observes that the curves for different  $N$  are not strictly ordered.

Based on Fig. V.5 alone, it is not possible to identify the relevant mechanism for this phenomenon. The following speculations are conceivable explanations: analogous to the crystal model in Chapter II one might expect (i) the buildup of standing waves by quantum interference (see Sec. IV.3.3) and, additionally, (ii) Pauli blocking might inhibit further ionization and thus influence also the populations of bound states and not only the charge density. Furthermore, (iii) the formation of a band structure<sup>2</sup> might affect the ionization probabilities. Lastly, one might suppose that (iv) reflections suppress the diffusion of photoelectrons in spite of neither Fig. V.2 nor Fig. V.4 providing direct evidence for back and forth traveling waves. Note that due to the comparatively small systems, the buildup of the band structure is considered separately from the role of reflections although these phenomena are strongly related in crystals [306].

Further investigations for resolving this issue are presented in the ensuing sections. Anticipating Sec. V.2.3, one can refute assertion (iii) by calculating the density of states, which proved to be crucial for the interpretation of the results in Chapter IV. Likewise, hypothesis (iv) is shown below in Sec. V.2.4 not to be an essential component of the phenomenon described above.

### V.2.3. Ionization yield of SOC

In the following, the question is addressed as to how the localization mechanism affects the overall ionization in the SOC. Analogous to the delocalization yield  $Y_{\text{flow}}^{(N)}$  from Eq. (V.11), a further quantity, the ionization yield  $Y_{\text{esc}}^{(N)}$ , is defined in order to characterize the amount of electrons that have left the vicinity of the entire SOC

$$Y_{\text{esc}}^{(N)}(t) := 1 - \frac{1}{q_{\text{tot}}} \int_{-\frac{1}{2}L}^{\frac{1}{2}L} \rho(x, t) dx, \quad (\text{V.12})$$

where  $q_{\text{tot}} = -2N$  is the total charge of the electrons of interest and  $L = Nd$  is the length of the SOC. Unlike the definition of the delocalization yield  $Y_{\text{flow}}^{(N)}$ , the domain of integration of the ionization yield  $Y_{\text{esc}}^{(N)}$  is extended to contain the whole SOC and the normalization factor  $q_{\text{tot}}$  is adjusted so that the codomain of  $Y_{\text{esc}}^{(N)}$  is  $[0, 1]$ . The limiting case  $Y_{\text{esc}}^{(N)} = 0$  ( $Y_{\text{esc}}^{(N)} = 1$ ) corresponds to a situation where no (all) inner-shell electrons have escaped from the vicinity of the SOC.

<sup>2</sup>This explanation seems unlikely regarding the fact that the localization is apparent already for a SOC comprising  $N = 3$  atoms. It is still taken into consideration because this mechanism might be artificially enhanced in the 1d simulation.

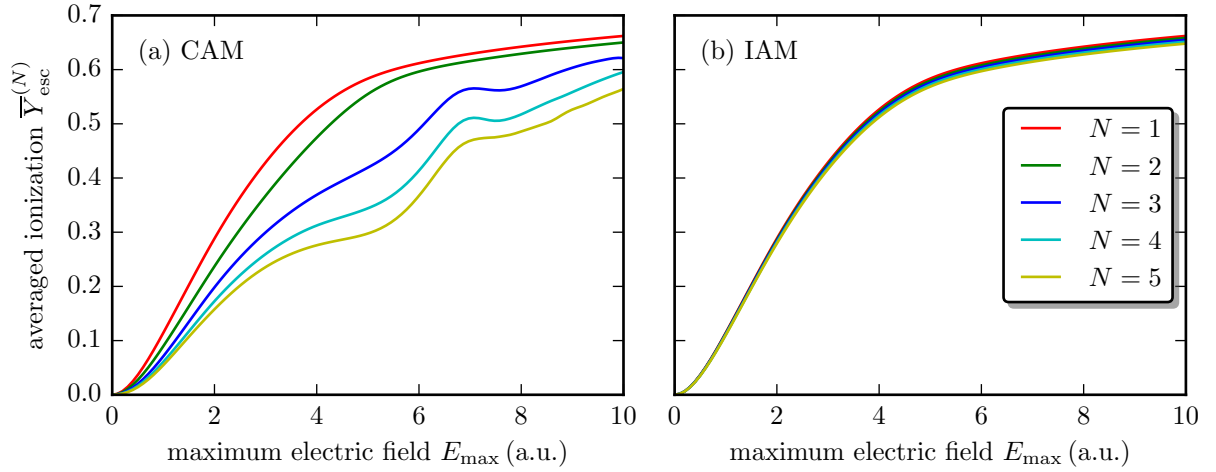


**Figure V.6.:** Fraction of electrons which escaped from the interval  $[-\frac{1}{2}Nd, \frac{1}{2}Nd]$  of a **SO**C comprising  $N$  atoms as measured by the time average of  $Y_{\text{esc}}^{(N)}(t)$  (see Eq. (V.12)) over the time interval  $[-4\tau, 4\tau]$ , simulated within the **CAM** (a) and the **IAM** (b).

Analogous to the previous section, the time-averaged ionization yield  $\bar{Y}_{\text{esc}}^{(N)}$  is considered to characterize the response of the **SO**C towards pulses with varying photon numbers  $N_{\text{ph}}$  implied by the range of the field amplitude  $E_{\text{max}}$ . Again, the definition of the ionization yield is designed to be fairly insensitive to changes of the number of atoms  $N$  in the **IAM** as depicted in Fig. V.6b. One discerns once more only a slight monotonic dependence on  $N$  attributed to the fact that the photoelectrons are considered to be in the vicinity of the **SO**C over a range of length  $L$ , which, in turn, increases linearly with the number of atoms  $N$ .

The ionization yield  $\bar{Y}_{\text{esc}}^{(N)}$  in Fig. V.6a demonstrates large deviations from the behavior expected for independent atoms, albeit less pronounced than the delocalization yield  $\bar{Y}_{\text{flow}}^{(N)}$  in Fig. V.5. The dependence on  $N$  is weakened because boundary atoms contribute to the integral, which, as observed above, behave similarly to the independent atoms and thus smooth out the curves. Nevertheless, the trapping mechanism obviously has a significant impact on the degree of ionization during the pulse. Consistent with the interpretation from above, the curve progression for a **SO**C comprising two boundary atoms,  $N=2$ , is both qualitatively and quantitatively more similar to the  $N=1$  than to the  $N=3$  case.

To accomplish deeper insights in the cause of the trapping (see the possible explanations mentioned on page 68), it will prove expedient to characterize the ionization yield not only by the charge density but also by the ground-state occupation probability. After all, the ionization yield as defined in Eq. (V.12) can be influenced by both standing waves that inhibit the flow out of the crystal and by a suppression of the prior process of promoting electrons to unbound states. However, when focusing on the ground-state dynamics, one encounters the problem that a fair comparison between the ground-state population of **SO**Cs with different lengths is not trivial. The situation is simplified by considering the following scenario. Let  $p_g^{(N)}(t)$  be the population of the ground state of a **SO**C comprising  $N$  atoms. If all atoms were identical and independent, one would have the relation

$$p_g^{(N)}(t) = (p_g^{(1)}(t))^N \quad (\text{V.13})$$

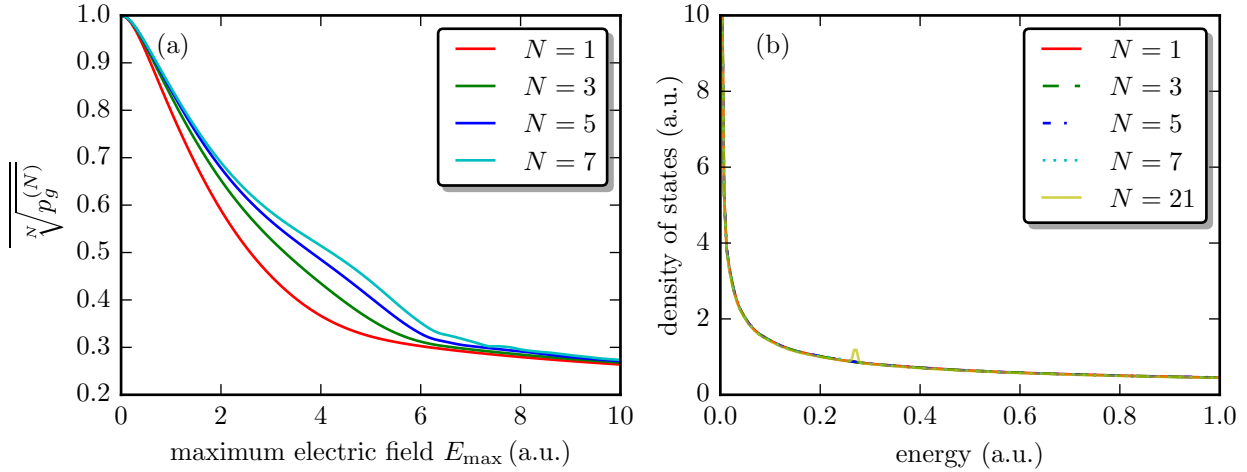


**Figure V.7.:** (a) Ground-state occupation attributed to a single atom  $\sqrt[N]{p_g^{(N)}}$  calculated with the CAM averaged in time over the interval  $[-4\tau, 4\tau]$ . (b) Density of states  $D(\varepsilon)$  for a CAM potential corresponding to a SOCs with  $N$  atoms. All curves virtually coincide with the analytic expression for a free particle  $D(\varepsilon) = \frac{1}{\pi} \sqrt{\frac{2}{\varepsilon}}$ . Only the graph for  $N = 21$  exhibits a small deviation in the region of interest, i.e., around  $\varepsilon \approx 0.33$  a.u.

Hence, it is more meaningful to compare  $\sqrt[N]{p_g^{(N)}(t)}$  rather than  $p_g^{(N)}(t)$ , which can be interpreted as the ground-state occupation attributed to a single atom for SOCs with different  $N$ . The time-averaged values of this quantity are shown in Fig. V.7a for the cases with  $N = 1, 3, 5,$  and  $7$  atoms. The situation is directly connected to the respective delocalization and ionization in Fig. V.5a and Fig. V.6a. For completely independent atoms, all curves would coincide exactly with the result for  $N = 1$ , making a comparison to the IAM superfluous. The graphs for  $N \geq 3$  exhibit a qualitatively different behavior while being subject to only small quantitative deviations. This suggests that the formation of a band structure accompanied by a mere change of ionization rates is not a decisive prerequisite for the trapping mechanism. This supposition is supported by Fig. V.7b, which demonstrates that the density of states for the CAM for  $N \geq 7$  is to a good approximation identical to the analytic result for a free particle. One can deduce that the transition rates are similar in the cases  $N = 1, 3, 5,$  and  $7$ , but the buildup of standing waves significantly enhances the trapping of photoelectrons, as seen above in Fig. V.6, and, simultaneously, the trapped electrons slightly inhibit further ionization due to Pauli blocking shown in Fig. V.7a.

#### V.2.4. The impact of reflections

The formation of a band structure as an explanation for the modified ionization in SOCs with different lengths was ruled out in the previous section. The findings rather suggested that standing waves emerge from the wave packets emitted during the ionization process, but it is not yet apparent whether this phenomenon is the result of the interference of wave packets between neighboring atoms or between a wave packet and its own reflection from adjacent potentials. Fortunately, one can establish an intermediate level of theory that is positioned between the

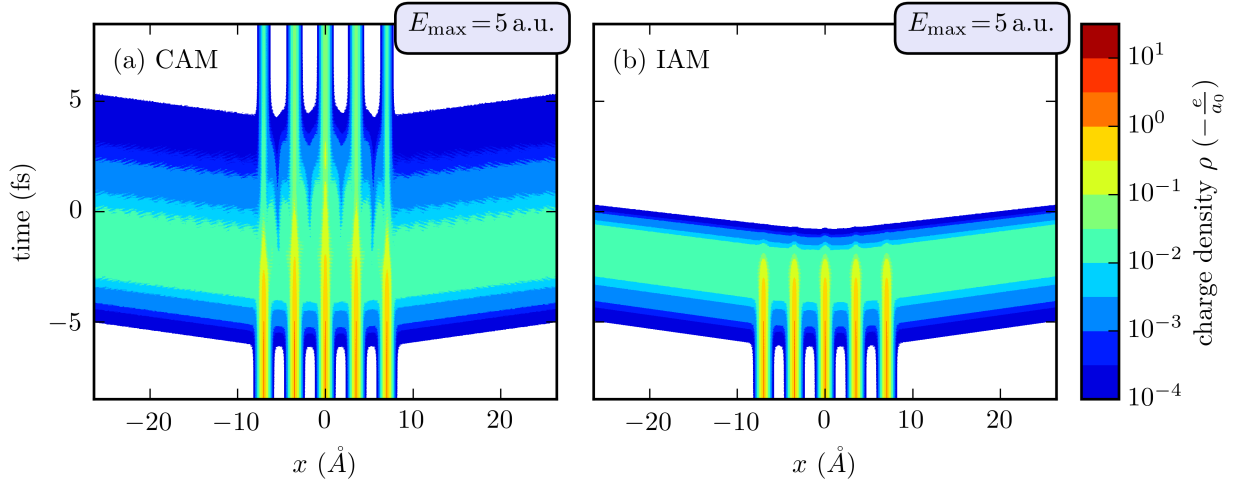


**Figure V.8.:** Logarithmic contour plot of the time-dependent charge density  $\rho(x, t)$  for a SOC with  $N=5$  atoms under irradiation with a laser pulse described by the electric field from Eq. (V.9) for  $E_{\max} = 5$  a.u. The simulations are based on the reflectionless CAM (a) and the reflectionless IAM (b).

CAM and the IAM by explicitly excluding potential reflections by means of a reflectionless potential as reported in Sec. V.1.3. The parameters of the reflectionless potential are adjusted to match the  $K$ -edge of the single-atom case in the CAM model<sup>3</sup>. To be specific, the length  $a$  and the dimensionless integer parameter  $n$  were chosen to be  $a = 0.73864$  a.u. and  $n = 2$ .

No detailed parameter study will be performed for this potential dealing with the question whether the absence of reflections weakens or enhances the trapping phenomenon because the different scenarios are not directly comparable. The most obvious discrepancy is the ionization rate of the reflectionless potential, which deviates considerably from the model based on the screened SC potential in spite of coinciding  $K$ -edges. This is demonstrated in Fig. V.8 for  $E_{\max} = 5$  a.u. The ionization rate is clearly increased as indicated by the corresponding IAM simulation shown in Fig. V.8b. Indeed, by comparing it to earlier results in Figs. V.4b and d, it resembles more the case of  $E_{\max} = 9$  a.u. in Fig. V.4d than  $E_{\max} = 5$  a.u. in Fig. V.4b.

However, despite the lack of a straightforward comparability to the results in previous sections, one can still learn from Figs. V.8a and b that the qualitative features of the trapping observed above in Sec. V.2.2 remain visible. Most importantly, the absence of potential reflections does not destroy the observed phenomenon and thus another possible interpretation (iv) mentioned on page 68 is made unlikely. Further, the origin of the interference (option (i)) is rendered more precisely. Hereafter, the coherent trapping phenomenon will be referred to as interference-induced localization/trapping.

<sup>3</sup>The precise parameters used in the CAM and IAM simulations are listed on page 62.

### V.2.5. The impact of disorder

Being familiar with **Anderson localization (AL)** [307–311], which is a phenomenon induced by disorder in crystalline structures resulting in a localization of wave functions, one might anticipate parallels, particularly because **AL** is also characterized by coherent quantum dynamics and known to be very important in **1d** systems [308, 312]. Furthermore, there are investigations on a dependence of **AL** on the system size which are commonly explained via the so-called *scaling theory* [308, 310, 311]. The mechanism is, however, different from the interference-induced localization observed in the present thesis. For the description of **AL**, impurity backscattering is typically taken into account. Backscattering per se was demonstrated not to be

crucial in the present treatment and crystal defects in **SOCs** can be associated only with the boundaries<sup>4</sup> because all other atomic positions resemble an ideal crystal. Therefore, one would expect that the localization decreases for increasing  $N$ , ultimately reaching a situation with negligible impact of boundary atoms. This tendency was not observed here. Nevertheless, it is tempting to think that disorder might affect the interference-induced localization.

To address this speculation, simulations for disordered systems were performed and compared to the ionization yield  $\bar{Y}_{\text{esc}}^{(7)}$  of a **SOC** comprising  $N = 7$  atoms as a reference. The resulting time-averaged ionization yield is shown in Fig. V.9 analogous to Fig. V.6. To be specific, the disordered systems are characterized by different random displacements from the **SOC** positions of each inner atom (uniformly distributed within  $\pm 1$  a.u.). The boundary atoms are kept fixed for the sole purpose of maintaining the meaning of the definition of  $Y_{\text{esc}}^{(N)}(t)$  in Eq. (V.12).

One can conclude from Fig. V.9 that the disorder generally, contrary to the expectation, even enhances the ionization yield. From a different perspective, one may interpret the similarity of the graphs over a broad parameter range as an extension of the significance of the model because the basic result remains valid even if the strict ordering according to the definition of **SOCs** is not fulfilled. Therefore, one can easily argue that the qualitative conclusions drawn in this chapter are likewise valid for **1d** clusters.

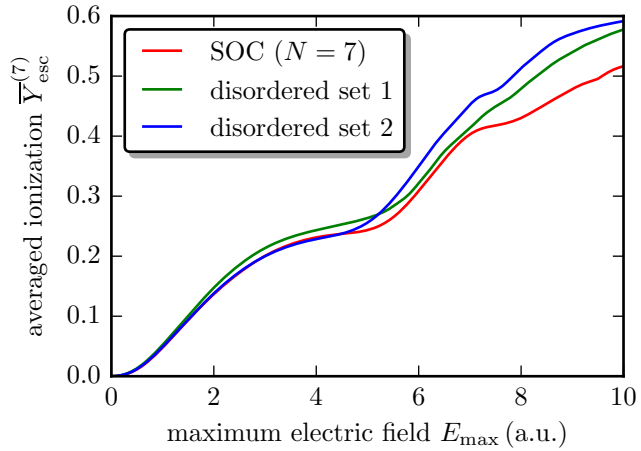


**Figure V.9.:** Ionization yields analogous to Fig. V.6 for a **SOC** with  $N = 7$  atoms and two further sets of atomic positions whose inner atoms have a random displacement from the **SOC** positions uniformly distributed within  $\pm 1$  a.u.

<sup>4</sup>Note that also the electric field is spatially homogeneous.

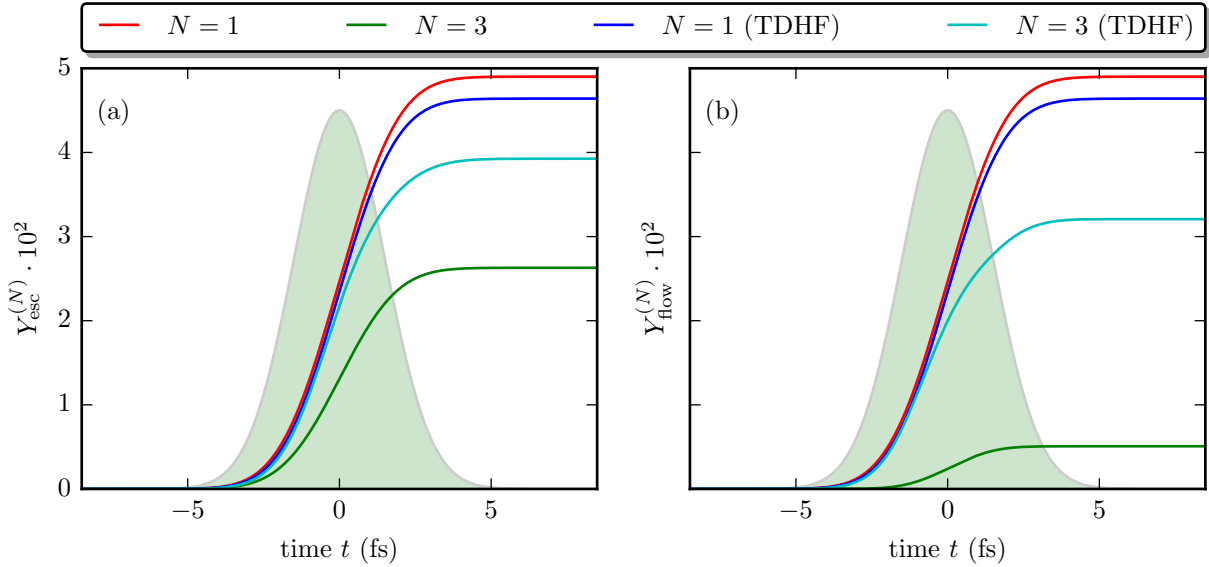


**Figure V.10:** Time-dependent ionization (a) and delocalization (b) yield as defined in Eqs. V.12 and V.11 calculated with the CAM where  $E_{\max} = 0.1$  a.u. and in the TDHF model where  $E_{\max} = 0.4$  a.u. for the single atom  $N = 1$  and a SOC comprising  $N = 3$  atoms. In the background, the pulse envelope of the intensity is depicted in arbitrary units.

### V.2.6. The impact of electrostatic trapping

It was already mentioned in the beginning of the present chapter on page 57 that there is another trapping mechanism in real systems due to electrostatic attraction of the residual ions. So far, this phenomenon was completely excluded from the discussion because it was intentionally disregarded in the model in order to enable the identification of a novel trapping mechanism that is guaranteed to be distinct from electrostatic trapping. Naturally, the question arises which of these two conceivable trapping mechanisms will dominate in reality. One can respond to this question only to a limited extent as long as the 1d approximation is kept. However, with moderate additional computational costs, one may find at least an adequate answer for 1d systems using the TDHF approach from Sec. V.1.4, which is capable of taking the electrostatic trapping into account while still maintaining the foundations for the coherent localization mechanism.

As stated before, the parameter  $a$  of the atomic potential has to be adjusted to compensate for the energy shift of HF orbitals due to the electron-electron interaction. Analogous to the comparison with the reflectionless potential (see Sec. V.2.4), the choice of  $a$  is based on establishing similar situations exclusively with regard to the  $K$ -edge. To be specific, the numerical value  $a = 0.2805$  a.u. leads to the same  $K$ -edge and thus the same excess energy of photoelectrons as in previous simulations. Of course, this holds only for weak pulses because the  $K$ -edge in TDHF simulations during an ionization process generally depends on time [256]. In particular, if the  $K$ -edge drops below the photon energy, which may occur quite easily in NTI, the results will exhibit artificial signatures that deviate strongly –even on a qualitative level– from the dynamics observed so far. In the present case, one can achieve similar dynamics for single atoms with respect to  $Y_{\text{esc}}^{(1)}(t)$  or  $Y_{\text{flow}}^{(1)}(t)$  for small photon numbers. As an example, the situations for

$E_{\max} = 0.1$  a.u. in the CAM and  $E_{\max} = 0.4$  a.u. in the TDHF model are compared to each other in Fig. V.10. Based on this choice of parameters, the time-dependent delocalization and ionization yield for  $N = 1$  evidently evolve similarly in both models. Note that the delocalization and ionization yield are identical in the single-atom case, i.e.,  $Y_{\text{esc}}^{(1)}(t) = Y_{\text{flow}}^{(1)}(t)$ . This is also seen in the present case by comparing Figs. V.10a and b.

First and foremost, Fig. V.10a indicates that a reduction of the overall ionization in a SOC for  $N > 1$ , albeit weakened, still occurs in simulations based on a TDHF model as reflected by the deviations between the curves for  $N = 1$  and 3. The localization in Fig. V.10b experiences the same tendencies. Certainly, the two theories, the CAM and TDHF model, are too dissimilar for a quantitative assessment of the trapping even though the  $K$ -edge and the laser intensity was adjusted. Nevertheless, it is interesting to discover that the system shows no signs of the two mechanisms adding up and thus increasing the localization. On the contrary, the phenomenon of localization and the reduced ionization is even less prominent in the TDHF theory. This can, for example, be attributed to the fact that the Hartree term in TDHF mimics the screening in the CAM only if the charge density is evenly smeared out over the entire SOC. Normally, however, the charge density is—in particular for the small intensities considered here—located near the atomic sites and leads to a flattening of the effective core potential through the Hartree term. The impact of neighboring potentials is then weakened and the CAM becomes increasingly similar to the IAM and thus exhibits less pronounced signatures of the trapping effect. Furthermore, it can be seen that the localization in Fig. V.10b is affected more significantly by the electron-electron interaction than the reduction of the overall ionization Fig. V.10a. This can be interpreted as an indication of the TDHF calculations being in favor of electrostatic trapping because the middle atom is expected to play a less important role in the case of a dominance of electrostatic over interference phenomena.

To summarize this subsection, it was shown that a trapping mechanism is still present in TDHF calculations. However, due to the lack of comparability of the two models it cannot be determined without further investigations whether the localization based on electrostatic or the interference effects dominates in 1d systems.

# VI

## Numerical methods

This chapter is exclusively dedicated to the algorithms and selected details of the implementation behind the simulations that led to the results shown in the previous chapters. Although the computational costs of the implemented **1d** models do not at all meet the limits of up-to date computer hardware, the numerical approach was, along with the work by [Kaiser \(2014\) \[4\]](#), planned to be extensible to solve the time evolution as described by the **time-dependent reduced density-matrix (TDRDM)** theory, i.e., a **partial differential equation (PDE)** in effectively four space dimensions (see Ref. [4]). It was pointed out by [Kaiser \(2014\) \[4\]](#) that the convergence of **TDRDM** calculations could not be guaranteed based on only a shared-memory parallelization due to memory limitations. For this reason, the strategy was to take advantage of distributed-memory parallelization gradually by adapting the algorithms first for the **TDSE**, then the orbital formulation of the **TDHF** theory (see Eq. (II.2)), the **one-body reduced density matrix (1RDM)** formulation of the **TDHF** theory (see Eq. (II.1)), and last the **TDRDM** approach. Within the scope of the present project, *distributed algorithms*<sup>1</sup> were implemented up to the **1RDM** formulation of the **TDHF** theory but not for the **TDRDM** approach. Accordingly, numerical strategies will be reviewed in detail for the **PDEs** of interest in order to facilitate potential future work. Because the numerics of **PDEs** is obviously a broad field, it is not intended to give a full summary of the research. In fact, there will be in most cases only recommendations of the pertinent literature if available. Sec. VI.5 can be regarded as guide through important technical aspects of the implementation, whereas the core issue, the numerical representation of operators within the **finite-element discrete variable representation (FEDVR)**, is dealt with extensively in Sec. VI.4. For this purpose, the reader is briefed beforehand about the **discrete variable representation (DVR)** in Secs. VI.2 and VI.3. It is assumed that the reader is familiar with the fundamentals of the numerical solution of **PDEs** such as the **finite difference method (FDM)** and the basic concept behind a *Galerkin* solution [314, 315].

Much emphasis is put on constructing and dealing with sparse matrices because the alternative, namely dense matrices, are intrinsically counterproductive for distributed algorithms. One way to understand this, is to consider a simple matrix-vector multiplication  $w = Mv$  with a dense matrix  $M$  and vectors  $v, w$ , where  $w$  and  $v$  typically have the same parallel layout in practical applications. Although there are different strategies for splitting the entries of  $M$  and  $v$  over a given number of processors  $p$ , usually  $v$  and  $w$  have entries on all processors<sup>2</sup>. A mapping represented by a dense matrix implies that all entries of the vector  $v$  contribute to each entry of  $w$ , i.e., each processor has to communicate with all others. Therefore, the workload of each processor with respect to communication increases with the total number of processors  $p$ , which, in turn, means that the performance of the algorithm may deteriorate for large  $p$ . For sparse matrices, by contrast, each processor in the present **1d** scenario communicates –independent of  $p$ –

---

<sup>1</sup>For a definition/explanation of the term *distributed algorithm*, consult, e.g., Ref. [313].

<sup>2</sup>For the sake of completeness, it is pointed out that, for example, the computational toolkit **PETSc** [316] supports redundant storage for faster access.

only with two adjacent processors, which results in a considerably more efficient parallelization.

To begin with, the simple but important problem of appropriate boundary conditions is illustratively discussed in Sec. VI.1. This matter can be interpreted as the step preceding the numerical implementation where boundaries are introduced to an infinite system with the aim that it still mimics the unbounded case in the sense that ideally no distortions of the solutions occur in a certain subdomain.

## VI.1. Boundary conditions

For the simulation of ionization experiments based on the time-dependent charge density as shown, for example, in Fig. V.4 of the previous chapter, the modeling of an *open system* is required in the sense that electrons are capable of leaving the finite numerical system. The naive approach of extending the computational boundaries is not feasible even in the case of the 1d calculations because it immediately encounters its limits if electrons are ejected with high kinetic energy, which is very likely in the X-ray regime. Since this proved to be an important issue in practice, the present chapter is devoted to, first of all, elucidating the problems accompanied by finiteness of the numerical system with the aid of a simple and elementary example. Subsequently, it is demonstrated how to significantly mitigate the finite-system artefacts by using a **complex absorbing potential (CAP)**.

To illustrate the underlying issue, one may consider a very simple system, namely the **time-dependent Schrödinger equation (TDSE)** for one particle in 1d. Specifically, one seeks the solution of

$$i \frac{\partial}{\partial t} \psi(x, t) = -\frac{1}{2} \frac{\partial^2}{\partial x^2} \psi(x, t) \quad (\text{VI.1})$$

with respect to the initial condition

$$\psi(x, t = 0) = \frac{1}{\sqrt[4]{\pi}} e^{-\frac{1}{2}x^2 + ipx}. \quad (\text{VI.2})$$

For a **(pure) initial value problem (IVP)** on the infinite interval  $x \in ]-\infty, \infty[$ , the time evolution of Gaussian wave packages is well-known and analytical solutions are easily obtained. Accordingly, this example is helpful for testing purposes of the implementations of numerical approaches described later (see App. C) and, further, it is adequate to illustrate the impact of unphysical numerical boundaries.

Consider the following scenario: one seeks a numerical solution of the **IVP** for  $p = 0.5$  in Eq. (VI.2). In many simulations of ionization experiments, it is sufficient to find the solution in the vicinity of the atomic sites unless, for example, photoelectrons are investigated explicitly [318]. For illustration purposes, it is assumed in the following that only  $\psi|_{[-5,5]}$ , the restriction of the wave function on the interval  $[-5, 5]$ , is of interest. Now compare the analytic solution of the **IVP** on the extended interval  $[-10, 10]$  in Fig. VI.1a with the solution of the **mixed initial-boundary value problem** on the same interval with Dirichlet boundary conditions,  $\psi(-10) = \psi(10) = 0$ , in Fig. VI.1b. Apparently, the wave package is reflected at the boundaries at times  $t > 2$  a.u., which subsequently leads to a modification of the global behavior of the time evolution. In particular, the wave function is altered on the interval of interest  $[-5, 5]$  even though the interval

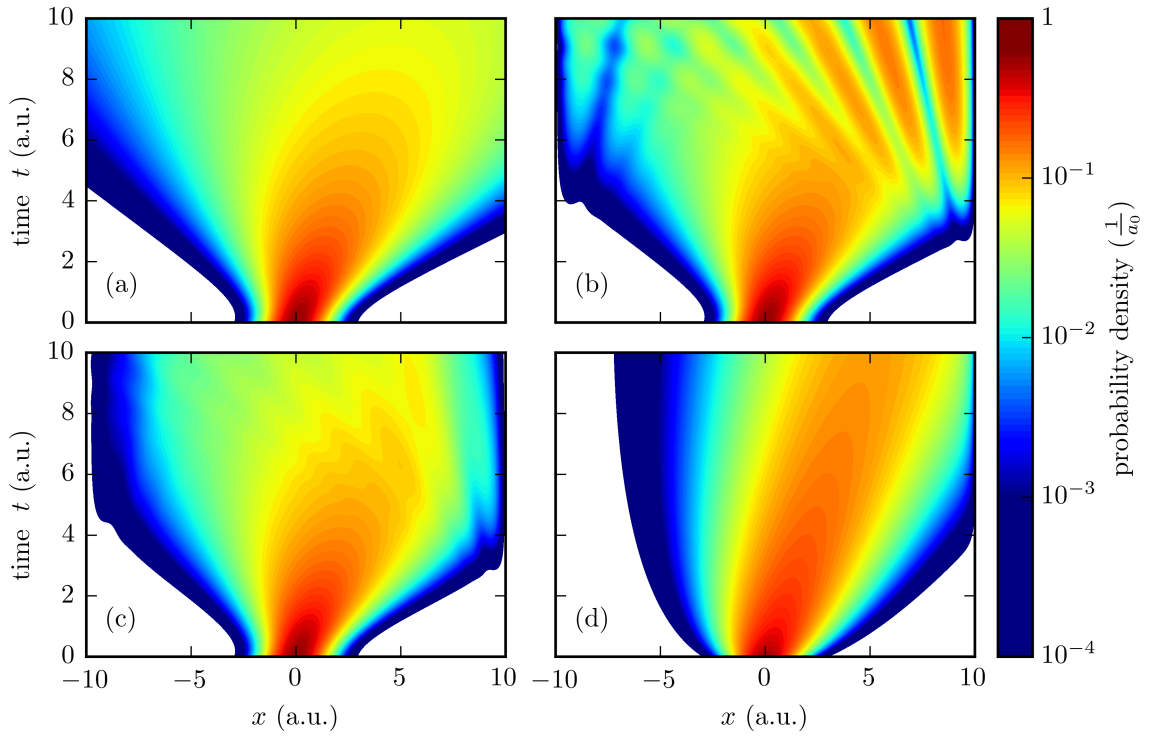


**Figure VI.1:** Time-dependent probability density of the solution of the TDSE shown in Eq. (VI.1) with respect to the initial state from Eq. (VI.2) [ $p = 0.5$ ] using (a) an infinite system, (b) Dirichlet boundary conditions, and (c) again Dirichlet conditions in conjunction with the CAP from Eq. (VI.3) [ $\alpha = 0.05$ ,  $r = 5$ ]. For comparison, the time-dependent solution to the Fokker-Planck type equation Eq. (VI.5) [ $p = 0.5$ ] with the initial condition  $\rho(x, t = 0) = |\psi(x, t = 0)|^2$  using Dirichlet conditions is shown in (d). The latter has been simulated with FiPy [317].

length of the simulation was doubled. This, of course, depends crucially on the time scale and the initial linear momentum  $p$ . The fundamental problem is that the particle does not leave the interval  $[-10, 10]$  due to the Dirichlet conditions because the probability current  $j = \Im(\psi^* \frac{\partial}{\partial x} \psi)$  vanishes at the boundaries. Hence, it is immediately clear that replacing Dirichlet with Neumann conditions will not resolve the present issue. A simple way of remedying this deficiency is, analogous to Refs. [81, 319], the introduction of a **complex absorbing potential (CAP)** of the form

$$W(x) = \begin{cases} -i\alpha(|x| - r)^2, & \text{if } |x| > r, \\ 0, & \text{otherwise,} \end{cases} \quad (\text{VI.3})$$

where  $r$  and  $\alpha \geq 0$  are adjustable parameters. The continuity equation corresponding to the probability density  $\rho = |\psi|^2$  resulting from the TDSE, Eq. (VI.1), is then complemented by a generation term, i.e.,

$$\frac{\partial}{\partial t} \rho(x, t) + \frac{\partial}{\partial x} j = 2\Im(W(x)) \rho(x, t). \quad (\text{VI.4})$$

The particle can be (partially) removed from the system if the probability density  $\rho$  is nonzero for  $|x| > r$ , where the removal of charge density is more rapid, the larger the parameter  $\alpha$ . The

time evolution of the probability density in the case of Dirichlet conditions in combination with a CAP for the parameters  $\alpha = 0.05$ ,  $r = 5$  are depicted in Fig. VI.1c. Although, the reflections are rigorously damped, they still affect the solution in the interval  $[-5, 5]$  compared to the IVP in Fig. VI.1a. In general, the parameter  $\alpha$  needs to be chosen with great care depending on the kinetic energy of the particle. If  $\alpha$  is chosen too small, the limiting case of the initial situation as seen in Fig. VI.1b will be approached. If  $\alpha$  is too large, reflections will occur at  $x = \pm r$ . Thus, there is often no alternative to an extension of the numerical interval, which is also the case in the illustration example Fig. VI.1c. For instance, the computational system size in the simulations shown in the previous chapter (see, for example, Fig. V.4) was roughly ten times larger than what is shown in the figures.

These circumstances certainly leave room for improvement, which is particularly essential for a potential extension of the level of theory to TDRDM. Indeed, there are investigations on reflection-free CAPs [265, 320–324] that were not taken advantage of in the present algorithms. Reflection-free CAPs are more complicated than the CAP in Eq. (VI.3). To give an idea of this concept consider the following. Assume that instead of adding a CAP, the TDSE is continuously transformed into a Fokker-Planck type equation in the vicinity of the boundaries. This has far-reaching consequences and shall thus be briefly demonstrated for the Fokker-Planck equation of the form

$$\frac{\partial}{\partial t}\rho(x, t) = \frac{1}{2}\frac{\partial^2}{\partial x^2}\rho(x, t) - p\frac{\partial}{\partial x}\rho(x, t). \quad (\text{VI.5})$$

Then, the probability current  $j = -\frac{1}{2}\frac{\partial}{\partial x}\rho + p\rho$  does not generally vanish at the boundaries for Dirichlet conditions. The time evolution described by the Fokker-Planck equation, depicted for comparison in Fig. VI.1d, behaves very similarly to the case of the open system as it does not exhibit reflections at the boundaries but instead allows the probability to leave the space interval  $[-10, 10]$ .

## VI.2. Discrete variable representation (DVR)

The **discrete variable representation (DVR)** is classified as a so-called pseudospectral method [325] or spectral-collocation method [326] and is, as such, one of many computational tools for discretizing **partial differential equations (PDEs)**. These classifications reflect the close relation to spectral methods, which rest upon finding the *Galerkin* solution in a specified basis set, and collocation methods, whose objective are approximate solutions that fulfill the PDE exactly at so-called collocation points. Accordingly, the DVR demonstrates conceptual similarities to both methods in the sense that both conditions are (approximately) equivalent due to a set of localized basis functions. Throughout the present and the following sections, the focus lies on the representation of operators and functions and *not* on the subsequent procedure of solving PDEs.

Scientific literature brought forth various types of DVRs [327] accompanied by different techniques of constructing the associated DVR bases. For this reason, it is difficult to give a general definition of DVR methods used in different publications such as Refs. [229, 328–330]. Nevertheless, for all DVR methods the crux of the matter is the respective DVR basis, which is composed of functions characterized by further desired properties besides orthogonality, namely the localization about discrete values of a chosen variable, often the spatial coordinates  $x$ . For the

time being, the term *localization* shall be considered as a characteristic that guarantees that local operators can be represented and evaluated at low computational cost in a good approximation, i.e., not necessarily exact. In the present scenario, the prime example of a local operator is the potential  $V(x)$ , which is then expressed as a diagonal operator in the DVR basis containing its local values on the grid associated with the localized basis functions. This preliminary definition will be rendered more precisely in the following.

For this purpose, the DVR will be presented within the general framework established in Refs. [331, 332], which were originally concerned with the extension of the DVR to multidimensional systems without limiting oneself to the trivial case of a Cartesian product. Despite the generality of the approach, the exact procedure is only given for standard DVR sets based on orthogonal polynomials.

As a first step, the Hilbert space  $\mathcal{H}$  is truncated in order to obtain a subspace  $\mathcal{S} \subset \mathcal{H}$  of finite dimension.  $\mathcal{S}$  can be chosen arbitrarily within the general DVR approach, but in the special case treated in this section it is defined by means of classical orthogonal polynomials: let  $\{p_k | k \in \{0, \dots, n-1\}\}$  be a set of classical orthogonal polynomials relative to the inner product

$$\langle f | g \rangle_\mu = \int f^* g \, d\mu = \int f^*(x) g(x) w(x) \, dx, \quad (\text{VI.6})$$

which is defined by a measure  $\mu$  or, alternatively, by its Lebesgue density<sup>3</sup> or weight function  $w(x)$ . For example, Legendre polynomials are the orthogonal polynomials with respect to the weight function  $w(x) = 1$  if  $|x| < 1$  and  $w(x) = 0$  otherwise. The support of the measure is thus  $\text{supp}(\mu) = [-1, 1]$  (cf. Ref. [336]).

Then, one obtains the truncated Hilbert space  $\mathcal{S}$  by defining its basis functions

$$\phi_k(x) := \sqrt{w(x)} p_k(x), \quad k \in \{0, \dots, n-1\}, \quad (\text{VI.7})$$

i.e.,  $\mathcal{S} := \text{span}(\{\phi_0, \dots, \phi_{n-1}\})$ . In the case of Legendre polynomials,  $\mathcal{S}$  consists of all polynomial functions up to degree  $n-1$  restricted on  $[-1, 1]$  and continued by the zero function on  $\mathbb{R}$ . Although this basis of the  $n$ -dimensional subspace  $\mathcal{S}$  is orthonormal in the usual sense, one has not yet obtained an adequate DVR basis due to lack of locality of the basis functions  $\{\phi_k\}$ . Note, however, that the original continuous problem on a Hilbert space  $\mathcal{H}$  is already converted to a discrete problem with a finite basis. Hence, one might as well stop the mathematical endeavors at this point and start with the numerical implementation by seeking the *Galerkin* solution to the respective PDE problem. This alternative approach is called spectral method [325].

As a second step, a more convenient basis comprising in a certain sense localized functions of the  $n$ -dimensional subspace  $\mathcal{S}$  is constructed, namely the DVR basis. One interpretation of the DVR method pursues the idea of projecting perfectly localized functions from the original Hilbert space  $\mathcal{H}$  (approximating the Dirac delta function) onto  $\mathcal{S}$ . To this end, one defines the projection operator  $\mathbb{P}$  on  $\mathcal{H}$  as

$$\mathbb{P} := \sum_{k=0}^{n-1} |\phi_k\rangle \langle \phi_k| \quad (\text{VI.8})$$

<sup>3</sup>In the following, a compact notation for integrals will be used which is common in measure theory [333] or probability theory [334, 335]. Nevertheless, no deeper insights in these subject areas are required from the reader.

by making use of the known orthonormal basis of  $\mathcal{S}$  from Eq. (VI.7). One can now generate  $n$  basis functions localized about grid values  $x_k$  ( $k = 0, \dots, n-1$ ) of the form  $\varphi_k(x) \propto \mathbb{P}(\delta(x - x_k))$  for adequate grid values. Constructing an orthogonal basis in this manner has the advantage that it automatically fulfills the so-called interpolation property

$$\langle \varphi_k | \varphi_m \rangle = \varphi_m(x_k) \stackrel{!}{=} \delta_{mk} v_m, \quad v_m > 0 \quad \forall k, m \in \{0, \dots, n-1\}, \quad (\text{VI.9})$$

and vice versa, i.e., the interpolation property and orthogonality condition are equivalent (cf. Ref. [332, Sec. III]). In light of the various situations and geometries one is facing when developing a generic discretization technique for PDEs, finding appropriate grid values (which satisfy Eq. (VI.9)) is anticipated to be the most complicated part in constructing the DVR basis for the general multidimensional case.

For the present case of orthogonal polynomials, the situation is substantially easier: one can simply choose the  $n$  pairwise distinct zeros of  $p_n$  in  $\text{supp}(\mu)$  (cf. [337, p. 438]). Then, one can write the DVR basis explicitly as

$$\mathcal{B}_{\text{DVR}} = \left\{ \varphi_k(x) = \frac{\mathbb{P}(\delta(x - x_k))}{\|\mathbb{P}(\delta(x - x_k))\|} \mid x_0 < x_1 < \dots < x_{n-1} \text{ roots of } p_n \right\}. \quad (\text{VI.10})$$

The interpolation property Eq. (VI.9) (and thus also the orthogonality) for this choice of grid values can be verified using the Christoffel-Darboux formula [337, p. 438].

As an alternative to the expression in Eq. (VI.10), the decisive restrictions resulting from the interpolation property Eq. (VI.9) can be exploited as follows. One can easily conclude that the DVR basis functions are of the form  $\sqrt{w(x)}p(x)$  where  $p$  is a polynomial of degree  $\deg(p) = n-1$  with given roots. This is sufficient information to uniquely construct the basis functions by means of Lagrange polynomials.

As indicated above, the DVR method is characterized by its simple representation of local operators due to the locality of the DVR basis functions. For a closer understanding, one may analyze this feature from the perspective of a Gaussian quadrature formula. Interestingly, there is a related Gauss quadrature formula for each set of classical orthogonal polynomials with  $n$  nodes given by the grid values  $x_k$  chosen above [338, p. 236 et seq.]. This quadrature rule is exact for polynomials of degree  $\leq 2n-1$  and can be defined in terms of a discrete measure

$$\eta = \sum_{i=0}^{n-1} w_k \delta(x - x_k), \quad (\text{VI.11})$$

where  $w_k$  are the associated weights.

Analogous to Eq. (VI.6), one can define a corresponding inner product  $\langle \cdot, \cdot \rangle_\eta$  on  $\mathcal{S}$ . Note that the inner product  $\langle \cdot, \cdot \rangle_\eta$  is identical to the usual inner product for elements in  $\mathcal{S}$ , so the basis functions are orthonormal with respect to the inner product  $\langle \cdot, \cdot \rangle_\eta$  on  $\mathcal{S}$  and in the usual sense. For functions  $f \notin \mathcal{S}$ , the sesquilinear form  $\langle \cdot, \cdot \rangle_\eta$  features only the properties of a positive-semidefinite Hermitian form. Thus, one can replace local operators *approximately* by a diagonal operator, because each basis function contributes to the approximated integral only on its associated grid point. For instance, the matrix element of the operator  $\hat{V}$  corresponding to the potential  $V(x)$  is approximated by

$$\langle \varphi_m | \hat{V} | \varphi_k \rangle \approx \langle \varphi_m | \hat{V} | \varphi_k \rangle_\eta = \delta_{mk} V(x_k).$$

Note, however, that  $\hat{V}$  does not define an endomorphism on  $\mathcal{S}$  in most cases, i.e.,  $\hat{V}\mathcal{S} \not\subseteq \mathcal{S}$ . Hence, projecting on  $|\varphi_m\rangle$  implies an additional approximation. Then again, differential operators such as the operator for the kinetic energy can be evaluated exactly for Legendre DVR because, in this case,  $\mathcal{S}$  is an invariant subspace *and* the degree of the polynomial integrand does not increase.

### VI.3. Lobatto DVR

For a natural treatment of nonzero boundary conditions, the Lobatto DVR from Manolopoulos and Wyatt (1988) [329] is appropriate because it involves grid values which are directly located on the boundaries of the interval. Though being based on orthogonal polynomials, the so-called Lobatto polynomials<sup>4</sup>, the Lobatto DVR is not a mere special case of the DVR for orthogonal polynomials discussed in the previous section. The noteworthy difference is a slight modification which is required to enforce grid values at the boundary. This matter will be analyzed more precisely in the following.

In preparation for the construction of the Lobatto DVR, one should consider the following explicit formula of the Lobatto polynomials:

$$L_n(x) = \frac{d}{dx} P_{n+1}(x), \quad (\text{VI.12})$$

where  $P_m(x)$  is the Legendre polynomial of degree  $n$ , which can be evaluated according to Rodrigues' formula [337, p. 442]

$$P_n(x) = \frac{1}{2^n n!} \frac{d^n}{dx^n} [(x^2 - 1)^n]. \quad (\text{VI.13})$$

Now, the Lobatto DVR basis is constructed by starting right with condition from Eq. (VI.9), where the grid points are chosen according to the Gauss-Lobatto (GL) quadrature [340]. Analogous to Eq. (VI.11) one defines a discrete measure  $\mathcal{L}$  associated with the Lobatto DVR:

$$\mathcal{L} = \sum_{i=0}^{n-1} w_i \delta(x - x_i), \quad (\text{VI.14})$$

where the  $n$  GL points  $x_0 < x_1 < \dots < x_{n-1}$  are the roots of  $(1 - x^2) L_{n-2}(x)$  and the corresponding GL weights are given by

$$w_i = \frac{2}{n(n-1)[P_{n-1}(x_i)]^2} > 0 \quad (\text{VI.15})$$

Explicit analytic expressions for the GL points for small  $n$  are listed in the appendix, Table B.1. The approach from the previous section by contrast suggests to use the roots of  $L_n(x)$  as grid

<sup>4</sup>Lobatto polynomials are orthogonal polynomials relative to the measure  $\mu$  with the Lebesgue density  $w(x) = (1 - x^2)$  for  $x \in \text{supp}(\mu) = [-1, 1]$  (cf. [339, Appendix A]).

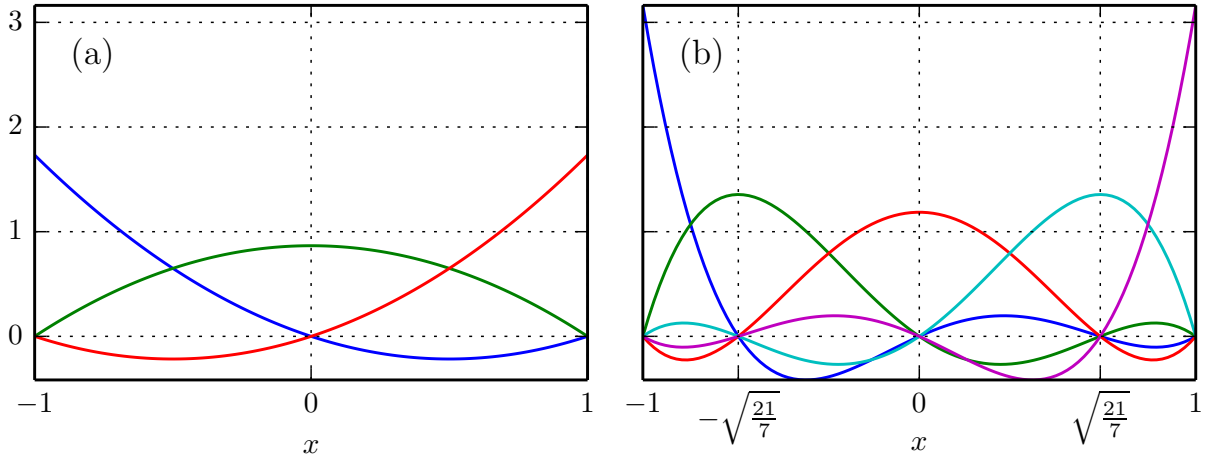


**Figure VI.2.:** DVR basis functions for  $n = 3$  (a) and  $n = 5$  (b). In both cases,  $\varphi_0$  is depicted in blue,  $\varphi_1$  in green,  $\varphi_2$  in red, etc.

values. This inconsistency will have consequences for the associated quadrature formula, which turns out to be similar to the Gauss-Legendre quadrature [337, p. 80]. Analogously to the Legendre DVR, one chooses  $\mathcal{S}$  to consist all polynomials of degree  $\leq n - 1$  and then constructs the DVR basis functions according to Eq. (VI.9) as Lagrange polynomials:

$$\varphi_m : [-1, 1] \rightarrow \mathbb{R}, \quad \varphi_m(x) = \frac{1}{\sqrt{w_m}} \prod_{k \neq m} \frac{x - x_k}{x_m - x_k} \quad (\text{VI.16})$$

Then, let the DVR basis of  $\mathcal{S}$  be denoted by  $\mathcal{B}_{\text{DVR}} = \{\varphi_m | m = 0, \dots, n-1\}$ .

Examples of Lobatto DVR basis functions are shown in Fig. VI.2 for very small subspaces  $\mathcal{S}$  of dimension  $n = 3$  and 5. Most striking with regard to the postulated locality of the basis functions is that all of them in both Figs. VI.2a and b are spread over the whole interval,  $\text{supp}(\varphi_m) = [-1, 1]$ . Being aware of the numerical values of grid points (cf. Table B.1 for a table of grid values), one can uniquely assign each basis function to an associated grid point because only one basis function is nonzero at each grid point. Observe that for both cases depicted in Figs. VI.2a and b the property  $\varphi_m(x) = \varphi_{n-m}(-x)$  is fulfilled. This is a general rule for all  $n$  because the symmetry of the Legendre and Lobatto polynomials in Eqs. VI.12 and VI.13 induces a symmetry for GL points and weights, i.e.,  $x_i = -x_{n-1-i}$  and  $w_i = w_{n-1-i}$  and likewise for the basis functions according to Eq. (VI.16).

Stemming from the modifications regarding the boundary conditions, the discrepancies between the DVR described in the previous section and the Lobatto DVR are briefly analyzed. For this purpose, one compares the quadrature formula based on classical orthogonal polynomials with Lobatto's integration formula (also referred to as GL quadrature) from ([341, p. 888])

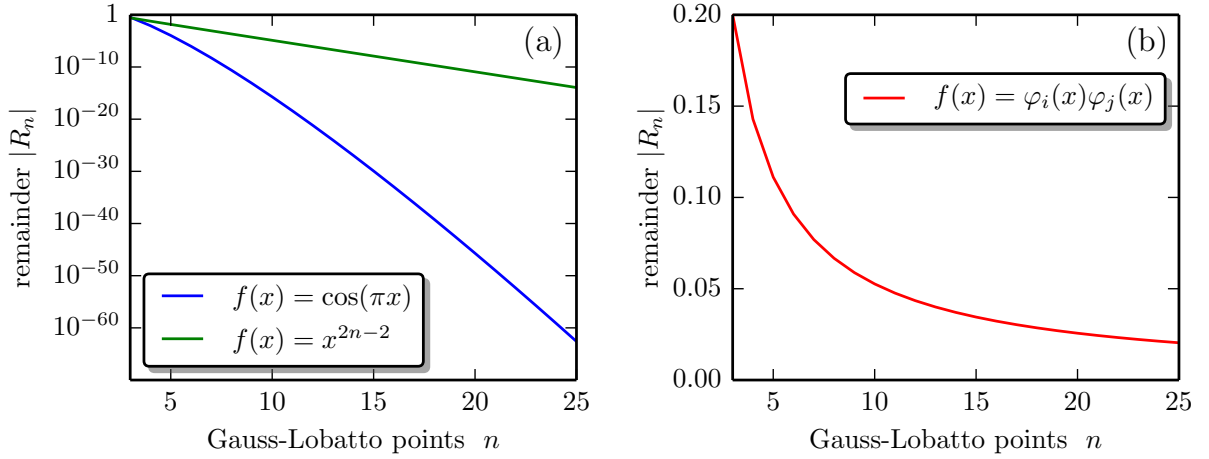


**Figure VI.3.:** Remainder  $R_n$  from Eq. (VI.18) for different functions to illustrate the qualitative behavior of approximation errors. Note that  $R_n$  does not depend on  $\xi$  for polynomials of degree  $\leq 2n - 2$ . (a) In the case of  $f(x) = \cos(\pi x)$ , the unknown parameter  $\xi$  is chosen to maximize the absolute value of  $R_n$ . (b) Likewise, the remainder  $R_n$  is shown for indices  $i, j$  that maximize the absolute value of  $R_n$ .

including the remainder  $R_n$ :

$$\int_{-1}^1 f(x) dx = \int f(x) d\mathcal{L}(x) + R_n, \quad (\text{VI.17})$$

$$\text{where } R_n = \frac{-n(n-1)^3 2^{2n-1} [(n-2)!]^4}{(2n-1)[(2n-2)!]^3} f^{(2n-2)}(\xi), \quad (-1 < \xi < 1) \quad (\text{VI.18})$$

In this case, the weight function  $w(x)$  does not appear in the integral of the left-hand side of Eq. (VI.17), making Lobatto's integration formula very similar to the Gauss-Legendre quadrature, as stated above. As a result, the preceding choice of  $\mathcal{S}$  becomes plausible even though the general treatment suggested to include the factor  $\sqrt{w(x)}$ .

However, compared to the Gauss-Legendre formula, one pays the price for fixing the two grid values at the boundary by reducing the accuracy of the quadrature formula. To be specific, the  $n$ -point quadrature formula integrates only polynomials of degree  $2n - 3$  exactly, whereas the  $n$ -point Gauss-Legendre formula is exact for polynomials of degree  $2n - 1$ . Hence, inner products on  $\mathcal{S}$ , which have integrands of degree up to  $2n - 2$  are not evaluated exactly. As a consequence, the DVR basis of Eq. (VI.16), which was chosen to be orthonormal with respect to the inner product  $\langle \cdot, \cdot \rangle_{\mathcal{L}}$  on  $\mathcal{S}$  defined by the GL quadrature, is only approximately orthogonal with respect to the usual inner product.

To have a quantitative estimate of the approximation introduced by the GL quadrature, some examples of the remainder are shown in Fig. VI.3. For a bounded function such as  $f(x) = \cos(\pi x)$ , which can be well approximated by a polynomial of finite degree within the interval  $[-1, 1]$ , one obtains exponential convergence as can be seen in Fig. VI.3a. The remainder for  $f(x) = x^{2n-2}$  behaves qualitatively similarly, albeit strongly reduced in accuracy. This is due to the sharp increase of  $f^{(2n-2)}(\xi) = (2n - 2)!$  with  $n$ . For the evaluation of inner products on  $\mathcal{S}$ , the function  $f(x) = x^{2n-2}$  plays a special role for being proportional to the only occurring

term that is not integrated exactly. Assessing the discrepancies between orthogonality in the sense of  $\langle \cdot, \cdot \rangle_{\mathcal{L}}$  and the usual inner product  $\langle \cdot, \cdot \rangle$ , one has to take into account that the coefficient of the term  $x^{2n-2}$  grows with an increasing number of **GL** points since the sum of all weights  $w_i$  is required to be equal to 1 (cf. Eqs. VI.15 and VI.16). The result is a rather poor convergence in Fig. VI.3b in comparison to the examples shown in Fig. VI.3a. It should be mentioned that in spite of these deviations from the usual inner product,  $\langle \cdot, \cdot \rangle_{\mathcal{L}}$  fulfills all characteristics of an inner product on  $\mathcal{S}$ . Hence, the linear independence of the basis functions in Eq. (VI.16) is guaranteed for all  $n$ .

In summary, the Lobatto **DVR** can be defined by its standard representation

$$\phi_{\mathcal{B}_{\text{DVR}}} : \mathcal{S} \rightarrow \mathbb{C}^n, \quad p(x) \mapsto \sum_{i=0}^{n-1} \hat{e}_i \langle p, \varphi_i \rangle_{\mathcal{L}} = \sum_{i=0}^{n-1} \frac{p(x_i)}{\sqrt{w_i}} \hat{e}_i, \quad (\text{VI.19})$$

where  $\hat{e}_k$  is the  $k$ -th element of the standard basis of  $\mathbb{C}^d$ . In the following, this mapping will be continued on  $\mathcal{H}$  as given in Eq. (VI.19) if required. Hence,  $\phi_{\mathcal{B}_{\text{DVR}}}^{-1} \circ \phi_{\mathcal{B}_{\text{DVR}}}$  may also be a projection operator on  $\mathcal{H}$  which projects upon the subspace  $\mathcal{S}$ .

Then, local operators on  $\mathcal{S}$ , such as  $\hat{V}$ , are straightforwardly represented by matrices on  $\mathbb{C}^d$  with matrix elements according to

$$V_{km} := \left( \phi_{\mathcal{B}_{\text{DVR}}} \circ \hat{V} \circ \phi_{\mathcal{B}_{\text{DVR}}}^{-1} \right)_{km} = \langle \varphi_k, V \cdot \varphi_m \rangle_{\mathcal{L}} = \delta_{km} V(x_k).$$

Again, this involves an approximation since  $\hat{V}$  is not an endomorphism on  $\mathcal{S}$ , i.e., it requires the use of the continuation of  $\phi_{\mathcal{B}_{\text{DVR}}}$ . Analogously, differential operators can be evaluated exactly, e.g.,

$$D_{km} := \left( \phi_{\mathcal{B}_{\text{DVR}}} \circ \frac{\partial}{\partial x} (x) \circ \phi_{\mathcal{B}_{\text{DVR}}}^{-1} \right)_{km} = \langle \varphi_k, \frac{\partial}{\partial x} \varphi_m \rangle = \langle \varphi_k, \frac{\partial}{\partial x} \varphi_m \rangle_{\mathcal{L}} = \sqrt{w_k} \varphi'_m(x_k), \quad (\text{VI.20})$$

because  $\mathcal{S}$  is an invariant subspace of  $\frac{\partial}{\partial x}$ . Besides, matrix elements are identical for both inner products due to the reduction of the integrand to a polynomial of degree  $2n-3$ .

Note that  $D_{km}$  is not strictly a skew-symmetric matrix because not all basis functions are zero at the boundaries. To be specific,  $D_{km}$  is a skew-symmetric matrix with exception of the two entries  $D_{00} = -D_{n-1, n-1} \neq 0$ ; for all other diagonal entries,  $D_{mm} = 0 = \sqrt{w_k} \varphi'_m(x_m)$  is valid. Graphically speaking, each *inner DVR* basis function has a local extremum at the associated grid point. This can be examined for the special cases  $n=3$  and  $5$  in Fig. VI.2. In this context, it should be mentioned that both the derivation and the kinetic energy operator are represented by dense matrices even though the **DVR** is designed to be local. For instance, each inner basis functions in Fig. VI.2 contributes to the derivation at every grid point distinct from its associated grid point. This observation holds for all  $n$  and is easily verified by a proof by contradiction: assume that a **DVR** basis function, i.e., a polynomial of degree  $n-1$  with  $n-1$  pairwise distinct zeros, has an extreme value at a grid point distinct from its associated grid point. Then, the multiplicity of this root has to be at least 2, which implies that the degree of the polynomial basis function is at least  $n$ . This is inconsistent with the definition of the basis, thus proving the claim.

Therefore, apart from relatively sparse matrix representations of the kinetic energy operator for direct product **DVRs** in the multidimensional case [327, 330], the **DVR** method involves

dense matrices. Dense matrices are very troublesome with regard to a parallel implementation of the algorithm (cf. page 75). For this reason, the Lobatto DVR method will be generalized in the following section in order to obtain sparse matrix representations for differential operators even in the 1d case.

## VI.4. Finite-element DVR (FEDVR)

The DVR discretization techniques described in the previous sections, Secs. VI.2 and VI.3, provide a diagonal representation of local operators but a dense representation of differential operators in 1d. One can achieve a sparse representation for both types of operators by constructing basis functions that have a small support compared to the domain to be discretized. This procedure is a fundamental idea behind the well-known finite element method (FEM) (see, e.g., [314]). In the following, this concept of the FEM will be emulated to improve the DVR method by ensuring a sparse representation of the Hamiltonian. One proceeds as follows. After dividing the domain (interval) into a collection of small subdomains (subintervals), one applies the Lobatto DVR on each of the subdomains while taking the communication of data between the subdomains into account by using suitable boundary conditions<sup>5</sup>. This method is employed in Refs. [4, 223, 232, 233, 255, 318, 342–345] for 1d and 3d systems. Accordingly, this technique will henceforth be called finite-element discrete variable representation (FEDVR). As the concept of the FEM is considerably more widespread than the DVR method, this section will be far less extensive than the previous sections. The recipe for constructing the FEDVR basis will be presented in conjunction with the resulting nonzero structure of the matrix which represents the Hamiltonian. This is in general a very helpful information for testing the implementation.

Let the interval of interest  $[a, b]$  be arbitrarily divided into  $n_e$  subintervals  $[x^i, x^{i+1}]$  where  $x^0 = a$  and  $x^{n_e-1} = b$ . Further, let  $M_i := \frac{1}{2}(x^{i+1} + x^i)$  be the center and  $s_i = \frac{1}{2}(x^{i+1} - x^i)$  be the scaling factor of the  $i$ -th interval with respect to the original interval  $[-1, 1]$ . On each subinterval, one constructs a  $n_g$  dimensional Lobatto DVR from Eq. (VI.16) via scaling and translation

$$\varphi_m^i : [a, b] \rightarrow \mathbb{R}, \quad \varphi_m^i(x) = \begin{cases} \varphi_m\left(\frac{x-M_i}{s_i}\right), & \text{if } x \in [x^i, x^{i+1}], \\ 0, & \text{otherwise.} \end{cases} \quad (\text{VI.21})$$

One can now easily define the continuous and normalized FEDVR basis functions in terms of the  $\varphi_m^i$ . For  $(i, m) \in I := (\{0, \dots, n_e - 1\} \times \{0, \dots, n_g - 2\}) \setminus \{(0, 0)\}$ , one writes

$$\chi_m^i(x) = \begin{cases} \frac{1}{\sqrt{s_{i-1}+s_i}} \left( \varphi_{n_g-1}^{i-1}(x) + \varphi_0^i(x) \right), & \text{if } m = 0 \wedge i \neq 0, \\ \frac{1}{\sqrt{s_i}} \varphi_m^i(x), & \text{otherwise.} \end{cases} \quad (\text{VI.22})$$

Correspondingly, the FEDVR basis is defined as  $\mathcal{B} := \{\chi_m^i(x) \mid (i, m) \in I\}$ . Note that the DVR functions localized about the same value of adjacent intervals are merged into one continuous basis function. The DVR functions localized at the boundary of the global interval are dropped, which complies with Dirichlet boundary conditions.

<sup>5</sup>Recall that the Lobatto DVR was constructed for an easy implementation of boundary conditions.

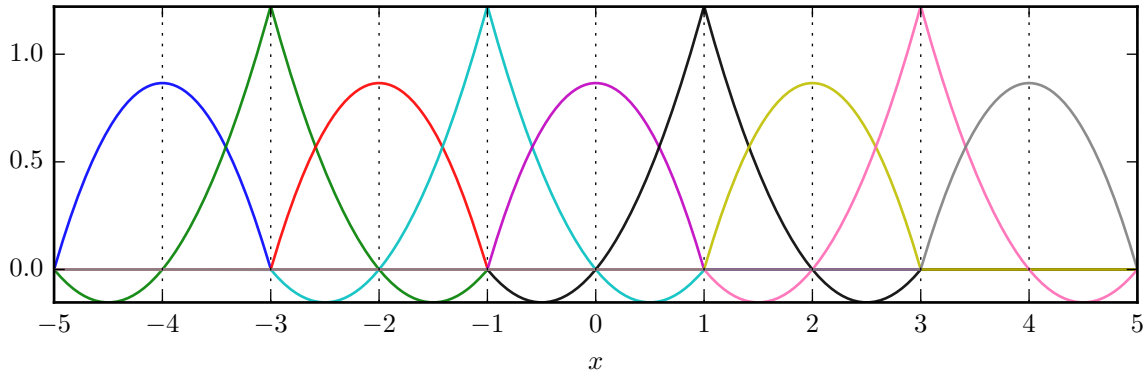


**Figure VI.4.:** Small FEDVR basis for  $n_g = 3$  and  $n_e = 10$  in the interval  $[-5, 5]$  with equally spaced boundaries of subintervals  $x^i \in \{\pm 1, \pm 3, \pm 5\}$ . The basis comprises 9 functions, which have zeros at each grid point with one exception. Each basis function is identified with the grid point at which it has a nonzero value:  $\chi_1^0$  (blue) is localized around  $x = -4$ ,  $\chi_1^1$  (green) around  $x = -3$ , etc. This small basis is not used in practice; it is shown for illustrative purposes only.

An example of a very small FEDVR basis is depicted in Fig. VI.4. The interval size is constant, and thus the scaling factor is trivially  $s_i = 1$  for all intervals. Therefore, the FEDVR basis essentially consists of the shifted DVR basis functions from Fig. VI.2a. Adopting the term of Balzer et al. (2010) [232], the merged FEDVR basis functions localized at the boundaries of the intervals are called *bridge functions*. In this special case, the bridge functions are, according to Eq. (VI.22), scaled in value by  $\frac{1}{\sqrt{2}}$  with respect to the DVR basis Fig. VI.2a to ensure normalization of the resulting bridge function. Moreover, one shall keep in mind that the bridge functions are obviously not differentiable at the associated grid point. This has further implications: firstly, regarding the representation of functions within the FEDVR, differentiable functions in the Hilbert space  $\mathcal{F} := \text{span}(\mathcal{B})$  spanned by the FEDVR are not arbitrary linear combinations of basis functions. This means that one might be restricted to subspaces such as  $\mathcal{F} \cap C^1([a, b])$  for certain purposes. Secondly, regarding the representation of operators within the FEDVR, differential operators are only well-defined on the subspace of “well-behaved” functions in  $\mathcal{F}$ . Consequently, differential operators do not have a unique continuation on  $\mathcal{F}$ . This ambiguity is, however, rather commonplace than irritating if one is accustomed to the finite difference method (FDM).

Analogous to the previous sections, Secs. VI.3 and VI.2, one can define a quadrature rule and likewise an inner product on  $\mathcal{F}$  by making use of the following discrete FEDVR measure

$$\mathcal{D} = \sum_{(i,m) \in I} w_m^i \delta(x - x_m^i), \quad (\text{VI.23})$$

where  $x_m^i := s_i x_m + M_i$  are the FEDVR grid points and  $w_m^i$  are FEDVR grid weights defined by  $w_m^i := (\chi_m^i(x_m^i))^{-2}$ .

The corresponding quadrature formula can be obtained from Eq. (VI.17) by splitting the interval into subintervals and transforming all arising integrals into integrals of the form Eq. (VI.17). As usual, the basis functions from Eq. (VI.22) are orthonormal with respect to the inner product  $\langle \cdot, \cdot \rangle_{\mathcal{D}}$ . Before presenting the utilized standard representation, which determines the nonzero



$$\text{where } D_{mk}^{\text{loc}} = \sqrt{w_k w_m} \int_{-1}^1 \varphi_k(x) \varphi'_m(x) dx. \quad (\text{VI.27})$$

In general, the nonzero diagonals of  $D_{mk}^{\text{loc}}$  (cf. the derivation operator in the **DVR**) cancel each other out, thus generating a skew-symmetric matrix due to Dirichlet boundary conditions. For test purposes, there is an instructive example for differential operators in App. B.3.3. It is also shown that in this special case, the **FEDVR** can be reduced to a nontrivial **FDM**, which may be more intuitive for the reader.

The matrix representing the kinetic-energy operator can be chosen to have the same nonzero structure as the derivation operator in Eq. (VI.26) except for the diagonal. This is shown in App. B.3.2, expressed in simpler terms as in the original publications [232, 233] without loss of generality. It is worth mentioning that the matrix for the kinetic energy is *not* utilized in the form  $\frac{1}{2}D^T D$  or  $-\frac{1}{2}D^2$  because, first, there is a sparser representation and, second, problems due to finite floating-point precision can be mitigated (see also Sec. VI.5).

The **FEDVR** provides sparse representations of the relevant operators in a very flexible way, allowing for an arbitrary enhancement of the local accuracy (increase  $n_g$ ) at the expense of sparsity. On a side note, the dense matrices appearing in the orbital form of the **TDHF** equation Eq. (II.2) due to the nonlocal exchange operator do not necessarily mean that the **DVR** is preferable over the **FEDVR** because a dense matrix is involved anyway<sup>6</sup>. Common time-propagation algorithms may distinguish between terms with different properties, so one can still benefit from the sparsity (cf. the ensuing section).

## VI.5. Numerical time propagation

Various numerical time propagation schemes have been established to cover a broad spectrum of applications as documented by the abundant literature on this subject [346, and references therein], implying that a complete overview would certainly go beyond the scope of the present thesis. Nevertheless, it is intended to outline the principles behind the techniques which proved to be useful while providing a wider context to briefly demonstrate their superiority over alternative methods. For the sake of brevity, emphasis is placed on pointing out selected non-obvious issues to give the reader an intuition rather than to develop a consistent mathematical formalism. Subsequently, reference is made to the potential solutions without explaining them in detail.

Being confronted with memory limitations, Kaiser (2014) [4] suggested to implement the **TDRDM** approach on a distributed memory machine, which is generally accompanied by severe additional programming effort because all algorithms –if sufficiently suited for parallelization at all– have to be adapted. As runtime is also an issue, one strives for so-called *scalable* algorithms, i.e., algorithms that are characterized by the *ideal* speedup  $S(p) := T_{\text{sim}}(1) / T_{\text{sim}}(p) = p$ , where  $T_{\text{sim}}(p)$  is the runtime of the program on  $p$  processors [347, 348]. In simple words,  $p$  times as many processors ideally are  $p$  times as fast. On a side note, the cases of superlinear speedup

<sup>6</sup>In addition, the **DVR** potentially produces sparse matrices in the multidimensional cases of Eq. (II.1) and the **TDRDM** (as stated above).

$S(p) > p$  occurring rarely in practice due to cache effects are, though frequently reported in the literature [347, 349], not discussed here. For clarification of the technical aspects, it should be mentioned that all parallelized algorithms were implemented based on MPI [350, 351] with parallel I/O achieved by means of the HDF5 library [352]. MPI can be considered as a quasi-standard [353] and, similarly, HDF5 is widely spread<sup>7</sup> and proven to be very efficient [355].

It is instructive to begin with an illustrative example that is reduced to its essentials. Consider the 1d heat equation as a simple parabolic PDE to be solved with a FDM. For demonstration purposes, the FDM is deliberately preferred over the FEDVR because the latter is more complicated and it shall be emphasized that this problem is not exclusive to the FEDVR. Now assume that a corresponding initial value problem is numerically solved via the  $\theta$ -method [346, p. 35 et seqq.], which includes the (forward/explicit) Euler ( $\theta = 0$ ), backward/implicit Euler ( $\theta = 1$ ), and the Crank-Nicolson (CN) ( $\theta = \frac{1}{2}$ ) method as special cases. It is very important to note that Euler and backward Euler are both consistent of order 1 but exhibit completely different stability properties, which clearly manifests itself in the practical applications. Although it is not intended to repeat findings already well established in textbooks, it shall be made clear that and why one *never* should use Euler – not even for testing purposes. Despite using very small time steps, one will often not obtain convergent results. The underlying issue is demonstrated by means of Fig. VI.5, which focuses on one of the many problems one may experience when using Euler. Let  $g(x) = \exp(-\frac{1}{2}x^2)$  be the initial state at time  $t = 0$  stored on a finite grid (see caption for details), and let  $\Delta_d$  be the standard second-order central difference that is very common in the FDM for parabolic problems [314, 356]. The time-dependent solution  $g(x, t)$  at time  $t$  after  $n$  steps obtained of the Euler method is then written in a somewhat sloppy notation as

$$g(x, t) = \left(1 + \frac{t}{n}\Delta_d\right)^n \exp\left(-\frac{1}{2}x^2\right). \quad (\text{VI.28})$$

Hence, many consecutive numerical derivations, as seen in Fig. VI.5, are evaluated, which are subject to an rapidly growing error due to the finite discretization and the finite floating-point precision. Interestingly,  $\Delta_d^2 g$  perfectly estimates the analytical solution on the scale of Fig. VI.5 but is in fact subject to numerical noise, i.e., small fluctuations between adjacent grid points. If a subsequent numerical derivation is applied to obtain  $\Delta_d^3 g$ , the procedure yields an approximate to the derivative of the noise and not of the smooth curve  $\Delta_d^2 g$ . Crucially depending on the discretization in space, the emergence of large errors very likely leads to divergent results. This is in strong contrast to ODEs of the form  $y' = f(t, y)$  where the numerical evaluation of the “right-hand side” function  $f(t, y)$  is virtually exact. In the case of Fig. VI.5, the finite floating-point precision is of paramount concern, whereas increasing the consistency order does not mitigate the situation [not shown]. Regarding the region of absolute stability, the Euler method is anticipated to be even worse for the TDSE [338, p. 284 et seqq.].

In sharp contrast, the backward Euler method is *L-stable* [346, p. 146], i.e., it introduces numerical damping. Accordingly, there is, due to limited floating-point precision, a decisive difference between the forward and backward Euler method in practice even though both methods are consistent of the same order. There is an important lesson to learn from this: consistency is not everything. Nevertheless, the CN scheme is often more attractive because it is only *A-stable*,

<sup>7</sup>also for XFEL data in SFX experiments [354]

i.e., it induces no artificial damping, and is consistent of order 2. Note, however, that L-stability can prove advantageous in certain cases. For a formal definition of A- and L-stability see, e.g., Ref. [357, p. 40 et seqq.]. The situation is somewhat intuitive in the sense that the inverse of the discretized derivation operator can be associated with integration, which, in turn, exhibits a smoothing property [358, 359].

Likewise, explicit propagation methods within the FEDVR are facing the same intrinsic problem. One might conjecture that this can be avoided within the FEDVR by increasing  $n_g$  and lowering  $n_e$  at the expense of the locality of the derivation operator as outlined above in Eq. (VI.26). However, this idea, analogous to the attempted solution in the FDM based on increasing the consistency order of the derivation operator, does not resolve the present issue.

For practical calculations the computational toolkits PETSc [316] and SLEPc [360] were utilized. Here, one follows the philosophy behind PETSc that allows for choosing various numerical time-propagation schemes via runtime options because it is often too time-consuming to investigate beforehand which algorithm best matches the respective problem. This philosophy applies in particular to the deeper level of the implicit methods concerned with the solution the underlying sparse linear systems. Accordingly, many different numerical approaches have been tested and proven useful, including purely explicit methods such as those described in the following.

The utility of well-established embedded Runge-Kutta (RK) formulae has been investigated, which are in each case associated with three integers. One of them is number of *stages*, which is related to the number of evaluations of the “right-hand side” per time step (but is not necessarily identical due to standard optimizations [361, p. 167]). A precise definition of the term *stages* of an explicit RK method can be found in Ref. [361, p. 134]. Then, using the notation from Ref. [361, p. 166], one characterizes an embedded RK method of order  $n(m)$  by the property that it consists of a scheme of order  $n$  and an error estimator of order  $m$  and therewith specifies the remaining two integers. The following embedded RK schemes have been tested: the Bogacki-Shampine (RK3BS) method of order 3(2) with four stages, the Fehlberg (RK5F) of order 4(5) with six stages, and the Dormand-Prince (RK5DP) method of order 5(4) with seven stages. It is interesting to note that for the calculations performed in the course of Chapter V, RK3BS significantly outperformed both the RK5F and RK5DP method with respect to the requirements in computational runtime and iterations. This is related to the numerical phenomenon seen above in Fig. VI.5 because the performance deteriorates upon increasing the order. However,

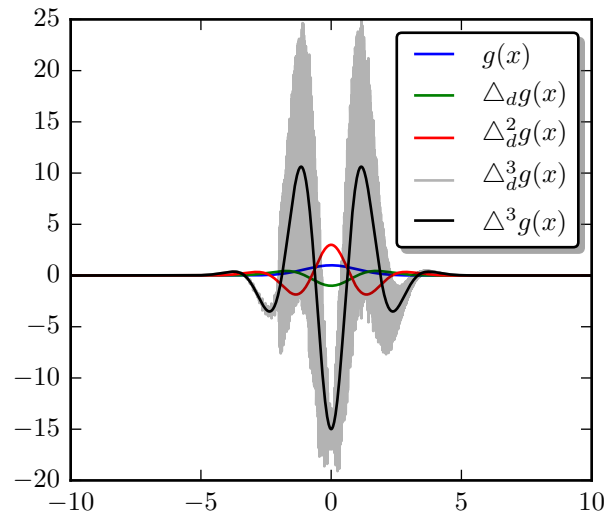


**Figure VI.5.:** The function  $g(x) = \exp(-\frac{1}{2}x^2)$  and its discrete derivations with double-precision floating-point numbers on a uniform grid of 6000 points on the interval  $[-10, 10]$  using the standard second-order central difference. With the discrete method failing dramatically for  $\Delta_d^3 g$ , the analytic solution  $\Delta^3 g$  is shown as well.

this conclusion is of course not universal as it depends on the grid spacing, so the situation can change considerably for a different photon energy, which may produce faster photoelectrons and thus require a finer numerical grid.

Moreover, **strong stability-preserving (SSP)** or **total variation diminishing (TVD)** time discretization methods [362–364] have been tested to meet a practicality comparable to the embedded **RK** methods. **SSP/TVD** methods fulfill the **TVD** property<sup>8</sup>, i.e., the methods avoid artificial oscillatory behavior even for problems with discontinuous solutions. Interestingly, the explicit Euler method maintains the **TVD** property for sufficiently small time steps as proven in Ref. [346, p. 226 et seqq.] followed by an example why one should still not use this method but rather its extensions.

The **split-operator (SO)** technique reliably produced convergent results in **1d TDSE** calculations at high runtime performance without a trial-and-error search for adequate parameters even for the inexperienced user. The basic concept of the **SO** method is the decomposition of matrix exponentials [342, 346, 365–367] according to

$$\psi(x, t + \delta t) = \exp(-iV(t + \delta t) \frac{\delta t}{2}) \exp(-iT\delta t) \exp(-iV(t) \frac{\delta t}{2}) \psi(x, t) + \mathcal{O}(\delta t^3), \quad (\text{VI.29})$$

where  $\psi(x, t)$  is the time-dependent solution to the **TDSE** described by the Hamiltonian  $H(t) = T + V(t)$  with the kinetic operator  $T$ , whose **FEDVR** representation is a matrix with the structure from Eq. (VI.26), and a time-dependent potential term  $V(t)$ , which is represented by a diagonal matrix. On the one hand, numerically evaluating the matrix exponential of the diagonal matrices and the subsequent matrix-vector multiplication is computationally inexpensive, and there is thus no need for further discussion of these terms. On the other hand, the straightforward calculation of the term  $\exp(-iT\delta t)$  yields a dense matrix, which strongly impairs the efficiency of parallelization as noted on page 75. Different strategies arose to circumvent this drawback. For example, one can proceed by splitting  $T$  into a sum of two block matrices and applying the same decomposition without affecting the consistency order [342]. However, the implementation of this approach showed that the stability was considerably reduced. Alternatively, one may use one of many algorithms to directly evaluate  $\exp(M)v$  for a sparse matrix  $M$  and a vector  $v$  [368]. Here, the algorithm from Ref. [369, p. 136 et seqq.], which is implemented in **SLEPc**, proved to be reliable and efficient for the **TDSE**, but the rapid convergence slowed down markedly for the mathematically equivalent calculations based on the **1RDM**.

In **TDHF** simulations the concept of **implicit-explicit (IMEX)** methods [346, 370–372] is favorable because it allows to distinguish terms of the dynamical equations according to their stiffness, i.e., their suitability for a numerical treatment with explicit methods. Accordingly, the nonlinear Fock term, which is represented by a relatively dense matrix<sup>9</sup> in **FEDVR** (see below in Sec. VI.6), is treated as a non-stiff term.

So far, it was not addressed how the sparse linear systems appearing in, e.g., the **IMEX** and the **CN** method are solved. This subject area shall be merely mentioned in passing due to the availability of standard textbooks [373, 374] and implementations of various algorithms (for example, in **PETSc**) to solve such systems. It should be noted that algorithms developed for dense linear systems such as Gaussian elimination, albeit suitable for a parallel implementation

<sup>8</sup>A formal definition of the **TVD** property can be found in Refs. [346, 362].

<sup>9</sup>The corresponding matrix is, of course, not necessarily explicitly stored in memory.

[338, p. 150 et seq.], can commonly not be efficiently applied without more ado because, for instance, Gaussian elimination tends to destroy the sparsity of matrices [373]. Alternatively, iterative algorithms such as the **generalized minimal residual (GMRES)** method are frequently used despite the fact that fast convergence of **GMRES** is debatable in the general case [375].

Finally, it shall be briefly explained why the numerical eigenvalue problem is barely touched. First, the standard algorithms provided by the similar framework of **SLEPc** [360] were generally unproblematic and, second, the size of the numerical grid can be markedly reduced in ground-state calculations due to the absence of photoelectrons (see Sec. VI.1). The result can then be extrapolated to obtain the initial state on a grid appropriate for the time-dependent problem.

## VI.6. Time-dependent Hartree-Fock

For the sake of completeness, the **FEDVR** representations of the two formulations of the **time-dependent Hartree-Fock (TDHF)** theory are given without further explanation because they can be straightforwardly derived from Sec. VI.4. Using a somewhat sloppy notation, it is not explicitly distinguished between an operator  $O$  and its **FEDVR** matrix representation  $\phi_B \circ O \circ \phi_B^{-1}$  (standard representation  $\phi_B$  from Eq. (VI.25)) as the difference can be easily inferred from the context. It should be mentioned that **Hartree-Fock (HF)** calculations can alternatively be performed based on well-established toolkits such as the **GAMESS** suite of programs [376] and the **NWChem** software package [377, 378]. They were, however, not employed here from the start; primarily for the reason that an extension to **TDRDM** was aspired. In general, the numerical time propagation is similar to iterations for self-consistent solution of **HF** orbitals, so one may refer to the abundant literature on the topic of an efficient implementation of the Fock operator [379–382].

The **FEDVR** representation of the orbital formulation of **TDHF**, Eq. (II.2), for  $2N$  electrons in  $N$  doubly occupied orbitals  $\varphi_i$ ,  $i = 1, \dots, N$  reads

$$i \frac{d}{dt} \vec{\beta}^{(i)} = (H_0 - xE(t)) \vec{\beta}^{(i)} + F(\vec{\beta}^{(1)}, \dots, \vec{\beta}^{(N)}) \vec{\beta}^{(i)}, \quad (\text{VI.30})$$

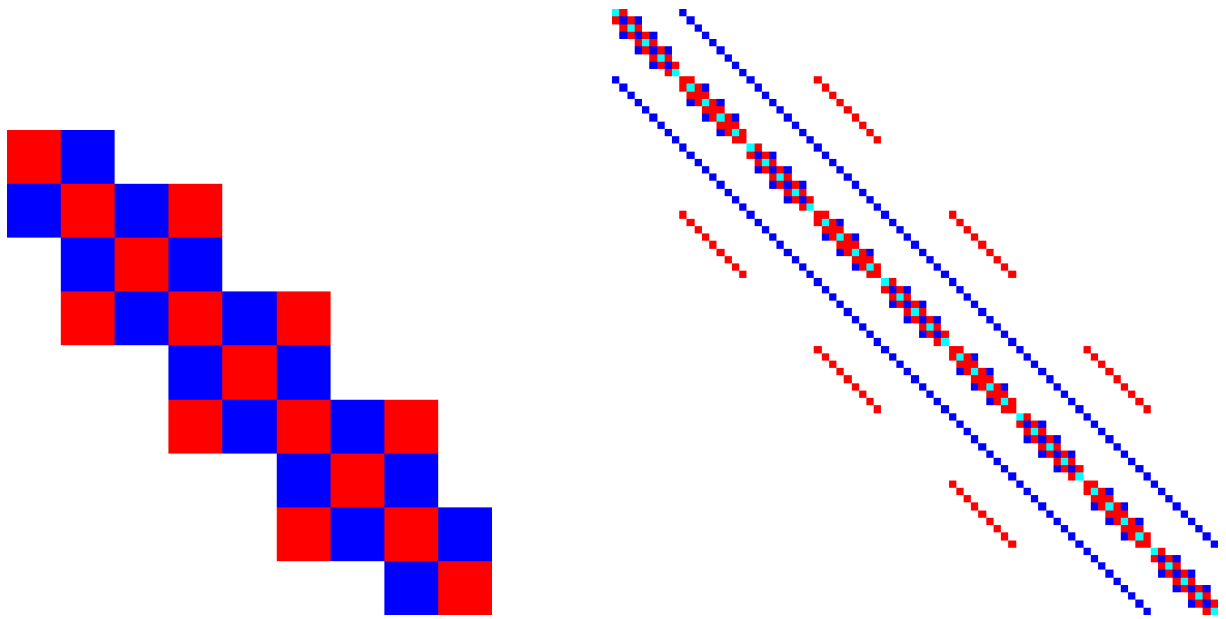
with discretized orbitals  $\vec{\beta}^{(i)} := \phi_B(\varphi_i) \in \mathbb{C}^d$ , a sparse matrix  $H_0 = T + V_{\text{core}}$  ( $T = -\frac{\partial^2}{\partial x^2}$  is sparse,  $V_{\text{core}}$  is diagonal), a diagonal matrix  $x$ , and a nonlinear term in the form of the dense **HF** matrix  $F$ . The latter is defined as

$$F_{lk}(\vec{\beta}^{(1)}, \dots, \vec{\beta}^{(N)}) = -V_{\text{ee}}(x_l - x_k) \sum_{i=0}^N (\beta_k^{(i)})^* \beta_l^{(i)} + 2\delta_{lk} \sum_{k'=0}^{d-1} V_{\text{ee}}(x_l - x_{k'}) \sum_{i=0}^N |\beta_{k'}^{(i)}|^2. \quad (\text{VI.31})$$

Obviously,  $F$  does not stem from a local operator, but still the entries of its matrix representation can typically be truncated for large  $|x_l - x_k|$ . Avoiding the explicit storage of the dense matrix, one can implement  $F$  based on matrix-free methods.

The **FEDVR** representation of the density-matrix formulation of **TDHF**, Eq. (II.1), on a Cartesian grid, i.e.,

$$\varrho(x_1, x_2) = \sum_{k,l=0}^{d-1} \gamma_{kl} \chi_k(x_1) \chi_l(x_2), \quad (\text{VI.32})$$



(a) Nonzero structure associated with the FEDVR  $d \times d$  matrix representation of the operator  $H_0$  in Eq. (VI.30).

(b) Nonzero structure associated with the FEDVR  $d^2 \times d^2$  matrix representation of the commutator with respect to  $H_0$  in Eq. (VI.33).

**Figure VI.6.:** Illustration of the nonzero structure of Jacobian matrices as produced by means of PETSc in the corresponding time-propagation schemes with respect to  $H_0$  on a very small grid with  $n_g = 3$ ,  $n_e = 5$ , and  $d = 9$ .

can be written in terms of matrices,  $(\gamma)_{kl} = \gamma_{kl}$ , namely

$$i \frac{\partial}{\partial t} \gamma = [H_0, \gamma] - E(t) [x, \gamma] + [F(\gamma), \gamma]. \quad (\text{VI.33})$$

The HF operator can be expressed as a function of the discretized density matrix  $\gamma$ :

$$F_{kl}(\gamma) = -\frac{1}{2} V_{ee}(x_k - x_l) \gamma_{kl} + \delta_{kl} \sum_{m=0}^{d-1} \gamma_{mm} V_{ee}(x_k - x_m). \quad (\text{VI.34})$$

On a side note, the Hartree-Fock-Slater (HFS) approach (see Sec. II.2, employed in 3d calculations) instead of a Hartree-Fock (HF) model generates a diagonal approximation of the HF operator, which significantly reduces the computational costs.

To apply, for instance, the IMEX methods mentioned in the previous section, it is helpful to form the sparse matrices associated with  $H_0$  or with the corresponding commutator. For illustrative purposes, the respective matrices are shown in Fig. VI.6. The matrix shown in Fig. VI.6a appears to be relatively dense at first sight, but this is attributed to the low dimension  $d = 9$ , and is thus not a practical issue. The implementation of the Jacobian matrix in time-propagation schemes corresponding to  $\gamma \rightarrow [H_0, \gamma]$  and its associated nonzero structure, as seen in Fig. VI.6b, requires a larger programming effort.

Then, the physical quantities of interest such as the occupation probability  $P_\varphi$  of an orbital  $\varphi$  can be easily calculated as

$$P_\varphi(\gamma) = \vec{\beta}^H \gamma \vec{\beta}, \quad (\text{VI.35})$$

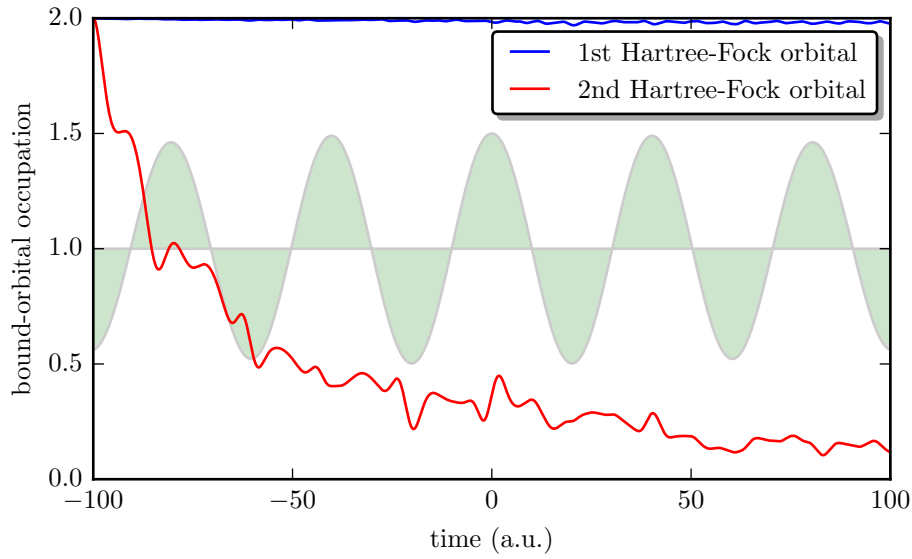


**Figure VI.7.:** Figure reproduced from Ref. [234, Fig. 3 (a)] using a numerical **time-dependent Hartree-Fock (TDHF)** propagation based on the **finite-element discrete variable representation (FEDVR)** outlined in Sec. VI.4. The time-dependent electric field is depicted in green in the background.

where  $\vec{\beta} := \phi_B(\varphi) \in \mathbb{C}^d$  and  $\vec{\beta}^H$  is the Hermitian transpose of  $\vec{\beta}$ .

It is common practice to test programs via simple test cases. Possessing many visible features, the curves produced on the level of **TDHF in 1d** by [Hochstuhl et al. \(2010\)](#) [234] depicted in Fig. VI.7 are an ideal candidate for checking the implementation. The precise parameters can be learned from the original publication; they are not repeated here. Many more (simpler) test cases were utilized which are suitable for automatic testing. These are summarized in App. C.

# VII

## Conclusions and outlook

In summary, the ionization dynamics of different model systems, from an isolated atom to an infinite crystal, have been inspected for peculiar features attributed to coherences. The conclusions drawn from the different models are briefly outlined in the following and, additionally, it is pointed out in all cases what ideas and open questions are potentially be interesting for future research.

In Chapter III, resonant [two-photon absorption \(TPA\)](#) was discussed in general terms using a model that is principally suitable for the description of a resonant transition in both helium in the [VUV](#) regime and in highly charged neon  $\text{Ne}^{8+}$  in the soft [X-ray](#) region. It was analytically demonstrated within a partially coherent theory that the ionization probability as a function of the total number of incident photons is prior to saturation subject to either a linear or a quadratic scaling in different intensity regimes or rather in different ranges of the Rabi frequency. A similar observation was made based on rate equations with the decisive difference however that the photon number instead of the Rabi frequency is key for the separation of these two regimes. The deviation introduced to the system by disregarding the coherences between the two discrete states was then clearly apparent in the intensity regime of the crossover between the linear and the quadratic scaling behavior. Although the considered model with only three real-valued material parameters seems to be very simplistic at first sight, the parameter study did not address the impact of all of them. It was intensely discussed how the absorption cross sections  $\sigma_{GX}$  (referring to transitions between the ground and the excited state) and  $\sigma_X$  (referring to transitions between the excited state and the continuum) affect the ionization probability while the parameter  $\sigma_A$ , which is related to dispersion effects, was set to zero. The case  $\sigma_A \neq 0$  was excluded from the analysis because it has far-reaching consequences that have been previously discussed by [Kaiser \(2014\) \[4\]](#). To be more precise, [Kaiser \(2014\) \[4\]](#) analyzed the influence of a detuning, which was demonstrated to be mathematically equivalent to  $\sigma_A \neq 0$  in the case of flat-top pulses. Future studies may shed some light on how the ionization probability is affected if both  $\sigma_A$  does not vanish *and* the laser pulse has a different temporal profile. One might expect, for example, that the system effectively behaves as if a chirped laser pulse interacts with the atom.

In Chapter IV, the ionization dynamics of an infinite [1d](#) crystal was investigated in the [XUV](#) regime or, more precisely, for photon energies ranging from 120 to 165 eV adjusted to the *K*-edge of the model system to ensure that predominantly slow photoelectrons are generated. Particular attention was paid to the pulse-length dependence of the ionization probability during ultrashort pulses. Contrary to the idea of the atoms independently interacting with the laser field through inner-shell ionization, the pulse length turned out to strongly affect the ionization yield for pulse durations between 0.01 and 5 fs. Moreover, the potential emergence of Rabi-like oscillations for 1 fs pulses was discussed with respect to their implications on occupation probabilities and the electron density. The low photon energies, however, do not support an experimental verification based on elastic scattering. This outcome may seem discouraging at first but, of course, not all possibilities have been exhausted. An alternative idea which was not yet pursued in order to

find experimental proof for the Rabi-like dynamics is analogous to an early study by Freund and Levine (1970) [383] that was aimed at optical modulations in X-ray diffraction. The Rabi-like oscillations could presumably lead to similar modulations.

Chapter V was devoted to the photon-matter interaction of a short ordered chain (SOC) in 1d with  $N = 1, \dots, 21$  atoms as a intermediate system between the isolated atom and the infinite crystal, containing each of them as a limiting (1d crystal for  $N \rightarrow \infty$ ) or a special case (single atom for  $N = 1$ ). It was demonstrated that coherent dynamics is responsible for a prominent localization phenomenon in SOCs already for  $N > 3$  atoms due to the inhibition of the escape of photoelectrons. The electron-electron interaction was switched off in the majority of cases in order to correctly identify the origin of this feature. This strategy then unveiled another trapping mechanism independent of electrostatic effects. The equidistant spacing of the atoms in SOCs proved not to be vital for observation of the localization mechanism, which, on the one hand, allows the results to be generalized to 1d clusters and, on the other hand, points out the differences to Anderson localization (AL).

The analyses of Chapters IV and V can be extended in many ways. For instance, one open question is how the reduction to 1d affects the observed localization effects, suggesting that an extension of the FEDVR to 3d [255, 318] would provide deeper insights. Another candidate for further development is motivated by the findings of Kaiser (2014) [4], which indicated that Auger decay can be consistently included on the level of the TDRDM theory. It might further support electron-electron scattering of trapped electrons, which was absent in the simulations performed for this work but is a fundamental process in real systems. This is important especially in view of the fact that Pauli blocking, which is the only many-particle effect considered here, may not be capable of qualitatively replacing the Coulomb interaction for free electrons. However, a 1d TDRDM theory has potential downsides. Firstly, assuming that scattering between free electrons turns out to be essential in the SOC, the practicality of the 1d approximation is highly questionable. Secondly, considering a scenario whose outcome considerably depends on Auger decay implies that at least two shells of an atom are filled. This premise may also be an issue because it is not guaranteed that the 1d model correctly reproduces the relative absorption probabilities, which is key to the qualitative description of the ionization process. Thirdly, it was extensively discussed in Chapter II that the TDRDM approach involves a very high numerical effort in the X-ray regime; the computational requirements are possibly too demanding for an application at photon energies characteristic for SFX experiments. Significant progress would also be achieved if the models of near-threshold ionization were adapted to the X-ray region by taking fluorescence into account. The absence of this process was the main reason that the major part of this dissertation was dedicated to XUV pulses because NTI in the X-ray regime requires heavy atoms whose inner-shell vacancies are subject to a rapid decay due to fluorescence.

Nevertheless, this thesis contributes to the understanding of the ionization dynamics in different samples by investigating fundamental processes beyond the rate-equation approach in the XUV regime. For instance, a previously not discussed trapping mechanism was identified in a 1d system that might, as soon as the analysis is extended to a more realistic scenario, lead to novel interpretations of the ionization dynamics in clusters.

# A

## Atomic units

This appendix is intended as an overview of *atomic units*, which were used in all equations throughout the main text. For readers who are not used or even not familiar with the concept of atomic units, a list of the most frequently appearing physical quantities and the respective value in common or **SI** units is provided in Table A.1.

Analogous to the **International System of Units (SI)**, atomic units can be written in terms of a few base units, but contrary to **SI**, which defines exactly seven base units, atomic units directly rest upon the following fundamental constants: the electron rest mass  $m_e$ , the elementary (positive) charge  $e$ , the reduced Planck constant  $\hbar$ , the Boltzmann constant  $k_B$ , vacuum permittivity  $\varepsilon_0$ , and the speed of light in vacuum  $c$  [384, 385]. The atomic unit of energy is then defined as the *hartree*  $E_h = \frac{\hbar^2}{m_e a_0^2}$  and the unit of length is the *bohr*  $a_0 = \frac{4\pi\varepsilon_0 \hbar^2}{m_e e^2}$ . In general, the units have to be inferred from context. For example, an energy of 1 a.u. is equal to one hartree,  $E_h$ , and a length of 1 a.u. corresponds to one bohr,  $a_0$ . Accordingly, no distinction is made in the main text between the photon energy and the frequency. The dimensionless fine-structure constant  $\alpha = \frac{1}{4\pi\varepsilon_0} \frac{e^2}{\hbar c} \approx \frac{1}{137}$  appears in many equations.

The derived atomic units follow naturally in most cases but there are some exceptions; one of them is the atomic unit of intensity. The latter is not always used consistently in the literature. For example, the definition in Ref. [218] differs from Ref. [385] (the present thesis conforms to Ref. [218]). The unit of the vector potential (see, e.g., Eq. (IV.3)) is chosen according to Santra (2009) [39].

Physical quantity	Value in common units
mass	$m_e \approx 9.109 \cdot 10^{-31} \text{ kg}$
length	$a_0 \approx 0.5291 \text{ \AA}$
energy	$E_h \approx 27.21 \text{ eV}$
time	$\frac{\hbar}{E_h} \approx 0.02419 \text{ fs}$
electric charge	$e \approx 1.602 \cdot 10^{-19} \text{ C}$
electric field	$\frac{E_h}{ea_0} \approx 5.142 \cdot 10^{11} \frac{\text{V}}{\text{m}}$
vector potential	$\frac{\hbar}{\alpha ea_0} \approx 1.705 \cdot 10^{-3} \frac{\text{Vs}}{\text{m}}$
photon flux	$\frac{E_h}{\hbar a_0^2} \approx 1.476 \cdot 10^{37} \frac{1}{\text{m}^2 \text{s}}$
intensity	$\frac{E_h^2}{\hbar a_0^2} \approx 6.436 \cdot 10^{15} \frac{\text{W}}{\text{cm}^2}$
velocity	$\alpha c \approx 21.88 \frac{\text{\AA}}{\text{fs}}$
polarizability	$\frac{e^2 a_0^2}{E_h} \approx 1.649 \cdot 10^{-41} \frac{\text{A}^2 \text{s}^4}{\text{kg}}$

**Table A.1.:** Table of frequently used atomic units. The expressions and conversion factors are consistent with Ref. [384, Table 3-5, p. 27].



# B

## Technical details of the FEDVR

### B.1. Gauss-Lobatto (GL) points

The **Gauss-Lobatto (GL)** quadrature rule, Eq. (VI.17), and the formulation of the Lobatto **DVR** basis in Eq. (VI.16) assume the knowledge of the **GL** weights and points. The latter can be calculated for any number of desired **GL** points  $n$  as the roots of the Lobatto polynomials, Eq. (VI.12). For an implementation of the **FEDVR**, the **GL** points are typically required only for small  $n$ . In those cases, analytical expressions, such as those listed in Table B.1, are available. Alternatively, the numerical values are provided in [341, p. 920].

$n$	<b>Gauss-Lobatto (GL) points</b>			
3	0	$\pm 1$		
4	$\pm\sqrt{\frac{1}{5}}$	$\pm 1$		
5	0	$\pm\sqrt{\frac{3}{7}}$	$\pm 1$	
6	$\pm\sqrt{\frac{1}{3}\left(1 - \frac{2}{\sqrt{7}}\right)}$	$\pm\sqrt{\frac{1}{3}\left(1 + \frac{2}{\sqrt{7}}\right)}$	$\pm 1$	
7	0	$\pm\sqrt{\frac{1}{11}\left(5 - 2\sqrt{\frac{5}{3}}\right)}$	$\pm\sqrt{\frac{1}{11}\left(5 + 2\sqrt{\frac{5}{3}}\right)}$	$\pm 1$

**Table B.1.:** Analytic expressions for the **Gauss-Lobatto (GL)** points for small  $n$ .

The numerical values are easily obtained in practice –including cases with large  $n \gg 7$ – because efficient and robust root-finding algorithms are available for polynomials [386]. In fact, the problem of finding the **GL** points can be solved with only one function call in both Python [387] or Maple [388]. For this reason, the following workflow was adopted: the **FEDVR** basis is generated in Python and stored in **HDF5** format to provide a starting point for a C++ program based on **PETSc**. This procedure has another advantage as the main program is decoupled from the creation of the **FEDVR** basis, which is in general not fully characterized by a few values but by the length of all intervals (cf. Ref. [4, p. 72]) and is thus not suitable for a specification via runtime options.

### B.2. Lobatto shape functions

For the calculation of the matrix representation of derivation operators in the ensuing section, the following definition of a set of functions  $\{f_m | m = 0, \dots, n - 1\}$  which is identical to the

DVR basis, Eq. (VI.16), except for normalization turns out to be practical:

$$f_m := \sqrt{w_m} \varphi_m \quad \forall m \in \{0, \dots, n-1\}. \quad (\text{B.1})$$

It is easy to see that the set of functions  $\{f_m\}$  fulfills the property  $f_m(x_k) = \delta_{mk}$ , which, in turn, fully characterizes the polynomials  $\{f_m\}$  of degree  $n-1$  analogous to Eq. (VI.16). This feature can be exploited to evaluate the coefficients  $\alpha_m^j \in \mathbb{R}$  of the polynomials  $\{f_m\}$  as follows. Let  $f_m$  be of the form

$$f_m(x) = \sum_{j=0}^{n-1} \alpha_m^j x^j. \quad (\text{B.2})$$

Then, the property  $f_m(x_k) = \delta_{mk}$  leads to  $n^2$  linear equations which can be expressed as

$$\begin{pmatrix} \alpha_0^0 & \alpha_0^1 & \dots & \alpha_0^{n-1} \\ \alpha_1^0 & \alpha_1^1 & \dots & \alpha_1^{n-1} \\ \vdots & \vdots & \ddots & \vdots \\ \alpha_{n-1}^0 & \alpha_{n-1}^1 & \dots & \alpha_{n-1}^{n-1} \end{pmatrix} \begin{pmatrix} x_0^0 & x_1^0 & \dots & x_{n-1}^0 \\ x_0^1 & x_1^1 & \dots & x_{n-1}^1 \\ \vdots & \vdots & \ddots & \vdots \\ x_0^{n-1} & x_1^{n-1} & \dots & x_{n-1}^{n-1} \end{pmatrix} = \begin{pmatrix} 1 & 0 & \dots & 0 \\ 0 & 1 & \dots & 0 \\ \vdots & \vdots & \ddots & \vdots \\ 0 & 0 & \dots & 1 \end{pmatrix}. \quad (\text{B.3})$$

All coefficients of the polynomials  $\{f_m\}$  can be obtained via matrix inversion of the  $n \times n$  Vandermonde matrix, which is obviously nonsingular due to the pairwise distinct GL points  $x_0, \dots, x_{n-1}$  (cf. Ref. [339, Appendix A]).

Now, one defines analogous to Refs. [232, 233] the so-called *Lobatto shape functions*  $\{f_m^i | m = 0, \dots, n_g - 1 \wedge i = 0, \dots, n_e - 1\}$  as in Eq. (VI.21) apart from the normalization and the merging of boundary DVR functions:

$$f_m^i : [a, b] \rightarrow \mathbb{R}, \quad f_m^i(x) = \begin{cases} f_m\left(\frac{x-M_i}{s_i}\right), & x \in [x^i, x^{i+1}], \\ 0, & \text{otherwise.} \end{cases} \quad (\text{B.4})$$

Hence, the support of each  $f_m^i$  is always the  $i$ -th interval, which avoids the necessity of a distinction of cases with respect to bridge functions  $\{\chi_0^i | i = 1, \dots, n_e - 2\}$  after replacing the FEDVR basis functions  $\chi_m^i$  by the Lobatto shape functions  $f_m^i$ . Neither the basis nor the functions have to be stored explicitly as the evaluation of both can be reduced to values of the  $n_g$  functions  $\{f_m\}$  by means of Eq. (B.4). The latter and its derivatives can then be efficiently calculated using Horner's method.

It is important to note that the polynomials in Eq. (B.2) can be evaluated for any  $x \in \mathbb{R}$ , i.e., the FEDVR contains a natural interpolation scheme. The implementation of the latter is very useful in general because it can be easily tested and allows the change of FEDVR bases, of which one can take advantage by employing so-called *multigrid methods* [389].

### B.3. FEDVR representation of operators

Using the bijective mapping  $\mathcal{M}$  from Eq. (VI.24) for an arbitrary matrix  $M$ , one can explicitly distinguish between the indices that pertain to an interval  $i, j$  and those which refer to a function within the interval (or a bridge function)  $k, m$ :

$$M_{mk}^{ij} := M_{\mathcal{M}((i,m)), \mathcal{M}((k,j))}. \quad (\text{B.5})$$

This notation will facilitate the distinction of cases to be carried out in the following.

### B.3.1. First-derivative matrix

Changing the notation according to Eq. (B.5), one obtains the following expression for the matrix representation of the first derivative in Eq. (VI.20):

$$D_{mk}^{ij} = \langle \chi_k^j, \frac{\partial}{\partial x} \chi_m^i \rangle = \int_a^b \chi_k^j(x) \frac{\partial}{\partial x} \chi_m^i(x) dx = \langle \chi_k^j, \frac{\partial}{\partial x} \chi_m^i \rangle_{\mathcal{D}}. \quad (\text{B.6})$$

Since the bridge functions are continuous but not continuously differentiable, the integrand has a jump discontinuity at the interval boundaries. This is, however not an issue for the integration. It is easy to show that this definition is equivalent to the interpolation addressed above in App. B.2 and a subsequent analytical derivation for each differentiable function.

Now, it is shown how to obtain the result from Eq. (VI.26). Consider, for instance, the case  $k \neq 0 \wedge m \neq 0$ . First, the FEDVR basis functions are written in terms of Lobatto shape functions  $f_m^i$ . These are, in the next step, reduced to the polynomials  $\{f_m\}$  from Eq. (B.1) via substitution, whereby the integration interval is transformed to  $[-1, 1]$ . Translated in formulas,

$$\begin{aligned} D_{mk}^{ij} &= \chi_k^j(x_k^j) \chi_m^i(x_m^i) \delta_{ij} \int_{x^j}^{x^{j+1}} f_k^j(x) \frac{\partial}{\partial x} f_m^j(x) dx, \\ &= \chi_k^j(x_k^j) \chi_m^i(x_m^i) \delta_{ij} \underbrace{\int_{-1}^1 f_k(x) \frac{\partial}{\partial x} f_m(x) dx}_{=D_{mk}^{\text{loc}}}, \end{aligned}$$

where  $D_{mk}^{\text{loc}}$  from Eq. (VI.27) was identified. The other cases can be calculated analogously and yield altogether:

$$D_{mk}^{ij} = \chi_k^j(x_k^j) \chi_m^i(x_m^i) \cdot \begin{cases} \delta_{ij} D_{mk}^{\text{loc}}, & \text{if } m > 0 \wedge k > 0, \\ \delta_{ij} D_{0k}^{\text{loc}} + \delta_{i,j+1} D_{n_g-1,k}^{\text{loc}}, & \text{if } m = 0 \wedge k > 0, \\ \delta_{ij} D_{m0}^{\text{loc}} + \delta_{i,j-1} D_{m,n_g-1}^{\text{loc}}, & \text{if } m > 0 \wedge k = 0, \\ \delta_{i,j+1} D_{n_g-1,0}^{\text{loc}} + \delta_{i,j-1} D_{0,n_g-1}^{\text{loc}}, & \text{if } m = 0 \wedge k = 0. \end{cases} \quad (\text{B.7})$$

### B.3.2. Kinetic-energy matrix

Similar to Eq. (B.6), the matrix representation of the kinetic-energy operator can be expressed as

$$T_{mk}^{ij} = \frac{1}{2} \langle \frac{\partial}{\partial x} \chi_k^j, \frac{\partial}{\partial x} \chi_m^i \rangle = \frac{1}{2} \int_a^b \frac{\partial}{\partial x} \chi_m^i(x) \frac{\partial}{\partial x} \chi_k^j(x) dx = \frac{1}{2} \langle \frac{\partial}{\partial x} \chi_k^j, \frac{\partial}{\partial x} \chi_m^i \rangle_{\mathcal{D}}. \quad (\text{B.8})$$

One can again verify that this definition is consistent with the interpolation scheme. It is easy to show that  $T_{mk}^{ij}$  can be written in terms of

$$T_{mk}^{\text{loc}} = \frac{1}{2} \int_{-1}^1 f'_m(x) f'_k(x) dx \quad (\text{B.9})$$

by means of straightforward substitutions, resulting in

$$T_{mk}^{ij} = \chi_k^j(x_k^j) \chi_m^i(x_m^i) \cdot \begin{cases} \delta_{ij} \frac{1}{s_i} T_{m,k}, & \text{if } m > 0 \wedge k > 0, \\ \delta_{i,j} \frac{1}{s_i} T_{0,k} + \delta_{i,j+1} \frac{1}{s_j} T_{n_g-1,m_2}, & \text{if } m = 0 \wedge k > 0, \\ \delta_{i,j} \frac{1}{s_j} T_{m_1,0} + \delta_{i+1,j} \frac{1}{s_j} T_{m,n_g-1}, & \text{if } m > 0 \wedge k = 0, \\ \delta_{ij} \left( \frac{1}{s_i} T_{0,0} + \frac{1}{s_{i-1}} T_{n_g-1,n_g-1} \right) + \\ + \delta_{i,j+1} \frac{1}{s_i} T_{0,n_g-1} + \delta_{i+1,j} \frac{1}{s_j} T_{n_g-1,0}, & \text{if } m = 0 \wedge k = 0. \end{cases} \quad (\text{B.10})$$

Hence, the  $d \times d$  matrix  $T_{mk}^{ij}$  is traced back to a  $n_g \times n_g$  matrix  $T_{mk}^{\text{loc}}$ . Due to this relation, only one calculation of  $T_{mk}^{\text{loc}}$  is required, which can then be used to fill all overlapping blocks of the matrix as shown in the main text in Fig. VI.6a on page 93.

### B.3.3. Example

In the following, it is briefly demonstrated that the FEDVR in the case  $n_g = 3$  can be reduced to a nontrivial finite difference method (FDM) on an equidistant grid. To start with, one extracts the Lobatto DVR basis functions in the special case with three GL points,  $n_g = 3$ , from Eq. (VI.16) as

$$\begin{aligned} \varphi_0(x) &= \frac{1}{2} \sqrt{3} x(x-1), \\ \varphi_1(x) &= -\frac{1}{2} \sqrt{3} (x-1)(x+1), \\ \varphi_2(x) &= \frac{1}{2} \sqrt{3} x(x+1). \end{aligned}$$

As stated in Sec. VI.3, the basis functions are not orthonormal in the usual sense. The remainder  $R_n$  from Eq. (VI.18) for a product of two arbitrary basis functions is in fact rather large,  $R_n = \pm \frac{1}{5}$  (independent of  $\xi$ ). Nevertheless, the basis functions are guaranteed to be linearly independent, so the basis is well-defined. The FEDVR derivation matrix  $D_{mk}$  from Eq. (VI.20) is then

$$D_{mk} = \begin{pmatrix} -\frac{3}{2} & 1 & -\frac{1}{2} \\ -1 & 0 & 1 \\ \frac{1}{2} & -1 & \frac{3}{2} \end{pmatrix}$$

So far, one cannot immediately recognize a consistent FDM because the GL weights are generally different for each grid point. However, the row sum of the middle row vanishes as the grid weights are symmetric, i.e., the grid points  $\pm 1$  have the same associated weights. This is not the case for the upper and lower row, where the grid weight of the basis function centered in

the interval is four times as large as the weight of the basis functions located at the interval boundaries  $\pm 1$ .

Defining the constant step size  $h = \frac{1}{2}(x^{i+1} - x^i) = s$  (two steps per interval) and taking into account the grid weights, one approximates the derivative of an analytic function  $y(x)$  in the center of each interval  $x_1^i$  and at the boundaries  $x_0^i$  by

$$y'(x_m^i) \approx \begin{cases} \frac{1}{h} \left[ -\frac{1}{2}y(x-h) + \frac{1}{2}y(x+h) \right], & \text{if } m = 1, \\ \frac{1}{h} \left[ \frac{1}{4}y(x-2h) - y(x-h) + y(x+h) - \frac{1}{4}y(x+2h) \right], & \text{if } m = 0, \end{cases}$$

$$= y'(x) + \mathcal{O}(h^2).$$

This form of the **FEDVR** is very similar to the **FDM**. Note, however, that the kernel of the derivative matrix does not exclusively consist of the constant grid function. For instance, the numerical derivative of the grid function  $y(x_m^i) = \delta_{m1}$ , which represents a non-differentiable function (the sum of all “inner” functions in Fig. VI.4), vanishes at all grid points and can thus not be distinguished from the zero function. Therefore, great caution needs to be exercised when trying to numerically estimate of the antiderivative  $Y$  to a function  $y$  by finding the solutions of  $DY = y$ .



In practice, programming involves a lot of testing. In this respect, the versatility of the **FEDVR** approach from Chapter **VI** has the important advantage that it includes analytically solvable textbook examples as special cases. This appendix briefly mentions the model systems that were implemented to test the code.

**Eigenvalues and eigenfunctions:** standard textbook examples such as the harmonic oscillator and the  $\text{sech}^2$  potential [268, p. 94 et seqq.]; **HF** energies from [390, Table I].

**Dynamics of Gaussian wave packets:** assume a Hamiltonian  $H$  of the form

$$H = -\frac{1}{2} \frac{\partial^2}{\partial x^2} + Ex. \quad (\text{C.1})$$

One seeks the solution  $\psi(x, t)$  of the (pure) initial value problem (IVP) with respect to the initial condition

$$\psi(x, t = 0) = \varphi(x) := (\sigma^2 \pi)^{-\frac{1}{4}} \exp\left(-\frac{x^2}{2\sigma^2}\right) \exp(ip_0 x). \quad (\text{C.2})$$

Consider, for example, the following time-dependent solutions [268, 391]:

- dispersive propagation for  $E = 0$  and  $p_0 = 0$ :

$$\psi_{\text{disp}}(x, t) = \frac{1}{\sqrt{1 + i\frac{t}{\sigma^2}}} \varphi\left(\frac{x}{\sqrt{1 + i\frac{t}{\sigma^2}}}\right) \quad \text{with} \quad \langle x \rangle = 0.$$

- propagation with a uniform velocity for  $E = 0$  and  $p_0 \neq 0$ :

$$\psi_{\text{vel}}(x, t) = \psi_{\text{disp}}(x - ip_0 \sigma^2, t) \exp\left(-\frac{1}{2} p_0^2 \sigma^2\right) \quad \text{with} \quad \langle x \rangle = p_0 t.$$

- uniformly accelerated particle for  $E \neq 0$  and  $p_0 = 0$ :

$$\psi_{\text{acc}}(x, t) = \psi_{\text{disp}}\left(x + \frac{1}{2} Et^2, t\right) \exp\left(-iEt\left(x + \frac{1}{6} Et^2\right)\right) \quad \text{with} \quad \langle x \rangle = -\frac{1}{2} Et^2.$$

**Test cases of TDHF:** see, for instance, Fig. **VI.7**.



# Bibliography

- [1] D. Attwood, *Soft X-Rays and Extreme Ultraviolet Radiation. Principles and Applications* (Cambridge University Press, 1999).
- [2] S. P. Hau-Riege, *High-Intensity X-Rays – Interaction with Matter* (Wiley-VCH, Weinheim, Germany, 2011).
- [3] H. Yoneda, Y. Inubushi, M. Yabashi, T. Katayama, T. Ishikawa, H. Ohashi, H. Yumoto, K. Yamauchi, H. Mimura, and H. Kitamura, *Saturable absorption of intense hard X-rays in iron*, *Nat. Commun.* **5**, 5080 (2014).
- [4] B. Kaiser, *Photoionization of atoms with ultrashort XUV laser pulses at extreme intensities*, PhD thesis (University of Bayreuth, 2014).
- [5] Bundesministerium für Bildung und Forschung (BMBF), *Verbundprojekt Innovative Experimente für XFEL: Teilprojekt 2: Veränderung atomarer Formfaktoren durch ultrakurze intensive Röntgenpulse eines XFEL und deren Auswirkungen auf Röntgenbeugungsmuster*. Förderkennzeichen 05K10WCA, 2010 – 2013.
- [6] S.-K. Son, L. Young, and R. Santra, *Impact of hollow-atom formation on coherent x-ray scattering at high intensity*, *Phys. Rev. A* **83**, 033402 (2011).
- [7] *Lightsources.org*, <http://www.lightsources.org>, [Online; accessed 2 September 2015], 2015.
- [8] V. Ayvazyan, N. Baboi, J. Bähr, V. Balandin, B. Beutner, A. Brandt, I. Bohnet, A. Bolzmann, et al., *First operation of a free-electron laser generating GW power radiation at 32 nm wavelength*, *Eur. Phys. J. D* **37**, 297 (2006).
- [9] J. Feldhaus, *FLASH—the first soft x-ray free electron laser (FEL) user facility*, *J. Phys. B: At. Mol. Opt. Phys.* **43**, 194002 (2010).
- [10] E. Allaria, C. Callegari, D. Cocco, W. M. Fawley, M. Kiskinova, C. Masciovecchio, and F. Parmigiani, *The FERMI@Elettra free-electron-laser source for coherent x-ray physics: photon properties, beam transport system and applications*, *New J. Phys.* **12**, 075002 (2010).
- [11] E. Allaria, R. Appio, L. Badano, W. A. Barletta, S. Bassanese, S. G. Biedron, A. Borga, E. Busetto, et al., *Highly coherent and stable pulses from the FERMI seeded free-electron laser in the extreme ultraviolet*, *Nat. Photonics* **6**, 699 (2012).
- [12] P. Emma, R. Akre, J. Arthur, R. Bionta, C. Bostedt, J. Bozek, A. Brachmann, P. Bucksbaum, et al., *First lasing and operation of an ångstrom-wavelength free-electron laser*, *Nat. Photonics* **4**, 641 (2010).
- [13] S. Jamison, *X-ray science: X-ray FEL shines brightly*, *Nat. Photonics* **4**, 589 (2010).

- [14] W. E. White, A. Robert, and M. Dunne, *The Linac Coherent Light Source*, *J. Synchrotron Rad.* **22**, 472 (2015).
- [15] T. Ishikawa, H. Aoyagi, T. Asaka, Y. Asano, N. Azumi, T. Bizen, H. Ego, K. Fukami, et al., *A compact X-ray free-electron laser emitting in the sub-ångstrom region*, *Nat. Photonics* **6**, 540 (2012).
- [16] D. Pile, *X-rays: First light from SACLA*, *Nat. Photonics* **5**, 456 (2011).
- [17] D. Pile, M. Yabashi, and H. Tanaka, *And then there were two*, *Nat. Photonics* **6**, 566 (2012).
- [18] T. Sato, T. Togashi, K. Tono, Y. Inubushi, H. Tomizawa, Y. Tanaka, S. Adachi, K. Nakamura, R. Kodama, and M. Yabashi, *Development of ultrafast pump and probe experimental system at SACLA*, *J. Phys: Conf. Ser.* **425**, 092009 (2013).
- [19] W. Decking and F. Le Pimpec, *European XFEL construction status*, in *Proceedings of FEL2014* (36th International Free Electron Laser Conference, 2014).
- [20] M. Altarelli and A. P. Mancuso, *Structural biology at the European X-ray free-electron laser facility*, *Phil. Trans. R. Soc. B* **369**, 20130311 (2014).
- [21] B. D. Patterson, R. Abela, H.-H. Braun, U. Flechsig, R. Ganter, Y. Kim, E. Kirk, A. Oppelt, et al., *Coherent science at the SwissFEL x-ray laser*, *New J. Phys.* **12**, 035012 (2010).
- [22] B. D. Patterson, P. Beaud, H. H. Braun, C. Dejoie, G. Ingold, C. Milne, L. Patthey, B. Pedrini, J. Szlachentko, and R. Abela, *Science Opportunities at the SwissFEL X-ray Laser*, *CHIMIA* **68**, 73 (2014).
- [23] E. Weckert, *The potential of future light sources to explore the structure and function of matter*, *IUCrJ* **2**, 230 (2015).
- [24] S. Khan, *Free-electron lasers*, *J. Mod. Opt.* **55**, 3469 (2008).
- [25] P. R. Ribic and G. Margaritondo, *Status and prospects of x-ray free-electron lasers (X-FELs): a simple presentation*, *J. Phys. D: Appl. Phys.* **45**, 213001 (2012).
- [26] J. N. Galayda, J. Arthur, D. F. Ratner, and W. E. White, *X-ray free-electron lasers-present and future capabilities*, *J. Opt. Soc. Am. B-Opt. Phys.* **27**, B106 (2010).
- [27] S. Mobilio, F. Boscherini, and C. Meneghini, eds., *Synchrotron Radiation. Basics, Methods and Applications* (Springer, Berlin, Heidelberg, 2015).
- [28] J. Feldhaus, J. Arthur, and J. B. Hastings, *X-ray free-electron lasers*, *J. Phys. B: At. Mol. Opt. Phys.* **38**, S799 (2005).
- [29] E. L. Saldin, E. A. Schneidmiller, and M. V. Yurkov, *The Physics of Free Electron Lasers*, Advanced Texts in Physics (Springer, Berlin, Heidelberg, 2000).
- [30] P. Schmüser, M. Dohlus, J. Rossbach, and C. Behrens, *Free-Electron Lasers in the Ultraviolet and X-Ray Regime*, Vol. 258, Springer Tracts in Modern Physics (Springer International Publishing, 2014).
- [31] T. Tschentscher, A. S. Schwarz, and D. Rathje, *Bewegte Bilder aus dem Nanokosmos. Der Freie-Elektronen-Laser European XFEL*, *Phys. Unserer Zeit* **41**, 64 (2010).

- [32] B. W. J. McNeil and N. R. Thompson, *X-ray free-electron lasers*, *Nat. Photonics* **4**, 814 (2010).
- [33] B. Flöter, *Strahlcharakterisierung von Freie-Elektronen-Lasern im weichen Röntgen-Spektralbereich*, Vol. 8, Göttingen series in x-ray physics (Universitätsverlag Göttingen, 2012).
- [34] K. F. Renk, *Basics of Laser Physics. For Students of Science and Engineering*, Graduate Texts in Physics (Springer, Berlin, Heidelberg, 2012).
- [35] C. Pellegrini, *The history of X-ray free-electron lasers*, *Eur. Phys. J. H* **37**, 659 (2012).
- [36] J. M. J. Madey, *Stimulated Emission of Bremsstrahlung in a Periodic Magnetic Field*, *J. Appl. Phys.* **42**, 1906 (1971).
- [37] R. Colella and A. Luccio, *Proposal for a free electron laser in the X-ray region*, *Opt. Commun.* **50**, 41 (1984).
- [38] H. Yumoto, H. Mimura, T. Koyama, S. Matsuyama, K. Tono, T. Togashi, Y. Inubushi, T. Sato, et al., *Focusing of X-ray free-electron laser pulses with reflective optics*, *Nat. Photonics* **7**, 43 (2013).
- [39] R. Santra, *Concepts in x-ray physics*, *J. Phys. B: At. Mol. Opt. Phys.* **42**, 023001 (2009).
- [40] S. Suckewer and P. Jaeglé, *X-Ray laser: past, present, and future*, *Laser Phys. Lett.* **6**, 411 (2009).
- [41] K.-J. Kim, Y. Shvyd'ko, and S. Reiche, *A Proposal for an X-Ray Free-Electron Laser Oscillator with an Energy-Recovery Linac*, *Phys. Rev. Lett.* **100**, 244802 (2008).
- [42] Y. V. Shvyd'ko, S. Stoupin, A. Cunsolo, A. H. Said, and X. Huang, *High-reflectivity high-resolution X-ray crystal optics with diamonds*, *Nat. Phys.* **6**, 196 (2010).
- [43] Y. Shvyd'ko, S. Stoupin, V. Blank, and S. Terentyev, *Near-100% Bragg reflectivity of X-rays*, *Nat. Photonics* **5**, 539 (2011).
- [44] J. Andruszkow, B. Aune, V. Ayvazyan, N. Baboi, R. Bakker, V. Balakin, D. Barni, A. Bazhan, et al., *First Observation of Self-Amplified Spontaneous Emission in a Free-Electron Laser at 109 nm Wavelength*, *Phys. Rev. Lett.* **85**, 3825 (2000).
- [45] E. L. Saldin, E. A. Schneidmiller, and M. V. Yurkov, *Statistical and coherence properties of radiation from x-ray free-electron lasers*, *New J. Phys.* **12**, 035010 (2010).
- [46] S. Ackermann, A. Azima, S. Bajt, J. Bödewadt, F. Curbis, H. Dachraoui, H. Delsim-Hashemi, M. Drescher, et al., *Generation of Coherent 19- and 38-nm Radiation at a Free-Electron Laser Directly Seeded at 38 nm*, *Phys. Rev. Lett.* **111**, 114801 (2013).
- [47] E. Allaria, D. Castronovo, P. Cinquegrana, P. Craievich, M. Dal Forno, M. B. Danailov, G. D'Auria, A. Demidovich, et al., *Two-stage seeded soft-X-ray free-electron laser*, *Nat. Photonics* **7**, 913 (2013).
- [48] J. Amann, W. Berg, V. Blank, F.-J. Decker, Y. Ding, P. Emma, Y. Feng, J. Frisch, et al., *Demonstration of self-seeding in a hard-X-ray free-electron laser*, *Nat. Photonics* **6**, 693 (2012).

- [49] N. Rohringer, D. Ryan, R. A. London, M. Purvis, F. Albert, J. Dunn, J. D. Bozek, C. Bostedt, et al., *Atomic inner-shell X-ray laser at 1.46 nanometres pumped by an X-ray free-electron laser*, *Nature* **481**, 488 (2012).
- [50] N. Rohringer and R. London, *Atomic inner-shell x-ray laser pumped by an x-ray free-electron laser*, *Phys. Rev. A* **80**, 013809 (2009).
- [51] D. M. Ritson, *A weapon for the twenty-first century*, *Nature* **328**, 487 (1987).
- [52] D. M. Mills, J. R. Helliwell, Å. Kvik, T. Ohta, I. A. Robinson, and A. Authier, *Report of the Working Group on Synchrotron Radiation Nomenclature – brightness, spectral brightness or brilliance?*, *J. Synchrotron Rad.* **12**, 385 (2005).
- [53] C. Bourassin-Bouchet and M.-E. Couprie, *Partially coherent ultrafast spectrography*, *Nat. Commun.* **6**, 6465 (2015).
- [54] L. Young, E. P. Kanter, B. Kraessig, Y. Li, A. M. March, S. T. Pratt, R. Santra, S. H. Southworth, et al., *Femtosecond electronic response of atoms to ultra-intense X-rays*, *Nature* **466**, 56 (2010).
- [55] B. Rudek, S.-K. Son, L. Foucar, S. W. Epp, B. Erk, R. Hartmann, M. Adolph, R. Andritschke, et al., *Ultra-efficient ionization of heavy atoms by intense X-ray free-electron laser pulses*, *Nat. Photonics* **6**, 858 (2012).
- [56] S. Düsterer, P. Radcliffe, C. Bostedt, J. Bozek, A. L. Cavalieri, R. Coffee, J. T. Costello, D. Cubaynes, et al., *Femtosecond x-ray pulse length characterization at the Linac Coherent Light Source free-electron laser*, *New J. Phys.* **13**, 093024 (2011).
- [57] U. Fröhling, M. Wieland, M. Gensch, T. Gebert, B. Schütte, M. Krikunova, R. Kalms, F. Budzyn, et al., *Single-shot terahertz-field-driven X-ray streak camera*, *Nat. Photonics* **3**, 523 (2009).
- [58] I. Grguraš, A. R. Maier, C. Behrens, T. Mazza, T. J. Kelly, P. Radcliffe, S. Düsterer, A. K. Kazansky, et al., *Ultrafast X-ray pulse characterization at free-electron lasers*, *Nat. Photonics* **6**, 852 (2012).
- [59] W. Helml, A. R. Maier, W. Schweinberger, I. Grguraš, P. Radcliffe, G. Doumy, C. Roedig, J. Gagnon, et al., *Measuring the temporal structure of few-femtosecond free-electron laser X-ray pulses directly in the time domain*, *Nat. Photonics* **8**, 950 (2014).
- [60] M. Drescher, U. Fröhling, M. Krikunova, T. Maltezopoulos, and M. Wieland, *Time-diagnostics for improved dynamics experiments at XUV FELs*, *J. Phys. B: At. Mol. Opt. Phys.* **43**, 194010 (2010).
- [61] F. Tavella, N. Stojanovic, G. Geloni, and M. Gensch, *Few-femtosecond timing at fourth-generation X-ray light sources*, *Nat. Photonics* **5**, 162 (2011).
- [62] M. Beye, O. Krupin, G. Hays, A. H. Reid, D. Rupp, S. de Jong, S. Lee, W. S. Lee, et al., *X-ray pulse preserving single-shot optical cross-correlation method for improved experimental temporal resolution*, *Appl. Phys. Lett.* **100**, 121108 (2012).

- [63] M. Harmand, R. Coffee, M. R. Bionta, M. Chollet, D. French, D. Zhu, D. M. Fritz, H. T. Lemke, et al., *Achieving few-femtosecond time-sorting at hard X-ray free-electron lasers*, *Nat. Photonics* **7**, 215 (2013).
- [64] N. Hartmann, W. Helml, A. Galler, M. R. Bionta, J. Gruenert, S. L. Molodtsov, K. R. Ferguson, S. Schorb, et al., *Sub-femtosecond precision measurement of relative X-ray arrival time for free-electron lasers*, *Nat. Photonics* **8**, 706 (2014).
- [65] A. Marinelli, D. Ratner, A. A. Lutman, J. Turner, J. Welch, F. J. Decker, H. Loos, C. Behrens, et al., *High-intensity double-pulse X-ray free-electron laser*, *Nat. Commun.* **6**, 6369 (2015).
- [66] S. Schulz, I. Grguraš, C. Behrens, H. Bromberger, J. T. Costello, M. K. Czwalińska, M. Felber, M. C. Hoffmann, et al., *Femtosecond all-optical synchronization of an X-ray free-electron laser*, *Nat. Commun.* **6**, 5938 (2015).
- [67] E. Allaria, B. Diviacco, C. Callegari, P. Finetti, B. Mahieu, J. Viefhaus, M. Zangrando, G. De Ninno, et al., *Control of the Polarization of a Vacuum-Ultraviolet, High-Gain, Free-Electron Laser*, *Phys. Rev. X* **4**, 041040 (2014).
- [68] C. Gutt, P. Wochner, B. Fischer, H. Conrad, M. Castro-Colin, S. Lee, F. Lehmkuhler, I. Steinke, et al., *Single Shot Spatial and Temporal Coherence Properties of the SLAC Linac Coherent Light Source in the Hard X-Ray Regime*, *Phys. Rev. Lett.* **108**, 024801 (2012).
- [69] B. Henrich, J. Becker, R. Dinapoli, P. Goettlicher, H. Graafsma, H. Hirsemann, R. Klanner, H. Krueger, et al., *The adaptive gain integrating pixel detector AGIPD a detector for the European XFEL*, *Nucl. Instrum. Methods Phys. Res., Sect. A* **633**, S11 (2011).
- [70] G. Doumy, C. Roedig, S.-K. Son, C. I. Blaga, A. D. DiChiara, R. Santra, N. Berrah, C. Bostedt, et al., *Nonlinear Atomic Response to Intense Ultrashort X Rays*, *Phys. Rev. Lett.* **106**, 083002 (2011).
- [71] B. Rudek, D. Rolles, S.-K. Son, L. Foucar, B. Erk, S. Epp, R. Boll, D. Anielski, et al., *Resonance-enhanced multiple ionization of krypton at an x-ray free-electron laser*, *Phys. Rev. A* **87**, 023413 (2013).
- [72] H. Fukuzawa, S.-K. Son, K. Motomura, S. Mondal, K. Nagaya, S. Wada, X.-J. Liu, R. Feifel, et al., *Deep Inner-Shell Multiphoton Ionization by Intense X-Ray Free-Electron Laser Pulses*, *Phys. Rev. Lett.* **110**, 173005 (2013).
- [73] K. Motomura, H. Fukuzawa, S.-K. Son, S. Mondal, T. Tachibana, Y. Ito, M. Kimura, K. Nagaya, et al., *Sequential multiphoton multiple ionization of atomic argon and xenon irradiated by X-ray free-electron laser pulses from SACLA*, *J. Phys. B: At. Mol. Opt. Phys.* **46**, 164024 (2013).
- [74] H. Wabnitz, A. R. B. de Castro, P. Gürtler, T. Laarmann, W. Laasch, J. Schulz, and T. Möller, *Multiple Ionization of Rare Gas Atoms Irradiated with Intense VUV Radiation*, *Phys. Rev. Lett.* **94**, 023001 (2005).

- [75] A. A. Sorokin, S. V. Bobashev, T. Feigl, K. Tiedtke, H. Wabnitz, and M. Richter, *Photoelectric Effect at Ultrahigh Intensities*, *Phys. Rev. Lett.* **99**, 213002 (2007).
- [76] A. A. Sorokin, M. Wellhöfer, S. V. Bobashev, K. Tiedtke, and M. Richter, *X-ray-laser interaction with matter and the role of multiphoton ionization: Free-electron-laser studies on neon and helium*, *Phys. Rev. A* **75**, 051402 (2007).
- [77] M. Richter, M. Y. Amusia, S. V. Bobashev, T. Feigl, P. N. Juranić, M. Martins, A. A. Sorokin, and K. Tiedtke, *Extreme Ultraviolet Laser Excites Atomic Giant Resonance*, *Phys. Rev. Lett.* **102**, 163002 (2009).
- [78] M. Richter, S. V. Bobashev, A. A. Sorokin, and K. Tiedtke, *Multiphoton ionization of atoms with soft x-ray pulses*, *J. Phys. B: At. Mol. Opt. Phys.* **43**, 194005 (2010).
- [79] L. Fang, M. Hoener, O. Gessner, F. Tarantelli, S. T. Pratt, O. Kornilov, C. Buth, M. Gühr, et al., *Double Core-Hole Production in N<sub>2</sub>: Beating the Auger Clock*, *Phys. Rev. Lett.* **105**, 083005 (2010).
- [80] B. F. Murphy, T. Osipov, Z. Jurek, L. Fang, S.-K. Son, M. Mücke, J. H. D. Eland, V. Zhaunerchyk, et al., *Femtosecond X-ray-induced explosion of C<sub>60</sub> at extreme intensity*, *Nat. Commun.* **5**, 4281 (2014).
- [81] R. Santra and C. H. Greene, *Multiphoton ionization of xenon in the vuv regime*, *Phys. Rev. A* **70**, 053401 (2004).
- [82] M. O. Krause, *Atomic radiative and radiationless yields for K and L shells*, *J. Phys. Chem. Ref. Data* **8**, 307 (1979).
- [83] B. Nagler, U. Zastra, R. R. Faustlin, S. M. Vinko, T. Whitcher, A. J. Nelson, R. Sobierajski, J. Krzywinski, et al., *Turning solid aluminium transparent by intense soft X-ray photoionization*, *Nat. Phys.* **5**, 693 (2009).
- [84] A. Sytcheva, S. Pabst, S.-K. Son, and R. Santra, *Enhanced nonlinear response of Ne<sup>8+</sup> to intense ultrafast x rays*, *Phys. Rev. A* **85**, 023414 (2012).
- [85] P. J. Ho, C. Bostedt, S. Schorb, and L. Young, *Theoretical Tracking of Resonance-Enhanced Multiple Ionization Pathways in X-ray Free-Electron Laser Pulses*, *Phys. Rev. Lett.* **113**, 253001 (2014).
- [86] N. Gerken, S. Klumpp, A. A. Sorokin, K. Tiedtke, M. Richter, V. Bürk, K. Mertens, P. Juranić, and M. Martins, *Time-Dependent Multiphoton Ionization of Xenon in the Soft-X-Ray Regime*, *Phys. Rev. Lett.* **112**, 213002 (2014).
- [87] T. Mazza, A. Karamatskou, M. Ilchen, S. Bakhtiarzadeh, A. J. Rafipoor, P. O’Keeffe, T. J. Kelly, N. Walsh, et al., *Sensitivity of nonlinear photoionization to resonance substructure in collective excitation*, *Nat. Commun.* **6**, 6799 (2015).
- [88] B. L. Berman and S. C. Fultz, *Measurements of the giant dipole resonance with monoenergetic photons*, *Rev. Mod. Phys.* **47**, 713 (1975).
- [89] P. Ring and P. Schuck, *The Nuclear Many-Body Problem*, 1st ed., Texts and monographs in physics, 3rd printing, study ed. (Springer, Berlin, Heidelberg, 2004).

- [90] V. Schmidt, *Photoionization of atoms using synchrotron radiation*, *Rep. Prog. Phys.* **55**, 1483 (1992).
- [91] A. D. Shiner, B. E. Schmidt, C. Trallero-Herrero, H. J. Woerner, S. Patchkovskii, P. B. Corkum, J.-C. Kieffer, F. Legare, and D. M. Villeneuve, *Probing collective multi-electron dynamics in xenon with high-harmonic spectroscopy*, *Nat. Phys.* **7**, 464 (2011).
- [92] S. Pabst and R. Santra, *Strong-Field Many-Body Physics and the Giant Enhancement in the High-Harmonic Spectrum of Xenon*, *Phys. Rev. Lett.* **111**, 233005 (2013).
- [93] M. G. Makris, P. Lambropoulos, and A. Mihelič, *Theory of Multiphoton Multielectron Ionization of Xenon under Strong 93-eV Radiation*, *Phys. Rev. Lett.* **102**, 033002 (2009).
- [94] Y.-J. Chen, S. Pabst, A. Karamatskou, and R. Santra, *Theoretical characterization of the collective resonance states underlying the xenon giant dipole resonance*, *Phys. Rev. A* **91**, 032503 (2015).
- [95] I. V. Hertel and C.-P. Schulz, *Atome, Moleküle und optische Physik I. Atomphysik und Grundlagen der Spektroskopie*, Springer-Lehrbuch (Springer, Berlin, Heidelberg, 2008).
- [96] J. M. Holton, *A beginner's guide to radiation damage*, *J. Synchrotron Rad.* **16**, 133 (2009).
- [97] Z. Jurek and G. Faigel, *The effect of inhomogenities on single-molecule imaging by hard XFEL pulses*, *EPL* **86**, 68003 (2009).
- [98] M. Hoener, L. Fang, O. Kornilov, O. Gessner, S. T. Pratt, M. Gühr, E. P. Kanter, C. Blaga, et al., *Ultraintense X-Ray Induced Ionization, Dissociation, and Frustrated Absorption in Molecular Nitrogen*, *Phys. Rev. Lett.* **104**, 253002 (2010).
- [99] Z. Jurek, G. Faigel, and M. Tegze, *Dynamics in a cluster under the influence of intense femtosecond hard X-ray pulses*, English, *Eur. Phys. J. D* **29**, 217 (2004).
- [100] B. Ziaja, Z. Jurek, V. Saxena, and R. Santra, *Modeling of Nanoplasmas Created from Finite Systems by Ultrafast Intense X-ray Pulses*, *Contrib. Plasma Phys.* **55**, 58 (2015).
- [101] H. Thomas, A. Helal, K. Hoffmann, N. Kandadai, J. Keto, J. Andreasson, B. Iwan, M. Seibert, et al., *Explosions of Xenon Clusters in Ultraintense Femtosecond X-Ray Pulses from the LCLS Free Electron Laser*, *Phys. Rev. Lett.* **108**, 133401 (2012).
- [102] M. Krikunova, M. Adolph, T. Gorkhover, D. Rupp, S. Schorb, C. Bostedt, S. Roling, B. Siemer, et al., *Ionization dynamics in expanding clusters studied by XUV pump-probe spectroscopy*, *J. Phys. B: At. Mol. Opt. Phys.* **45**, 10 (2012).
- [103] A. Thompson, D. Attwood, E. Gullikson, M. Howells, K.-J. Kim, J. Kirz, J. Kortright, I. Lindau, et al., *X-Ray Data Booklet* (Lawrence Berkeley National Laboratory, University of California, 2009).
- [104] S. P. Hau-Riege, R. A. London, and A. Szoke, *Dynamics of biological molecules irradiated by short x-ray pulses*, *Phys. Rev. E* **69**, 051906 (2004).
- [105] B. F. Murphy, L. Fang, M.-H. Chen, J. D. Bozek, E. Kukk, E. P. Kanter, M. Messerschmidt, T. Osipov, and N. Berrah, *Multiphoton L-shell ionization of H<sub>2</sub>S using intense x-ray pulses from a free-electron laser*, *Phys. Rev. A* **86**, 053423 (2012).

- [106] C. Domesle, S. Dziarzhytski, N. Guerassimova, L. S. Harbo, O. Heber, L. Lammich, B. Jordon-Thaden, R. Treusch, A. Wolf, and H. B. Pedersen, *Photoionization and fragmentation of  $H_3O^+$  under XUV irradiation*, *Phys. Rev. A* **88**, 043405 (2013).
- [107] B. Erk, D. Rolles, L. Foucar, B. Rudek, S. W. Epp, M. Cryle, C. Bostedt, S. Schorb, et al., *Inner-shell multiple ionization of polyatomic molecules with an intense x-ray free-electron laser studied by coincident ion momentum imaging*, *J. Phys. B: At. Mol. Opt. Phys.* **46**, 164031 (2013).
- [108] B. Erk, D. Rolles, L. Foucar, B. Rudek, S. W. Epp, M. Cryle, C. Bostedt, S. Schorb, et al., *Ultrafast Charge Rearrangement and Nuclear Dynamics upon Inner-Shell Multiple Ionization of Small Polyatomic Molecules*, *Phys. Rev. Lett.* **110**, 053003 (2013).
- [109] H. Wabnitz, L. Bittner, A. R. B de Castro, R. Döhrmann, P. Gürtler, T. Laarmann, W. Laasch, J. Schulz, et al., *Multiple ionization of atom clusters by intense soft X-rays from a free-electron laser*, *Nature* **420**, 482 (2002).
- [110] R. Santra and C. H. Greene, *Xenon Clusters in Intense VUV Laser Fields*, *Phys. Rev. Lett.* **91**, 233401 (2003).
- [111] C. Siedschlag and J.-M. Rost, *Small Rare-Gas Clusters in Soft X-Ray Pulses*, *Phys. Rev. Lett.* **93**, 043402 (2004).
- [112] C. Bostedt, H. Thomas, M. Hoener, T. Moeller, U. Saalman, I. Georgescu, C. Gnodtke, and J.-M. Rost, *Fast electrons from multi-electron dynamics in xenon clusters induced by inner-shell ionization*, *New J. Phys.* **12**, 083004 (2010).
- [113] T. Gorkhover, M. Adolph, D. Rupp, S. Schorb, S. W. Epp, B. Erk, L. Foucar, R. Hartmann, et al., *Nanoplasma Dynamics of Single Large Xenon Clusters Irradiated with Superintense X-Ray Pulses from the Linac Coherent Light Source Free-Electron Laser*, *Phys. Rev. Lett.* **108**, 245005 (2012).
- [114] L. S. Cederbaum, J. Zobeley, and F. Tarantelli, *Giant Intermolecular Decay and Fragmentation of Clusters*, *Phys. Rev. Lett.* **79**, 4778 (1997).
- [115] R. Santra and L. S. Cederbaum, *Coulombic Energy Transfer and Triple Ionization in Clusters*, *Phys. Rev. Lett.* **90**, 153401 (2003).
- [116] T. Jahnke, H. Sann, T. Havermeier, K. Kreidi, C. Stuck, M. Meckel, M. Schoeffler, N. Neumann, et al., *Ultrafast energy transfer between water molecules*, *Nat. Phys.* **6**, 139 (2010).
- [117] R. W. Dunford, S. H. Southworth, D. Ray, E. P. Kanter, B. Krässig, L. Young, D. A. Arms, E. M. Dufresne, et al., *Evidence for interatomic Coulombic decay in Xe K-shell-vacancy decay of  $XeF_2$* , *Phys. Rev. A* **86**, 033401 (2012).
- [118] K. Schnorr, A. Senftleben, M. Kurka, A. Rudenko, L. Foucar, G. Schmid, A. Broska, T. Pfeifer, et al., *Time-Resolved Measurement of Interatomic Coulombic Decay in  $Ne_2$* , *Phys. Rev. Lett.* **111**, 093402 (2013).
- [119] S. M. Vinko, O. Ciricosta, B. I. Cho, K. Engelhorn, H.-K. Chung, C. R. D. Brown, T. Burian, J. Chalupsky, et al., *Creation and diagnosis of a solid-density plasma with an X-ray free-electron laser*, *Nature* **482**, 59 (2012).

- [120] O. Ciricosta, S. M. Vinko, H.-K. Chung, B.-I. Cho, C. R. D. Brown, T. Burian, J. Chalupský, K. Engelhorn, et al., *Direct Measurements of the Ionization Potential Depression in a Dense Plasma*, *Phys. Rev. Lett.* **109**, 065002 (2012).
- [121] S. M. Vinko, O. Ciricosta, T. R. Preston, D. S. Rackstraw, C. R. D. Brown, T. Burian, J. Chalupsky, B. I. Cho, et al., *Investigation of femtosecond collisional ionization rates in a solid-density aluminium plasma*, *Nat. Commun.* **6**, 6397 (2015).
- [122] J. C. Stewart and K. D. Pyatt, *Lowering of Ionization Potentials in Plasmas*, *Astrophys. J.* **144**, 1203 (1966).
- [123] S.-K. Son, R. Thiele, Z. Jurek, B. Ziaja, and R. Santra, *Quantum-Mechanical Calculation of Ionization-Potential Lowering in Dense Plasmas*, *Phys. Rev. X* **4**, 031004 (2014).
- [124] S. M. Vinko, O. Ciricosta, and J. S. Wark, *Density functional theory calculations of continuum lowering in strongly coupled plasmas*, *Nat. Commun.* **5**, 3533 (2014).
- [125] T. E. Glover, D. M. Fritz, M. Cammarata, T. K. Allison, S. Coh, J. M. Feldkamp, H. Lemke, D. Zhu, et al., *X-ray and optical wave mixing*, *Nature* **488**, 603 (2012).
- [126] S. Shwartz, M. Fuchs, J. B. Hastings, Y. Inubushi, T. Ishikawa, T. Katayama, D. A. Reis, T. Sato, et al., *X-Ray Second Harmonic Generation*, *Phys. Rev. Lett.* **112**, 163901 (2014).
- [127] K. Tamasaku, E. Shigemasa, Y. Inubushi, T. Katayama, K. Sawada, H. Yumoto, H. Ohashi, H. Mimura, et al., *X-ray two-photon absorption competing against single and sequential multiphoton processes*, *Nat. Photonics* **8**, 313 (2014).
- [128] H. Haken and H. C. Wolf, *Molekülphysik und Quantenchemie. Einführung in die experimentellen und theoretischen Grundlagen*, Springer-Lehrbuch (Springer, Berlin, Heidelberg, 2006).
- [129] C. Weninger, M. Purvis, D. Ryan, R. A. London, J. D. Bozek, C. Bostedt, A. Graf, G. Brown, J. J. Rocca, and N. Rohringer, *Stimulated Electronic X-Ray Raman Scattering*, *Phys. Rev. Lett.* **111**, 233902 (2013).
- [130] C. Weninger and N. Rohringer, *Stimulated resonant x-ray Raman scattering with incoherent radiation*, *Phys. Rev. A* **88**, 053421 (2013).
- [131] M. Beye, S. Schreck, F. Sorgenfrei, C. Trabant, N. Pontius, C. Schuessler-Langeheine, W. Wurth, and A. Foehlich, *Stimulated X-ray emission for materials science*, *Nature* **501**, 191 (2013).
- [132] M. Leitner, *Studying Atomic Dynamics with Coherent X-rays*, Springer Theses (Springer, Berlin, Heidelberg, 2012).
- [133] S. K. Sinha, Z. Jiang, and L. B. Lurio, *X-ray Photon Correlation Spectroscopy Studies of Surfaces and Thin Films*, *Adv. Mater.* **26**, 7764 (2014).
- [134] M. Leitner, B. Sepiol, L.-M. Stadler, B. Pfau, and G. Vogl, *Atomic diffusion studied with coherent X-rays*, *Nat. Mater.* **8**, 717 (2009).
- [135] G. B. Stephenson, A. Robert, and G. Grübel, *Revealing the atomic dance*, *Nat. Mater.* **8**, 702 (2009).

- [136] S. O. Hruszkewycz, M. Sutton, P. H. Fuoss, B. Adams, S. Rosenkranz, K. F. Ludwig, W. Roseker, D. Fritz, et al., *High Contrast X-ray Speckle from Atomic-Scale Order in Liquids and Glasses*, *Phys. Rev. Lett.* **109**, 185502 (2012).
- [137] M. Krikunova, T. Maltezopoulos, P. Wessels, M. Schlie, A. Azima, T. Gaumnitz, T. Gebert, M. Wieland, and M. Drescher, *Strong-field ionization of molecular iodine traced with XUV pulses from a free-electron laser*, *Phys. Rev. A* **86**, 043430 (2012).
- [138] K. Schnorr, A. Senftleben, M. Kurka, A. Rudenko, G. Schmid, T. Pfeifer, K. Meyer, M. Kübel, et al., *Electron Rearrangement Dynamics in Dissociating  $I_2^+$  Molecules Accessed by Extreme Ultraviolet Pump-Probe Experiments*, *Phys. Rev. Lett.* **113**, 073001 (2014).
- [139] P. Beaud, A. Caviezel, S. O. Mariager, L. Rettig, G. Ingold, C. Dornes, S.-W. Huang, J. A. Johnson, et al., *A time-dependent order parameter for ultrafast photoinduced phase transitions*, *Nat. Mater.* **13**, 923 (2014).
- [140] W. Zhang, R. Alonso-Mori, U. Bergmann, C. Bressler, M. Chollet, A. Galler, W. Gawelda, R. G. Hadt, et al., *Tracking excited-state charge and spin dynamics in iron coordination complexes*, *Nature* **509**, 345 (2014).
- [141] K. S. Burley, H. M. Berman, et al., *RCSB Protein Data Bank*, <http://www.rcsb.org/pdb/>, [Online; accessed 2 September 2015], 2015.
- [142] H. N. Chapman and K. A. Nugent, *Coherent lensless X-ray imaging*, *Nat. Photonics* **4**, 833 (2010).
- [143] B. Rupp, *Biomolecular Crystallography. Principles, Practice, and Application to Structural Biology* (Garland Science, New York, 2010).
- [144] X.-C. Bai, G. McMullan, and S. H. W. Scheres, *How cryo-EM is revolutionizing structural biology*, *Trends Biochem. Sci.* **40**, 49 (2015).
- [145] I. D. Campbell, *The march of structural biology*, *Nat. Rev. Mol. Cell Biol.* **3**, 377 (2002).
- [146] H. M. Berman, J. Westbrook, Z. Feng, G. Gilliland, T. N. Bhat, H. Weissig, I. N. Shindyalov, and P. E. Bourne, *The Protein Data Bank*, *Nucleic Acids Res.* **28**, 235 (2000).
- [147] T. L. Blundell, H. Jhoti, and C. Abell, *High-throughput crystallography for lead discovery in drug design*, *Nat. Rev. Drug Discovery* **1**, 45 (2002).
- [148] G. Scapin, D. Patel, and E. Arnold, eds., *Multifaceted Roles of Crystallography in Modern Drug Discovery*, NATO Science for Peace and Security Series A: Chemistry and Biology (Springer Netherlands, 2015).
- [149] H. N. Chapman, C. Caleman, and N. Timneanu, *Diffraction before destruction*, *Phil. Trans. R. Soc. B* **369**, 20130313 (2014).
- [150] L. Lomb, T. R. M. Barends, S. Kassemeyer, A. Aquila, S. W. Epp, B. Erk, L. Foucar, R. Hartmann, et al., *Radiation damage in protein serial femtosecond crystallography using an x-ray free-electron laser*, *Phys. Rev. B* **84**, 214111 (2011).

- [151] L. Redecke, K. Nass, D. P. DePonte, T. A. White, D. Rehders, A. Barty, F. Stellato, M. Liang, et al., *Natively Inhibited Trypanosoma brucei Cathepsin B Structure Determined by Using an X-ray Laser*, *Science* **339**, 227 (2013).
- [152] R. Neutze, R. Wouts, D. van der Spoel, E. Weckert, and J. Hajdu, *Potential for biomolecular imaging with femtosecond X-ray pulses*, *Nature* **406**, 752 (2000).
- [153] H. N. Chapman, *X-ray imaging beyond the limits*, *Nat. Mater.* **8**, 299 (2009).
- [154] A. Barty, J. Küpper, and H. N. Chapman, *Molecular Imaging Using X-Ray Free-Electron Lasers*, *Annu. Rev. Phys. Chem.* **64**, 415 (2013).
- [155] K. J. Gaffney and H. N. Chapman, *Imaging Atomic Structure and Dynamics with Ultrafast X-ray Scattering*, *Science* **316**, 1444 (2007).
- [156] U. Lorenz, N. M. Kabachnik, E. Weckert, and I. A. Vartanyants, *Impact of ultrafast electronic damage in single-particle x-ray imaging experiments*, *Phys. Rev. E* **86**, 051911 (2012).
- [157] J. M. Slowik, S.-K. Son, G. Dixit, Z. Jurek, and R. Santra, *Incoherent x-ray scattering in single molecule imaging*, *New J. Phys.* **16**, 073042 (2014).
- [158] A. Barty, C. Caleman, A. Aquila, N. Timneanu, L. Lomb, T. A. White, J. Andreasson, D. Arnlund, et al., *Self-terminating diffraction gates femtosecond X-ray nanocrystallography measurements*, *Nat. Photonics* **6**, 35 (2012).
- [159] S. Kassemeyer, J. Steinbrener, L. Lomb, E. Hartmann, A. Aquila, A. Barty, A. V. Martin, C. Y. Hampton, et al., *Femtosecond free-electron laser x-ray diffraction data sets for algorithm development*, *Opt. Express* **20**, 4149 (2012).
- [160] T. A. White, A. Barty, F. Stellato, J. M. Holton, R. A. Kirian, N. A. Zatsepin, and H. N. Chapman, *Crystallographic data processing for free-electron laser sources*, *Acta Crystallogr., Sect. D: Biol. Crystallogr.* **69**, 1231 (2013).
- [161] A. Barty, R. A. Kirian, F. R. N. C. Maia, M. Hantke, C. H. Yoon, T. A. White, and H. Chapman, *Cheetah: software for high-throughput reduction and analysis of serial femtosecond X-ray diffraction data*, *J. Appl. Crystallogr.* **47**, 1118 (2014).
- [162] O. M. Yefanov and I. A. Vartanyants, *Orientation determination in single-particle x-ray coherent diffraction imaging experiments*, *J. Phys. B: At. Mol. Opt. Phys.* **46**, 16 (2013).
- [163] O. Yefanov, C. Gati, G. Bourenkov, R. A. Kirian, T. A. White, J. C. H. Spence, H. N. Chapman, and A. Barty, *Mapping the continuous reciprocal space intensity distribution of X-ray serial crystallography*, *Phil. Trans. R. Soc. B* **369**, 20130333 (2014).
- [164] P. J. Ho and R. Santra, *Theory of x-ray diffraction from laser-aligned symmetric-top molecules*, *Phys. Rev. A* **78**, 053409 (2008).
- [165] C. J. Hensley, J. Yang, and M. Centurion, *Imaging of Isolated Molecules with Ultrafast Electron Pulses*, *Phys. Rev. Lett.* **109**, 133202 (2012).
- [166] R. Boll, D. Anielski, C. Bostedt, J. D. Bozek, L. Christensen, R. Coffee, S. De, P. Declava, et al., *Femtosecond photoelectron diffraction on laser-aligned molecules: Towards time-resolved imaging of molecular structure*, *Phys. Rev. A* **88**, 061402 (2013).

- [167] J. Küpper, S. Stern, L. Holmegaard, F. Filsinger, A. Rouzée, A. Rudenko, P. Johnsson, A. V. Martin, et al., *X-Ray Diffraction from Isolated and Strongly Aligned Gas-Phase Molecules with a Free-Electron Laser*, *Phys. Rev. Lett.* **112**, 083002 (2014).
- [168] G. Taylor, *The phase problem*, *Acta Cryst. D* **59**, 1881 (2003).
- [169] A. Nischwitz, M. Fischer, P. Haberäcker, and G. Socher, *Computergrafik und Bildverarbeitung. Band II: Bildverarbeitung*, 3rd ed. (Vieweg+Teubner Verlag, 2011).
- [170] J. Miao, T. Ishikawa, E. H. Anderson, and K. O. Hodgson, *Phase retrieval of diffraction patterns from noncrystalline samples using the oversampling method*, *Phys. Rev. B* **67**, 174104 (2003).
- [171] J. Miao, C.-C. Chen, C. Song, Y. Nishino, Y. Kohmura, T. Ishikawa, D. Ramunno-Johnson, T.-K. Lee, and S. H. Risbud, *Three-Dimensional GaN-Ga<sub>2</sub>O<sub>3</sub> Core Shell Structure Revealed by X-Ray Diffraction Microscopy*, *Phys. Rev. Lett.* **97**, 215503 (2006).
- [172] J. Miao, T. Ishikawa, Q. Shen, and T. Earnest, *Extending X-ray crystallography to allow the imaging of noncrystalline materials, cells, and single protein complexes*, *Annu. Rev. Phys. Chem.* **59**, 387 (2008).
- [173] J. C. H. Spence, R. A. Kirian, X. Wang, U. Weierstall, K. E. Schmidt, T. White, A. Barty, H. N. Chapman, S. Marchesini, and J. Holton, *Phasing of coherent femtosecond X-ray diffraction from size-varying nanocrystals*, *Opt. Express* **19**, 2866 (2011).
- [174] R. A. Kirian, R. J. Bean, K. R. Beyerlein, M. Barthelmess, C. H. Yoon, F. Wang, F. Capotondi, E. Pedersoli, A. Barty, and H. N. Chapman, *Direct Phasing of Finite Crystals Illuminated with a Free-Electron Laser*, *Phys. Rev. X* **5**, 011015 (2015).
- [175] R. P. Millane and J. P. J. Chen, *Aspects of direct phasing in femtosecond nanocrystallography*, *Phil. Trans. R. Soc. B* **369**, 20130498 (2014).
- [176] S.-K. Son, H. N. Chapman, and R. Santra, *Multiwavelength Anomalous Diffraction at High X-Ray Intensity*, *Phys. Rev. Lett.* **107**, 218102 (2011).
- [177] H. N. Chapman, A. Barty, M. J. Bogan, S. Boutet, M. Frank, S. P. Hau-Riege, S. Marchesini, B. W. Woods, et al., *Femtosecond diffractive imaging with a soft-X-ray free-electron laser*, *Nat. Phys.* **2**, 839 (2006).
- [178] R. B. G. Ravelli, H.-K. S. Leiros, B. Pan, M. Caffrey, and S. McSweeney, *Specific Radiation Damage Can Be Used to Solve Macromolecular Crystal Structures*, *Structure* **11**, 217 (2003).
- [179] S. Banumathi, P. H. Zwart, U. A. Ramagopal, M. Dauter, and Z. Dauter, *Structural effects of radiation damage and its potential for phasing*, *Acta Cryst. D* **60**, 1085 (2004).
- [180] S.-K. Son, H. N. Chapman, and R. Santra, *Determination of multiwavelength anomalous diffraction coefficients at high x-ray intensity*, *J. Phys. B: At. Mol. Opt. Phys.* **46**, 164015 (2013).
- [181] M. M. Seibert, T. Ekeberg, F. R. N. C. Maia, M. Svenda, J. Andreasson, O. Joensuu, D. Odic, B. Iwan, et al., *Single mimivirus particles intercepted and imaged with an X-ray laser*, *Nature* **470**, 78 (2011).

- [182] H. N. Chapman, P. Fromme, A. Barty, T. A. White, R. A. Kirian, A. Aquila, M. S. Hunter, J. Schulz, et al., *Femtosecond X-ray protein nanocrystallography*, [Nature](#) **470**, 73 (2011).
- [183] R. Koopmann, K. Cupelli, L. Redecke, K. Nass, D. P. DePonte, T. A. White, F. Stellato, D. Rehders, et al., *In vivo protein crystallization opens new routes in structural biology*, [Nat. Methods](#) **9**, 259 (2012).
- [184] L. C. Johansson, D. Arnlund, T. A. White, G. Katona, D. P. DePonte, U. Weierstall, R. B. Doak, R. L. Shoeman, et al., *Lipidic phase membrane protein serial femtosecond crystallography*, [Nat. Methods](#) **9**, 263 (2012).
- [185] P. Jordan, P. Fromme, H. T. Witt, O. Klukas, W. Saenger, and N. Krauss, *Three-dimensional structure of cyanobacterial photosystem I at 2.5 Å resolution*, [Nature](#) **411**, 909 (2001).
- [186] M. Liang, G. J. Williams, M. Messerschmidt, M. M. Seibert, P. A. Montanez, M. Hayes, D. Milathianaki, A. Aquila, et al., *The Coherent X-ray Imaging instrument at the Linac Coherent Light Source*, [J. Synchrotron Rad.](#) **22**, 514 (2015).
- [187] S. Boutet, L. Lomb, G. J. Williams, T. R. M. Barends, A. Aquila, R. B. Doak, U. Weierstall, D. P. DePonte, et al., *High-Resolution Protein Structure Determination by Serial Femtosecond Crystallography*, [Science](#) **337**, 362 (2012).
- [188] A. Cho, *News Flash: X-ray Laser Produces First Protein Structure*, [Science](#) **338**, 1136 (2012).
- [189] J. Kern, R. Alonso-Mori, J. Hellmich, R. Tran, J. Hattne, H. Laksmono, G. Carina, N. Echols, et al., *Room temperature femtosecond X-ray diffraction of photosystem II microcrystals*, [PNAS](#) **109**, 9721 (2012).
- [190] W. Liu, D. Wacker, C. Gati, G. W. Han, D. James, D. Wang, G. Nelson, U. Weierstall, et al., *Serial Femtosecond Crystallography of G Protein-Coupled Receptors*, [Science](#) **342**, 1521 (2013).
- [191] L. C. Johansson, D. Arnlund, G. Katona, T. A. White, A. Barty, D. P. DePonte, R. L. Shoeman, C. Wickstrand, et al., *Structure of a photosynthetic reaction centre determined by serial femtosecond crystallography*, [Nat. Commun.](#) **4**, 2911 (2013).
- [192] M. Sugahara, E. Mizohata, E. Nango, M. Suzuki, T. Tanaka, T. Masudala, R. Tanaka, T. Shimamura, et al., *Grease matrix as a versatile carrier of proteins for serial crystallography*, [Nat. Methods](#) **12**, 61 (2015).
- [193] H. Zhang, H. Unal, C. Gati, G. W. Han, W. Liu, N. A. Zatsepin, D. James, D. Wang, et al., *Structure of the Angiotensin Receptor Revealed by Serial Femtosecond Crystallography*, [Cell](#) **161**, 833 (2015).
- [194] H. M. Ginn, M. Messerschmidt, X. Ji, H. Zhang, D. Axford, R. J. Gildea, G. Winter, A. S. Brewster, et al., *Structure of CPV17 polyhedrin determined by the improved analysis of serial femtosecond crystallographic data*, [Nat. Commun.](#) **6**, 6435 (2015).

- [195] C. Gati, G. Bourenkov, M. Klinge, D. Rehders, F. Stellato, D. Oberthür, O. Yefanov, B. P. Sommer, et al., *Serial crystallography on in vivo grown microcrystals using synchrotron radiation*, *IUCrJ* **1**, 87 (2014).
- [196] A. Barty, *Time-resolved imaging using x-ray free electron lasers*, *J. Phys. B: At. Mol. Opt. Phys.* **43**, 194014 (2010).
- [197] C. M. Guenther, B. Pfau, R. Mitzner, B. Siemer, S. Roling, H. Zacharias, O. Kutz, I. Rudolph, et al., *Sequential femtosecond X-ray imaging*, *Nat. Photonics* **5**, 99 (2011).
- [198] J. Tenboer, S. Basu, N. Zatsepin, K. Pande, D. Milathianaki, M. Frank, M. Hunter, S. Boutet, et al., *Time-resolved serial crystallography captures high-resolution intermediates of photoactive yellow protein*, *Science* **346**, 1242 (2014).
- [199] C. Kupitz, S. Basu, I. Grotjohann, R. Fromme, N. A. Zatsepin, K. N. Rendek, M. S. Hunter, R. L. Shoeman, et al., *Serial time-resolved crystallography of photosystem II using a femtosecond X-ray laser*, *Nature* **513**, 261 (2014).
- [200] A. Aquila, M. S. Hunter, R. B. Doak, R. A. Kirian, P. Fromme, T. A. White, J. Andreasson, D. Arnlund, et al., *Time-resolved protein nanocrystallography using an X-ray free-electron laser*, *Opt. Express* **20**, 2706 (2012).
- [201] C. Bostedt, E. Eremina, D. Rupp, M. Adolph, H. Thomas, M. Hoener, A. R. B. de Castro, J. Tiggesbäumker, et al., *Ultrafast X-Ray Scattering of Xenon Nanoparticles: Imaging Transient States of Matter*, *Phys. Rev. Lett.* **108**, 093401 (2012).
- [202] G. Dixit, J. M. Slowik, and R. Santra, *Proposed Imaging of the Ultrafast Electronic Motion in Samples using X-Ray Phase Contrast*, *Phys. Rev. Lett.* **110**, 137403 (2013).
- [203] G. Dixit and R. Santra, *Role of electron-electron interference in ultrafast time-resolved imaging of electronic wavepackets*, *J. Chem. Phys.* **138**, 134311 (2013).
- [204] M. J. J. Vrakking and T. Elsaesser, *X-Ray photonics: X-rays inspire electron movies*, *Nat. Photonics* **6**, 645 (2012).
- [205] F. Zamponi, P. Rothhardt, J. Stingl, M. Woerner, and T. Elsaesser, *Ultrafast large-amplitude relocation of electronic charge in ionic crystals*, *PNAS* **109**, 5207 (2012).
- [206] H. N. Chapman, S.-P. Hau-Riege, M. J. Bogan, S. Bajt, A. Barty, S. Boutet, S. Marchesini, M. Frank, et al., *Femtosecond time-delay X-ray holography*, *Nature* **448**, 676 (2007).
- [207] M. P. Minitti, J. M. Budarz, A. Kirrander, J. S. Robinson, D. Ratner, T. J. Lane, D. Zhu, J. M. Glowacki, et al., *Imaging Molecular Motion: Femtosecond X-Ray Scattering of an Electrocyclic Chemical Reaction*, *Phys. Rev. Lett.* **114**, 255501 (2015).
- [208] T. R. M. Barends, L. Foucar, S. Botha, R. B. Doak, R. L. Shoeman, K. Nass, J. E. Koglin, G. J. Williams, et al., *De novo protein crystal structure determination from X-ray free-electron laser data*, *Nature* **505**, 244 (2014).
- [209] R. Thiele, S.-K. Son, B. Ziaja, and R. Santra, *Effect of screening by external charges on the atomic orbitals and photoinduced processes within the Hartree-Fock-Slater atom*, *Phys. Rev. A* **86**, 033411 (2012).

- [210] N. Medvedev, B. Ziaja, M. Cammarata, M. Harmand, and S. Toleikis, *Electron Kinetics in Femtosecond X-Ray Irradiated SiO<sub>2</sub>*, *Contrib. Plasma Phys.* **53**, 347 (2013).
- [211] A. Leonov, D. Ksenzov, A. Benediktovitch, I. Feranchuk, and U. Pietsch, *Time dependence of X-ray polarizability of a crystal induced by an intense femtosecond X-ray pulse*, *IUCrJ* **1**, 402 (2014).
- [212] M. Protopapas, C. H. Keitel, and P. L. Knight, *Atomic physics with super-high intensity lasers*, *Rep. Prog. Phys.* **60**, 389 (1997).
- [213] M. Y. Ivanov, M. Spanner, and O. Smirnova, *Anatomy of strong field ionization*, *J. Mod. Opt.* **52**, 165 (2005).
- [214] S.-K. Son and R. Santra, *Monte Carlo calculation of ion, electron, and photon spectra of xenon atoms in x-ray free-electron laser pulses*, *Phys. Rev. A* **85**, 063415 (2012).
- [215] Z. Jurek, R. Thiele, B. Ziaja, and R. Santra, *Effect of two-particle correlations on x-ray coherent diffractive imaging studies performed with continuum models*, *Phys. Rev. E* **86**, 036411 (2012).
- [216] B. Ziaja, H. N. Chapman, R. Fäustlin, S. Hau-Riege, Z. Jurek, A. V. Martin, S. Toleikis, F. Wang, E. Weckert, and R. Santra, *Limitations of coherent diffractive imaging of single objects due to their damage by intense x-ray radiation*, *New J. Phys.* **14**, 115015 (2012).
- [217] N. Rohringer and R. Santra, *Resonant Auger effect at high x-ray intensity*, *Phys. Rev. A* **77**, 053404 (2008).
- [218] P. V. Demekhin and L. S. Cederbaum, *Strong interference effects in the resonant Auger decay of atoms induced by intense x-ray fields*, *Phys. Rev. A* **83**, 023422 (2011).
- [219] E. P. Kanter, B. Krässig, Y. Li, A. M. March, P. Ho, N. Rohringer, R. Santra, S. H. Southworth, et al., *Unveiling and Driving Hidden Resonances with High-Fluence, High-Intensity X-Ray Pulses*, *Phys. Rev. Lett.* **107**, 233001 (2011).
- [220] S. Pabst, L. Greenman, P. J. Ho, D. A. Mazziotti, and R. Santra, *Decoherence in Attosecond Photoionization*, *Phys. Rev. Lett.* **106**, 053003 (2011).
- [221] N. Rohringer and R. Santra, *Strongly driven resonant Auger effect treated by an open-quantum-system approach*, *Phys. Rev. A* **86**, 043434 (2012).
- [222] P. V. Demekhin and L. S. Cederbaum, *Dynamic Interference of Photoelectrons Produced by High-Frequency Laser Pulses*, *Phys. Rev. Lett.* **108**, 253001 (2012).
- [223] D. Hochstuhl, C. M. Hinz, and M. Bonitz, *Time-dependent multiconfiguration methods for the numerical simulation of photoionization processes of many-electron atoms*, *Eur. Phys. J.-Spec. Top.* **223**, 177 (2014).
- [224] A. D. McLachlan and M. A. Ball, *Time-Dependent Hartree-Fock Theory for Molecules*, *Rev. Mod. Phys.* **36**, 844 (1964).
- [225] K. C. Kulander, *Time-dependent Hartree-Fock theory of multiphoton ionization: Helium*, *Phys. Rev. A* **36**, 2726 (1987).

- [226] M. S. Pindzola, P. Gavras, and T. W. Gorczyca, *Time-dependent unrestricted Hartree-Fock theory for the multiphoton ionization of atoms*, *Phys. Rev. A* **51**, 3999 (1995).
- [227] A. J. Tolley, *A new model for intense laser-atom interactions in helium*, *J. Phys. B: At. Mol. Opt. Phys.* **32**, 3449 (1999).
- [228] T. Sato and K. L. Ishikawa, *The structure of approximate two electron wavefunctions in intense laser driven ionization dynamics*, *J. Phys. B: At. Mol. Opt. Phys.* **47**, 204031 (2014).
- [229] D. Hochstuhl, S. Bauch, and M. Bonitz, *Multiconfigurational time-dependent Hartree-Fock calculations for photoionization of one-dimensional Helium*, *J. Phys. Conf. Ser.* **220**, 012019 (2010).
- [230] M. Bonitz, D. Hochstuhl, S. Bauch, and K. Balzer, *Quantum Kinetic Approach to Time-Resolved Photoionization of Atoms*, *Contrib. Plasma Phys.* **50**, 54 (2010).
- [231] N. E. Dahlen, A. Stan, and R. van Leeuwen, *Nonequilibrium Green function theory for excitation and transport in atoms and molecules*, *J. Phys. Conf. Ser.* **35**, 324 (2006).
- [232] K. Balzer, S. Bauch, and M. Bonitz, *Efficient grid-based method in nonequilibrium Green's function calculations: Application to model atoms and molecules*, *Phys. Rev. A* **81**, 022510 (2010).
- [233] K. Balzer, S. Bauch, and M. Bonitz, *Finite elements and the discrete variable representation in nonequilibrium Green's function calculations. Atomic and molecular models*, *J. Phys. Conf. Ser.* **220**, 012020 (2010).
- [234] D. Hochstuhl, K. Balzer, S. Bauch, and M. Bonitz, *Nonequilibrium Green function approach to photoionization processes in atoms*, *Physica E* **42**, 513 (2010).
- [235] K. Balzer and M. Bonitz, *Nonequilibrium Green's Functions Approach to Inhomogeneous Systems*, Vol. 867, Lecture Notes in Physics (Springer, Berlin, Heidelberg, 2013).
- [236] L. Greenman, P. J. Ho, S. Pabst, E. Kamarchik, D. A. Mazziotti, and R. Santra, *Implementation of the time-dependent configuration-interaction singles method for atomic strong-field processes*, *Phys. Rev. A* **82**, 023406 (2010).
- [237] N. Rohringer, S. Peter, and J. Burgdörfer, *Calculating state-to-state transition probabilities within time-dependent density-functional theory*, *Phys. Rev. A* **74**, 042512 (2006).
- [238] M. Thiele, E. K. U. Gross, and S. Kümmel, *Adiabatic Approximation in Nonperturbative Time-Dependent Density-Functional Theory*, *Phys. Rev. Lett.* **100**, 153004 (2008).
- [239] C. Sousa, C. de Graaf, A. Rudavskiy, R. Broer, J. Tatchen, M. Etinski, and C. M. Marian, *Ultrafast Deactivation Mechanism of the Excited Singlet in the Light-Induced Spin Crossover of  $Fe(2,2'-bipyridine)_3]^{2+}$* , *Chem. Eur. J.* **19**, 17541 (2013).
- [240] M. A. Marques, N. T. Maitra, F. M. S. Nogueira, E. Gross, and A. Rubio, eds., *Fundamentals of Time-Dependent Density Functional Theory*, Vol. 837, Lecture Notes in Physics (Springer, Berlin, Heidelberg, 2012).

- [241] B. Schäfer-Bung and M. Nest, *Correlated dynamics of electrons with reduced two-electron density matrices*, *Phys. Rev. A* **78**, 012512 (2008).
- [242] A. Akbari, M. J. Hashemi, A. Rubio, R. M. Nieminen, and R. van Leeuwen, *Challenges in truncating the hierarchy of time-dependent reduced density matrices equations*, *Phys. Rev. B* **85**, 235121 (2012).
- [243] V. M. Axt and S. Mukamel, in *Nonlinear optical materials*, Vol. 101, edited by J. V. Moloney, The IMA Volumes in Mathematics and its Applications (Springer New York, 1998), pp. 33–47.
- [244] R. Loudon, *One-Dimensional Hydrogen Atom*, *Am. J. Phys.* **27**, 649 (1959).
- [245] L. K. Haines and D. H. Roberts, *One-Dimensional Hydrogen Atom*, *Am. J. Phys.* **37**, 1145 (1969).
- [246] J. Javanainen, J. H. Eberly, and Q. Su, *Numerical simulations of multiphoton ionization and above-threshold electron spectra*, *Phys. Rev. A* **38**, 3430 (1988).
- [247] Q. Su, J. H. Eberly, and J. Javanainen, *Dynamics of atomic ionization suppression and electron localization in an intense high-frequency radiation field*, *Phys. Rev. Lett.* **64**, 862 (1990).
- [248] Q. Su and J. H. Eberly, *Suppression of ionization and atomic electron localization by short intense laser pulses*, *Phys. Rev. A* **43**, 2474 (1991).
- [249] L. Roso-Franco, A. Sanpera, M. L. Pons, and L. Plaja, *Photoionization of the hydrogen atom: Three-dimensional results and pseudo-one-dimensional model*, *Phys. Rev. A* **44**, 4652 (1991).
- [250] M. S. Pindzola, D. C. Griffin, and C. Bottcher, *Validity of time-dependent Hartree-Fock theory for the multiphoton ionization of atoms*, *Phys. Rev. Lett.* **66**, 2305 (1991).
- [251] D. G. Lappas and R. van Leeuwen, *Electron correlation effects in the double ionization of He*, *J. Phys. B: At. Mol. Opt. Phys.* **31**, L249 (1998).
- [252] M. Lein, E. K. U. Gross, and V. Engel, *Intense-Field Double Ionization of Helium: Identifying the Mechanism*, *Phys. Rev. Lett.* **85**, 4707 (2000).
- [253] C. Ruiz, L. Plaja, and L. Roso, *Lithium Ionization by a Strong Laser Field*, *Phys. Rev. Lett.* **94**, 063002 (2005).
- [254] M. Thiele and S. Kümmel, *Photoabsorption spectra from adiabatically exact time-dependent density-functional theory in real time*, *Phys. Chem. Chem. Phys.* **11**, 4631 (2009).
- [255] D. Hochstuhl and M. Bonitz, *Two-photon ionization of helium studied with the multiconfigurational time-dependent Hartree-Fock method*, *J. Chem. Phys.* **134**, 084106 (2011).
- [256] B. Kaiser, A. Vagov, V. M. Axt, and U. Pietsch, *Ultrafast photoionization dynamics at high laser intensities in the xuv regime*, *Phys. Rev. A* **84**, 043431 (2011).
- [257] S. Bauch and M. Bonitz, *Theoretical description of field-assisted postcollision interaction in Auger decay of atoms*, *Phys. Rev. A* **85**, 053416 (2012).

- [258] F. Grossmann, *Theoretical Femtosecond Physics*, Graduate Texts in Physics (Springer International Publishing, 2013).
- [259] P.-F. Loos, C. J. Ball, and P. M. W. Gill, *Chemistry in one dimension*, *Phys. Chem. Chem. Phys.* **17**, 3196 (2015).
- [260] H. Le Rouzo, *Calculation of band structures by a discrete variable representation based on Bloch functions*, *Am. J. Phys.* **73**, 962 (2005).
- [261] G. Czycholl, *Theoretische Festkörperphysik*, 3rd ed., Springer-Lehrbuch (Springer, Berlin, Heidelberg, 2008).
- [262] A. Brand, *Einfluss zeitabhängiger Formfaktoren auf Röntgenbeugungsmuster bei gepulster Anregung*, Diploma thesis (University of Bayreuth, 2011).
- [263] P. Meystre and M. Sargent III, *Elements of Quantum Optics*, 4th ed. (Springer, Berlin, Heidelberg, 2007).
- [264] G. Grynberg, A. Aspect, and C. Fabre, *Introduction to Quantum Optics. From the Semi-classical Approach to Quantized Light* (Cambridge University Press, 2010).
- [265] C. Buth and R. Santra, *Theory of x-ray absorption by laser-dressed atoms*, *Phys. Rev. A* **75**, 033412 (2007).
- [266] B. W. J. McNeil, N. R. Thompson, and D. J. Dunning, *Transform-Limited X-Ray Pulse Generation from a High-Brightness Self-Amplified Spontaneous-Emission Free-Electron Laser*, *Phys. Rev. Lett.* **110**, 134802 (2013).
- [267] D. Krebs, S. Pabst, and R. Santra, *Introducing many-body physics using atomic spectroscopy*, *Am. J. Phys* **82**, 113 (2014).
- [268] S. Flügge, *Practical Quantum Mechanics*, Vol. 177, Classics in Mathematics (Springer, Berlin, Heidelberg, 1999).
- [269] I. V. Hertel and C.-P. Schulz, *Atome, Moleküle und optische Physik 2. Moleküle und Photonen - Spektroskopie und Streuphysik*, Springer-Lehrbuch (Springer, Berlin, Heidelberg, 2010).
- [270] G. B. Pradhan, J. Jose, P. C. Deshmukh, L. A. LaJohn, R. H. Pratt, and S. T. Manson, *Cooper minima: a window on nondipole photoionization at low energy*, *J. Phys. B: At. Mol. Opt. Phys.* **44**, 201001 (2011).
- [271] P. V. Demekhin, *On the breakdown of the electric dipole approximation for hard x-ray photoionization cross sections*, *J. Phys. B: At. Mol. Opt. Phys.* **47**, 025602 (2014).
- [272] H. R. Varma, M. F. Ciappina, N. Rohringer, and R. Santra, *Above-threshold ionization in the x-ray regime*, *Phys. Rev. A* **80**, 053424 (2009).
- [273] T. Sekikawa, A. Kosuge, T. Kanai, and S. Watanabe, *Nonlinear optics in the extreme ultraviolet*, *Nature* **432**, 605 (2004).
- [274] F. Schwabl, *Quantenmechanik (QM I). Eine Einführung*, 7th ed., Springer-Lehrbuch (Springer, Berlin, Heidelberg, 2007).
- [275] F. Schwabl, *Quantenmechanik für Fortgeschrittene (QM II)*, 5th ed., Springer-Lehrbuch (Springer, Berlin, Heidelberg, 2008).

- [276] T. Tsuneda, *Density Functional Theory in Quantum Chemistry* (Springer Japan, 2014).
- [277] J. C. Slater, *A Simplification of the Hartree-Fock Method*, *Phys. Rev.* **81**, 385 (1951).
- [278] J. H. Hubbell, *Review and history of photon cross section calculations*, *Phys. Med. Biol.* **51**, R245 (2006).
- [279] X. S. Li, S. M. Smith, A. N. Markevitch, D. A. Romanov, R. J. Levis, and H. B. Schlegel, *A time-dependent Hartree-Fock approach for studying the electronic optical response of molecules in intense fields*, *Phys. Chem. Chem. Phys.* **7**, 233 (2005).
- [280] J. A. Maruhn, P.-G. Reinhard, and E. Suraud, *Simple Models of Many-Fermion Systems* (Springer, Berlin, Heidelberg, 2010).
- [281] K. Sekizawa and K. Yabana, *Particle-number projection method in time-dependent Hartree-Fock theory: Properties of reaction products*, *Phys. Rev. C* **90**, 064614 (2014).
- [282] D. N. Fittinghoff, P. R. Bolton, B. Chang, and K. C. Kulander, *Observation of Nonsequential Double Ionization of Helium with Optical Tunneling*, *Phys. Rev. Lett.* **69**, 2642 (1992).
- [283] B. Walker, B. Sheehy, L. F. DiMauro, P. Agostini, K. J. Schafer, and K. C. Kulander, *Precision Measurement of Strong Field Double Ionization of Helium*, *Phys. Rev. Lett.* **73**, 1227 (1994).
- [284] K. J. Schafer, in *Strong Field Laser Physics*, Vol. 134, edited by T. Brabec, Springer Series in Optical Sciences (Springer, New York, 2009), pp. 111–145.
- [285] N. Rohringer and R. Santra, *X-ray nonlinear optical processes using a self-amplified spontaneous emission free-electron laser*, *Phys. Rev. A* **76**, 033416 (2007).
- [286] B. Ziaja, R. A. London, and J. Hajdu, *Ionization by impact electrons in solids: Electron mean free path fitted over a wide energy range*, *J. Appl. Phys.* **99**, 033514 (2006).
- [287] T. Sato, A. Iwasaki, K. Ishibashi, T. Okino, K. Yamanouchi, J. Adachi, A. Yagishita, H. Yazawa, et al., *Determination of the absolute two-photon ionization cross section of He by an XUV free electron laser*, *J. Opt. Soc. Am. B: Opt. Phys.* **44**, 161001 (2011).
- [288] B. Kaiser, A. Brand, M. Glässl, A. Vagov, V. M. Axt, and U. Pietsch, *Photoionization of resonantly driven atomic states by an extreme ultraviolet-free-electron laser: intensity dependence and renormalization of Rabi frequencies*, *New J. Phys.* **15**, 093016 (2013).
- [289] B. L. Beers and L. Armstrong, *Exact solution of a realistic model for two-photon ionization*, *Phys. Rev. A* **12**, 2447 (1975).
- [290] P. L. Knight, *Saturation and Rabi oscillations in resonant multiphoton ionization*, *Opt. Commun.* **22**, 173 (1977).
- [291] P. L. Knight, *AC Stark splitting of bound-continuum decays*, *J. Phys. B: At. Mol. Phys.* **12**, 3297 (1979).
- [292] E. Kyrölä, *N levels and the continuum*, *J. Phys. B: At. Mol. Phys.* **19**, 1437 (1986).

- [293] T. Sako, J. Adachi, A. Yagishita, M. Yabashi, T. Tanaka, M. Nagasono, and T. Ishikawa, *Suppression of ionization probability due to Rabi oscillations in the resonance two-photon ionization of He by EUV free-electron lasers*, *Phys. Rev. A* **84**, 053419 (2011).
- [294] J. Javanainen, *The rotating-wave approximation in bound-free transitions*, *J. Phys. B: At. Mol. Phys.* **16**, 1343 (1983).
- [295] J. Grochmalicki, J. Mostowski, and K. Rzazewski, *Near-threshold ionization of atomic hydrogen*, *Phys. Rev. A* **36**, 2718 (1987).
- [296] R. Loudon, *The Quantum Theory of Light*, 3rd ed. (Oxford University Press Inc., New York, 2003).
- [297] W. Schülke, *Electron Dynamics by Inelastic X-Ray Scattering* (Oxford University Press Inc., New York, 2007).
- [298] H.-K. Chung, M. H. Chen, and R. W. Lee, *Extension of atomic configuration sets of the Non-LTE model in the application to the  $K\alpha$  diagnostics of hot dense matter*, *High Energy Density Phys.* **3**, 57 (2007).
- [299] A. Brand, B. Kaiser, A. Vagov, V. M. Axt, and U. Pietsch, *Non-Markovian behavior of ultrafast coherent ionization dynamics in a crystal exposed to a seeded free-electron-laser pulse*, *Phys. Rev. A* **89**, 063404 (2014).
- [300] F. Rossi and T. Kuhn, *Theory of ultrafast phenomena in photoexcited semiconductors*, *Rev. Mod. Phys.* **74**, 895 (2002).
- [301] G. Zschornack, *Handbook of X-Ray Data* (Springer, Berlin, Heidelberg, 2007).
- [302] A. Brand, B. Kaiser, A. Vagov, V. M. Axt, and U. Pietsch, *Model study on how an ordered grouping of atoms affects their inner-shell photoionization*, *Phys. Rev. A* **92**, 033424 (2015).
- [303] F. Cooper, A. Khare, and U. Sukhatme, *Supersymmetry and quantum mechanics*, *Phys. Rep.* **251**, 267 (1995).
- [304] J. Lekner, *Reflectionless eigenstates of the  $\text{sech}^2$  potential*, *Am. J. Phys.* **75**, 1151 (2007).
- [305] M. R. Nadler and C. P. Kempier, *Crystallographic Data 186. Lithium*, *Anal. Chem.* **31**, 2109 (1959).
- [306] C. Kittel, *Einführung in die Festkörperphysik*, 14. (Oldenbourg, 2006).
- [307] P. W. Anderson, *Absence of Diffusion in Certain Random Lattices*, *Phys. Rev.* **109**, 1492 (1958).
- [308] P. A. Lee and T. V. Ramakrishnan, *Disordered electronic systems*, *Rev. Mod. Phys.* **57**, 287 (1985).
- [309] N. E. Hurt, *Mathematical Physics of Quantum Wires and Devices. From Spectral Resonances to Anderson Localization*, Vol. 506, Mathematics and Its Applications (Springer Netherlands, 2000).
- [310] A. Lagendijk, B. van Tiggelen, and D. S. Wiersma, *Fifty years of Anderson localization*, *Phys. Today* **62**, 24 (2009).

- [311] P. Phillips, *Anderson Localization and the Exceptions*, *Annu. Rev. Phys. Chem.* **44**, 115 (1993).
- [312] N. F. Mott and W. D. Twose, *The Theory of Impurity Conduction*, *Adv. Phys.* **10**, 107 (1961).
- [313] M. Raynal, *Distributed Algorithms for Message-Passing Systems* (Springer, Berlin, Heidelberg, 2013).
- [314] S. Larsson and V. Thomée, *Partial Differential Equations with Numerical Methods*, Vol. 45, Texts in Applied Mathematics (Springer, Berlin, Heidelberg, 2003).
- [315] V. Thomée, *Galerkin Finite Element Methods for Parabolic Problems*, 2nd ed., Vol. 25, Springer Series in Computational Mathematics (Springer, Berlin, Heidelberg, 2006).
- [316] S. Balay, S. Abhyankar, M. F. Adams, J. Brown, P. Brune, K. Buschelman, V. Eijkhout, W. D. Gropp, et al., *PETSc Web page*, <http://www.mcs.anl.gov/petsc>, [Online; accessed 2 September 2015], 2014.
- [317] J. E. Guyer, D. Wheeler, and J. A. Warren, *FiPy: Partial Differential Equations with Python*, *Comput. Sci. Eng.* **11**, 6 (2009).
- [318] P. V. Demekhin, D. Hochstuhl, and L. S. Cederbaum, *Photoionization of hydrogen atoms by coherent intense high-frequency short laser pulses: Direct propagation of electron wave packets on large spatial grids*, *Phys. Rev. A* **88**, 023422 (2013).
- [319] N. Rohringer and R. Santra, *Multichannel coherence in strong-field ionization*, *Phys. Rev. A* **79**, 053402 (2009).
- [320] U. V. Riss and H.-D. Meyer, *Reflection-free complex absorbing potentials*, *J. Phys. B: At. Mol. Opt. Phys.* **28**, 1475 (1995).
- [321] U. V. Riss and H.-D. Meyer, *The transformative complex absorbing potential method: a bridge between complex absorbing potentials and smooth exterior scaling*, *J. Phys. B: At. Mol. Opt. Phys.* **31**, 2279 (1998).
- [322] N. Moiseyev, *Derivations of universal exact complex absorption potentials by the generalized complex coordinate method*, *J. Phys. B: At. Mol. Opt. Phys.* **31**, 1431 (1998).
- [323] O. Shemer, D. Brisker, and N. Moiseyev, *Optimal reflection-free complex absorbing potentials for quantum propagation of wave packets*, *Phys. Rev. A* **71**, 032716 (2005).
- [324] Y. Sajeev, M. Sindelka, and N. Moiseyev, *Reflection-free complex absorbing potential for electronic structure calculations: Feshbach type autoionization resonance of Helium*, *Chem. Phys.* **329**, 307 (2006).
- [325] B. Shizgal, *Spectral Methods in Chemistry and Physics*, Scientific Computation (Springer Netherlands, 2015).
- [326] J. Shen, T. Tang, and L.-L. Wang, *Spectral Methods*, Vol. 41, Springer Series in Computational Mathematics (Springer, Berlin, Heidelberg, 2011).
- [327] J. C. Light and T. Carrington, in *Adv. chem. phys.* Vol. 114, edited by I. Prigogine and S. A. Rice, Advances in Chemical Physics (John Wiley & Sons, Inc., 2000), pp. 263–310.

- [328] J. C. Light, I. P. Hamilton, and J. V. Lill, *Generalized discrete variable approximation in quantum mechanics*, *J. Chem. Phys.* **82**, 1400 (1985).
- [329] D. E. Manolopoulos and R. E. Wyatt, *Quantum scattering via the log derivative version of the Kohn variational principle*, *Chem. Phys. Lett.* **152**, 23 (1988).
- [330] D. T. Colbert and W. H. Miller, *A novel discrete variable representation for quantum mechanical reactive scattering via the S-matrix Kohn method*, *J. Chem. Phys.* **96**, 1982 (1992).
- [331] R. G. Littlejohn and M. Cargo, *Multidimensional discrete variable representation bases: Sinc functions and group theory*, *J. Chem. Phys.* **116**, 7350 (2002).
- [332] R. G. Littlejohn, M. Cargo, T. Carrington, K. A. Mitchell, and B. Poirier, *A general framework for discrete variable representation basis sets*, *J. Chem. Phys.* **116**, 8691 (2002).
- [333] D. L. Cohn, *Measure Theory*, 2nd ed., Birkhäuser Advanced Texts Basler Lehrbücher (Springer, New York, 2013).
- [334] A. Klenke, *Probability Theory. A Comprehensive Course*, 2nd ed., Universitext (Springer, London, 2014).
- [335] I. Steinwart and A. Christmann, *Support Vector Machines*, Information Science and Statistics (Springer, New York, 2008).
- [336] W. Gautschi, *Numerical Analysis*, 2nd ed. (Birkhäuser, Boston, 2012).
- [337] F. W. Olver, D. W. Lozier, R. F. Boisvert, and C. W. Clark, eds., *NIST Handbook of Mathematical Functions* (Oxford University Press, New York, 2010).
- [338] A. Greenbaum and T. P. Chartier, *Numerical Methods* (Princeton University Press, Princeton, New Jersey, 2012).
- [339] A. Fichtner, *Full Seismic Waveform Modelling and Inversion*, Advances in Geophysical and Environmental Mechanics and Mathematics (Springer, Berlin, Heidelberg, 2011).
- [340] J. S. Hesthaven and T. Warburton, *Nodal Discontinuous Galerkin Methods*, Vol. 54, Texts in Applied Mathematics (Springer, New York, 2008).
- [341] M. Abramowitz and I. A. Stegun, eds., *Handbook of Mathematical Functions* (Dover Publications, 1965).
- [342] B. I. Schneider, L. A. Collins, and S. X. Hu, *Parallel solver for the time-dependent linear and nonlinear Schrödinger equation*, *Phys. Rev. E* **73**, 036708 (2006).
- [343] X. Guan, K. Bartschat, and B. I. Schneider, *Dynamics of two-photon double ionization of helium in short intense xuv laser pulses*, *Phys. Rev. A* **77**, 043421 (2008).
- [344] S. X. Hu, *Optimizing the FEDVR-TDCC code for exploring the quantum dynamics of two-electron systems in intense laser pulses*, *Phys. Rev. E* **81**, 056705 (2010).
- [345] I. Březinová, L. A. Collins, K. Ludwig, B. I. Schneider, and J. Burgdörfer, *Wave chaos in the nonequilibrium dynamics of the Gross-Pitaevskii equation*, *Phys. Rev. A* **83**, 043611 (2011).

- [346] W. Hundsdorfer and J. Verwer, *Numerical Solution of Time-Dependent Advection-Diffusion-Reaction Equations*, Vol. 33, Springer Series in Computational Mathematics (Springer, Berlin, Heidelberg, 2003).
- [347] C. S. R. Murthy, K. N. B. Murthy, and S. Aluru, *New parallel algorithms for direct solution of linear equations* (Wiley-Interscience, 2001).
- [348] T. Rauber and G. Rünger, *Parallel Programming*, 2nd ed. (Springer, Berlin, Heidelberg, 2013).
- [349] H. Bauke and S. Mertens, *Cluster Computing. Praktische Einführung in das Hochleistungsrechnen auf Linux-Clustern*, X.systems.press (Springer, Berlin, Heidelberg, 2006).
- [350] W. Gropp, E. Lusk, and A. Skjellum, *Using MPI. Portable Parallel Programming with the Message-Passing Interface*, 2nd ed., Scientific and Engineering Computation (MIT Press, Cambridge, Massachusetts, 1999).
- [351] W. Gropp, E. Lusk, and R. Thakur, *Using MPI-2. Advanced Features of the Message-Passing Interface*, Scientific and Engineering Computation (MIT Press, Cambridge, Massachusetts, 1999).
- [352] The HDF Group, *Hierarchical Data Format, version 5*, <http://www.hdfgroup.org/HDF5/>, [Online; accessed 2 September 2015], 1997–2015.
- [353] H. Fehske, R. Schneider, and A. Weiße, *Computational Many-Particle Physics*, Vol. 739, Lecture Notes in Physics (Springer, Berlin, Heidelberg, 2008).
- [354] T. A. White, R. A. Kirian, A. V. Martin, A. Aquila, K. Nass, A. Barty, and H. N. Chapman, *CrystFEL: a software suite for snapshot serial crystallography*, *J. Appl. Crystallogr.* **45**, 335 (2012).
- [355] S. Byna, J. Chou, O. Rubel, Prabhat, H. Karimabadi, W. S. Daughter, V. Roytershteyn, E. W. Bethel, et al., *Parallel I/O, Analysis, and Visualization of a Trillion Particle Simulation*, in *Proceedings of the 2012 International Conference for High Performance Computing, Networking, Storage and Analysis*, SC '12 (2012), pp. 1–12.
- [356] B. S. Jovanović and E. Süli, *Analysis of Finite Difference Schemes. For Linear Partial Differential Equations with Generalized Solutions*, Vol. 46, Springer Series in Computational Mathematics (Springer, London, 2014).
- [357] E. Hairer and G. Wanner, *Solving Ordinary Differential Equations II. Stiff and Differential-Algebraic Problems*, Vol. 14, Springer Series in Computational Mathematics (Springer, Berlin, Heidelberg, 1996).
- [358] M. Luskin, R. Rannacher, and W. Wendland, *On the Smoothing Property of the Crank-Nicolson Scheme*, *Appl. Anal.* **14**, 117 (1982).
- [359] J. T. Beale, *Smoothing Properties of Implicit Finite Difference Methods for a Diffusion Equation in Maximum Norm*, *SIAM J. Numer. Anal.* **47**, 2476 (2009).
- [360] V. Hernandez, J. E. Roman, and V. Vidal, *SLEPc: a scalable and flexible toolkit for the solution of eigenvalue problems*, *ACM Trans. Math. Software* **31**, 351 (2005).

- [361] E. Hairer, G. Wanner, and S. P. Nørsett, *Solving Ordinary Differential Equations I. Nonstiff Problems*, Vol. 8, Springer Series in Computational Mathematics (Springer, Berlin, Heidelberg, 1993).
- [362] S. Gottlieb, C.-W. Shu, and E. Tadmor, *Strong Stability-Preserving High-Order Time Discretization Methods*, *SIAM Rev.* **43**, 89 (2001).
- [363] D. I. Ketcheson, *Highly Efficient Strong Stability-Preserving Runge-Kutta Methods with Low-Storage Implementations*, *SIAM J. Sci. Comput.* **30**, 2113 (2008).
- [364] S. Gottlieb, D. I. Ketcheson, and C.-W. Shu, *High Order Strong Stability Preserving Time Discretizations*, *J. Sci. Comput.* **38**, 251 (2009).
- [365] M. Suzuki, *Decomposition formulas of exponential operators and Lie exponentials with some applications to quantum mechanics and statistical physics*, *J. Math. Phys.* **26**, 601 (1985).
- [366] M. Suzuki, *General theory of fractal path integrals with applications to manybody theories and statistical physics*, *J. Math. Phys.* **32**, 400 (1991).
- [367] P. Bader, S. Blanes, and F. Casas, *Solving the Schrödinger eigenvalue problem by the imaginary time propagation technique using splitting methods with complex coefficients*, *J. Chem. Phys.* **139**, 12 (2013).
- [368] C. Moler and C. Van Loan, *Nineteen Dubious Ways to Compute the Exponential of a Matrix, Twenty-Five Years Later*, *SIAM Rev.* **45**, 3 (2003).
- [369] R. B. Sidje, *Expokit: A Software Package for Computing Matrix Exponentials*, *ACM Trans. Math. Softw.* **24**, 130 (1998).
- [370] C. A. Kennedy and M. H. Carpenter, *Additive Runge-Kutta schemes for convection-diffusion-reaction equations*, *Appl. Numer. Math.* **44**, 139 (2003).
- [371] L. Pareschi and G. Russo, *Implicit-explicit Runge-Kutta schemes and applications to hyperbolic systems with relaxation*, *J. Sci. Comput.* **25**, 129 (2005).
- [372] S. Boscarino, L. Pareschi, and G. Russo, *Implicit-Explicit Runge-Kutta Schemes for Hyperbolic Systems and Kinetic Equations in the Diffusion Limit*, *SIAM J. Sci. Comput.* **35**, A22 (2013).
- [373] Y. Saad, *Iterative Methods for Sparse Linear Systems*, 2nd ed., Other Titles in Applied Mathematics (SIAM, Soc. for Industrial and Applied Mathematics, 2003).
- [374] A. Greenbaum, *Iterative Methods for Solving Linear Systems*, Frontiers in Applied Mathematics (SIAM, Soc. for Industrial and Applied Mathematics, 1997).
- [375] A. Greenbaum, V. Pták, and Z. Strakoš, *Any Nonincreasing Convergence Curve is Possible for GMRES*, *SIAM J. Matrix Anal. Appl.* **17**, 465 (1996).
- [376] M. S. Gordon and M. W. Schmidt, in *Theory and Applications of Computational Chemistry*, edited by C. E. Dykstra, G. Frenking, K. S. Kim, and G. E. Scuseria (Elsevier, Amsterdam, 2005), pp. 1167–1189.

- [377] M. Valiev, E. J. Bylaska, N. Govind, K. Kowalski, T. P. Straatsma, H. J. J. Van Dam, D. Wang, J. Nieplocha, et al., *NWChem: A comprehensive and scalable open-source solution for large scale molecular simulations*, *Comput. Phys. Commun.* **181**, 1477 (2010).
- [378] M. Braun, *Finite element Hartree-Fock calculations in three dimensions for atoms and small molecules*, *J. Comput. Appl. Math.* **270**, 100 (2014).
- [379] A. T. Wong and R. J. Harrison, *Approaches to Large-Scale Parallel Self-Consistent Field Calculations*, *J. Comput. Chem.* **16**, 1291 (1995).
- [380] R. J. Harrison, M. F. Guest, R. A. Kendall, D. E. Bernholdt, A. T. Wong, M. Stave, J. L. Anchell, A. C. Hess, et al., *Toward High-Performance Computational Chemistry: II. A Scalable Self-Consistent Field Program*, *J. Comput. Chem.* **17**, 124 (1996).
- [381] I. T. Foster, J. L. Tilson, A. F. Wagner, R. L. Shepard, R. J. Harrison, R. A. Kendall, and R. J. Littlefield, *Toward High-Performance Computational Chemistry: I. Scalable Fock Matrix Construction Algorithms*, *J. Comput. Chem.* **17**, 109 (1996).
- [382] V. Weber and M. Challacombe, *Parallel algorithm for the computation of the Hartree-Fock exchange matrix: Gas phase and periodic parallel ONX*, *J. Chem. Phys.* **125**, 104110 (2006).
- [383] I. Freund and B. F. Levine, *Optically Modulated X-Ray Diffraction*, *Phys. Rev. Lett.* **25**, 1241 (1970).
- [384] F. Cardarelli, *Encyclopaedia of Scientific Units, Weights and Measures. Their SI Equivalences and Origins*, rev. and expanded ed. (Springer, London, 2003).
- [385] V. P. Krainov, H. R. Reiss, and B. M. Smirnov, *Radiative Processes in Atomic Physics* (John Wiley & Sons, Inc., 1997).
- [386] V. Y. Pan, *Solving a polynomial equation: Some history and recent progress*, *SIAM Rev.* **39**, 187 (1997).
- [387] E. Jones, T. Oliphant, P. Peterson, et al., *SciPy: Open source scientific tools for Python*, <http://www.scipy.org/>, [Online; accessed 2 September 2015], 2001–2015.
- [388] *Maple 2015*, Maplesoft, a division of Waterloo Maple Inc., Waterloo, Ontario. 2015.
- [389] I. Yavneh, *Why Multigrid Methods Are So Efficient*, *Comput. Sci. Eng.* **8**, 12 (2006).
- [390] R. Grobe and J. H. Eberly, *One-dimensional model of a negative ion and its interaction with laser fields*, *Phys. Rev. A* **48**, 4664 (1993).
- [391] R. W. Robinett, *Quantum mechanical time-development operator for the uniformly accelerated particle*, *Am. J. Phys.* **64**, 803 (1996).



# Publications

- [288] B. Kaiser, A. Brand, M. Glässl, A. Vagov, V. M. Axt, and U. Pietsch, *Photoionization of resonantly driven atomic states by an extreme ultraviolet-free-electron laser: intensity dependence and renormalization of Rabi frequencies*, [New J. Phys. \*\*15\*\*, 093016 \(2013\)](#).
- [299] A. Brand, B. Kaiser, A. Vagov, V. M. Axt, and U. Pietsch, *Non-Markovian behavior of ultrafast coherent ionization dynamics in a crystal exposed to a seeded free-electron-laser pulse*, [Phys. Rev. A \*\*89\*\*, 063404 \(2014\)](#).
- [302] A. Brand, B. Kaiser, A. Vagov, V. M. Axt, and U. Pietsch, *Model study on how an ordered grouping of atoms affects their inner-shell photoionization*, [Phys. Rev. A \*\*92\*\*, 033424 \(2015\)](#).



# Acknowledgments

I am grateful to everyone who has supported me during the work on this dissertation:

- I would like to express my sincere gratitude to my advisor Vollrath Martin Axt for his guidance, patience, extraordinary support, and providing a great atmosphere for doing research.
- I am grateful to our collaborator Ullrich Pietsch for his support, valuable feedback, and sharing his ideas.
- I would like to thank all members and alumni of the group, in particular: Benjamin Kaiser, Andreas Barth, Martin Gläßl, Moritz Cygorek, Christoph Thurn, Markus Hofmann, Alexei Vagov, and Monika Birkelbach.
- I would like to thank Helmut R. Brand for sharing his wisdom in all areas of physics.
- I am grateful to a referee of unknown identity for her/his constructive criticism on Ref. [299].
- I would like to give my sincere thanks to Robin Santra for his visit to Bayreuth (and again Martin Gläßl for inviting him).
- I would like to praise our almighty admin Markus Hilt.
- I greatly appreciated the fast bug fixes by Jose E. Roman from [SLEPc](#). When I dared to use the experimental part of the library, emails worked better than any debugger.
- I gratefully acknowledge the financial support by the [Bundesministerium für Bildung und Forschung \(BMBF\)](#) through the grant 05K10WCA [5].
- I would like to thank the University of Bayreuth Graduate School for the financial support regarding conferences and for the organization of very interesting events/seminars.
- I am grateful to my family and friends, in particular: Peter Rupprecht.



# Eidesstattliche Versicherung

Hiermit versichere ich an Eides statt, dass ich die vorliegende Arbeit selbstständig verfasst und keine anderen als die von mir angegebenen Quellen und Hilfsmittel verwendet habe.

Weiterhin erkläre ich, dass ich die Hilfe von gewerblichen Promotionsberatern bzw. -vermittlern oder ähnlichen Dienstleistern weder bisher in Anspruch genommen habe noch künftig in Anspruch nehmen werde.

Zusätzlich erkläre ich hiermit, dass ich keinerlei frühere Promotionsversuche unternommen habe.

Bayreuth, den 29. Januar 2016

---

André Brand